

Using in-field and remote sensing data to monitor permafrost dynamics in Northern Quebec

DISSERTATION AN DER FAKULTÄT FÜR GEOWISSENSCHAFTEN DER LUDWIG-
MAXIMILIANS-UNIVERSITÄT MÜNCHEN

Vorgelegt von Inga May

14.09.2011

1. Gutachter: Prof. Dr. Ralf Ludwig
2. Gutachter: Prof. Dr. Monique Bernier

Tag der Disputation: 09.11.2011

*ippasaq qaangirsimajuq
qauppat qaujimananngituq
kisiani ullumi atiqalaqjuq taimaak-
qupanuaq ullungatitut anninarami*



*Yesterday is history
Tomorrow is a mystery
Today is a gift –
that's why it is called present*

ACKNOWLEDGMENTS

The work presented in this thesis was conducted as part of a joint research project between the department of Geography at the Ludwig -Maximilians University of Munich (LMU) and the Centre – Eau Terre Environment at the Institut national de la recherche scientifique (INRS-ETE). Finance was mainly provided by the University of Munich, but travel costs for field work and workshops were covered by contributions from both the DFG (Deutsche Forschungsgemeinschaft) and the Canadian ArticNet initiative, in which the project was officially embedded.

Together with my doctoral advisors Prof. Dr. Ralf Ludwig (LMU) and Prof. Dr. Monique Bernier (INRS-ETE), I was able to write a proposal and accomplish the goals laid out; and I am more than grateful to them for giving me this wonderful and unique opportunity to work independently, despite the subject not being one of their major research fields. I really appreciate the confidence they placed in me, which enabled me to develop my own ideas and explore and discover new methods. Their endless enthusiasm and support in my project has repeatedly motivated me. I must mention in particular at this point how much I enjoyed the time we spent together in the field and I really hope they had a great time there too.

I would like to thank Prof. Dr. Ralf Ludwig in particular; who has been present alongside me and my studies since my early days at the University. He always helped and supported me; we have worked together on so many different projects and studies, and I have definitely profited and learned a great deal from his attitude and working experience.

Also I must mention the outstandingly warm welcome from Prof. Dr. Monique Bernier and her teams during every one of my visits to Quebec, my stays at the institute have been really agreeable, fruitful and funny.

An enormous thank-you also goes to Dr. Jenny Baesemen, director of the Association of Polar Earlier Career Scientist (APECS), and to Dr. Hugues Lantuit from the Alfred- Wegener Institute in Potsdam: the time and energy you have both spent in helping me to shape my career has amazed me. It is only because of you that I have been so successful in the last two years in the scientific world of polar research, as a result of the meetings you took me to, the scientists you introduced me to and the opportunities you gave me to get involved.

Another important figure during my time as a PhD student was my colleague and good friend Dr. Monika Prasch. All the good advice and hints she gave me, and all the discussions we had, were absolutely necessary to deal with and solve all the problems related to this work. The same is true of my PhD-fellow and roommate Philip Marzahn.

I am also more than grateful to my mentor Prof. Dr. Bettina Reichenbacher of the *LMU Mentoring GeoSciences Program* for her interest in my progress, for always listening to my problems, and confirming my ideas and intentions. I really enjoyed every one of our meetings.

For the great time in the field I would like to express my gratitude to Prof. Dr. Michel Allard from the University of Laval, Quebec, who gave me the best introduction in permafrost research; to Yannick Duguay, who even collected some data for me when I could not join the trips; and to Denis Sarrazin for his untiring help.

Of crucial importance to the progress of my work was Dr. Daniel Waldman who invested several days to work and solve some computer and software related problems. Without him I would probably have needed twice as much time to finish.

My special thanks also go to my good friends Harry Borlase, Mariette Wheeler, Catherine Brown, Nicole Couture and Helen Atkinson who spent their time correcting my English, and to Caroline Larrivée who not only helped me with the French version of the summary, but also was mainly responsible for the development of the project itself.

Of course I would also like to thank all my other colleagues from the University in Munich and INRS with whom I spent some really great moments, and who made this occasionally tough time much more agreeable. The same applies to all my APECS fellows – it was amazing to work with so many motivated and active people from all over the world.

Wholeheartedly I would like to thank my parents: You are simply the best! Your endorsement and interest in my work was much more than everything you already give and I know that none of this would have happened without you!

TABLE OF CONTENTS

ACKNOWLEDGMENTS	IV
TABLE OF CONTENTS	VI
LIST OF FIGURES	VIII
LIST OF TABLES	XIII
LIST OF ACRONYMS	XV
LIST OF SYMBOLS	XVII
1 Introduction	1
1.1 Outline of the thesis	2
2 Arctic climate and climate change	4
2.1 Arctic climate: past and present	4
2.2 The Arctic climate during the 20th century	7
2.2.1 Temperature	7
2.2.2 Precipitation	8
2.2.3 Further climate parameters	8
2.3 The Arctic climate prior to 100 years BP	8
2.4 The Arctic climate: Future	9
3 Permafrost	12
3.1 Distribution of permafrost	12
3.2 Permafrost: Structure and behavior	14
3.3 Typical permafrost features	16
3.4 The thermal state of the permafrost	17
3.4.1 Observed alterations in permafrost.....	18
3.4.2 Global consequences.....	19
4 State of the art and motivation	22
5 Test Site: Umiujaq	24
5.1 Climate	24
5.2 Geomorphology and geology.....	25
5.2.1 Recent morphology	27
5.3 Vegetation	27
5.4 Population	28
5.5 Climate change and consequences for Umiujaq	28
6 Field Work	30
6.1 Description of field work.....	30
6.2 Correlation between vegetation, snow cover and active layer thickness	32
6.2.1 Introduction	32
6.2.2 Methods and results	34
6.2.3 Conclusion	44
6.3 Geodetical survey of lithalsas	46
6.3.1 Differential GPS	46
7 Remote Sensing Data	62
7.1 Optical Sensors	62
7.1.1 Available Data	64
7.1.2 Methods.....	66
7.1.3 Results.....	73

7.1.4	Conclusion	82
7.2	Radar.....	82
7.2.1	Radar system theory	82
7.2.2	Differential interferometry	86
7.2.3	Data selection process.....	100
7.2.4	Results and discussion	105
7.2.5	Discussion.....	118
7.2.6	Comparison of differential interferometry and the field data	121
8	Conclusion and Outlook.....	125
9	Summary	130
9.1	Summary.....	130
9.2	Zusammenfassung	131
9.3	Résumé	134
10	References	137
11	Appendix	155
12	Curriculum Vitae.....	180

LIST OF FIGURES

Figure 2.1: Arctic boundary (red line) based on the 10°C July isotherm. The letters A-E indicate the location of climate stations discussed later (modified after AMAP 1998, AMAP 1997, CAFF 2001).....	5
Figure 2.2: Five exemplary circumpolar climate stations. Their locations can be found in figure 2.1 indicated with the letter A – E.	6
Figure 2.3: Temperature anomalies during the last century (modified after ACIA 2001)	7
Figure 2.4: The four main storylines defined by the IPCC with a more detailed description for the scenarios A2 and B2 used for the results represented in this Chapter	9
Figure 2.5: Temperature changes (left) and precipitation changes (right) averaged over the five designated B2 projections (modified after KATSOV & KÄLLÉN 2005).....	10
Figure 3.1: Permafrost distribution on the Northern Hemisphere (modified after IPA 1998)	13
Figure 3.2: Temperature profiles of different soil types near Ft. Simpson (modified after BURGESS & SMITH 2010).....	14
Figure 3.3: The different ground ice forms and the related land surface features	15
Figure 3.4: Ice wedge polygons as an example of pattern ground (SHORT no date).....	17
Figure 5.1: Location of the test site Umiujaq, Northern Quebec, Canada	24
Figure 5.2: Climate diagram from Umiujaq based on the mean climate values recorded by Environment Canada (2004) for the time period 1971-2000	25
Figure 5.3: Map of the two Precambrian entities (modified after LÈVESQUE ET AL. 1988)	26
Figure 6.1: Overview of the dates of the data acquisition for the remote sensing data (top) and the field data (bottom)	31
Figure 6.2: Recorded snow depths [cm] at the different sample points in 2009 (light grey) and 2010 (dark grey).....	35
Figure 6.3: Snowfall [cm] for the months October, November, December, January, February and March in 2009 (light grey) and 2010 (dark grey).....	35
Figure 6.4: Deviations of each point [%] from the mean of all samples from 2009 (light gray) and 2010 (dark gray).....	36
Figure 6.5: Recorded snow densities [g/cm ³] at the different sample points in 2009 (light grey) and 2010 (dark grey).....	37
Figure 6.6: Correlation between snow depth and snow density, On the left the values for 2009 and on the right those for 2010	39
Figure 6.7: Two selected snow temperature profiles from the 17.04.2009 (left) and the 18.04.2009 (right).....	39
Figure 6.8: Air- snow temperature gradient [K] versus the measured snow depth [cm] in 2010	40
Figure 6.9: Relationship between the measured snow depth [cm] and the classified vegetation	43
Figure 6.10: Interrelation of the factors topography, active layer, vegetation and snow cover.....	45

Figure 6.11: Location of the surveyed lithalsas R, M and I near the village of Umiujaq; the left map shows the position in the area, whereas the right shows a focus on the three lithalsas I, R and M	48
Figure 6.12: Set up of the differential GPS.....	49
Figure 6.13: Location of the sample points of lithalsa R; in the background is the classification map is displayed. The local topography is represented by the framed letters	50
Figure 6.14: The dzl values average of all sample points of lithalsa R for each acquisition; Low values are standing for higher elevations. Records for the first acquisition date are only marginally taken into account for the analysis, as the base station was placed on a different spot	50
Figure 6.15: Left: Diagram showing the dzl values measured in August 2009 and 2010; Right: Table listing the differences between the dzl values of August 2009 and 2010. Red values are standing for subsidence, black for uplift.....	52
Figure 6.16: Location of the sample points of lithalsa M; in the background is the classification map is displayed. The local topography is represented by the framed letters.	53
Figure 6.17: The dzl values average of all sample points of lithalsa M for each acquisition; Low values are standing for higher elevations. Records for the first acquisition date are only marginally taken into account for the analysis, as the base station was placed on a different spot.	53
Figure 6.18: Left: Diagram showing the dzl values measured in August 2009 and 2010; Right: Table listing the differences between the dzl values of August 2009 and 2010. Red values are standing for subsidence, black for uplift.....	55
Figure 6.19: Location of the sample points of lithalsa I; in the background is the classification map is displayed. The local topography is represented by the framed letters.	56
Figure 6.20: The dzl values average of all sample points of lithalsa I for each acquisition; Low values are standing for higher elevations. Records for the first acquisition date are only marginally taken into account for the analysis, as the base station was placed on a different spot.	56
Figure 6.21: Left: Diagram showing the dzl values measured in August 2009 and 2010; Right: Table listing the differences between the dzl values of August 2009 and 2010. Red values are standing for subsidence, black for uplift.....	58
Figure 6.22: Trend of the lithalsa's elevation [m] over 20 months in relation to the base station and multiplied by -1. Averaged over 39 sample points and interpolated for the entire period. A separated curve for each lithalsa is displayed in grey	58
Figure 6.23: Steady- state temperature beneath the shoreline of a water body (modified after BROWN 1963)	61
Figure 7.1: A generalized illustration of the spectral response curve for bare soil (brown), vegetation (green) and water (blue) (modified after LILLESAND ET AL. 2008)	63
Figure 7.2: Coverage cycle, Landsat 1, 2 and 3. Each numbered line designates a northeast – to southwest pass of the satellite; the first pass on the next day (orbit 15) is immediately adjacent to pass 1 on the preceding day (CAMBPELL 2009).....	64

Figure 7.3: Exemplary a 3x3 kernel for high-pass filtering (left) and for low-pass filtering (right) are applied for the original image in the middle. The output values as well as the resulting image changes are displayed on both sides. It get obvious that the high-pass filter results in a contrast enhancement of the image, whereas the low-pass filter has a smoothing impact on the image.....	68
Figure 7.4: Schematic presentation of the classification process: On the left there is the original image, with different grey values in each band. The middle represent a grouping of pixels with similar values (spectral characteristics) which finally results in the image on the right, only representing the two classes A = Forest and B = Water (modified after ESPÍNOLA ET AL. 2008).....	68
Figure 7.5: Example for a confusions matrix. Values in bold (diagonal) are correct classified pixels. The value in the right bottom corner represent the total of correct classified pixels. The matrix shows furthermore all incorrect classified pixels, there were 48 pixels wrongly assigned to the class water, which would actually belong to the class forest (modified after MAUSER 2010).....	70
Figure 7.6: Principle of change detection analysis. The two black dots represent one pixel at different dates and their different location in the feature space. The change vector (red arrow) indicates the shift of the pixel within the feature space.....	73
Figure 7.7: Percentages of the entire area for the five land cover classes forest, bush, lichen/moss, rock and shallow water for years 1986 (grey) and 2008 (black).....	75
Figure 7.8: Percentages of the five land cover classes forest, bush, lichen/moss, rock and shallow water for years 2004 (grey) and 2009 (black).....	78
Figure 7.9: The maps show changed areas explored by the utilization of the WFMI, whereas red indicates increased vegetation and green decreased. The map on the left is generated by using the near infrared channel, the map on the right is based on the blue band.....	80
Figure 7.10: The map on the left shows the NDVI difference map of 2004 and 2005, whereas red indicates decreasing NDVI values and green increased.	81
Figure 7.11: Illustration of the different spatial resolution in a radar image (modified after ARONOFF 2005)	83
Figure 7.12: Principle of SAR operation. By processing the returns from the object (A) for the entire time it is illuminated by the radar beam, a short antenna can operate as if it was much longer (B) than its real length. This provides improved spatial resolution in flight direction (modified after ARONOFF 2005)	86
Figure 7.13: Left original SLC 140809 as delivered from the DLR; right cutted SLC 140809 as used for the processing.....	89
Figure 7.14: Unflattened unwrapped interferogram from 14.08.2009/ 25.08.2009	91
Figure 7.15: Flattened interferogram 14.08.09/ 25.08.09.....	93
Figure 7.16: Filtered interferogram 14.08.09/ 25.08.09.....	93
Figure 7.17: Principe of the unwrapping process, when the phase available in the sinus mode gets transformed into a continuous phase over the entire image (modified after SANTITAMNONT 1998)	94

Figure 7.18: Definition of a residue: If the circle numbers reflect the values and centres of pixels, the summation of the gradients between neighbouring pixels determines whether the loop is neutral (no residue) or whether a positive or a negative residue appears. In this case according to eq. 7.15 would be $0 = \text{no residue}$	95
Figure 7.19: Top: unwrapped interferogram 14.08.09/ 25.08.09 still remaining excluded areas which are not unwrapped; Bottom: unwrapped interferogram 14.08.09/ 25.08.09 with fulfilled gaps after the interpolation process.....	96
Figure 7.20: Relation between baseline and phase Difference (modified after ZEBKER ET AL. 2004) ...	97
Figure 7.21: Differential interferogram based on the two interferometric pairs 14.08.09/ 25.08.09 and 14.08.09/ 07.05.09	98
Figure 7.22: Vertical displacement map based on the differential interferogram generated by the interferometric pairs 14.08.09/ 25.08.09 and 14.08.09/ 07.05.09; one fringe represents one cm displacement	99
Figure 7.23: Final geocoded vertical displacement map based on the interferometric pairs 14.08.09/ 25.08.09 and 14.08.09/ 07.05.09; one fringe equals to one 1 cm vertical change.....	100
Figure 7.24: The different acquisition modes ScanSAR, StripMap and Spotlight from the TerraSAR-X satellite (modified after Infoterra GmbH 2011).....	101
Figure 7.25: Possible impact of the Cuestas on the radar signal	103
Figure 7.26: The combination of the different acquisition dates and their denotation. Top: the images dating to 2009; middle: images dating to 2010; bottom: image example of the combination of Int.1 and Int.2 to Diff.1	105
Figure 7.27: Main processing steps for the generation of a displacement map by means of the 3-Pass differential interferometry	106
Figure 7.28: Validity mask generated for the unwrapping process of Int.1 2009. It is based on the earlier computed coherence map and highlights all areas (black) that have to be excluded from the initial phase unwrapping due to their low coherence values. The used threshold therefore was 0.3	107
Figure 7.29: Composite image of the 14.08.2009, areas of radar shadow east of the Cuestas in the same way as water and reveal as very low coherent pixels in the coherence map	108
Figure 7.30: The two unwrapped interferograms Int.1 2009 (left) and Int.1 2010 (right). On top the DEM as reference. It can be clearly seen that both outcomes are very well reproducing the topography. The dashed black circle depicts some small hills visible in all maps. Phase display is 6π per color cycle	109
Figure 7.31: Example for the coregistration and resampling process. The red cross indicated the pixel that corresponds to the pixel in the master image (top). The right image shows the slave image before the coregistration and the red cross several meters east of the corresponding master pixel. In the left image the resulting resampled image shows a much better fit of the pixels	110
Figure 7.32: Unwrapped and unflattened Int.2 2009 (left) and Int.2 2010 (right). Int.2 2009 reflects much more the relief than Int.2 2010, probably caused by the longer spatial baseline. Phase display is 6π per color cycle	111

Figure 7.33: Diff.2 2009 with an IKONOS image in the background. The black surrounded area stands for the Cuesta subset. The strange appearing bend on the east side is a result of a small pond on the Cuestas that should not be included in the subset.....	112
Figure 7.34: Diff2.2010 (cleaned) vertical displacement map embedded in ArcGIS. Green areas experienced subsidence, lilac areas uplift	113
Figure 7.35: Location of the sampling points for the analysis, in the background the classification map based on the GeoEye image of 2009	114
Figure 7.36: Unwrapped and flattened Int.2 September (left), Int.2 October 2009 (middle) and Int.2 October 2010 (right); Phase display is 6π per color cycle	115
Figure 7.37: Left: Unwrapped and flattened Int.2 for the interannual differential interferogram; one fringe equals to one ; Right: The final vertical displacement map; one fringe equals to one cm displacement	117
Figure 7.38: Remaining snow patches in May (07.05.2010). Only in depressions and where dense vegetation causes snow accumulation the snow stays until May. (Photo I. May)	119
Figure 7.39: Comparison of differential interferometry and the field data	120
Figure 7.40: Comparison of the d-GPS measurements and the D-InSAR data for the time period May 2010 and August 2010 for the sample points on lithalsa R. All points having the same inside and outside color are showing similar behavior	122
Figure 7.41: Comparison of the d-GPS measurements and the D-InSAR data for the time period May 2010 and August 2010 for the sample points on lithalsa M. All points having the same inside and outside color are showing similar behavior	122
Figure 7.42: Comparison of the d-GPS measurements and the D-InSAR data for the time period August 2010 and October 2010 for the sample points on lithalsa I. All points having the same inside and outside color are showing similar behavior	123

LIST OF TABLES

Table 2.1:	Selected five AOGCM models	11
Table 3.1:	The percentage of permafrost occurrence for the different permafrost types	12
Table 3.2:	Summary of measured changes in the permafrost temperature	19
Table 6.1:	Overview of the different field campaigns, the measured parameters as well as the people involved.	31
Table 6.2:	Deviations in [%] from the mean for 2009 and 2010 for all sampling points where no accordance exists.	36
Table 6.3:	Dependencies of the different analyzed parameters. YES indicates coexistence, NO indicates no coexistence	45
Table 6.4:	Calculated differences for all sample points on R, between the different acquisition dates. Red numbers indicate subsidence, blue numbers indicate uplift. Blue framed columns represent the dates when uplift was expected. Dashed blue framed columns could be either uplift or subsidence. Numbers of the first column are italic as the measurements of April 2009 are questionable and are only marginal considered for the analysis.	51
Table 6.5:	Calculated differences for all sample points on M, between the different acquisition dates. Red numbers indicate subsidence, blue numbers indicate uplift. Blue framed columns represent the dates when uplift was expected. Dashed blue framed columns could be either uplift or subsidence. Numbers of the first column are italic as the measurements of April 2009 are questionable and are only marginal considered for the analysis.	54
Table 6.6:	Calculated differences for all sample points on M, between the different acquisition dates. Red numbers indicate subsidence, blue numbers indicate uplift. Blue framed columns represent the dates when uplift was expected. Dashed blue framed columns could be either uplift or subsidence. Numbers of the first column are italic as the measurements of April 2009 are questionable and are only marginal considered for the analysis.	56
Table 7.1:	Utilized images for the detection of vegetation changes and wetland expansion.....	64
Table 7.2:	Overview of the main parameters of the satellite delivering the data for this study	66
Table 7.3:	Overall accuracy [%] and kappa-coefficient for the six acquisition dates considered in this study	74
Table 7.4:	Percentages of changed land cover, subdivided in the different classes, for 1986 and 2008. The percentages are related to the total amount of pixels for each class. As the class water is not represented in this table, the percentages are not summing up to 100%	76
Table 7.5:	Percentages of changed land cover, subdivided in the different classes, for 1986 and 2008. The percentages are related to the total area [ha] for each class. As the class water and sand is not represented in this table, the percentages are not summing up to 100%	79
Table 7.6:	Occurrence of the four NDVI groups [%] in each scene	81
Table 7.7:	Overview of the different available radar bands, the corresponding wavelength and their main applications. In bold: The used band for this study	85
Table 7.8:	Different approaches of differential interferometry (modified after GAMMA 2008)	88

Table 7.9: Overview of the spatial resolution resulting from the acquisition modes decided for this study (modified after CAF 2009).....	102
Table 7.10: Overview of the properties of the used imagery.....	104
Table 7.11: All used acquisitions; In red the date for the master image	104
Table 7.12: Vertical displacement in cm in of all the five computed differential interferograms, for the Cuesta subset as well as for the three investigated lithalsas R, M and I (The movements of the lithalsas are not including the Cuesta uplift anymore).....	115
Table 7.13: Overview of the outcomes from all calculated image pairs, including coregistration accuracy, starting points and their coherences for the unwrap process and the both components of the spatial baseline	118
Table 7.14: Calculated differences [cm] between May 2010 and August 2010 for the three lithalsas based on the d-GPS and on the D-InSAR outcomes	121

LIST OF ACRONYMS

ACIA	Arctic Climate Impact Assessment
AMAP	Arctic Monitoring and Assessment Programme
ANTPAS	Antarctic Permafrost And Soils
AO	Arctic Oscillation
AOGCM	Atmosphere- Ocean General Circulation Model
ASTER	Advanced Spaceborne Thermal Emission and Reflection Radiometer
GIS	Geographical Information System
CAFF	Conservation of Arctic Flora and Fauna
CSRC	Canadian Spatial Reference System
CEN	Centre d'Études Nordiques
DEM	Digital Elevation Model
DFG	Deutsche Forschungsgemeinschaft
d-GPS	Differential Global Positioning System
D-InSAR	Differential Interferometric Synthetic Aperture Radar
DLR	Deutsches Zentrum für Luft- und Raumfahrt
ERDAS	Earth Resource Data Analysis System
ESRI	Environmental Systems Research Institute
ETM +	Enhanced Thematic Mapper
GHCN	Global Historical Climatology Network
GNSS	Global Navigation Satellite System
GPS	Global Position System
H	Horizontal Polarization
INRS-ETE	Institut National de la Recherche Scientifique – Centre Eau Terre Environnement
ICSU	International Council for Science
IPA	International Permafrost Association
IPCC	International Panel on Climate Change
IPY	International Polar Year
ISHD	International Surface Hourly Dataset
ISODATA	Iterative Self-Organizing Data Analysis
LMU	Ludwig-Maximilians University
MAGT	Mean annual ground temperature
MCF	Minimum Cost Flow
MNDWI	Modified Normalized Differential Water Index

MSS	Multispectral Scanner
MODIS	Moderate-resolution Imaging Spectroradiometer
NAHO	National Aboriginal Health Organization
NASA	National Aeronautics and Space Administration
NCDC	National Climatic Data Centre
NDWI	Normalized Differential Water Index
NDVI	Normalized Differential Vegetation Index
NIR	Near Infrared
NOAA	National National Oceanic and Atmospheric Administration
NRCan	Natural Resources Canada
NSIDC	National Snow and Ice Data Centre
PERMASAR	Stands for a Norwegian project that monitors Permafrost with SAR techniques
PPP	Precise Point Position
Radar	Radio detection and Ranging
RGB	Red Green Blue (color scheme)
SAR	Synthetic Aperture Radar
RTK	Real Time Kinematic
SIR-C	Spaceborne Imaging Radar - C
SLC	Single Look Complex
SLR	Side-looking Radar
SLAR	Side-looking Radar
SRES	Special Report on Emissions Scenarios
SRTM	Shuttle radar topography mission
SSC	Single Look Slant Range Complex
TanDEM-X	TerraSAR-X add-on for Digital Elevation Measurement
TCT	Tasseled-Cap-Transformation
TIN	Triangular irregular network
TIROS	Television and Infrared Observation Satellite
TM	Thematic Mapper
UL	University of Laval
UQTR	Université du Québec à Trois-Rivières
V	Vertical Polarization
WFMI	Write Function Memory Insertion
WGS	World Geodetic System

LIST OF SYMBOLS

Symbol	Description	Unit
B_n	Critical baseline	m
$B_{II} \text{ \& } B_{III}$	Baseline parallel to the look direction	m
c	Speed of light	m/s
d	Antenna diameter	m
δp	Component of the baseline parallel to the look direction	
d_{zl}	Difference basis station d-GPS and measured lithalsa hight	m
Δp	Phase change due to deformation	
θ	Incident angle	°
k	Band number in the multispectral range	
L_c	Size of the resolution cell in slant range	m
λ	Wavelength	m
μ_{ic}	Mean reflectance value in band k for class c	
N	sum of all pixel in the matrix	
n	Number of bands	
p_a	Azimuth resolution	m
p_g	Ground range resolution	m
p_r	Slant range	m
σ_{ck}	Standard deviation of the reflectance values in band k of all pixels of class c	
R	Sensor – target distance	m
r	Reflectance in band k of pixel at point i, j	
T	Height of satellite	m
t_p	Reflected pulse	
$\Phi \text{ \& } \Phi_I$	Phase difference (two sensors)	
x_{jj}	Number of correct claddified pixels of one class in row j and column j	
x_{j+}	sum of all classified pixels in row j	
x_{+j}	sum of all classified pixels in column j	
$\Psi_1 \text{ \& } \Psi_2$	Phase values	
z_b	Height of basis station d-GPS	m
$z_{l1} \text{ \& } z_{l2}$	Measured lithalsa height	m

1 Introduction

Permafrost underlies 25.6% percent of the northern hemisphere and has a huge impact on the affected regions in terms of their local ecosystem (ZHAN ET AL. 1999), but also for the resident population building their infrastructure on permanently frozen ground.

Permafrost has received much attention recently, due to the increasing surface temperatures in most affected regions of the Earth, bringing permafrost to the edge of widespread thawing and degradation. Not only the scientific community, but also global popular press all over the world is debating about permafrost degradation and makes it a highly delicate and important topic (e.g. Welt, Germany, 17.02.2011 'Zwei Drittel der Permafrostböden schmelzen bis 2200'; 7sur7, France, 25.02.2011 'Le dégel du pergélisol? Une bombe à retardement'; The Independent, UK, 30.05.2011 'Melting of the Arctic will accelerate climate change within 20 years').

The recent report about the 'State of the Arctic Coast 2010' (FORBES ET AL. 2011) was particularly influential in igniting a big discussion in Europe and Northern America and raised the public's awareness of the topic.

Yet, permafrost thawing occurs at the southern limits of the permafrost zone and it will very likely entail serious changes in ecosystems, in water and carbon cycles, and in infrastructure performance. If such trends proceed over the next decades, there is no doubt that communities in the regions of concern will be faced with many new problems including ecological, economical and social issues.

Among the most severe are changes to the northern ecosystem, by ways of alterations of the hydrological regime and the change of vegetation cover, expanding marsh and wetlands, or the decline of slope compaction and thus an elevated risk of landslide. Damage and increased remedial work and maintenance are expected for roads, runways, residences and community buildings in the growing villages of the North. Consequently, the native population could suffer from psychosocial stresses, related to the displacement of infrastructure and hunting and fishing grounds or modifications to nutrition.

Supervened to this problem is the prognosticated release of greenhouse gases, now stored in the frozen ground, that is very likely to evoke positive feedbacks on the warming climate.

Although it is widely understood that such alterations will happen, there is still much uncertainty about possible pathways of permafrost degradation and about the dimensions of such a decline.

Thus there is a high demand on a sound understanding of the biogeophysical processes involved in permafrost dynamics. Yet, the major problem is the research subject in itself, as the acquisition of related data is difficult due to the extreme climatic conditions for technical equipment, the size and remoteness of affected areas and the heterogeneity of permafrost in areal distribution and depth.

The findings discussed in this thesis deliver an important contribution to recent permafrost research. It is the output of a conjoint project between the department of Geography at the Ludwig -Maximilians University of Munich (LMU) and the Centre – Eau Terre Environment at the Institut national de la recherche scientifique (INRS-ETE) that was proposed and accomplished by Inga May under the supervision of Prof. Dr. Ralf Ludwig (LMU) and Prof. Dr. Monique Bernier (INRS-ETE). It was started in September 2008 and included six stays in the test site, as well as longer periods at both institutes. A strong collaboration and an intense exchange with scientists from the University of Laval (Prof. Michel

Allard) and the University of Trois-Rivières (Prof. Ester Levesque) ensured proper guidance in this research field and region.

The study was mainly financed by the University of Munich, but travel costs for the field work were partially covered by the DFG (Deutsche Forschungsgemeinschaft) and partially by the Canadian ArticNet initiative, in which the project was officially embedded. ArcticNet is a Network of Centres of Excellence that brings together scientists and managers in the natural, human health and social sciences with their partners in Inuit organizations, northern communities, federal and provincial agencies and the private sector to study the impacts of climate change in the coastal Canadian Arctic (ArcticNet 2004).

The investigation was conducted on a test site of about 60 km² in size around the Inuit village of Umiujaq in Northern Quebec, Canada, located at the eastern coast of the Hudson Bay.

The study explores the possibilities to use satellite imagery for the required observation and monitoring of the permafrost distribution and dynamics, and hence deliver an approach, that can overcome the remoteness problem. The most challenging research question thereby is the non-visibility of frozen ground at the landsurface. That drives into a method which only detects indicators for permafrost occurrence, but not the permafrost itself. Accordingly, the work of this project was mainly composed of two main scientific objectives:

1. The identification of visible features at the surface that indicates the permafrost state. This was implemented by the analysis and statistical evaluation of field data collected during field campaigns.
2. The debugging and development of remote sensing techniques which are feasible to detect the defined indicators. For it, optical data served for the testing of several change detection methods and radar data was used to explore the applicability of differential interferometry to monitor elevation changes.

In addition to an advanced knowledge about surface changes attributed to permafrost dynamics and the new skills to spatially detect such, the outcomes of this project also deliver the necessary understanding for future monitoring and modeling systems: The understanding about the co-occurrences of permafrost and features at land surface, and their appearance in remote sensing data can enable the development of modeling systems fed by remote sensing data by ways of parameter retrieval and data assimilation.

1.1 Outline of the thesis

According to these two major research topics, the thesis is subdivided into a field work section and a section containing the remote-sensing analysis. Beforehand chapter 2, 3, 4 and 5 will provide the essential background information about the research.

Chapter 2 gives a general overview about the climatic situation of the northern hemisphere and the expected developments in the future. The following chapter 3 introduces permafrost by talking about its distribution, its physical properties and its development during the last decades and in the future, as well as entailed consequences.

A summary of the recent state-of-the-art (Chapter 4) presents the numerous works that have already been conducted in this research field, but also outlines research fields that are still missing and formulates the motivation for this study. The background section ends with the presentation of the study site (Chapter 5), describing the main geographical aspects and the specific expected impacts of permafrost thawing.

The following section, composing the field work as well as the remote-sensing analysis, forms the major part of this thesis. It starts with the description of the field campaigns (Chapter 6), and is distinguished in a first section dealing with the correlation between the permafrost thawing and the occurring snow and vegetation cover (Chapter 6.1). The second section explains the monitoring of the elevation movements of frost mounds (Chapter 6.2), caused by permafrost thawing and freezing, surveyed by means of a differential global positioning system (d-GPS).

Similar, the remote sensing part first discusses the possibilities of using optical sensors in order to detect land surface changes (Chapter 7.1) and second presents the implementation of differential interferometry (d-InSAR) techniques and their feasibility to observe elevation changes (Chapter 7.2).

Chapter 7.2.6 compares the outcomes of the field and the remote sensing data and concludes this section.

Finally, a conclusion (Chapter 8) summarizes the most important results and gives some necessities for forth-coming studies.

2 Arctic climate and climate change

The Earth's climate plays an important role for the entire global system and influences our daily life to an unconceivable extent.

It is responsible for the available energy, in terms of solar radiation and water, and consequently the reason for the development of the different vegetation zones on Earth. Hence the availability of food resources, plants as well as meat, are dependent on the regional climate conditions and allow settlements in some regions, hindered life conditions in others and even rule out the establishment of human infrastructure in parts of the world.

Since the beginning of civilization, people have tried to adapt to the given climatic situations and expand their living space. Nowadays many different cultures, dealing with different environmental conditions exist around the globe, depending on their ambient nature.

Consequently, changing climatic conditions have been already recorded at many places, and the global temperature which now rises at a rate unprecedented in the experience of modern human society, is a problem that needs to be tackled by every country (ANISIMOV & FITZHARRIS 2001).

Recent climatic changes have been experienced particularly intense in the Arctic. Because this region plays a special role in global climate, such alterations will affect the rest of the world in many ways. Beginning with the IPCC report from 2001 and repeated in the fourth Assessment Report (2007), the situation of the Polar Regions is described as following:

Climate change in Polar Regions is expected to be among the largest and most rapid of any region on the Earth, and will cause major physical, ecological, sociological, and economic impacts, especially in the Arctic, Antarctic Peninsula, and Southern Ocean [...]. Polar Regions contain important drivers of climate change. Once triggered, they may continue for centuries, long after greenhouse gas concentrations are stabilized, and cause irreversible impacts on ice sheets, global ocean circulation, and sea-level rise (IPCC 2001).

To understand the dimensions of climate change in the Arctic, as well as the impacts for the globe, the next chapter (Chapter 2.1) presents the past and present situation of the Arctic climate, followed by a discussion of the predicted future situation (Chapter 2.2).

2.1 Arctic climate: past and present

There are different approaches that geographically define the 'Arctic' or 'Arctic Regions'; these include examples that are based on bathymetry or on administrative boundaries. In this study 'Arctic Regions' encompasses all areas suited between 60° and 90° North, as well as areas where the average temperature of July is less than 10°C (Figure 2.1). This definition was chosen, because it closely corresponds to the ecological circumstances, such as the occurrence of permafrost and the dominating vegetation, and hence matches best the topics of this work.

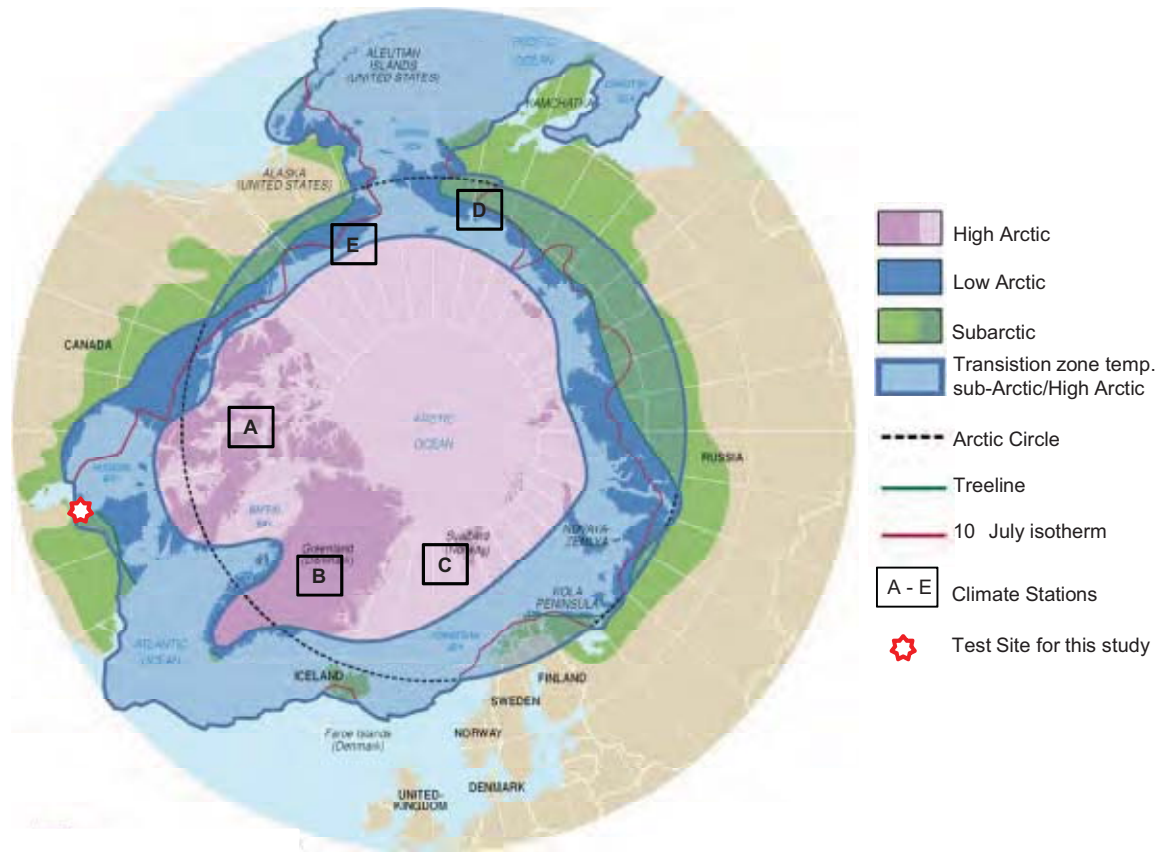


Figure 2.1: Arctic boundary (red line) based on the 10°C July isotherm. The letters A-E indicate the location of climate stations discussed later (modified after AMAP 1998, AMAP 1997, CAFF 2001)

The Arctic is the northern polar component of the global climate system, characterized by a low amount or absence of sunlight in winter and long days during summer. It interacts with climates of more southern latitudes in the form of atmospheric fluxes and ocean currents. The Arctic oscillation (AO) is a measure for this interaction, varies over time with no particular periodicity, and is defined by surface atmospheric pressure patterns. A positive AO value normally is related to lower pressure in polar regions often accompanied by strong zonal winds. A negative AO index in contrast, indicates higher pressure in the Arctic, less zonal winds, and a transport of cold air masses into middle latitudes (THOMPSON & WALLACE 1998).

Due to the sparse population and the remoteness of many Arctic regions, there is limited observational climate data, especially when it comes to long-term time series. Thus the estimate of the different climate parameters and in particular an assessment about trends is very difficult; it is therefore complicating to distinguish between the signals of climate variability and change (MCBEAN 2005). This gives rise to the fact that all statements about the climate contain a high amount of uncertainty and hence have to be handled with care.

Systematic in-situ Arctic meteorological observation started in the late 18th century in the Atlantic sector (TABONY 1981). Nowadays all Arctic countries are equipped with a synoptic observation system. In addition to the national climate stations, several international networks and institutions are collecting and sharing different kinds of datasets:

- The Integrated Surface Hourly Dataset (ISHD), run by the National Climatic Data Center (NCDC), incorporates all synoptic observations, distributed through the Global Telecommunication System during the past 30 years (NCDC 2011).
- The Comprehensive Aerological Reference Data Set collects all windsonde observations in the Arctic (NCDC et al. 2000).
- The World Data Centre is responsible for all the sea-ice data (ICSU 2006) available.
- The National Aeronautics and Space Administration (NASA) and the National Oceanic and Atmospheric Administration (NOAA) (National Climatic Data Center, National Snow and Ice Data Center – NSIDC) provide data about cloudiness, radiation budget, snow water equivalent, sea-ice and snow cover extent (ARMSTRONG & BRODZIK 2001; ROSSOW & SCHIFFER 1999; WIELICKI ET AL. 1995).

Based on a combination of the named data sources, the recent state of the climate as well as the development during the 20th century will be described in the following paragraph.

In general, the Arctic climate can be described as cold, as compared to the rest of the world, with low annual precipitation sums but with a high spatial heterogeneity: the mean annual surface temperature ranges from +4°C in Reykjavik, Iceland (64°N) to -28.1°C at the crest of the Greenland Ice Sheet at 3000 m elevation (71°N) (MCBEAN 2005). The lowest official recorded temperature in the northern hemisphere was in the East Russian province Verkhoyansk in 1892 and reached -69.8 °C (TRESHNIKIV 1985).

Also, the precipitation rates vary between less than 300 mm in Greenland (HUNTINGTON & WELLER 2005) to more than 1500 mm over the North Atlantic (SEEREZE & BARRY 2005). Most of the precipitation falls as either rain or snow, but in most of the regions snow is the dominant form. Only the high part of the Greenland Ice Sheet receives all of its precipitation as snow (SEEREZE & BARRY 2005). As an example of the circumpolar climate, the climate diagrams of Resolute (Canada, 74°N, 66 m), Centrale (Greenland, 72°N, ca. 2500 m), Isfjord (Norway, 78°N, 0 m), Tiksi (Russia, 71°N, 71 m), Point Barrow (USA, 71°N, 2m) are displayed in Figure 2.2.

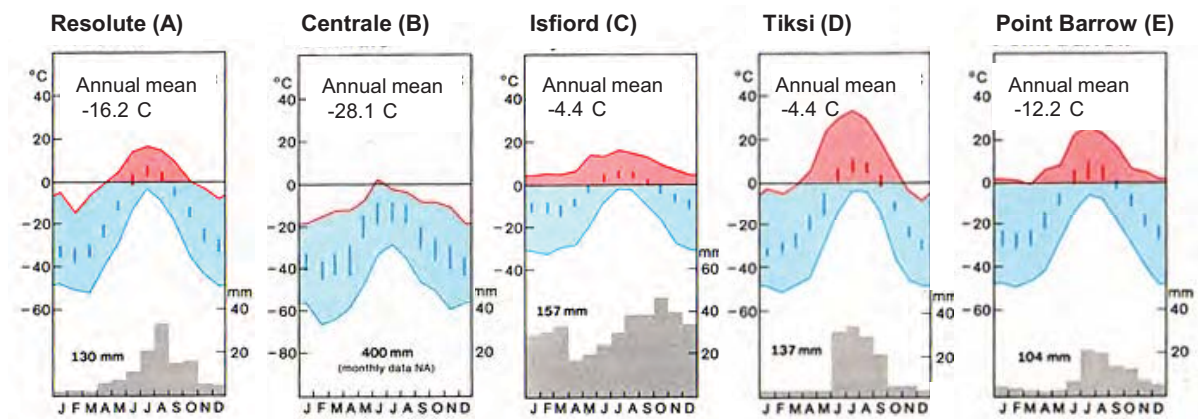


Figure 2.2: Five exemplary circumpolar climate stations. Their locations can be found in figure 2.1 indicated with the letter A – E. (modified after SEEREZE & BARRY 2005)

2.2 The Arctic climate during the 20th century

2.2.1 Temperature

Although it is difficult to assess trends in the Arctic, especially due to missing validation data, several analyses (COMISO 2003; POLYAKOV ET AL. 2003) have examined large-scale temperature variations and it appears as if they have increased throughout the Arctic during most of the 20th century (MCBEAN 2005). With augmenting temperatures of + 0.06 K per decade, the observed trend in the Arctic exceeds the global upward trend (IPCC 2001).

During the 20 year period between 1946 and 1965, widespread cooling was observed, however during this same time period, parts of Canada and Asia experienced warming. In the following years – between 1966 and 2003 - high decadal increases in most parts of northern Canada, Asia and Europe characterized the climate, whereas the most pronounced alterations happened in winter and spring (PETERSON ET AL. 1999).

Data prior to 1945 have to be tackled with caution as the scarcity of the measurement does only allow for vague statements. Nevertheless, based on analysis by POLYAKOV ET AL. (2003) from coastal station records, generally high average temperature in the 1930 can be observed, especially for Scandinavia. More interior stations show a higher warming than the coastal stations during the same time period (POLYAKOV ET AL. 2003). Still it remains difficult to distinguish whether the Arctic as a whole saw warm increases in the 30's in particular, or during the entire of the 20th century. In Figure 2.3 temperature anomalies during the last century are displayed.

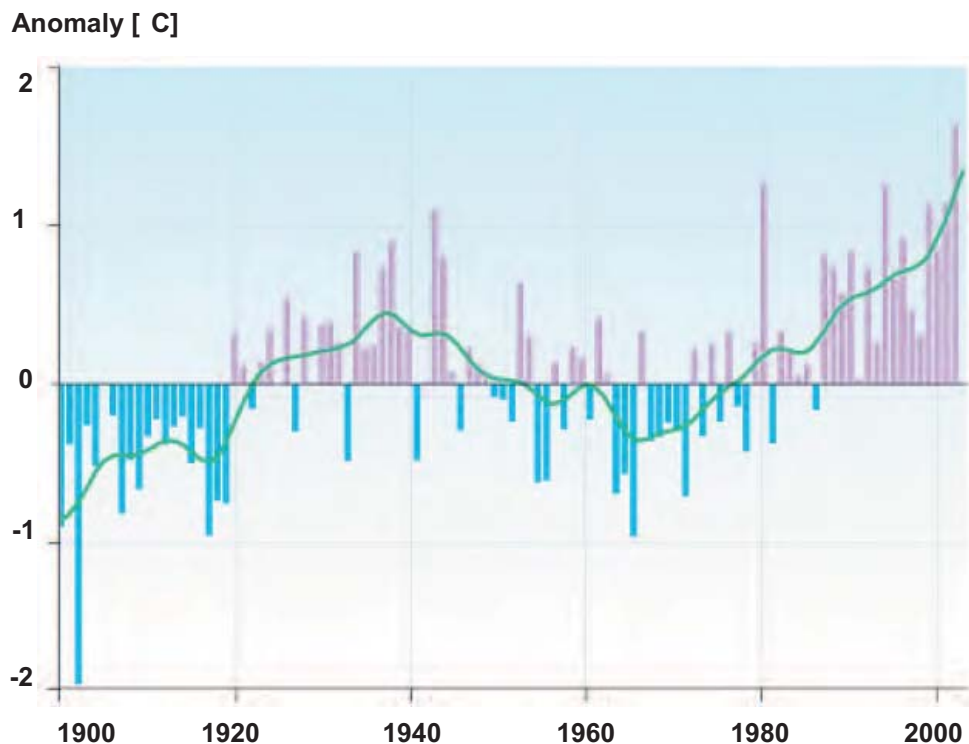


Figure 2.3: Temperature anomalies during the last century (modified after ACIA 2001)

More recently, RICHTER – MENGE AND OVERLAND (2010) stated in the 2010 Arctic Report Card 'In 2010, there was continued widespread and, in some cases, dramatic ... warming [of the] Arctic, where deviations from the average air temperature are amplified by a factor of two or more ... relative to lower latitudes' (RICHTER-MENGE & OVERLAND 2010). The reasons therefore are very likely the

distinctive physical settings of high-latitude regions that result not only in increased change in mean surface temperature for a given perturbation of planetary heat balance, but also an enhanced regional and seasonal environmental response due to non-uniformity in pole wards heat flux, and to the energy relationships of phase change and albedo change connected with ice and snow cover (ROOTS 1989).

2.2.2 Precipitation

Concerning the precipitation, the limited measurement probabilities for rainfall and snowfall in cold environments and especially the different treatment for correcting the data, hinders adequate assessments (GOODISON ET AL. 1998).

Nevertheless the IPCC report from 2007 (SOLOMON ET AL. 2007) concludes that a widespread increase in heavy and extreme rainfall events in the high latitudes of the northern hemisphere occurred similar to the total amount of precipitation rates. MEKIS AND HOGG (1999) highlighted Northern Canada as an area especially affected by such heavy rainfall events. STONE ET AL. (2000) also noted that between 1950 and 2000 heavy and intermediate daily precipitation events increased, concerning their intensity and frequency in over one-third of all Canadian districts.

2.2.3 Further climate parameters

- The AO showed a general trend toward positive values between 1970 and the early 1990s, which is still ongoing, after negative records in the 1960s (THOMPSON & WALLACE 1998).
- The average surface temperature increased by around + 0.09 K/ decade 'which is 50% greater than the + 0.06 K/decade increase observed over the entire northern hemisphere' (IPCC 2001).
- It is very likely that the atmospheric pressure over the Arctic Basin experienced a dropping during the last century (MCBEAN 2005).
- The sea-ice and especially the multi-year sea-ice very probably lost high amounts of its extent and thickness during the past 50 years (MCBEAN 2005).

In addition, it should be mentioned that at the moment the Arctic is undergoing significant other changes including accelerated population, technological progress, economic and social transformation as well as shifting jurisdictions and institutions. This all goes together with many educational and health challenges (HAMILTON & MITIGUY, 2009; STAMMLER 2009; YOUNG & BJERREGAARD 2008; YOUNG & MÄKINEN 2009). The very recently published 'State of the Arctic Coast' delivers an elaborate summary of the climate change impacts and threats for the affected communities (FORBES ET AL. 2011), such as their wellbeing, the infrastructure and the loss of hunting grounds.

2.3 The Arctic climate prior to 100 years BP

The reconstruction of the Arctic climate over several millions years ago, reveals that high variability in climate occurred to a substantial extent. There is widespread evidence that the period of the last 20000 years, including the last ice age, tended to be very unstable, with rapid large changes, especially temperature increases that occurred quickly (within a few decades or less). It is also known now that between 400 and 100 years BP the climate was again exceptionally cold and that glaciers reached a maximum during this period (MCBEAN 2005).

2.4 The Arctic climate: Future

As already argued, the current problem of limited databases, specifically long-time records, impedes reliable simulations of climate scenarios for the next decades. However numerous modeling approaches were put into service to appraise future climate conditions. The demonstrated projection copy the next 80 years (until 2090), and are all based on a combination of global coupled atmosphere-ocean general circulation models (AOGCMs) (Table 2.1 at the end of this chapter). Their selection was based on the five suggested criteria by SMITH ET AL. (1998)

- Vintage
- Resolution
- Validity
- Representativeness of results
- Accessibility of model outputs

As driving emission scenarios served A2 and B2 (Figure 2.4) defined in the Special Report on Emissions Scenarios (SRES) by the IPCC in 2000. The output uniformly projects an enduring warming, notably occurring in northern high latitudes, shrinking snow and sea-ice cover and a continuing retreat of glaciers and ice caps. Frost days and the incidence of cold waves are very likely to be diminished, and in the wake of higher air temperatures the ground temperature will rise (MCBEAN 2005).

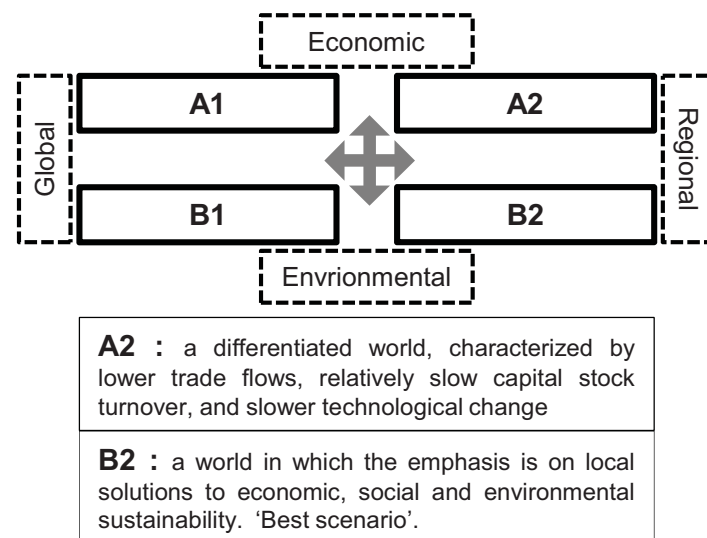


Figure 2.4: The four main storylines defined by the IPCC with a more detailed description for the scenarios A2 and B2 used for the results represented in this chapter

It is also predicted that the northern hemisphere circulation will become weaker, impacting the water surface temperature of the sub-Arctic North Atlantic (KATTISOV & KÄLLÉN 2005). Regarding the AO, clear agreement between the models is lacking.

Figure 2.5 pictures the simulated temperature and precipitation sum for the three time periods 2011 – 2030, 2041 – 2060 and 2071 – 2090, subdivided into four seasons (December – February; March – May; June – August; September – November). They originate from the Arctic Climate Impact Assessment and are based on the average of the five designated models, ran against the B2 scenario. The illustration of the temperature demonstrates significant warming within the next decades, with pronounced heat during winter and fall. Most notable is the temperature rise of about + 9 K over the North Pole, predicted for the last time span during autumn. It is remarkable that no area that shows cooling can be spotted out, and only the maps for the summer months tend to show no

temperature trend in some areas. Likewise, in the precipitation pattern most apparent alterations emerge in winter and fall, with over 30 % more precipitation than in the last century. However, in contrast to the temperature, some regions reveal a decline of about 10 %. By combining the model outcomes for the temperature and the precipitation it is also very likely that much more of the predicted precipitation will fall as rain in future decades.

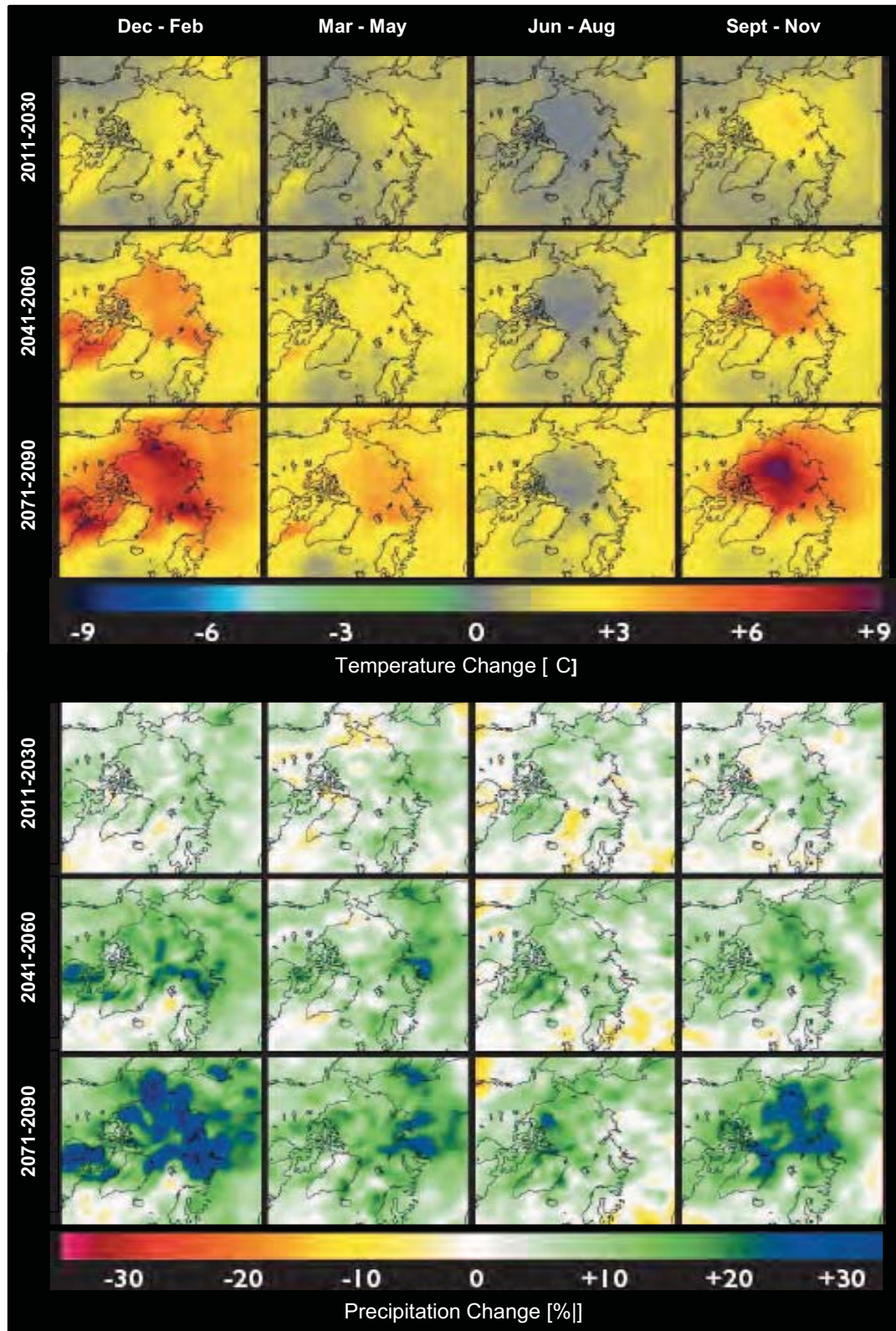


Figure 2.5: Temperature changes (left) and precipitation changes (right) averaged over the five designated B2 projections (modified after KATTSOV & KÄLLÉN 2005)

The discussed climatic change is of course affecting the entire Arctic ecosystem, including the cryosphere. Decreasing extent and thickness of Arctic sea-ice, altering ice sheets and ice shelves, fewer river and lake –ice as well as permafrost thawing were already observed and are evidence for such changes.

Referring to ANISIMOV AND FITZHARRIS (2001) the role of permafrost in the climate system is threefold:

- ‘First, because it provides a temperature archive, permafrost is a “geoindicator” of environmental change. At depths below 15 to 20 m, there is generally little or no annual cycle of temperature, so seasonality does not influence warming or cooling’
- Second, because it serves as means of transportation of the atmospheric temperature changes to the hydrological and biological components of the Earth system.
- Third, because changes in permafrost can feed back to climate change in forms of trace gas emissions (CO₂ and CH₄).

The next chapter deals with the permafrost characteristics, its responses to climate warming and the consequences that are due to it.

Table 2.1: Selected five AOGCM models

Model	Institute	Reference
CGCM2	Canadian Centre for Climate Modelling and Analysis, Canada	FLATO & BOER 2001
CSM_1.4	National Centre for Atmospheric Research, United States	BOVILLE ET AL. 2001
ECHAM4/OPYC3	Max-Planck Institut for Meteorology, Germany	ROECKNER ET AL. 1996
GFDL-R30_c	Geophysical Fluid Dynamics Laboratory, United States	DELWORTH ET AL. 2002
HadCM3	Hadley Centre for Climate Prediction and Research, United Kingdom	GORDON ET AL. 2000

3 Permafrost

Permafrost is defined as being all ground, including soil, rock, ice and organic material, with temperatures at or below 0°C for at least two consecutive years (BROWN 1974). As it is solely defined by temperature, the existence of ice is not obligatory, as it might be the case of nonporous bedrock, but it usually occurs.

Permafrost is widely developed in the solar system and was already discovered on Mars, Pluto as well as through several satellites of other planets such as Jupiter, Saturn and Uranus. This is a not very surprising fact when taking into account the prevailing temperatures of the Universe (YERSHOV 1990). Permafrost is widely distributed on planet Earth over both hemispheres and occurs on land and beneath offshore Arctic and Antarctic continental shelves, whereas its thickness varies from less than 1 meter to greater than 1000 meters. It is not restricted to the polar and sub-polar regions but can be found up to 64° away from the poles in the Himalaya region at 26°N (NSIDC 2008). Hence permafrost itself, as well as its research is divided into lowland permafrost and alpine permafrost. As a part of the cryosphere its exploration started within the last century and expanded greatly since then. Whereas the initial interest was mainly driven by an increased demand for natural resources, especially oil, gas and minerals, its role for the regional and the global ecosystem became more and more fundamental, and nowadays the analysis of its behavior related to climatic change is one of the major scientific questions in polar research (BROWN 1974; IPA 2008 2010).

3.1 Distribution of permafrost

A general problem when quantifying the extent of permafrost on Earth is whether glaciers and ice sheets have to be excluded or included in the statistics. ZHANG ET AL. (1999) argued that referring to the definition of permafrost glaciers and ice sheets do not count as permafrost, as they are not ground, soil or rock. Applying this argument to the northern hemisphere would total a difference of about 2 Mio km², depending on the study. As it is very likely that most of the ground covered by glaciers or ice sheets is affected by permafrost, the following presented numbers are all including these areas.

According to this definition, permafrost underlies around 25.6 % (24.91 Mio km²) of the land surface on the Earth's northern hemisphere and it ranges from the most northern parts of Greenland and Norway at 84°N to the very elevated regions of the Himalaya, where permafrost can even be found at 26°N (ZHANG ET AL. 2003) only around 2900 km distant from the equator. In general it can be stated that the occurrence of permafrost is mainly related to air temperatures. The latitude as well as the altitude are the main important driving factors, but also the proximity to large water bodies can have an impact on the permafrost occurrence. ROUSE (1991) highlighted in his study about Northern Quebec the influence of the Hudson Bay for the surrounding areas.

The occurrence of permafrost in the Arctic and sub-Arctic is usually divided into continuous, discontinuous, sporadic and isolated permafrost. These names are indicating the percentage of the area affected (Table 3.1). Although this definition exists, the boundaries between the zones have to be taken as estimates (ZHANG 2005).

Table 3.1: The percentage of permafrost occurrence for the different permafrost types

Permafrost type	Affected area
Continuous	More than 90%
Discontinuous	50 – 90%
Sporadic	10 – 50%
Isolated	Less than 1 %

Except for the high mountains, the southern boundary of the maximum extent of seasonally frozen ground is within 35°N to 40°N (ZHANG ET AL. 2003). The major factors influencing this distribution are the proximity to large water bodies as well as differences in the seasonal snow cover (ZHANG 2005; WILLIAMS & SMITH 1989). Figure 3.1 displays the permafrost distribution in the northern hemisphere.



Figure 3.1: Permafrost distribution on the northern hemisphere (modified after IPA 1998)

Most permafrost in the northern hemisphere is located between 60°E and 180°E, including vast parts of Siberia, Russia, Mongolia, Tibet and northeastern China, and around 37 % occurs in North America (ZHANG ET AL. 1999).

In the southern hemisphere, permafrost is mostly located on the Antarctic continent, but can also be found in southern Africa, Tasmania, New Zealand, Argentina and the maritime and sub-Antarctic regions. In Antarctica only 0.3 % of the land is bare ground, all underlay by permafrost, and it is also expected that it occurs underneath the Antarctic ice shield (NSIDC 2008). Compared to the knowledge available for the northern hemisphere, little is known about distribution, thickness, age, and physical and geochemical properties (ANTPAS no date).

The exact determination of the location and extent of soils affected by permafrost is still a major challenge in science; it is often assumed that a rough estimate is that the ground temperature equals the overlying air temperature. However, recent investigations show that this is often not the case and that even in areas where the mean annual air temperature is below freezing, permafrost may not exist. Furthermore land covered by glaciers, streams and rivers is often free of permafrost despite freezing air temperature (WILLIAMS AND SMITH 1989).

3.2 Permafrost: Structure and behavior

Referred to the previous chapter, permafrost exists at almost every latitude around the world and thus a uniform description of the geophysics of permafrost is not possible. Numerous different permafrost types, depending on climate, soil type and many more factors, can be distinguished. They all show different behavior concerning their thermal regime and their impact on the micro- geomorphology and also their development varies.

However these differences form a basic structure, composed of three distinguished layers, which is valid for all kinds of permafrost solely varying in depth and shape:

The upper layer is characterized by seasonal thawing and freezing processes and is called the 'active layer'. Its depth varies depending on the summerly air temperatures and can penetrate up to 3 m into the ground. Beneath the active layer, permanently frozen soil with seasonally variable temperatures follows, whereas in the bottom layer the temperatures are constant over the entire year (BROWN 1974).

The ground thermal regime or the temperature curve in the soil respectively, is primarily dependant on the atmospheric climate, as well as on the soil's grain size. However, there are also many more site specific factors like the exposition, the snow cover, the vegetation or the relief that are impacting temperature. Figure 3.2 shows three temperature curves in the Fort Simpson area, taken from boreholes in different soils (BURGES & SMITH 2010).

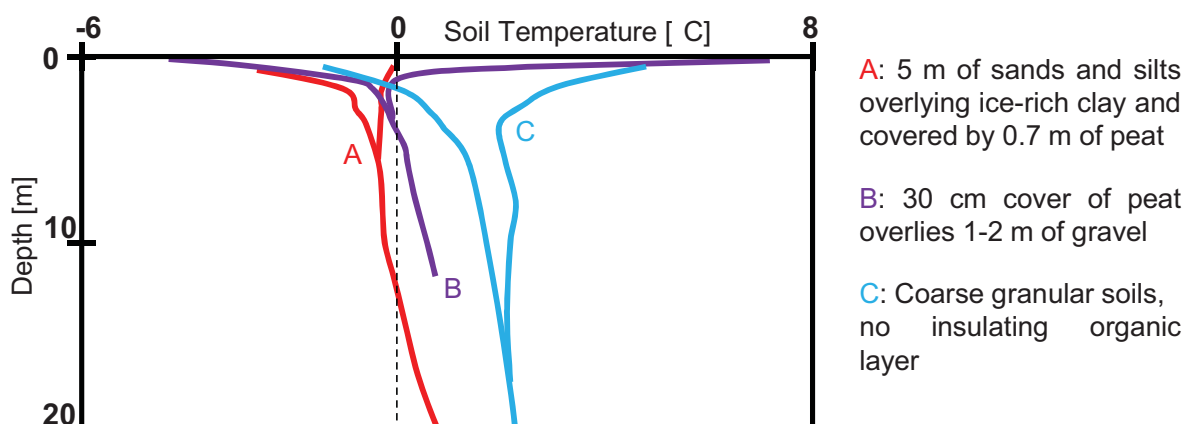


Figure 3.2: Temperature profiles of different soil types near Fort Simpson (modified after BURGES & SMITH 2010)

It was already pointed out that there is a primary division into lowland permafrost - Arctic and Antarctic permafrost-, and alpine permafrost. As the study at hand is attributed to Arctic permafrost research, the descriptions of the different types are focused on Arctic permafrost.

There are principally three ground ice forms existing: excess ice, pore ice, and ice of external origin. They mainly differ in their origin of the water sources and the transfer processes. Depending on the form, diverse surface features are developed (Figure 3.3) (MACKAY 1972).

Excess ice is present in excess of the volume of the soils pores in the unfrozen state. The formation of the so formed ice can be various; from very thin layers or even only flakes up to massive ice bodies within 50-60 m of the ground surface and it is naturally the last to thaw (WILLIAMS & SMITH 1989). The origin of excess ice can either be evoked by different matric potential, and is then referred as *segregation ice*, or by an elevated hydrostatic pressure in the water of the adjacent soil and then called *intrusive ice*. Intrusive ice also includes pore water.

Segregation ice is mainly found in very fine soils, where the co-existence of frozen and unfrozen water induces a pressure gradient and activates a migration of liquid water to the frozen part. The formed ice is mostly visible in thin layers, parallel to the surface, ice lenses or closely spaced flakes, but it can also be the reason for several meter thick massive ice bodies and is hence also responsible for frost heaving processes.

In contrast, intrusive ice primarily occurs in coarse soils and builds up ice veins, sills or ice wedges. It is also assumed to be the driving process for the development of pingos and other frost mounds, described in chapter 3.3, however, in most cases a clear distinguish between the two processes is only seldom possible and a combination of both categories seems to be most appropriate (WILLIAMS & SMITH 1989).

More or less independent from the dominant forming process, is the origin of water prior to freeze, which either infiltrated in the ground and froze, or has already been in the ground as subsurface water. This is in contrast to atmospheric water that can build open-cavity ice by vapour diffusion (MACKAY 1972).

Ice of external origin can sometimes be difficult to distinguish from the explained excess ice in the field, but formed completely different. This includes old buried glaciers, snow, lake and river ice or *Aufeis*. Although it might appear very similar to permafrost, it does not account to it and has to be regarded separately. For example ÖSTREM (1963) and WILLIAMS AND SMITH (1989) discussed such ice occurrence in their studies and it is referred to their publications for further information.

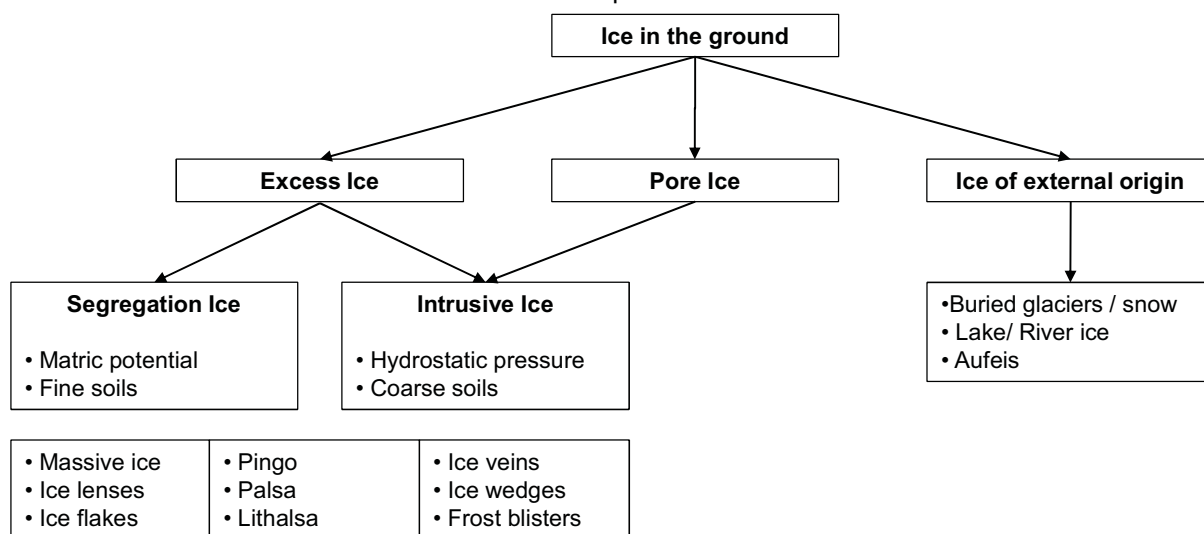


Figure 3.3: The different ground ice forms and the related land surface features

3.3 Typical permafrost features

The presence of ice in the ground and the freezing and thawing processes that take place in the soils greatly modify the properties and behavior of the ground and are responsible for some unique small-scaled relief features, which are briefly described in this chapter.

Again, the development of the different objects are highly dependent on the location and the soil types, and they can be classified into forms caused by accumulation of ice, by thawing permafrost, or a periodical freezing-thawing process.

The accumulation of ice in the ground mainly affects an expansion of the ground's volume which becomes obvious at the surface in forms of mounds in several sizes. The most common, widespread and most impressive of such frost mounds are *pingos*, often having a volcanic –shaped form and reaching heights up to 50 m (WILLIAMS & SMITH 1989). They usually form where ponded water occurs over a *talik* (permafrost free area) which starts to cool due to altered micro-climatic conditions. The following rising water pressure in the ground feeds a core of massive segregated ice which becomes exposed due to frost heave. Still covered by soil this mound now represents the pingo.

Much smaller mounds – about 5 m height - are *palsas* and *lithalsas*, typically located in the discontinuous permafrost zone (SEPPÄLA 1979) and often occurring in close proximity with many others. In contrast to the pingos they consist of a core of ice-rich frozen soil, which can be seen as a small isolated body of permafrost. It is caused more by colder temperatures inside the mound than the surroundings, explained by greater winter cooling due to the exposed surface (SKAVEN-HAUG 1959). The thereby arising gradient in temperature and pressure evokes the building of segregation ice, which causes frost heave.

The difference between a palsa and a lithalsa is a covering peat layer, absent in the case of a lithalsa. Lithalsas are also the main study objects of this work.

The smallest mounds are the so-called *frost blisters* and, in contrast to the previous described features, they grow by intrusive ice. Their formation is explained by an 'upward movement of water to the bottom to the frozen layer where it freezes' (Kovacs 1992). In the following crystallization forces push the soil canopy, including the underlying ice mass, upwards and form a mound (POLLARD & FRENCH 1985).

Landscape features created by permafrost thawing are summarized with the term *thermokarst*, whereas it can be distinguished between forms caused by solifluction and forms caused by subsidence.

Solifluction, also described as landslides and mudflows, occur when soil gets oversaturated and loses its stability. The results are avalanche tongues resembling lobes, mainly located on slopes, which vary in size and height, depending on the movement's velocity. One special process is the so-called *retrogressive thaw slump*, a type of backwashing thermokarst at Arctic coasts that occurs when large masses of ground slide into the ocean and cause coastal erosion (LANTUIT & POLLARD 2005).

If very large ice bodies are thawing extensive subsidence of the ground will inevitably happen and create depressions, usually filled with water. These lakes, also referred as thermokarst lakes, can occur in many different sizes and shapes, but are normally limited to shallow areas (SMITH & WILLIAMS 1989).

One of the most popular phenomenon related to frozen ground is *patterned ground* (Figure 3.4); a unique formation at the surface, restricted to cold regions and originate to cryoturbation. Patterned ground can be visible in the form of earth circles, stone polygons, regular arranged ice wedges or

hummocks. All these structures are attributed to the seasonal thawing and freezing processes in the ground that leads to periodically expansion and contraction. An earth circle is a cluster of patches more or less circular and vegetation free, which are mainly found in tundra regions (SMITH & WILLIAMS 1989). In contrast, *stone polygons* or *rings* are assemblages of boulders in a polygonal or ring-like network. Their size usually is depending on the dominant size of stones, but can be up to several meters (PISSART 1974). The origins of these polygons are typically cracks, caused by thermal contraction, in which the stones accumulate due to first cryoturbation and later gravity-caused falling or rolling in the cracks. If the cracks that are filled with water freeze, ice wedges are formed. Fairly frequent, ice wedges also appear on the top of each other, which can be explained by changing climatic conditions or the fact that sediment on the top 'lead to a rise in the level of the top of the permafrost' (MACKAY 1984).

If the ground's surface is very bumpy and disturbed, it is usually the case of *hummocks*. They are well-defined and regularly spaced mounds up to 50 cm in height, whose origin could not fully be clarified until now and several attempts to explain are existing.

For a more detailed description of the various amounts of land surface features in permafrost regions it shall be referred to SMITH AND WILLIAMS (1989).



Figure 3.4: Ice wedge polygons as an example of pattern ground (SHORT no date)

3.4 The thermal state of the permafrost

The recent existing permafrost can mostly be dated back to the last glacial period. Only some shallow permafrost was formed during the second part of the Holocene about 6000 years ago and some 400 to 150 years ago during the little ice age (IPA 2010).

During the last International Polar Year (IPY) 2007 -2008, an initiative was started to record the recent thermal state of the circumpolar permafrost. For it, many new test sites and boreholes have been established and numerous researchers and institutions were involved in these projects. The following chapter summarizes the outcomes of these studies, as well as the findings of the assessments of the last IPCC report, to give an overview about the recent state of the permafrost.

3.4.1 Observed alterations in permafrost

Globally, the permafrost temperature increased all over the northern hemisphere during the last decades, except in Northern Quebec, where ALLARD ET AL. (1995) measured a decrease of -1 K between the late 1980s and the mid 1990s. The lowest increase with less than +1 K has been recorded at Chinese test sites (ZHAO ET AL. 2004) and maximum increase with up to +4 K was measured by LACHENBRUCH AND MARSHALL (1986) between the 1910s and 1980s in Northern Alaska. On average, the temperatures rose around +1 K, a fact which is also mirrored in the thawing rate that ranges from 0.04 m/ year since 1992 in Alaska and 0.02 m/ year since 1960 on the Tibet Plateau (LEMPKE ET AL. 2007).

For the detailed monitoring of permafrost in North America there were about 350 sites installed throughout the permafrost region, with boreholes that vary in depth from 30 m – to 100 m (SMITH ET AL. 2010). In general, the measured mean annual ground temperatures (MAGT) of the continuous permafrost zone are in a much wider range from -15 °C to above -2 °C than in the discontinuous permafrost zone, where the MAGTs fall into a narrow range within 2 °C of the thawing point (SMITH ET AL. 2010). Beginning as early as the late 1960's a general increase in many locations of the ground temperature could be observed; only 'in some newly exposed drained lake basins and aggrading shorelines where permafrost is forming' (IPA 2010) decreases were recorded. In addition, almost all recorded permafrost temperatures during the IPY initiative across North America showed increased values over the past decades. It could also be noticed that the 'warm' permafrost (around 0 °C) underlies a smaller magnitude than the 'cold' (always <0 °C), but is already undergoing internal thaw at temperatures less than 0 °C (SMITH ET AL. 2010). Furthermore it seems as if the permafrost reacts more sensitive to changing climate conditions at tundra sites and in bedrock than below the tree-line or ice-rich soils (SMITH ET AL. 2010).

Results from PAVLOV (1996) for the Siberian permafrost summarized in the IPCC report from 2007 are depicting a deepening of the active layer of about 21 cm over a 34 year period (1956 – 1990). Similar trends could also be observed at European test sites, where the active layer thickness reached its maximum in the summers of 2002 and 2003 (HARRIS ET AL., 2003) and in the Asian regions where an increase up to 1 m along the Qinghai-Xizang Highway over the Tibetan Plateau was measured since 1980 (ZHAO ET AL., 2004).

The experienced warming of the MAGT and the increase in the active layer thickness is also accompanied by a significant permafrost decrease: at almost all permafrost affected areas a migration of the southern boundary of the permafrost zone takes place (HALSEY ET AL. 1995) and thermokarst processes, as well as rapid mass movements caused by oversaturated soils are becoming more and more frequent. Subsidence rates of 24 cm/year could be observed in young thermokarst lakes and the analysis of satellite images reveal an increase in the total lake area in many regions (SMITH ET AL. 2005).

The most severe changes are recorded at coasts with ice-bearing permafrost, exposed to the Arctic Ocean; here annual erosion rates up to 3.0 m per year can be found (RACHOLD ET AL. 2003).

Table 3.2 gives a summary of measured changes in the permafrost temperature observed and published by several research teams from the different areas.

Table 3.2: Summary of measured changes in the permafrost temperature

Region		PF Temp. Change [K]	Record Period	Measured at Depth [m]	Reference
United States					
Max	Northern Alaska	2.0 – 4.0	1910 - 1980s	~ 1	LACHENBRUCH AND MARSHAL 1986
Min	Interior of Alaska	0.5 - 1.5	1983 - 2003	20	OSTERKAMP 2005
Canada					
Max	Iqualuit Eastern Canada	2.0	1993 – 2000	5	SMITH ET AL. 2005
Min	Northern Quebec	< - 1.0	mid 1980s – mid 1990s	10	ALLARD ET AL. 1995
Russia					
Max	European North of Russia	1.2 – 2.8	1970 – 1995	6	PAVLOV 1996
Min	Northern West Siberia	0.3 – 0.7	1980 – 1990	10	OBERMAN AND MAZHITOVA 2001
Europe					
Max	Janssonshaugen Svalbard	1.0 – 2.0	1950s - 2000	~ 2	ISAKSEN ET AL. 2001
Min	Juwasshoe Southern Norway	0.5 – 1.0	1920s – 2000	~3	ISAKSEN ET AL. 2001
China					
Max	Da Hinggan Mountains	0.7 – 1.5	1978 – 1991	~ 2	ZOUH ET AL. 1996
Min	Tianshan Plateau	0.2 – 0.5	1973 – 2002	16 – 20	QIU ET AL. 2000

3.4.2 Global consequences

The global consequences for the expected permafrost thawing within the next decades are manifold and due to their enormous complexity are not yet completely understood. Supposed negative and/or positive feedbacks cannot be quantified, as not fully-understood tele-connections are making it almost impossible to give 100 % certain prognoses. Still some assessments can be done.

In general the impacts can be classified as direct and indirect threads. The increased greenhouse gas emissions, especially methane, as well as changes in the ecosystem are among the direct consequences, whereas the threats for communities and the affected people caused by a changing environment are indirect.

3.4.2.1 Increased greenhouse gas release

The frozen ground in the northern hemisphere stores about 455 Gt of carbon (C) in the form of organic matter, frozen in thick mineral soil, mostly yedoma (MILLER 1983, GORHAM 1991). This amount equals 60 % of the 750 Gt currently in the atmosphere as CO₂ (OECHEL 1993). Most of it is stored in Siberia regions, whereas in the Canadian peat lands around 45 Gt CO₂ are estimated (TARNOCAI 2006). The organic material was accumulated during the last 8000 years in sub- Arctic tundra and boreal forest

locations, where dead plants can hardly be decomposed due to the limited microbial activity in frozen soils (CAFF 2010). Under such conditions, permafrost served as a carbon sink within the past; however, this changed dramatically during the last decades, when temperatures increased and following the microbial activity started. Not only the increased decomposition of the organic material, but also free methane and carbondioxid stored in the frozen ground in about 30 m deep will ooze, when the ice thaws (HUBBERTEN 2010).

The consequences have already been studied by several research teams (LAURION ET AL. 2010; BRETON ET AL, 2009; KOUSHIK ET AL. 2006) and it seems as if the impacts are highest in the northern Siberian tundra, where the decomposition process is surprisingly fast. Researchers also found out that methane bubbles from thermokarst lakes, which serves as a huge source for greenhouse gas emissions to the atmosphere (WALTER ET AL. 2006, 2007). Although a number of studies dealing with this issue have already been conducted, there is still very little known about the amount and rate of this emissions and even less about the feedbacks in the atmosphere.

ZIMOV ET AL. (2006) stated in their study about the 'permafrost and the global carbon budget' that with extreme projections almost all yedoma, probably containing about 500 Gt of carbon, will thaw by the end of the 21th century. They estimate the future of the permafrost as a carbon reservoir as follows: with warming, the spatial extent of permafrost declines, 'causing rapid carbon loss; with cooling, the permafrost reservoir refills slowly, a dynamic that mirrors the past atmospheric record of CO₂. In a warmer climate, permafrost carbon is thus very likely to become part of a more actively cycling carbon reservoir.'

3.4.2.2 Changes in the ecosystem

The thawing of the permafrost will highly affect the ecosystem in many ways, varying locally and temporally. Every occurring alteration will again evoke changes and hence the total dimension is difficult to estimate.

Some of the most obvious effects are those on the hydrological regime: areas now serving as huge water reservoirs will drain after thawing and no longer store water. This will lead to an increased runoff, at least in the short term where topography allows drainage. If the permafrost thaws completely, the earlier existing impermeable ice layer disappears and the water will penetrate into the ground. Otherwise, if there is no relief existing and a frozen layer still remains, the water will firstly oversaturate the soil and finally wetlands and new lakes will develop (WALTER ET AL. 2006).

Such changes in the land cover and the hydrological regime are influencing the existing flora tremendously, as the recent vegetation cannot adapt as rapid to the humid conditions. For instance, the Siberian boreal forest is expected to experience a dramatic decline, because trees will not be able to survive on the wet ground (HUBBERTEN 2011). Many more transformations in the recent ecotones are to be expected and have been already observed in some areas. In particular, hydrophilic sedge types and bushes are benefiting from the changing environment and are expanding at the expense of moss, lichens and other shrubs. These include many species of berries, which are in turn a food source for many animals, and also for human beings, and hence a shift in the animal population is very likely.

Not only the changing available nutrients, but also the much softer ground will hinder some mammals, like the caribou, to migrate to their seasonal grazing land and species adapted to the frozen ground will very likely disappear. This may be for example the case for the Arctic Fox, *vulpes lagopus*, who stores his food during the summer in the permafrost (NSIDC 2008). In addition the summerly black fly, swarms, *Simuliidae*, will augment dramatically especially in areas where wetlands and lakes are expanding.

Changes in the vegetation pattern and the hydrological regime can furthermore influence the local micro-climate. Increasing evaporations rates, provoked by higher amounts of available water, can result in more precipitation, but it may also have a contrary effect in areas where water is now able infiltrate into the ground.

Chapter 5.5 deals with the happening alterations of the land cover patterns in the test site of this study and discuss some regional occurring features in more detail.

3.4.2.3 Indirect consequences

Consequences for indigenous people are manifold and will pose an omnipresent risk on their lives. The loss of the ground's stability and a softer surface due to less ice will significantly threaten the infrastructure in affected communities. Buildings and streets, as well as airports – which in most cases in Northern Canada are the only connection to other communities – will suffer from this changes and costly work will be necessary. At present, many new roads already contain cracks and houses are being destroyed. New infrastructure and housing are threatened by landslides and sudden subsidence. This is even worse in coastal areas, where the increasing coastal erosion leads to landslides, often under the roof. Another major problem are the long pipelines running in many permafrost affected areas and posing an immense economical as well as ecological risk if their destabilized by a loss of their stolid foundation (FORBES ET AL. 2011).

Especially in regions populated by Aboriginals, the growing areas of wetland have an additional negative effect on the traditional lifestyle, which is still mainly based on fishing and hunting. For it, people have to cover long distances to reach to appropriate hunting grounds, what they typically do by skidoo or all terrain vehicles. There are an abundance of paths existing, including frozen rivers and sea ice in winter, which slightly changes over the season. As these dirt roads are located on frozen ground, thawing also means the loss of access to their hunting camps or at least a much longer and less comfortable travel. The aforementioned alterations are already happening in many Northern communities and are noticed by the population; as Inuit resident of Kangiqsualujjuaq M. Snowball (2010) stated: 'It made it harder for hunters to travel through land [...] to go camping. But last year, they had to go by the long ways through the bumpy mountains, which is more dangerous. Also, because of that, they had to contain more gas and food. They also had to have their transportation in best shape if they want to go camping if they want to make it home safe' (SNOWBALL 2010). She also mentioned the fact that it is getting harder each year to visit friends and relatives living in other communities. As a consequence many people have no other choice than to give up their culture and traditional lives, which usually ends in unemployment, dissatisfaction, and social problems.

It is obvious that such circumstances evoke financial but also psychical stress for the resident population, and in many cases boosts the abuse of alcohol and the taking of drugs, which is already one of the major problems in those societies (NAHO 2011). This is further pronounced by more climate change related problems such as less sea ice or altered appearance of game, as it is the case for the Canada goose near Umiujaq.

4 State of the art and motivation

The presented problem clearly demonstrates the need for action in permafrost research.

In order to improve knowledge concerning the regions and dimensions of permafrost decline, a profound understanding of the permafrost's interaction with its environment and its accurate and detailed mapping is the most important cornerstone.

In recent years, enormous progress could be accomplished, mainly driven by the research initiatives established during the International Polar Year 2007/2008. Those initiatives allowed the installation of new boreholes that provide scientists with important datasets, and several programs have been started, dealing with the discussed topics. The following discussion gives an overview about accomplished studies relevant for this work.

The earliest investigations dealing with the effects of land surface processes on permafrost were conducted by BROWN 1963, 1965; MACKAY 1970; NICHOLSON 1978; RISEBOUROUGH 1985. In addition there are some recent publications, mainly from test sites in Sweden, which tackles the research question of the dependencies of permafrost, vegetation and snow cover in the context of climatic changes (JOHANSON & AKERMAN 2008; JORGENSEN ET AL. 2001).

Mapping of permafrost was traditionally the outcome of the evaluation of boundaries of permafrost zones by interpolating between key isotherms. The data therefore usually came from sparse climate stations measuring air temperature that was interpolated afterwards (HACHEM 2008). The first small scale maps covering large areas, were produced in Canada by BROWN (1970), HEGINBOTTOM AND DUBREUIL (1993), and JOHNSTON (1981), through to the circumpolar Arctic by BROWN ET AL. (1997) and also at regional scales, such as in Northern Quebec by ALLARD & SÉGUIN (1987 b).

Since this method gives only a very rough estimate about the real distribution of permafrost, and furthermore this boundary is not stationary, these maps must be updated since the latest was delivered by BROWN ET AL. in 1997.

Several attempts using remote sensing imagery have been conducted: COMISMO (2003), COMISMO AND PARKINSON (2004), ZHANG ET AL. (2003), and STOW ET AL. (2004), used optical sensors to observe climate change in the Arctic and changing vegetation cover.

In 2003 MIALON ET AL. published an approach to use passive microwaves to map permafrost and COMISMO (2003), TRAORÉ ET AL. (1997) and HAN ET AL. (2004) utilized the thermal infrared to reconstitute past thermal evolution in the Arctic. The most recent publication from HACHEM ET AL. (2008) presents successful permafrost mapping by using the MODIS land surface temperature product.

Besides these applications of satellite imagery on a fairly broad scale, FORTIER AND AUBÉ-MAURICE (1998) used aerial photos to detect small-scale changes in land surface characteristics around Umiujaq.

In terms of the physical processes that form frost mounds such as lithalsas, the earliest studies dates back to TABER in the years 1929 and 1930. More recently, their development and behavior was even subject of some modeling approaches (AN 1997; AN & ALLARD, 1995; GILPIN 1980; KONRAD 1990, 1994; KONRAD & MORGENSTERN 1980, 1981, 1982, 1983; KONRAD & SETO, 1994; NIXON 1991). Specifically in the region of the Hudson Bay, ALLARD & SEGUIN (1987) and ALLARD ET AL. (1987) started to firstly investigate the permafrost, followed by many further studies (CALMELS 2008; DELISLE ET AL. 2003;

FABRICE ET AL. 2008). Their work was mainly focused on the implementation of new monitoring technologies, such as high precision temperature sensors and a pressure sensor, and ground penetrating radar transillumination survey. The aim thereby was to detect long-term changes in the measured frost mounds.

Although the listed investigations deliver a sound understanding in permafrost research, no approach exists that enables permafrost monitoring on a local scale but widely distributed, that would deliver the data to feed and validate permafrost models. In fact, this is highlighted as the most critical research need in the cryosphere chapter of the 'State of the Arctic Coast 2010': 'In order to improve the credibility of model projections of the future permafrost change throughout the Arctic, [...] models must be validated in a more spatially manner.' Furthermore it is mentioned that 'the need for additional detail is particularly great for areas with thin permafrost' (FORBES ET AL. 2011).

According to these statements, and based on the earlier studies, the main scientific objective of this work was to explore different methods to observe permafrost dynamics by means of satellite images which conjointly deliver a base for the spatial monitoring of permafrost.

Therefore the following tasks were accomplished:

1. Collection of snow, vegetation and active layer data and their analysis to enlarge the knowledge about their mutual dependencies and impacts on permafrost distribution.
2. Monitor the seasonal lithalsas' dynamics by means of a d-GPS to define their elevation changes during the year and hence to understand their reaction on temperature changes.
3. Explore the possibilities of high-resolution optical remote sensing data to fathom the most suitable techniques for permafrost monitoring but also to define the limits of those approaches.
4. Investigate the possibilities to use high-resolution radar data acquired by the TerraSAR – X satellite, for the generation of differential interferograms in the area of interest, to detect vertical displacements.
5. Analyze the outcomes of the differential interferograms, to i) confirm their validity and to ii) gain information about the lithalsas' motions.
6. Compare the field and the remote sensing data to define conformity as well as discrepancies, to evaluate the tested methods and to identify still remaining lacks a required further research and data.

The most innovative and important part thereby was the working with radar data; as until now, no similar attempt has been carried out.

During the TerraSAR-X Science Meeting that took place in February 2011, studies using the TerraSAR-X imagery were presented, but only very few of them deal with differential interferometry and most of them applied it to detect horizontal motions for glaciers or mass-movements (PLANK 2011; VENKATARAMAN 2011; LARSEN 2011; NAGLER 2011). Only the research group from the technical University in Clausthal presented a study of vertical movements caused by mining activities (HEBEL 2011).

In terms of permafrost monitoring there is also the Norwegian PERMASAR project at the University Centre in Svalbard (UNIS 2009), but their research question is also the detection of horizontal movements. Hence this study is the first attempt to use imagery from the TerraSAR-X satellite in order to detect vertical topographical movements of permafrost landforms.

5 Test Site: Umiujaq

The test site of this study is about 60 km² in size and situated around the Inuit village of Umiujaq (56°33' N, 76°33' W) near the eastern shore of Hudson Bay in Nunavik, Northern Quebec, Canada (Figure 5.1). It is located in an area of discontinuous permafrost where high climate change sensitivity accompanied by severe effects is expected.

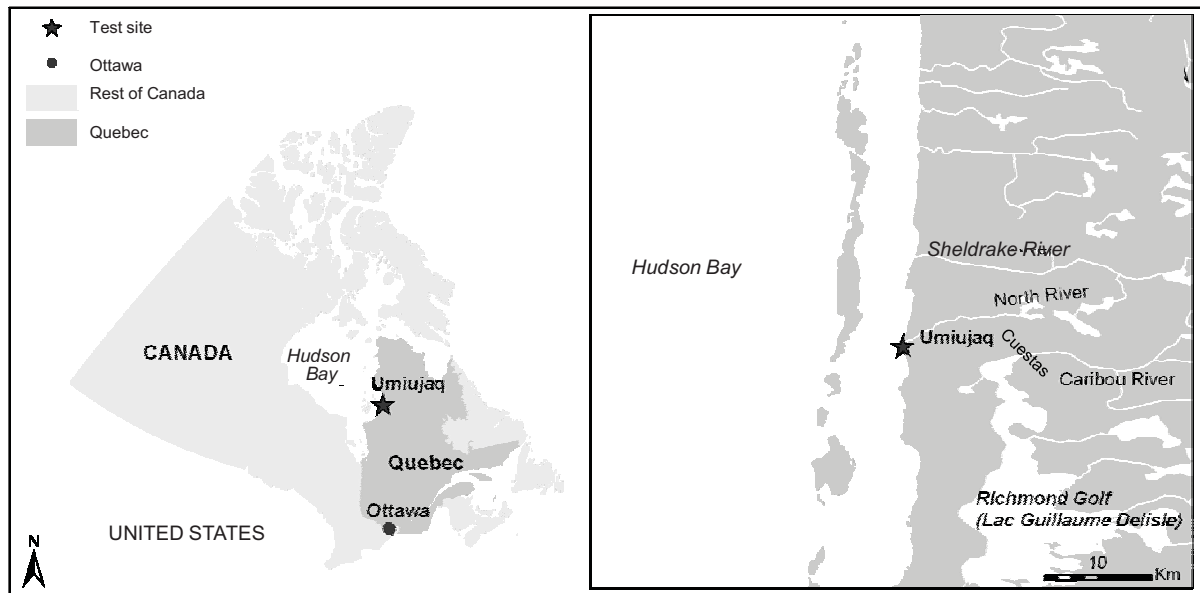


Figure 5.1: Location of the test site Umiujaq, Northern Quebec, Canada

The region was chosen to serve as study area due to its appropriate fitments for a climate change impact study. The major factor is its location at the borderline between the sub-Arctic and the Arctic which is mainly reflected by two very important features for this investigation: the northern timberline and the occurrence of discontinuous permafrost. Hence, the region lies in a transition zone between different macrochores and changing climate conditions will very likely be first observable in the respective region, emerged by alterations in vegetation and permafrost, and linked with the discussed land surface movements.

A further aspect concerning the decision for the test site is the already long lasting research around the area (ALLARD & SEGUIN 1985, DELISLE ET AL. 2003, VALLÉE & PAYETTE, 2007, FABRICE ET AL. 2008). There for, a good database of climate and soil records as well as information about its development over the last decades is at hand.

5.1 Climate

As the region is located at the borderline of the hemi-arctic and the Arctic zone (ROUSSEAU 1968), today's climate is harsh, with only 60- 80 frost free days per year (WILSON 1971). The annual average air temperature is about -5.4 °C but due to the affect of the Hudson Bay it shows a high variability during the year. From June until mid of December the climate has a maritime character with light daily amplitude and moderate temperatures around 8 °C. Due to the freezing of the Hudson Bay, the situation during the winter period is quite the contrary: the climate gets more continental and temperatures can reach values lower than -30 °C. The additional affect of the wind, reaching an

annual average speed of 20- 24 km/h (GAGNON & FERLAND 1967), causes record wind-chills of up to - 60°C (ENVIRONMENT CANADA 2004). The average annual precipitation sum is approximately 600 mm (PHILLIPS 1984) whereof 37 % represents snowfall (ENVIRONMENT CANADA 2004). Figure 5.2 graphs the climate diagram of the region.

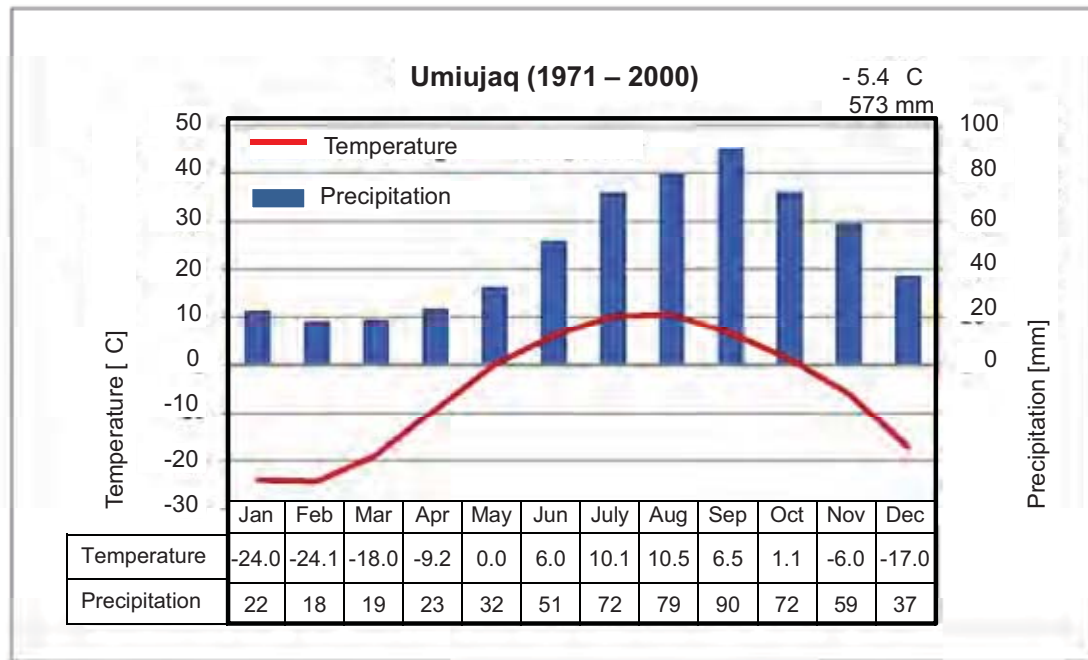


Figure 5.2: Climate diagram from Umiujaq based on the mean climate values recorded by Environment Canada (2004) for the time period 1971-2000

5.2 Geomorphology and geology

Regarding the geomorphologic aspect, the region can be separated into two major areas, divided by the natural boundary of the Cuestas: the western part in the coastal region with a slightly sloped topography and the eastern part with the Lac-Guillaume-Delisle graben (Figure 5.1). This graben has an extension of about 75 km in length and 45 km in width and is mainly covered by the brackwater lake Lac Guillaume-Delisle, also called Richmond Golf. The Cuestas belong to a 650 km long mountain chain between Kuujuarapik in the south and Unukjuak in the north.

The geology of the area includes two Precambrian entities of the Canadian Shield. The dominating one is about 2.5 milliards years old (Archeozoic) and comprises gneiss and granite. The other one dates back to the Proterozoic and consists of volcanic rocks such as basalt, and quartzite originated from province Churchill, situated south-west of Umiujaq (Figure 5.3). Influenced by the Trans-Hudsonian orogeny 2.0 - 1.8 billion years ago, only few rocks of this type occur. The base of the proterozoic layer is composed of quartzite; dolomites only surfaces at the front side of the Cuestas. Dominant at the rest of the surface are basalts situated at the top of this sequence and visible at the back side.

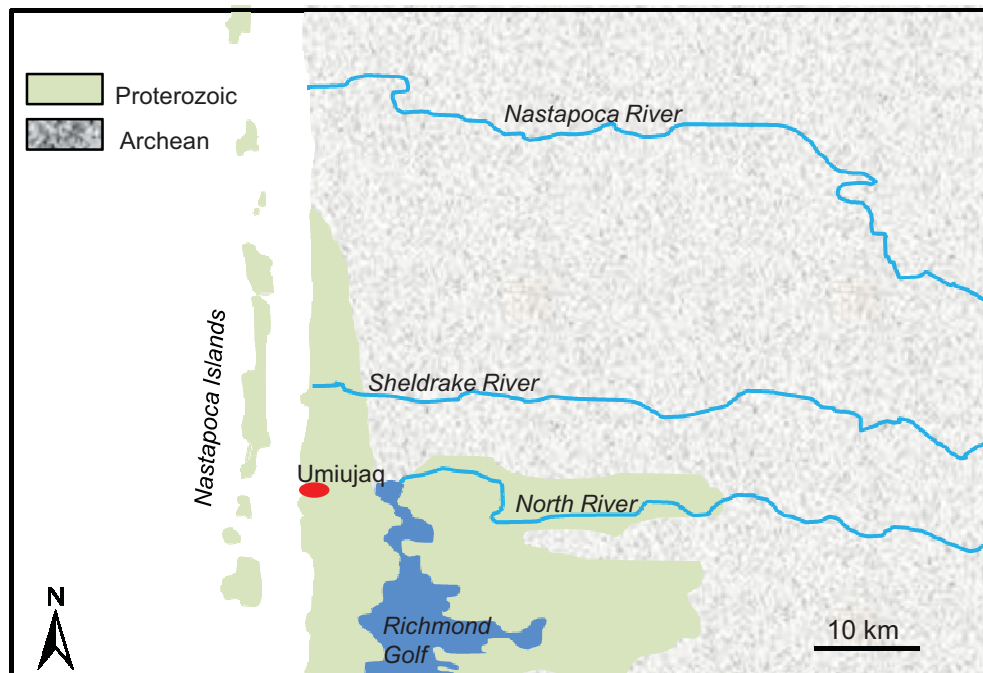


Figure 5.3: Map of the two Precambrian entities (modified after LÈVESQUE ET AL. 1988)

LEVESQUE ET AL. (1988) divided the regional relief into four main pysiographical units:

1. The Cuestas composed of volcanic sediments with summits up to 400 m located in the south-west, with a smooth slope (5° to 10°) towards the Bay (KRANCK 1951).
2. The bumpy hill ridge parallel to the coast with elevations over 300 m.
3. The 4 - 7 km broad coastal area, expanding between the ocean and the Cuestas or the hill ridge respectively.
4. The large inland plateau (200- 300 m high) that extends until Ungava Bay.

The landscape of the entire region has been reformed by the huge ice shields during the ice ages and hence shows the characteristic glaciological landforms. Drumlins, scrubbers as well as roches moutonnées indicate an east-west movement of the glaciers, whose last big expansion can be dated back to 7600 and 6600 years BP (LAJEUNESSE 2000). The retreat of the glaciers was interrupted by a hold along the front side of the Cuestas and the coastal hill ridge. During this hold, several submarine banks were sedimented into the coastal basin. These banks consist of a sandy gravel layer and a stratigraphic layer of sand and silt. As a consequence, the dominant soil that can be found nowadays near the coast is mainly sand. After the retreat of the glaciers, the isostatical depressed surface was around 270 - 280 m below its current level, which made the Tyrrell Sea (nowadays Hudson Bay) much larger. At this time the coastline was located about 60 km farther inland, whereof deep layer of sediments are evidence for.

Afterwards the depressed landmass started to uplift again. This process is still ongoing but compared to a ratio of +10 m per century at the beginning, it slowed down to only +1 m per century. The clayey sediments of the transgression phase can be found at the bottom of long west-east facing depressions.

Today, the uplifted beaches form the lines of the ancient coast and the different holds of the marine regression, whereas east of the limit marine moraine material as well as fluvial-glacial deposits cover the erratic rocky plateau.

5.2.1 Recent morphology

During the following Holocene the vegetation started to develop and an abundance of uplands moors were formed.

Only 3200 years ago, during the little ice age permafrost developed and caused the typical landforms such as lithalsas and palsas. Only very recently after the climate started to warm again, these features were affected by thermokarst processes in some parts of the area (ALLARD & SEGUIN 1987; ALLARD ET AL. 1987-a)

Consequently the recent landscape shows many forms caused by permafrost and a significant change with increasing distance from the ocean is visible: close to the coast mainly lithalsas occur and palsas are dominant further inland (HARRIS 1993). This distribution arises from the texture of the sediments: whereas the lithalsas are more or less solely composed by fine silty clay from the Thyrell Sea, the palsas are covered by an isolating peat layer, which allows them also to grow in areas containing coarser material (LAGAREC 1980, 1982; SEGUIN & ALLARD 1984; ALLARD ET AL. 1987-a, 1987-b).

Both types of landforms have ice-rich mineral cores. The top of these periglacial features stands a few meters above the surrounding ground due to the frost heaving and formation of segregation ice fed by cryosuction in frost susceptible fine-grained soils (PISSART 2002).

In general, palsas and lithalsas can be found side-by-side in the same area. A former palsa can evolve toward a lithalsa if the peat cover is eroded (ALLARD & ROUSSEAU 1999), while a lithalsa can form directly in freshly emerged glaciomarine sediments invaded by permafrost (ALLARD ET AL. 1996). They are typical for cold climate since the palsas are present in an environment with a mean annual air temperature from slightly below 0 °C at their Southern limit (DIONNE 1984) to -8 °C (PISSART 2002), while the lithalsas exist only in a range of mean annual air temperature between -3 °C and -6 °C (PISSART 2002). The fate of these ice-rich periglacial features is highly dependent on climate change (ALLARD ET AL. 1986, 1996; ALLARD & ROUSSEAU 1999; ALLARD & SEGUIN 1986; KERSHAW 1996; PISSART 2002). Their growth and decay was also modeled by AN AND ALLARD (1995) and BUTEAU ET AL. (2004).

5.3 Vegetation

The vegetation around Umiujaq consists of the typical plants of the Arctic Tundra: areas of dwarf shrubs, sedges, grasses, mosses and lichens are interspersed with small groups of little trees up to 2 m high.

In accordance to the two main geomorphologic units, also the vegetations can be distinguished between the western part mainly dominated by shrubs and the eastern part, where the natural scenery in the Lac-Guillaume-Delisle graben also includes little trees such as *Larix laricina*. This separation also represents the specific characteristics of the region, namely the tree-line, represented by the contact between the shrub-tundra to the west and the forest-tundra to the east, which cuts exactly through the area in a north-south direction (PAYETTE 1983). In the western shrub-tundra, krummholz vegetation made up of black spruce (*Picea mariana* (Mill.) BSP.) and various shrubs (*Betula glandulosa* Michx., *Salix* sp. and *Alnus crispa* (Ait.) Pursh) occurs. In the forest-tundra, woodland forest appears in valleys and sheltered areas.

A vegetation map based on high resolution satellite images, generated in the context for this study can be found in Appendix 4.

5.4 Population

Umiujaq has only existed since 1986 when Inuit from Kuujuarapik, a village 160 km further south, decided to relocate away from the area affected by the James Bay Hydro-electric Project. Based on a census from 2006, the total population amounts to 390, whereas 357 of the population are Inuit (Statistic Canada 2010; Statistics Canada 2011) and the average age is only 19.8 years; the male population is around 3 years younger (18.5) than the female (21.1) (Statistics Canada 2011). Typical for an Inuit village, only 230 people over the age of 15 years have an education certificate and thereof only a total number of 10 finished University. This is also reflected in the employment statistics: 56.8 % are not working for pay or in self-employment. In contrary they still practice their traditional style of life: almost 70 % hunt in order to get food, the same is valid for fishing and more than 80 % gather berries and plants for their daily nutrition (Statistics Canada 2004).

These facts disclose a very traditional way of living and also indicate a high dependency of the population on nature. Skills to work with modern techniques, such as computers and GPS, and the knowledge to manage a life without the recent environmental conditions are hence hardly existing or even completely lacking. Consequently a changing environment will severely hit the community and assign them to new and very challenging tasks, in particular by thinking of the increasing hydro-power facilities in these regions. Negative social and economical impacts hence are also very likely to happen in the village of Umiujaq.

5.5 Climate change and consequences for Umiujaq

In chapter 3, that deals with the permafrost in general, some of the expected changes due to changing climatic conditions already have been mentioned. This paragraph is now paying particular attention to alterations estimated or already experienced in the study area.

For this, it should first be pointed out that the situation of permafrost warming in Northern Quebec acquires itself somewhat different to the rest of the permafrost affected regions. Here, significant permafrost warming was only experienced since 1993 accompanied by an active layer deepening (KASPAR & ALLARD 2001), but before no remarkable decline in the MAGTs could be recorded and even cooling from 1989 to 1992 was observed (SMITH ET AL. 2010).

Although this 'delayed' initiation of warming ground temperatures, several studies source permafrost decay already before this measured changes; for example LABERGE AND PAYETTE (1995) depict in their article about 'Long-Term Monitoring of Permafrost Change in a Palsa Peatland in Northern Quebec, Canada: 1983-1993' a decrease of 33 % of total permafrost area in the region around Umiujaq, which results in an increase of thermokarst ponds during the respective 10 years period. Also FORTIER AND AUBÉ-MAURICE (2008) could ascertain in their study about permafrost degradation near Umiujaq a decline in permafrost related features since 1957.

Nowadays the MAGT all over Northern Quebec varies from -5.78 °C at Kuujuaq to -0.01 °C in Umiujaq and a clear increase could be recorded within the last years, with maximum temperatures in 2006, when the long-term mean was exceeded by +3.48 °C. According to the observation during the IPY, the summerly warming near Umiujaq has recently elevated; summer thaw now penetrates to a depth of 20 m (SMITH ET AL. 2010).

Based on climate model simulation, further ascending air temperatures in the region around Umiujaq are expected, with a distressing high increase for the winter months of up to +10 K (ALLARD ET AL. 2007) for the next 40 years. Such elevated air temperatures will of course also impact the soil temperature which are supposed to mount around +4 K (SUSHAMA ET AL. 2006). Consequently further

temperature which are supposed to mount around +4 K (SUSHAMA ET AL. 2006). Consequently further permafrost decline, accompanied by a decrease of the ground's stability and an expansion of wetlands, is very likely.

Keeping in mind the way of living of Umiujaq's inhabitants, such impacts will affect their society in a profound manner. Paths and small tracks, nowadays stabilized by the frozen ground, will turn into muddy and wet areas no longer passable, or even walkable. As a result big parts of their recent hunting areas are no longer accessible and routes to lakes and rivers for fishing may soon no longer exist. Additionally, if the wetlands and lakes escalate, other plants – not serving as food source - have can no longer survive.

Besides the changes in the ecosystem, permafrost thawing will also influence infrastructure: impacts are already visible on the main road connecting the airport and the town, where big cracks and corrugations evolved during the last few years (CHARBONNEAU ET AL. 2005). A major problem thereby is the will of the community's authorities to modernize the infrastructure, but sophisticated ideas how to deal with the thawing permafrost as well as the ken about the amount, speed and the magnitude for the constructions are still missing. This lack of knowledge often leads to ill-conceived activities, often evoking more damage, combined with high costs.

6 Field Work

Field work represents the first major component of this study. Its implementation as well as its output is addressed in the following article.

In general it can be divided into two main scientific objectives upon which the division of this chapter is also based, these are:

- i) The record of parameters of the vegetation cover, the snow cover and the active layer behavior (Chapter 6.2). The results help to better understand the correlation between these factors and allow the estimation of permafrost occurrence solely by means of the visible indicators at the surface.
- ii) The geodetic survey of lithalsas throughout the year to enhance the knowledge about the seasonal dynamics of these permafrost mounds (Chapter 6.3). This expanded knowledge of such movements in relation to changing temperatures can then also be used to estimate the amount of permafrost thawing caused by altered climatic conditions, as observed by the surface's motion.

Additionally, the data collected during the field campaigns served as evidence to validate the satellite data and to enhance the analysis and the remote sensing results. The field work was also necessary to obtain a detailed overview about the ecosystem in the area, which was essential in order to estimate the amount of climatic change impact and accompanied environmental risks and threats. The same is valid if the request for adaptation strategies in the area arises and decision support is required.

A further very important aspect of the field work was the contact with the indigenous people which helped in many ways to better understand the situation in the community and hence to estimate the consequences for the population if changes happen. In addition, their observation and experience about changing environmental conditions in the region were highly appreciated and influenced in many ways the analysis and evaluation of the study's outcomes.

6.1 Description of field work

For the collection of all parameters and records of this study, field work was conducted during 2009, 2010 and 2011. In total, field acquisitions from eight stays - four during winter/spring and four during summer/fall, were available (Figure 6.1) and provided the input for a comprehensive database. A field campaign usually had a duration of about one week and was generally carried out in cooperation with either scientists from the University of Laval or from the University of Trois-Rivières.

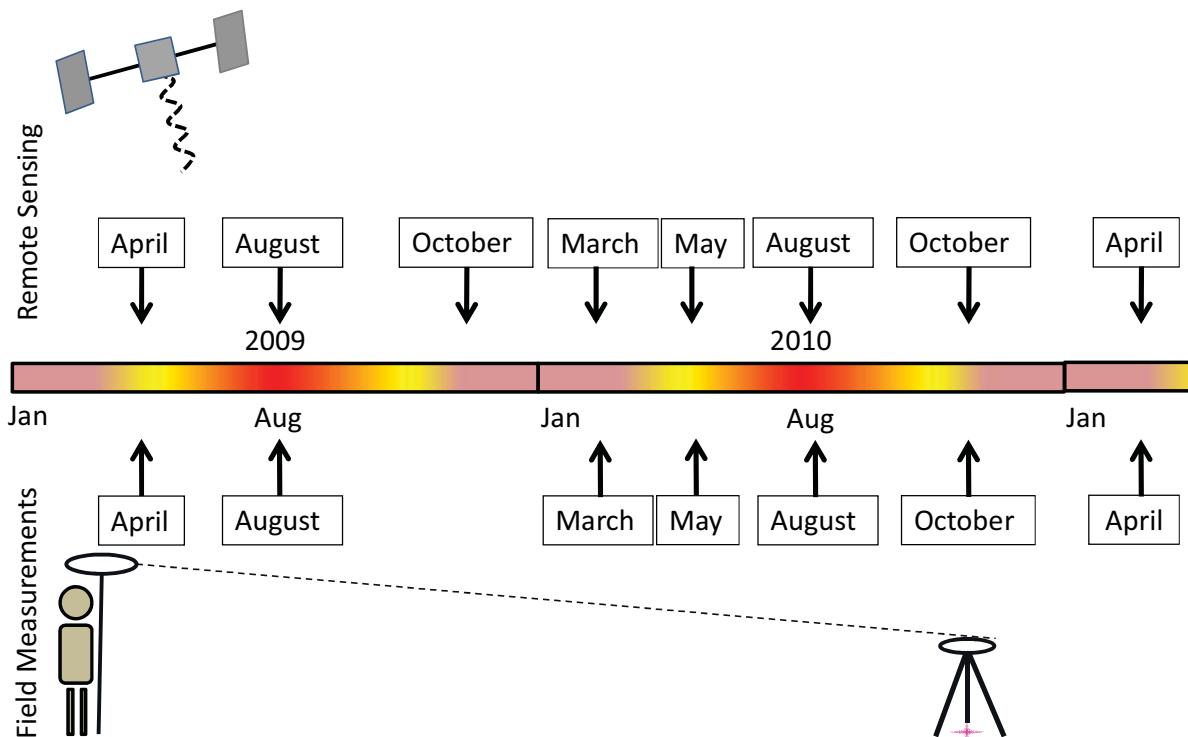


Figure 6.1: Overview of the dates of the data acquisition for the remote sensing data (top) and the field data (bottom)

The focus of the different field campaigns depended greatly on the season (Table 6.1). During the winter months the collection of different snow parameters was the main issue; during the summer, observation of the vegetation cover and measurements of the active layer thickness. The geodetic survey of the lithalsas was accomplished during the winter as well as during the summer.

For the transportation of the equipment as well as for help for the field work, local assistant Peter Novalinga was hired. Mr. Novalinga is an Inuit, familiar with their traditional skills and was therefore able to find safe travel paths over frozen rivers and lakes and to protect the group from dangerous game, such as bears and wolves in the area. Furthermore his involvement brought the exchange between traditional and scientific knowledge forward and led to a better understanding of the research subjects.

Table 6.1 gives an overview of the different field campaigns, the measured parameters as well as the people involved.

Table 6.1: Overview of the different field campaigns, the measured parameters as well as the people involved.

Date	Parameters	Persons involved
April 2009 14.04 – 21.04	Snow Temperature; Depth; Density; Crystallisation Lithalsas Elevation; Expansion	Inga May (LMU/INRS) Monique Bernier (INRS) Esther Levesque (UTR) Michel Allard (UL) Emmanuel l'Herault (UL)
August 2009 11.08 – 18.08	Vegetation Distribution; Structure; Density; Type Soil Active layer thickness; Humidity; Type Lithalsas Elevation	Inga May (LMU/INRS) Ralf Ludwig (LMU) Students (UTR)
March 2010 20.03 – 26.03	Snow Temperature; Depth; Density Lithalsas Elevation	Inga May (LMU/INRS) Yannick Duguay (INRS) Monique Bernier (INRS)
May 2010 03.05 – 08.05	Snow Temperature; Depth; Density Vegetation Distribution; Structure; Density; Type Lithalsas Elevation	Inga May (LMU/INRS) Yannick Duguay (INRS)
August 2010 10.08 – 14.08	Lithalsas Elevation	Yannick Duguay (INRS) Research Assistents (UL)
October 2010 22.10 – 28.10	Vegetation Distribution; Structure; Density; Type; Ground Truth Soil Active layer thickness; Humidity; Type Lithalsas Elevation; Expansion	Inga May (LMU/INRS) Denis Sarrazin (UL)
April 2011 07.04 – 12.04	Lithalsas Elevation	Yannick Duguay (INRS) Monique Bernier (INRS)
August 2011 23.08 – 12.09	Lithalsas Elevation	Inga May (LMU/INRS)

6.2 Correlation between vegetation, snow cover and active layer thickness

6.2.1 Introduction

The occurrence of permafrost depends on the ground thermal regime, which is governed by the surface temperature. Although it is primarily the climate that sets the stage for thermal conditions over the ground, there are many other factors that influence and complicate this relationship.

The most important ones are the duration and depth of the snow layer as well as the occurring land cover. As these factors show very heterogeneous patterns and can vary dramatically within short distances they are responsible for the microclimate that is of high importance for local ground thermal conditions.

Several studies, also in the Canadian Arctic, have already been conducted in order to investigate and quantify the relationship between the mentioned factors (BROWN 1955; MACKAY 1970) and the following assessments are summarized below.

It is widely recognized that snow acts as insulator and hence serves as a barrier to heat loss from the ground to the air in winter. NICHOLSON AND GRANBERG (1973) found that the variation in mean annual ground temperatures is generally determined by the snow depth, with variations during the summer period being less important. SMITH (1975) even stated in his study about the Mackenzie Delta that mean annual ground temperatures above 0 °C could be reached in some locations, due to snow accumulation, while the mean annual air temperature could still be -9 °C to -10 °C. 'Near the southern fringes of the permafrost distribution, snow cover alone may be the critical local factor determining whether permafrost is present or not' (WILLIAMS & SMITH 1989).

The impact of the vegetation has also been investigated by several observational studies, but in contrast to the snow cover's effect it is more complex and hence more difficult to quantify. For example ROUSE (1982) noticed a considerable reduction of the solar radiation due to the vegetation canopy having a strong effect on the depth and persistence of the snow cover. He also discovered (ROUSE 1984) that summer soil temperatures beneath an open spruce forest were lower than in the adjacent tundra, which might be a result of higher evaporation from a wetter surface and the radiation interception by the canopy. RISEBOROUGH (1985) highlighted a cooling effect in the summer months when higher evapotranspiration occurs in overgrown areas. Whereas ANNERSTEN (1964) mentioned the direct effect of the vegetation is much less important than its role as snow accumulator. Although these two contrary processes, most bush and forest covered soil reaches temperatures about 3 °C warmer on an annual basis compared to neighboring bare soils (ROUSE 1984).

Peat plays a very specific role related to the thermal ground regime. As with snow, it acts as an insulator, but unlike snow, it is present all year round and its conductivity alters seasonally, depending on its moisture conditions. During the summer, when it is typically dry, the conductivity is low and thus the underlying soil is shielded from the higher summer temperatures. Even if the peat remains humid during the warm season, higher evaporation rates cause a cooling effect. Consequently, areas where peat covers the soil normally show lower temperatures than areas without such cover (WILLIAMS & SMITH 1989).

Due to the much higher heterogeneity of the listed factors in sub-Arctic areas such as the surroundings of Umiujaq, than in the high Arctic, the impact is even more pronounced. Additional effects like the aeolian distribution of the snow, caused by very high wind speeds, and a very small-scaled relief makes it even more difficult to quantify their influence properly.

Even though BROWN (1979), LÈVESQUE ET AL. (1988), ALLARD (1993), and MENARD ET AL. (1998), amongst others, previously studied the correlation between the surface variables and the occurrence of permafrost in sub-Arctic Québec, more investigations were done in the context of this study in order to update theirs with recent measurements as well as to affirm and to specify their findings. Thus the main focus was the correlation between the snow cover depth and the vegetation and the following consequences for the active layer thickness during the summer.

6.2.2 Methods and results

Spread over the test site of 60 km², 100 sampling points were identified, at which snow cover characteristics were recorded during the winter and information about the vegetation was observed during the summer. At these plots the active layer depths were measured and soil parameters analyzed. This was conducted during five field campaigns in winter and summer 2009 and 2010 (Chapter 6.1).

The measured parameters of the snow cover shall be presented and discussed first, followed by the results of the vegetation mapping and active layer records.

6.2.2.1 Snow measurements

Snow samples were taken during three winter campaigns: April 2009, March and May 2010. The focus of the measurements was to collect information about the snow cover heterogeneity, concerning thickness and density, in order to correlate it with vegetation mappings and active layer measurements from the summer. In addition, the air temperature and the temperature at the bottom of the snow layer, from now on referred as air-snow temperature gradient, were measured and their interrelation to the other parameters analyzed. To gain a better understanding of the snow cover composition and its physical characteristics, several samplings have been analyzed with respect to their layers, grain size and grain form. Information of snow density and depth were obtained by the 1 m snow core device, Federal Snow Tubes-Standard-Metric (1004-010), from the Rickly Hydrological Company (2009).

The air-snow temperature gradient was measured by a bespoke instrument. This instrument consists of two one meter pipes made out of galvanized steel with a diameter of 0.25 cm (1/4 inch) that can be plugged into each other; hence it is possible to measure temperature down to 2 m depth. The pipes have a clearly readable scale and hand gear to drill the pole into the snow. A Pt 100 sensor, with an accuracy of +/- 0.07 % is fixed at the bottom, connected via a lithium coated cable inside the pole to a checking device. It is the matter about the high precision thermometer GMH 3710 from NEWPORT OMEGA electronics for Pt 100 sensors. By means of this instrument it was possible to measure the temperature in different heights of the snow cover to get profiles of the temperature. It was also used for the soil temperature record during the summer field work. In Appendix 1 the sketch of the device can be found.

In the following, the described and discussed measured snow parameter values are the mean out of three samples of one sampling spot.

Snow depths show a high variability in space and time (Figure 6.2). Values between zero snow cover and over 200 cm were measured in 2009 and between zero and 180 cm in 2010. The average thickness of the measured snow samples were 90.8 cm in 2009 and 70.19 cm in 2010. Almost all sampling points show less snow in 2010 and areas with snow more than 150 cm are more seldom in 2010 compared to 2009.

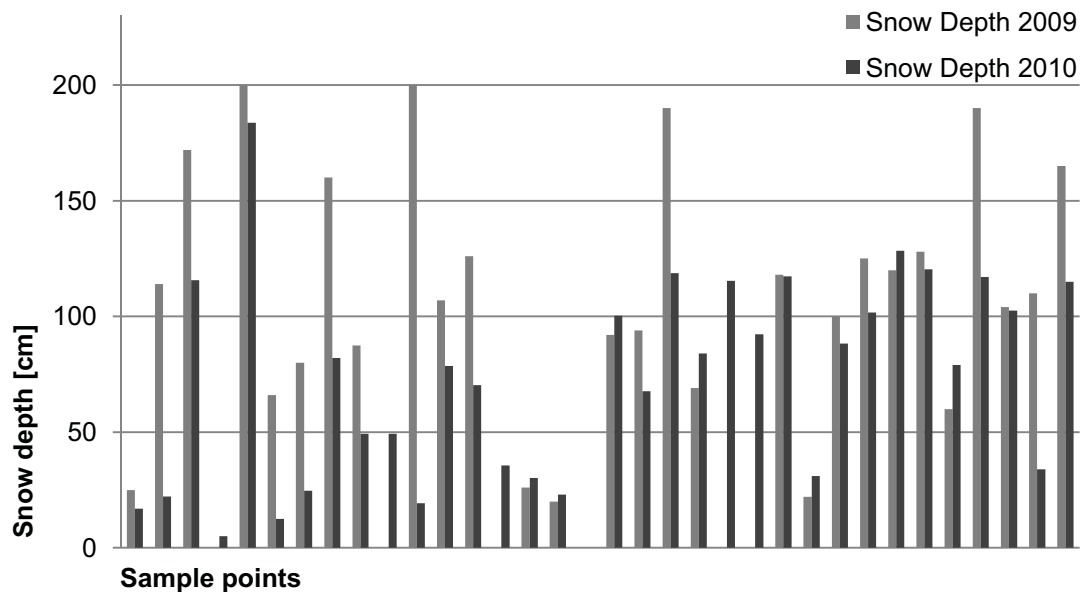


Figure 6.2: Recorded snow depths [cm] at the different sample points in 2009 (light grey) and 2010 (dark grey)

The differences in the total amount of snow can be easily explained by less precipitation in 2010. In order to validate this statement the snowfall records of two years of concern were taken into account (Figure 6.3). For this, the fallen snow precipitation between November 2008 and March 2009 was tallied up (in total 216.2 cm) as well as the amount between November 2009 and March 2010 (174.6 cm).

This period was chosen as it is assumed that most of the snow accumulates during these months without melting. The outcome of this is a plus of 40 cm for 2009, also if only factoring the ‘really’ cold months January, February and March, the measurements for 2009 sum up to 115.2 cm and only to 56 cm in 2010. The demonstrated offset already gives evidence to the much higher snow depths in 2009, but given the fact that in March 2009 there was 45.4 cm more snow than in March 2010 (60.8 cm in 2009 and 15.4 cm in 2010) confirms this even more. It is also important not to neglect the snow density for such interpretation, because differing snow compression could result in the deviation of the measured snow depth.

Owing to the density measurements, outlined later in this chapter, it appears as this is not the case, as even the density is higher in 2009 than in 2010.

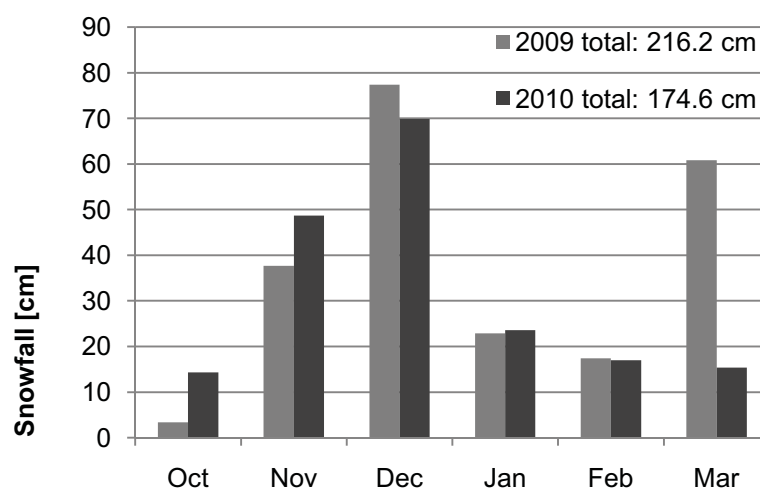


Figure 6.3: Snowfall [cm] for the months October, November, December, January, February and March in 2009 (light grey) and 2010 (dark grey).

The next important research objective was to get an impression about the spatial distribution of the snow and its variability. Although data of only two years is not too diagnostic, it helps to give an overall impression about the situation. Nevertheless, in order to substantiate the supposition based on this dataset, additional evidence was gained by concretely interrogating inhabitants and researchers familiar with the area.

For this analysis the deviations of each point [%] from the mean of all samples from 2009 as well as for 2010 was calculated (Figure 6.4). In doing so, it could be determined if the samples with above-average / below-average amount of snow in 2009 are the same as those in 2010.

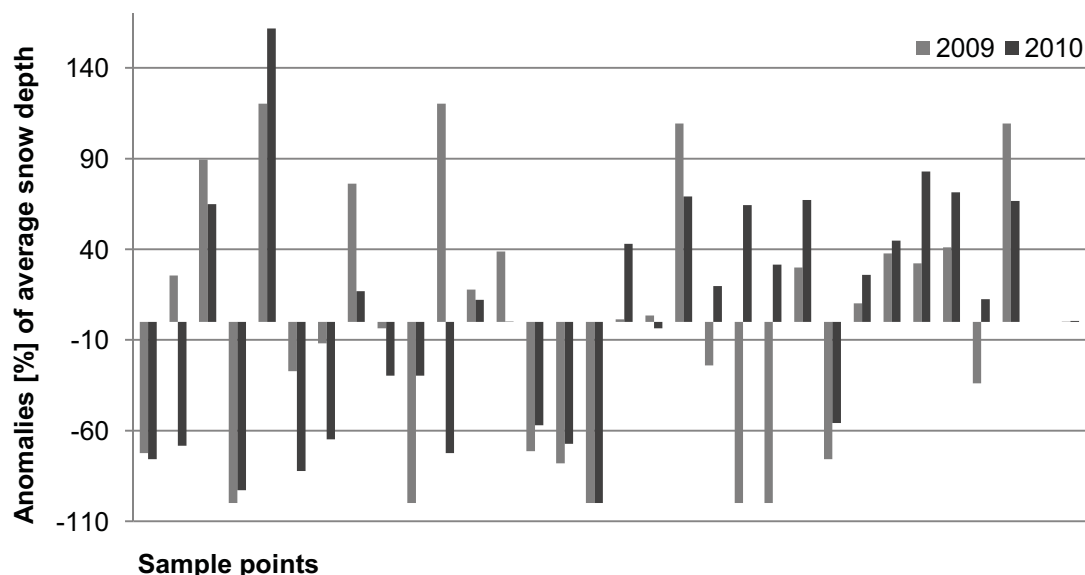


Figure 6.4: Deviations of each point [%] from the mean of all samples from 2009 (light gray) and 2010 (dark gray).

The comparison demonstrates 75 % accordance, however it has to be mentioned that at all points where no conformity occurs (Table 6.2), the contrary deviation in either 2009 or 2010 is in most cases small (+/- 3.52 % to +/- 25.55 %), though twice more than 60 %.

Table 6.2: Deviations in [%] from the mean for 2009 and 2010 for all sampling points where no accordance exists.

Anomalies [%]	
2009	2010
25.55	-68.42
120.27	-72.47
3.53	-3.60
-24.01	19.67
-100.00	64.31
-33.92	12.55

The 15 % differing samples were also analyzed in terms of their density, in order to understand whether the difference was due to more or less snow compression, but no such correlation could be ascertained.

With these results, plus the statements of the local people interviewed, the assumption can be made that the snow cover tends to form similar distribution patterns in every year, with spots experiencing higher accumulation than others.

This is an important fact, and essential to consider, if the influence of the snow cover (primarily its depth) on the thermal regime of the ground and the consequent impact on the permafrost are to be studied.

If the sample points are subdivided into east and west, the average snow depth is 116.19 cm in the east, around 22 % higher than in the west, which is very likely due to less vegetation in the west and much higher snow compaction. A detailed interpretation follows in the comparison part of this chapter. With respect to snow density, a high variability (Figure 6.5) is observed, with values ranging from 0.05 g/cm³, which equates very freshly fallen and fluffy snow, up to 0.7 g/cm³ which almost corresponds to the density of firn (RAGHUNATH 2006). In reference to the two years analyzed, higher densities were measured in 2009 reaching values from 0.13 g/cm³ (88 cm snow depth) to 0.7 g/cm³ (74 cm snow depth) and only 0.05 g/cm³ (29 cm snow depth) to 0.49 g/cm³ (115 cm snow depth) in 2010. The calculation of the average density shows an elevated number for 2009 (0.35 g/cm³) than for 2010 (0.28 g/cm³). This conforms to the experience gained during the field work: in 2009 at some points, especially in the west part, the snow cover was often so compact, that it was not even possible to take samples. Consequently the average of the density in 2009 would even be superior to the ones presented, as the density probes with highest density values are missing.

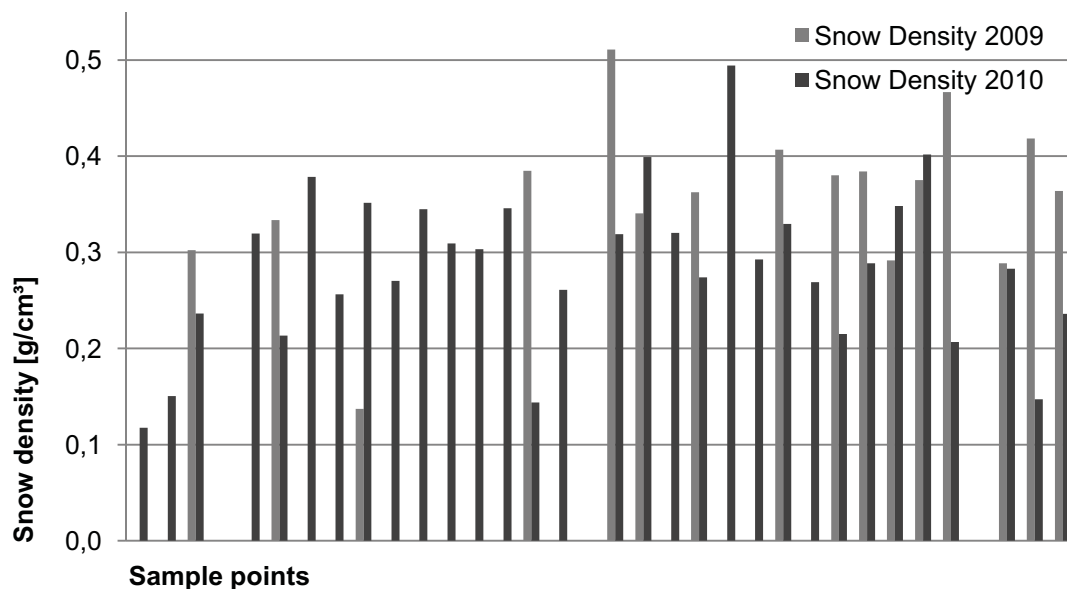


Figure 6.5: Recorded snow densities [g/cm³] at the different sample points in 2009 (light grey) and 2010 (dark grey)

The snow density is an outcome of the compaction processes the snowpack experiences and their combination. There are mainly three processes that work more or less independently and with different efficiency. The three processes are:

- Snow drift
- Metamorphism
- Deformation strain (ARMSTRONG & BRUN 2008)

The impact of snow drift depends primarily on the wind velocity and the surface's snow type. As soon as the wind speeds up and a certain threshold is exceeded the snow particles are sublimated and collision between the particles occurs. This process results in a transformation of the snow crystals to

smaller and much more rounded particles, which in turn results in snow compaction. Snow drift is understood to be the most important compaction process in Polar Regions (DANG ET AL. 1997).

Metamorphism means the transformation of snow particles within a snowpack, caused by temperature and water vapor gradient and starts immediately after the snow is deposited. In most cases the process starts with the shrinking of grains and involves snow compaction. This procedure is highly depending on temperature and liquid water content (ARMSTRONG & BRUN 2008).

Deformation strain is snowpack compaction caused from the snow's own weight and the gravity forces that affect the grains (GOLUBEV & FROLOV 1998). This implies that the more snow is available, the higher is the deformation strain.

To investigate which of the three introduced processes plays the major role in the test site of the study, further climate parameters, in particular the wind speed and the temperature were analyzed for the period concerned (March 2009 and 2010). The data for this was downloaded from the National Climate Data and Information Archive, run by Environment Canada, which provides hourly data for a climate station in Umiujaq (Station 7108568 at 56.53°N, 76.20°W, 76.20 m). Unfortunately, measurements are only available between 7 am and 5 pm LST (Local Standard Time) and sometimes even less. For this analysis, wind speed in general, but only maximum temperatures have to be considered, and it has been assumed that no misinterpretation arises by neglecting the nightly weather conditions.

The records show a mean temperature far below zero for 2009 as well as for 2010 (-17.18 °C and -11.64 °C) and in both years there is only one day when temperatures rose over 0 °C (+0.1 on the 26.03.09 and +0.4 °C on the 12.03.10). This actuality more or less excludes a high impact of the metamorphism process as values around or above zero would be a requirement.

In contrast, the wind does seem to have a greater effect on the snowpack. In 2009 the average wind speed was 24.11 km/h though a maximum of 70 km/h was recorded on the 11.03.2009. On the other hand 2010 only saw an average of 18.86 km/h and a maximum of 63 km/h on the 3.03.2010. These findings clearly indicate that snow drift is the major process behind snow compaction, and therefore also confirms the statement of DANG ET AL. (1997).

The fact that in 2009 more snow had fallen and higher snow depths were measured supervenes to the higher wind speeds and leads to additional compaction caused by deformation strain.

Considering the spatial occurrence of the snow density, the west part showed higher densities averaged over the two years, with a mean of 0.41 g/cm³, compared to 0.35 g/cm³ in the east. That equals to less dense snow of 14 % in the east and conforms to the results of the snow depths, which highlighted the east as the area with elevated numbers. Due to the location in the lee of this area, behind the Cuestas, and the augmented vegetation serving additionally as wind shelters, lower wind speed is suggested. Consequently this corroborates the belief that snow drift plays the most important role for the compaction process.

Further analysis was done in order to depict correlation between snow depth and snow density. The outcomes do not reflect a clear relationship between those two parameters as in 2009 the correlation coefficient R^2 only reaches 0.054 and in 2010 at least 0.216. Disregarding the statistical outcomes the correlations plotted in Figure 6.6, allow the statement, that a certain degree of dependency exists.

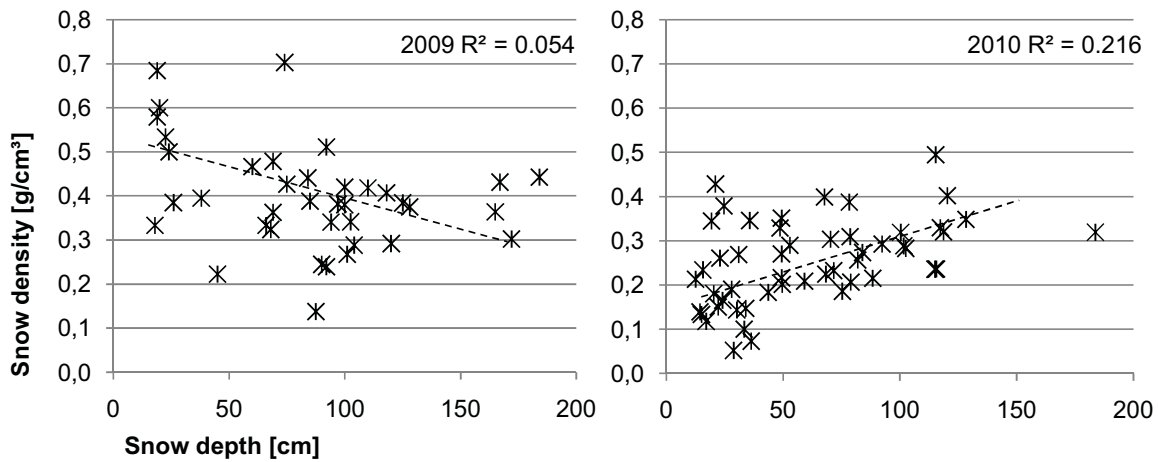


Figure 6.6: Correlation between snow depth and snow density, On the left the values for 2009 and on the right those for 2010

Moreover it is interesting to note, that in 2009 the density decreases with higher snow depth, whereas in 2010 increasing density corresponds to increasing snow depth. It should therefore be explored further to determine if the relation between depth and density may switch after a specific snow depth. Such a threshold might be the trigger point when the effect of the snowpack's weight overcomes the snow drift process. The results did not show any evidence for such a relation, and probably a subdivision of the snow profile into different layers would be required to reveal any such correlation.

Concerning the findings of the snow temperatures, the recorded temperature profiles are presented initially and two of them are exemplarily graphed Figure 6.7. Most of the snow profiles show similar trends: the deeper the snow the warmer its temperature. This is valid with the exception of some samples when the outside temperature was warm ($> 0^\circ\text{C}$) and the upper part of the snow cover was heated by the warm air. These primary findings confirm the hypotheses of the isolating effect of the snow cover.

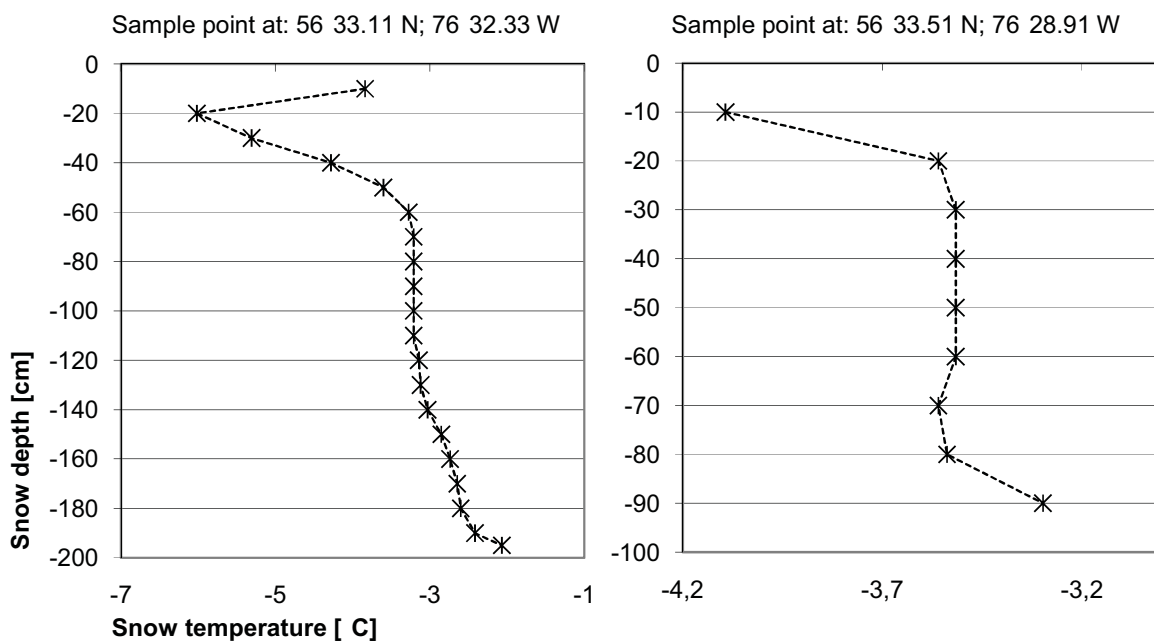


Figure 6.7: Two selected snow temperature profiles from the 17.04.2009 (left) and the 18.04.2009 (right)

To quantify further this ascertained impact, the study mainly focused on the temperature gradient between the surface of the snow cover and at the bottom (=air-snow temperature gradient). For this analysis different methods were implemented: initially the calculated air-snow temperature gradient was plotted versus the snow depth. Although there is no correlation for 2009 ($R^2 = 0.006$), a correlation coefficient of $R^2 = 0.4$ is reached in 2010. Also the visual interpretation of the graph (Figure 6.8) allows the assessment that dependency exists.

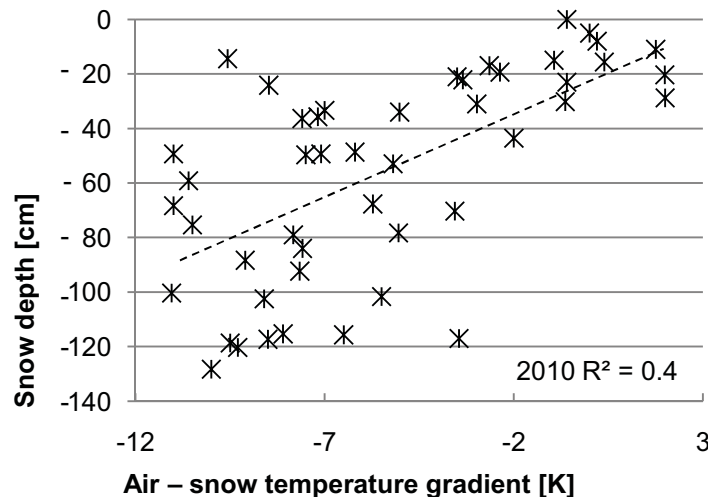


Figure 6.8: Air- snow temperature gradient [K] versus the measured snow depth [cm] in 2010

The difference between 2009 and 2010 can very likely be explained by the prevailing air temperatures during the measurements. During the field campaign in 2010 they differed between $-15\text{ }^{\circ}\text{C}$ and $-8\text{ }^{\circ}\text{C}$, while in 2009 varied around $0\text{ }^{\circ}\text{C}$. Consequently the air-snow temperature gradient could simple not reach values high enough to account for a persuasive correlation in 2009.

In a second step of analysis, the snow profiles investigated were subdivided into different 'depth-sections' of 25 cm (section 1. 0- 25 cm, section 2. 25 – 50 cm etc.) and the calculated air-snow temperature gradients were assigned to the proper snow depth section. The idea was to identify if there is a certain snow depth at which no more significant warming happens.

The results confirm again the increase of the temperature gradient with increasing snow depth: only in the upper 25 cm temperature decreases in the average about $+3.10\text{ K}$ (2009) ($+3.56\text{ K}$ in 2010), probably as a result of the cooling air temperature affecting the top layer. But starting at the next section the temperature increases steadily with snow depth. In 100 - 125 cm the average temperature gradient already amounts to 4.63 K (7.83 K) and at a depth of 125 – 150 cm even 5.67 K (10 K) were measured. These findings confirm previous calculations done by WILLIAMS & SMITH (1989), where they showed that the outflow of heat from the ground with a thick snow layer was only one-fifth to one-tenth of that at a site with only 25 cm or less of snow.

In 2009 as well as in 2010 the increasing temperature or decreasing temperature gradient respectively stops or even turns at depth deeper than 150 cm. Owing to this outcome, the isolating effect of the snow cover appears to reach saturation at 150 cm depth.

Regarding the dependency of the snow density and the temperature gradient, it appears obvious that with increasing density the temperature gradient decreases. This conforms to the physical characteristics of snow, assigning higher densities to exalted thermal conductivity [$\text{W} / (\text{m} \cdot \text{K})$] (GOODRICH 1982) and thus less isolation.

Some additional interesting findings from the analysis were identified by studying overgrown and bare soils separately. In fact a significant higher dependency of the temperature on the snow depth was observed at bare soil sample points, whereas hardly any correlation ($R^2 = 0.028$) could be found for samples where vegetation occurs.

In summary the discussion of the recorded snow parameters concludes:

- higher snow depth and density in 2009 than in 2010, due to elevated snow fall and higher wind speeds in 2009 during the time period assessed.
- higher snow depth in the east part yet lower density. This leads one to assume that lower wind speeds, due to the lee location behind the Cuestas and more vegetation serving as wind shelters, are playing an important role in the compaction process.
- hardly any R^2 correlation of snow depth and snow density in 2009, but visible relationship after plotting the values. Increasing snow depth corresponds to decreasing density.
- correlation of $R^2 = 0.2$ of snow depth and snow density in 2010 and a contrary dependency of the two parameters compared to 2009.
- increasing snow temperature with increasing snow depth until a depth of approximately 150 cm, at which the temperature remains constant.
- fewer air-snow temperature gradients with increasing snow density.

6.2.2.2 Vegetation analysis

The main purpose of the vegetation survey was to gain information about the impact of the vegetation on snow accumulation. Thus as a first step the snow depth of the sample points where vegetation occurs was compared to those with no vegetation. From this it was determined that the average snow depth at overgrown spots is over 30 % less than at no-vegetated areas, and the minimum measured snow accumulation at a vegetated habitat is 45 cm, while at non-vegetated areas zero snow cover was also metered. It was also determined that at only 18.5 % of the sample points where densities superior than 0.35 g/cm^3 were measured, plants occur. Therefore it is already obvious that a relation between vegetation and snow depth and density exists, assigning a more and denser snowpack to less vegetation.

To determine the influence of the vegetation it should not only be taken into account if vegetation exists or not, but also which type of vegetation has the biggest impact on the accumulation process. The exact description of the plants' specie and type was not necessarily important, but rather the actual parameters influencing this accumulation process, which were assumed to be three:

- height
- stability
- structure

In contrast to height, which is very simple to measure, the stability as well as the structure is much more difficult to quantify and hence a clear system was required that allows objective records.

The 'stability' of the plant shall represent its resistance when covered by snow and be a measure of the extent to which branches and leaves buckle under the weight of the snowpack. The more it buckles the less will be its effect on snow accumulation. Therefore the mapped vegetation areas were divided into 'grass-like' vegetation easy to press down by the snow and more 'bush-like' vegetation with woody branches, more resistant to the snow load. Furthermore areas with mosses, lichens and little trees

were listed separately. Based on this information, the vegetation was then classified in different 'stability classes'.

The idea of the 'structure' was to get information about the degree of ramification and the density of the plant, as more branched and dense bushes were assumed to serve as bigger obstacles than unique trips. The mapped vegetation was thus assigned to the six classes:

0. no vegetation
1. Trees
2. Krummholz
3. Bushes
4. Grass and Herbs
5. Mosses and lichens

The class of bushes was again subdivided into the three classes:

- 3.1 treelike bushes exceeding over 50 cm
- 3.2 smaller bushes (< 50 cm)
- 3.3 Shrubs only covering the ground and not exceeding 50 cm

By means of the introduced three vegetation parameters, each plant population could be clearly defined by a 5 digit number code. The first three digits represent the height in cm, the fourth stands for the stability class and the fifth indicates the structure class.

This information together with information delivered from a biologist team from the Université du Québec à Trois-Rivières (UQTR) lead by Esther Levesque, was used to create final vegetation classes which ultimately were related to the measured snow depths.

The data from UQTR was collected during 1990, 2004 and 2009. 301 sample plots of 30 x 30 m were mapped, whereas the special focus was on the separation of five categories: bushes, forests, rocks, water and other. For each category the percentage of the total area was noted. In 2009, different types of bushes and trees as well as the growing heights were also recorded (LEVESQUE & TREMBLAY 2010).

The combination of these datasets results in 8 vegetation classes for the purpose of this study, starting with class number 1 representing no vegetation and ending with class number 8, which stands for the most dense and tall bushes.

As initially mentioned, the vegetation cover plays an important role as a snow accumulator which could be confirmed by dint of this work, however the results are not as significant as expected. For interpretation the first step was to calculate the correlation between snow depth and the defined vegetation classes. The results, presented in Figure 6.9, demonstrate interrelation between the two parameters which is reflected by a correlation coefficient that amounts to $R^2 = 0.4$. In order to evaluate the necessity of the introduction of the above described classes a test comparison was conducted, to only use the vegetation height plotted against snow depth. This test yielded less correlation with R^2 of only 0.3 and thus the classification was retained.

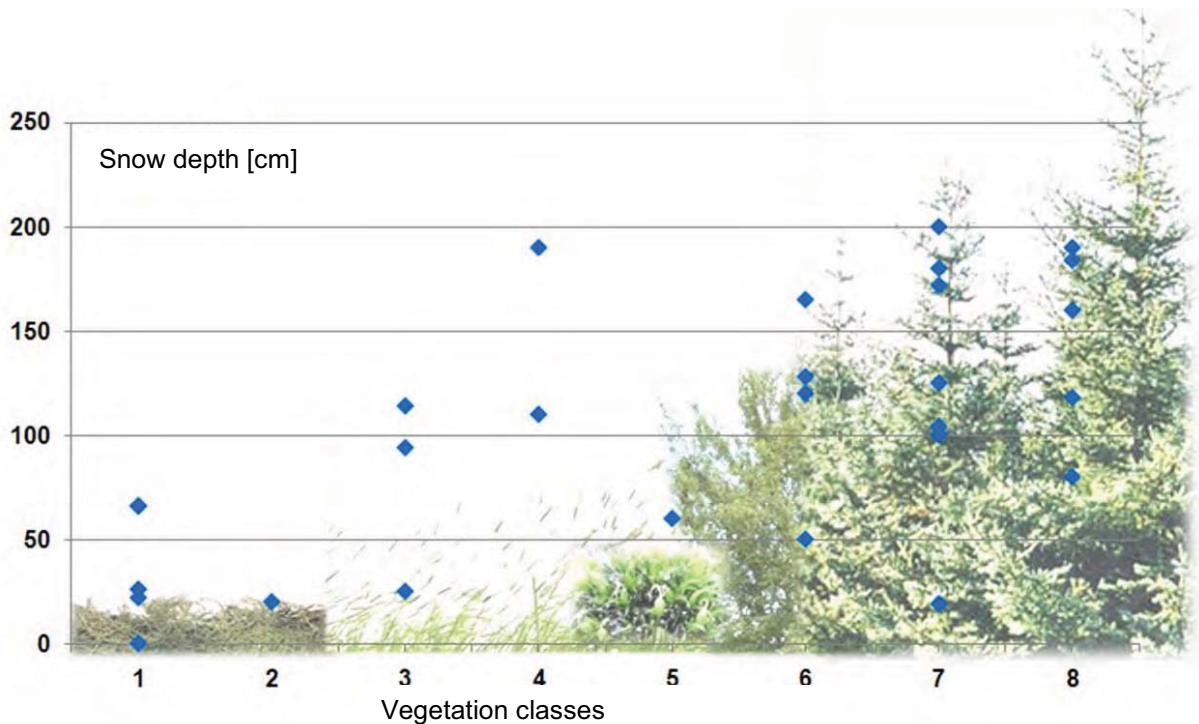


Figure 6.9: Relationship between the measured snow depth [cm] and the classified vegetation

Although Figure 6.9 graphs the relation between vegetation class and snow depth, no major differences are indicated between classes 6, 7 and 8, representing a combination of very high and dense bushes and trees. Considering also the correlation coefficient of 'only' 0.4 the question is raised: from a certain vegetation height and density does the prevention effect of the branches supercede the accumulating effect. In fact, this is very likely, especially when taken into account several trees and bushes and not only a single one. Such observation was already introduced by SMITH in 1975 and is very probable to be the reason for the low correlation coefficient in this study.

That said, the results of this study clearly identify the structure classes 3.1 and 3.2 (bushes) combined with heights between 50 and 100 cm as most efficient snow accumulator.

Although this can be done with only some uncertainty, it remains that the relief should be taken into account, and that its impact is also responsible for the sometimes fuzzy outcomes of this investigation. Although topography is not subject of this study, it shall be mentioned that a clear correlation between the relief and the snow depth was visible simply by walking in the area. Hardly one top of the frost mounds and other elevated terrain was covered by snow, yet accumulation up to 2 m between the hills was typical. Furthermore it is important to mention that a correlation between topography and vegetation cover is obvious and goes pretty well in conformity: depressions and small valleys mostly are covered with bushes up to 100 cm, whereas on exposed surfaces bare soil is dominant.

Summing up it can be stated that:

- At sample spots with no vegetation 30 % snow was accumulated and the snowpack's density was remarkably higher.
- Not only the vegetation height but also its structure and stability have an important impact on the accumulation process.
- The most snow accumulated at areas overgrown by small bushes (50 -100 cm)

Statements about the coexistence of the different factors can only be described with high uncertainty, but more investigation would be required to identify which one is the driving factor.

6.2.2.3 Active layer measurements

Besides the mapping of the vegetation, one goal of the summer campaign was the analysis of the active layer depth. The active layer is defined as top layer of the permafrost affected soil that thaws during the summer and freezes again during the autumn (HUGETT 2003), hence its depth and its spatial variation represents the summerly thermal regime of the ground.

By measuring this thawing depth during the summer at the same sample points where records of snow and vegetation were taken, the impact of the different surface conditions on the seasonal thawing should be identified.

To estimate the depth of the thawed layer, the same bespoke instrument described previously was used and plunged into the ground while the temperature was continuously observed. It was assumed that the permafrost table, corresponding to the bottom of the thawed layer, was reached when the resistance was so high that further penetration into the ground was no longer possible. To avoid misinterpretation caused by rocks, an additional premise was to reach 0 °C soil temperature. When both assumptions - hitting upon solid subfont and reaching a temperature close to 0 °C - applied, the depth was read off the instrument's scale. To validate this method several holes up to the potential frozen layer were dug by means of a spade and the occurrence of frozen soil could be confirmed.

The measurements display a very heterogeneous and especially small-scaled pattern of the active layer depth. Values between 30 cm and much more than the detectable 200 cm occur side by side. This coexistence is most pronounced by sampling points located on the top of a mound and on its, sometimes very steep, slope. It has to be mentioned at this point, that unfortunately only 29 useful samplings are available due to the very time consuming measurement process. Furthermore the accuracy of the measurements is questionable. The samples were located by means of a GPS, usually operating with a horizontal precision of 1 – 5 m. Thus it was possible that not exactly the same spot was sampled on different dates, and due to the very heterogeneous vegetation pattern and small-scaled topography this would cause severe misinterpretation. In order to enhance the relocation, it was thought to place sample points close to clearly recognizable non-moving features, but some uncertainty still remains.

The correlation between the active layer deepness and the snow depth was computed and analyzed, but no relation to snow depth could be discovered. These results would probably be different if also the soil texture would have been taken into account.

Thus by means of the measurements during field work, no evidence was obtained to confirm the hypothesis that a thicker snow cover causes a deeper active layer. Nevertheless, aside from the records, an impression about the active layers distribution attained by working in the field definitely confirms this belief. It was obvious that on elevated sites, where hardly any snow remained, the penetration of the thawing process was much less than in depressions with bushes and high snow depths in winter.

6.2.3 Conclusion

After the presentation of relationships and dependencies of the different parameters, summarizes the coexistence of the factors discussed. It becomes obvious that it is not only one parameter influencing another, but a very complex system that can only be taken as a whole.

Table 6.3 summarizes the coexistence of the factors discussed.

Table 6.3: Dependencies of the different analyzed parameters. YES indicates coexistence, NO indicates no coexistence

	Vegetation	Thick snow cover	Active Layer < 1.5 m	Elevated terrain
Vegetation	-	YES	NO	NO
Thick Snow Cover	YES	-	NO	NO
Active Layer < 1.5 m	NO	NO	-	YES
Elevated terrain	NO	NO	YES	-

By means of this study it can be ascertained that, by considering all the important conditions, there are some general rules:

1. An elevated area coexists with a very thin or zero snow cover and almost no vegetation is related to permafrost occurrence in the upper 2 meters.
2. A wind sheltered, low area coexists with a thick snow cover and much denser vegetation is related to no permafrost (at least not in the upper 2 meters).

Figure 6.10 schematically depicts the discussed dependencies.

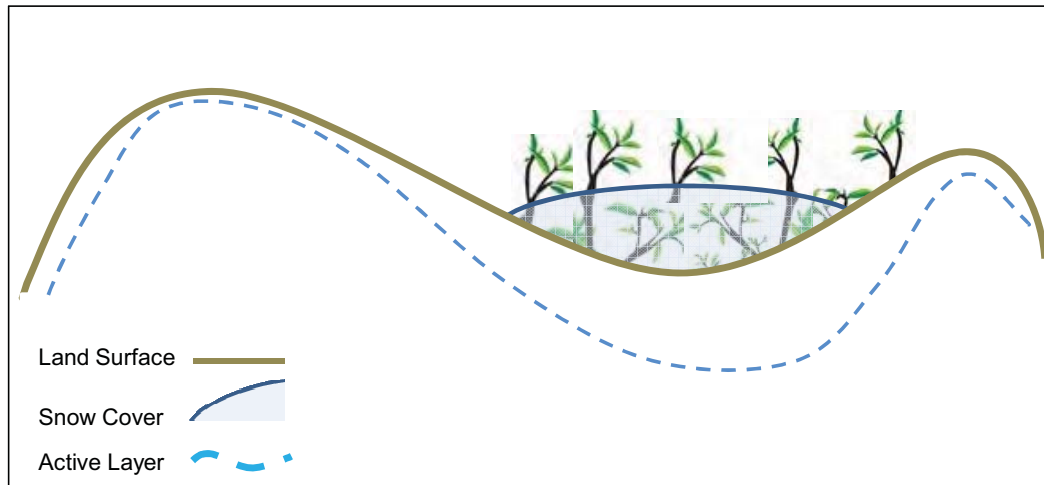


Figure 6.10: Sketch of the interrelation of the factors topography, active layer, vegetation and snow cover

Due to corresponding outcomes of similar studies, it is assumed that they are probably transferable for the discontinuous permafrost zone (JOHANSSON & AKERMAN 2008; JORGENSON ET AL. 2001).

This also summarizes and confirms previous studies conducted in this area. For example, MENARD ET AL. (1998) mentioned in their study of the surroundings of Umiujaq, that 'ground surface temperatures at the shrub and forest sites stands show that permafrost cannot be maintained in these sectors' as the ratio between the freezing and thawing indexes are too low, 'and the mean soil temperatures are too high for permafrost to form'.

Although a very advanced idea of the coexistence of the different factors involving permafrost occurrence could be gained, it still remains the question which parameter evokes another or is responsible for the existing of another and this study contributes to such investigations.

However, the aim of this study was not to identify such influences, but rather to deliver a synopsis of the different permafrost involving parameters, and to identify indicators on the land surface, which are evidence for permafrost occurrence and whose alterations are in turn a sign of dynamics happening in the permafrost. The knowledge gained about the two main indicators – snow cover and vegetation – as well as their interaction can serve to set up a spatial monitoring system that is feasible to detect and monitor permafrost solely by targets visible at the surface. Hence this data can additionally be assimilated for observation systems based on satellite imagery that would allow highly required permafrost surveillance in the vast and remote areas in the North.

In chapter 7.1 the possibilities and limitations of recent remote sensing techniques for such observation are introduced and discussed with the help of examples of the test site.

6.3 Geodetical survey of lithalsas

The second goal of the field study was the geodetic survey of lithalsas throughout the year to enhance the knowledge about the seasonal dynamics of these permafrost mounds. The knowledge gained about their elevation movements related to the outside air temperature should i) serve as validation data for the subsidence detection by means of differential interferometry, detailed discussed in chapter 7.2 and ii) contribute to set the physical base of adequate permafrost modeling.

The main purpose of the survey of the lithalsas was to get a better idea of their seasonal movements. Several studies have been conducted previously surveying the inter-annual dynamics (COULTISH & LEWKOWICS 2003), but only a few deal with seasonal behavior, this investigation should contribute to enlarge such knowledge.

The lithalsas were measured several times during the year: twice in 2009, four times in 2010 and once in 2011. Unfortunately due to wind speeds up to 100 km/h it was not possible to record all points during the campaign in October 2010, and only some for one of the lithalsas studied.

6.3.1 Differential GPS

A differential Global Positioning System (d-GPS) is an advanced GPS (Global Position System) that is able to ascertain locations with a much better accuracy than a simple GPS. A common GPS operates with one user segment (=receiver) that acquires signals from at least four satellites and performs mathematical algorithms to calculate the distance from a satellite, which in turn determines its position. Unfortunately inherent in the signals arriving at the receiver are some errors resulting mainly from satellite ephemeris, the troposphere and the ionosphere (MONTEIRO ET AL. 2005), hence their locations accuracy normally is in the range of several meters.

In contrast, a d-GPS works with two receivers: one stationary, referred as base station, and one moving rover (ESRI 2011). To improve the accuracy of the GPS' position, the idea of the d-GPS is to have the reference station at a known position (e.g. trigonometric points) while the rover moves around to different points that have to be surveyed and sends signals about its position to the base station. In contrast to common GPSs the reference receiver attacks the equation to calculate the position backwards. To wit, it figures out what travel time the GPS' signal should take and hence compares it with what they actually are (TRIMBLE 2011).

In order to finally obtain the positions of the unknown points recorded by the mobile station, two approaches exist: *real time surveying* or *post-processing*.

For the real time surveying, an additional radio receiver is required that captures the corrected signals and computes in 'real-time' the precise positions. Post-processing instead, stores the GPS measurements in two separate files, one containing the 'correct' data of the base station and one the still faulty records of the rover. These files are afterwards transferred to a computer that runs specific post-processing software which eliminates the errors.

In 2005 MONTEIRO ET AL. published their results about the accuracy of a d-GPS and highlighting the distance between base and rover station as the main cause of effect, which was earlier (1993) defined by the International Association of Marine Aids to Navigation and Lighthouse Authorities (IALA) to about 1 m accuracy degradation for each 150 km. Nowadays d-GPS producers state the accuracy for their instruments to less than 1 cm for x, y and z – direction for optimal conditions.

For the geodetic survey in this study, the differential global position system (d-GPS) ProMark 3D system from Magellan, together with the antenna type NAP100 – L1 GPS antenna (Magellan) was utilized. The post-processing software GNSS Solution v3.10.07, also provided by Magellan, was used to analyse the records, stored in the so-called *Ashtech* format. According to the user's guide, accuracy up to 1.5 cm is attainable when using a record time of at least 15 s, and can be enhanced by longer record times. For the measurements of this study, a record time of 60 s for each point was chosen and due to the fact that no obstacles interrupting the signal were present, the accuracy ranges were between 1 to 5 mm. Earlier studies conducted by LITTLE ET AL. (2003) already validated this method as suitable to measure frost heave and thaw.

6.3.1.1 Set up and related problems

After the definition of the lithalsas of interest (below) the first step was the selection of a suitable spot to place the reference station. As the main focus for this study was the exact measuring of the elevation or elevation between different dates respectively, it was most important to guarantee no movement, neither vertical nor horizontal. Thus every location situated on more or less weak ground was out of question and hence only stable ground, mostly represented by the rocky Cuestas had to be consulted. However a further problem supervenes: the entire landmass of Northern Québec is affected by an on-going postglacial uplift, elevating the entire landmass more or less uniformly by up to 1 cm per year (LAVOIE 2008). Due to this fact, mountainous regions would also show changing heights between the different acquisition dates.

Unfortunately there is no way to avoid this influence, but if aware of this fact, accurate statements about the relative movements can still be made; there is just no possibility to provide absolute values without additional recording of the exact amount of the isostatic uplift. Therefore the best was made of this 'unfortunate' situation and the known uplift was used to validate the findings of the differential interferometry, explained in chapter 7.1. And so the base station placed on solid rock, influenced only by the isostatic rebound. Consequently, the calculated differences between the winter and summer heights for the lithalsas, can be traced back to only the permafrost induced movements.

A further problem that had to be tackled was the missing trigonometric point with known coordinates and due to the remoteness of the test site there was no available permanent reference station, close enough that could have been used. This implied also that the error for the recorded position of the base station first had to be defined and the measured coordinates manually corrected, before running

the post-process. The correction of the base station coordinate was implemented using an online service provided by the NRCan's Geodetic Survey Division (www.geod.nrcan.gc.ca/index_e.php). Here it is possible to submit the recorded coordinates, under the specification of the processing mode and the reference system. Out of the Canadian Spatial Reference System (CSRS) the program then specifies the Precise Point Position (PPP) for the submitted data. For this the *Ashtech* format needs to be converted into the *Rinex* format.

In this study, the resulting x and y coordinates were corrected once and used for every subsequent acquisition, whereas the height was adjusted for every single record date.

The chosen position of the base station was located about 500 m from the lithalsas, on the top of a hill approximately 40 m above sea level. The coordinates defined by the CSRS are: 56.55° N and 76.54° W (56.553191709° N; -76.542366753° W).

The points recorded by the rover station were seeded randomly over the three lithalsas for the first time in the winter (2009). This was necessary to guarantee snow free patches for the measurements; furthermore it was taken care that no vegetation, apart from some lichens and moss, subsists. In Appendix 3 detailed information can be found for every single selected point, concerning its vegetation cover and exposition. The selected points were marked with a ca. 20 cm long pin, roughened into the ground and wrapped with pink tape.

6.3.1.2 Description of surveyed lithalsas

Eight field campaigns were performed in 2009, 2010 and 2011, covering all seasons of the year, to conduct geodetic surveys of permafrost mounds. Three lithalsas (referred to as R, M and I), close to the village of Umiujaq (Figure 6.11), were selected to build upon earlier studies in the area (FORTIER 2006; DELISLE ET AL. 2006). Lithalsas are permafrost mounds which are typical for discontinuous permafrost regions, which originate from segregation ice and are highly related to palsas (Chapter 3.3). But in contrast to palsas, lithalsas are missing an insulating peat cover (CALMELS ET AL. 2008; ZOLTAI & TARNOCAI 1975; ZUIDHOFF 2002; ZUIDHOFF & KOLSTRUP 2005).

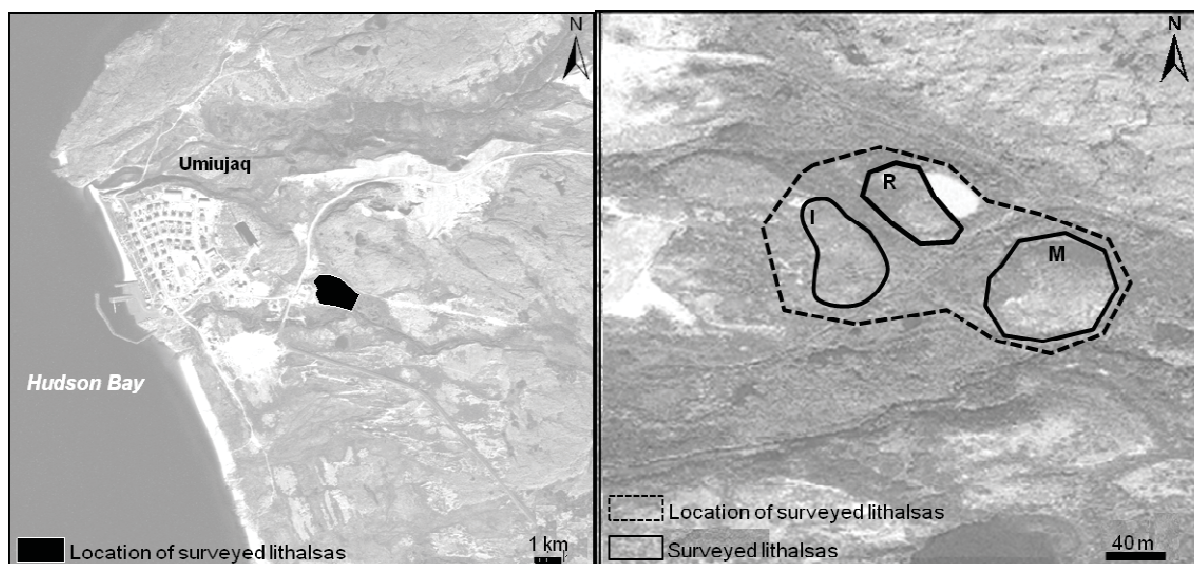


Figure 6.11: Location of the surveyed lithalsas R, M and I near the village of Umiujaq; the left map shows the position in the area, whereas the right shows a focus on the three lithalsas I, R and M

The absence of such an insulating layer makes lithalsas more sensitive to temperature changes, and consequently they exhibit more intense reactions to these (PISSART 2000; SEPPÄLÄ 1988). In the case

of the three lithalsas of interest, this sensitivity is even more acute as they are located in an area affected by very high wind speeds, which induce snow free conditions on the top of the lithalsas.

The three lithalsas are all about 40 m in diameter and between 5- 10 m in height. They differ in their vegetation cover as well as in their state of life cycle.

The most eastern one (R), is mainly covered by grass and shrubs with some additional dwarf birches up to 50 cm on its South-West slope. On its east side a thermokarst lake covers an area of about 220 m², an indicator for advanced degradation. Further to the south, lithalsa M contains mosses as the dominant vegetation. As with R, a thermokarst lake is contiguous to its east pointing slope, but its dimensions are small compared to the ones of the lithalsa and it can be inferred that degradation is only at an initial state. On the third lithalsa (I), lichens and mosses are growing, but several parts are just made of bare soil. It is the only one where no apparent degradation process is observed.

6.3.1.3 Results

As already mentioned at the beginning of this chapter all results have to be understood as relative values. Figure 6.12 shall illustrate the relation between the elevations measured and the presented outcomes.

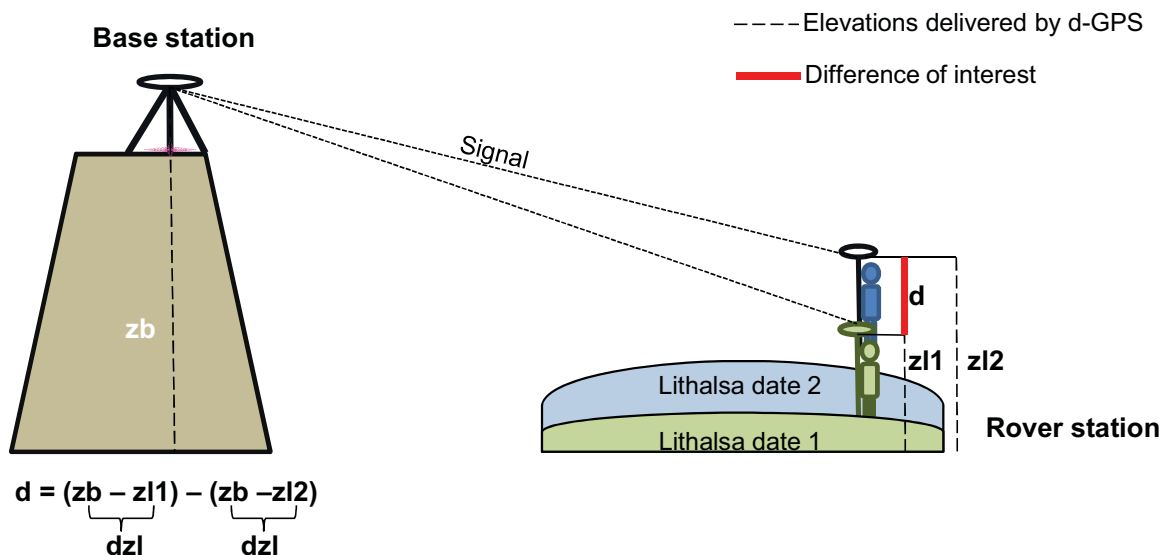


Figure 6.12: Set up of the differential GPS

The average of all points, or a selected number of points respectively, thus was calculated as following:

$$z_l = \left(\sum_{i=0}^n z_{li} \right) \quad (\text{eq. 6.1})$$

In the following section the measurements are presented for each lithalsa separately, starting with the average trend that could be stated, followed by an analysis of the single points and finishing with the discussion of some outstanding spots. After this assessment of the three lithalsas the results are compared and discussed in the next (Chapter 6.3.1.4).

Lithalsa R

At lithalsa R there were 12 points spread over the mound, and measured on five dates: April 2009, August 2009, March 2010, May 2010 and August 2010. The exact location of the samples, the occurring land cover and the local topography is displayed in the map below (Figure 6.13). For it a

classification map based on a GeoEye image captured in 2009 (Chapter 7.1.4) and notes about the relief taken during the field visits served as basis.

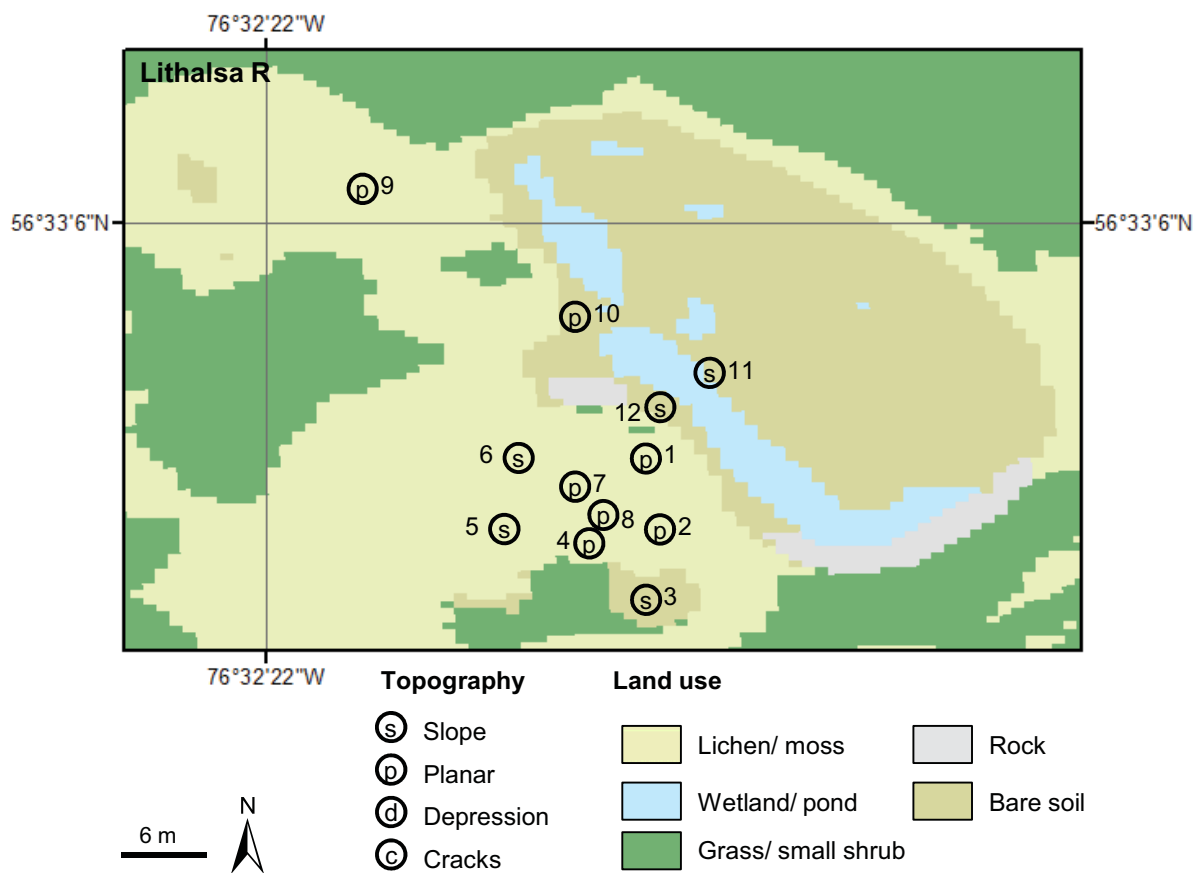


Figure 6.13: Location of the sample points of lithalsa R; in the background the classification map is displayed. The local topography is represented by the framed letters.

In Figure 6.14 the dzl values for each acquisition date are graphed. The higher the number the longer the distance between the base and the samples, and consequently the lithalsa's elevation is lower.

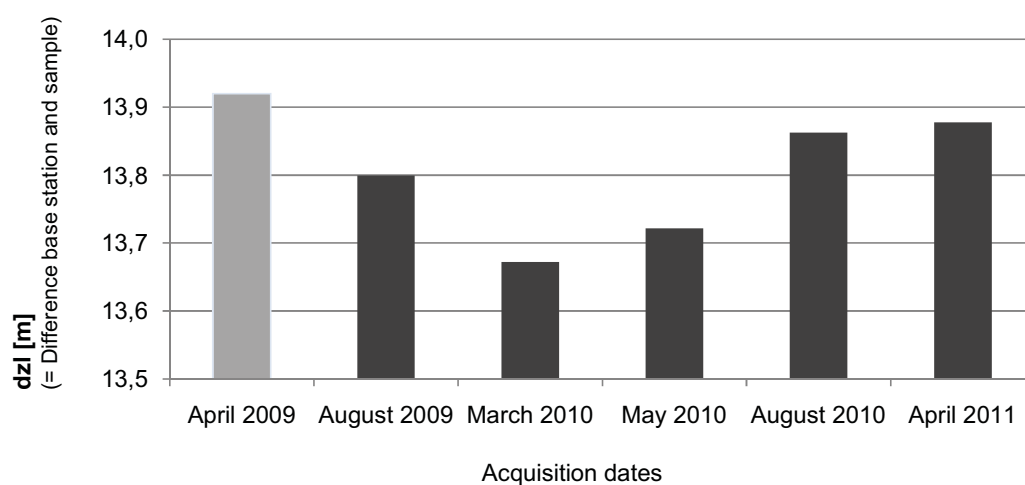


Figure 6.14: The dzl values average of all sample points of lithalsa R for each acquisition; Low values stand for higher elevations. Records for the first acquisition date are only marginally taken into account for the analysis, as the base station was placed on a different spot.

As the base station for the first recording date was placed at another location, a comparison of this number with the other dates is questionable. Although a correction of the values was tried by recalculating the base in relation to the 'new' base the results are very disputable. This is due to the unfortunate fact that the exact location of the 'first' base could not be relocated. As already a deviance of some centimeters in the horizontal position can lead to errors in the elevation of several centimeters, accurate relocation would have been crucial to guarantee error-free comparison. This circumstance also applies for lithalsa M and I.

Neglecting this first value the diagram shows low values for March 2010 and May 2010 and high value for the summer months (August 2009 and 2010). Surprisingly also the latest measurements from spring 2011 are a somewhat elevated. In Table 6.4 the differences between two consecutive record times of each sample point as well as the average are listed. All red numbers represent subsidence compared to the earlier data, whereas black numbers represent uplift.

The columns framed in blue are those periods, when uplift was expected based on the hypothesis that cold seasons are causing frost heaving processed. Between March and May, either uplift or subsidence is possible.

Table 6.4: Calculated differences for all sample points on R, between the different acquisition dates. Red numbers indicate subsidence, blue numbers indicate uplift. Blue framed columns represent the dates when uplift was expected. Dashed blue framed columns could be either uplift or subsidence. Numbers of the first column are italic as the measurements of April 2009 are questionable and are only marginal considered for the analysis.

Sample Point	<i>April 09 - Aug 09</i> [m]	Aug 09 - March 10 [m]	March 10 - May 10 [m]	May 10 - Aug 10 [m]	Aug 10 - April 11 [m]
R1	0.320	0.053	0.012	-0.168	NV
R 2	0.332	0.104	-0.048	-0.169	-0.012
R 3	0.096	0.034	0.032	-0.134	-0.043
R 4	0.181	0.062	-0.001	-0.166	0.058
R 5	-0.633	0.365	0.436	-0.745	0.126
R 6	-0.381	0.252	-0.423	0.418	-0.184
R 7	0.176	0.095	0.024	-0.146	-0.005
R 8	0.182	0.066	-0.128	-0.058	0.028
R 9	0.088	0.185	-0.175	-0.093	-0.014
R 10	0.231	0.283	-0.239	-0.141	-0.146
R 11	0.435	0.088	-0.068	-0.167	0.366
R 12	0.419	-0.055	-0.019	-0.122	-0.165
Average	0.121	0.128	-0.050	-0.141	0.001
Positiv values (black) indicate uplift ; negative values (red) indicate subsidence					
Blue framed columns stand for expected uplift caused by frost heave					

The average of the differences is positive for the time period August 2009 to March 2010, negative between March 2010 and May 2010 and also between May 2010 and August 2010. For the last period (August 2009 and April 2011) it is again positive, however with + 0.001 m only very little. These outcomes correspond to the expected upwards and downward movements of the lithalsas. In addition it can be stated, that in every time period there is at least one sample point that is not following the general trend, however such counter trend is only weak and below 0.1 m. There is no remarkable

concordance of the points disclosing a divergent trend for the different time step. Nevertheless it can be noticed the R 12 is always experiencing subsidence.

It is also very interesting to see, that points experiencing intense changes, are in most cases the same for all time periods: R 5 and R 6 move the most, in average about ± 0.418 m and ± 0.319 m respectively, while the least motion can be stated for R 3, R 4, R 7 and R 8 all never exceeding ± 0.150 m and in most cases below ± 0.050 m. By comparing this finding with Figure 6.13 it is notable that R 5 and R 6 are both located on lichen and moss at a slope. R 4, R 7 and R 8 are very close to each other on the planar top of the mound covered by lichens and moss. R 3 in turn is placed on a steep slope on bare soil and does hence not correspond to the surrounding conditions of the other three.

The differences between the two surveys in summer (August 2009 and August 2010) were calculated and the results are copied in Figure 6.15.

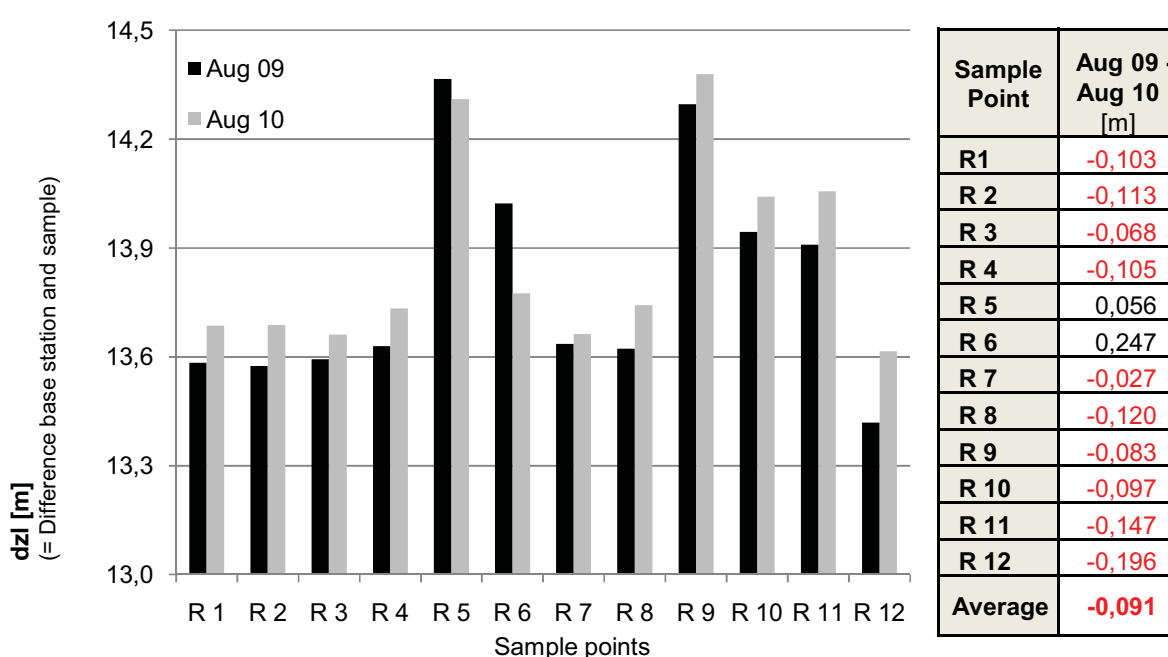


Figure 6.15: Left: Diagram showing the dzl values measured in August 2009 and 2010; Right: Table listing the differences between the dzl values of August 2009 and 2010. Red values are standing for subsidence, black for uplift

First of all, it can be noted that the relatively good accordance of the samples in 2009 and 2010 confirm accurate relocation of the points in 2010. Furthermore it is remarkable that 10 out of 12 samples are lower in 2010 than in 2009. Only for R 5 and R 6 dzl decreased and hence stand for uplift. The two points concerned are the same at which most movement happened in terms of the seasonal behavior.

The average movement amounts to -0.091 m which indicates a general subsidence of this lithalsa. R 11 and R 12 experienced greatest decrease, and they are both located near wetland. This fact shall be discussed in detail in the next chapter (Chapter 6.3.1.4).

Lithalsa M

At lithalsa M there were 14 points spread over the mound, and measured at the same five dates April 2009, August 2009, March 2010, May 2010 and August 2010. The exact location of the samples and their surroundings concerning land cover and local topography are displayed in the map below (Figure 6.16).

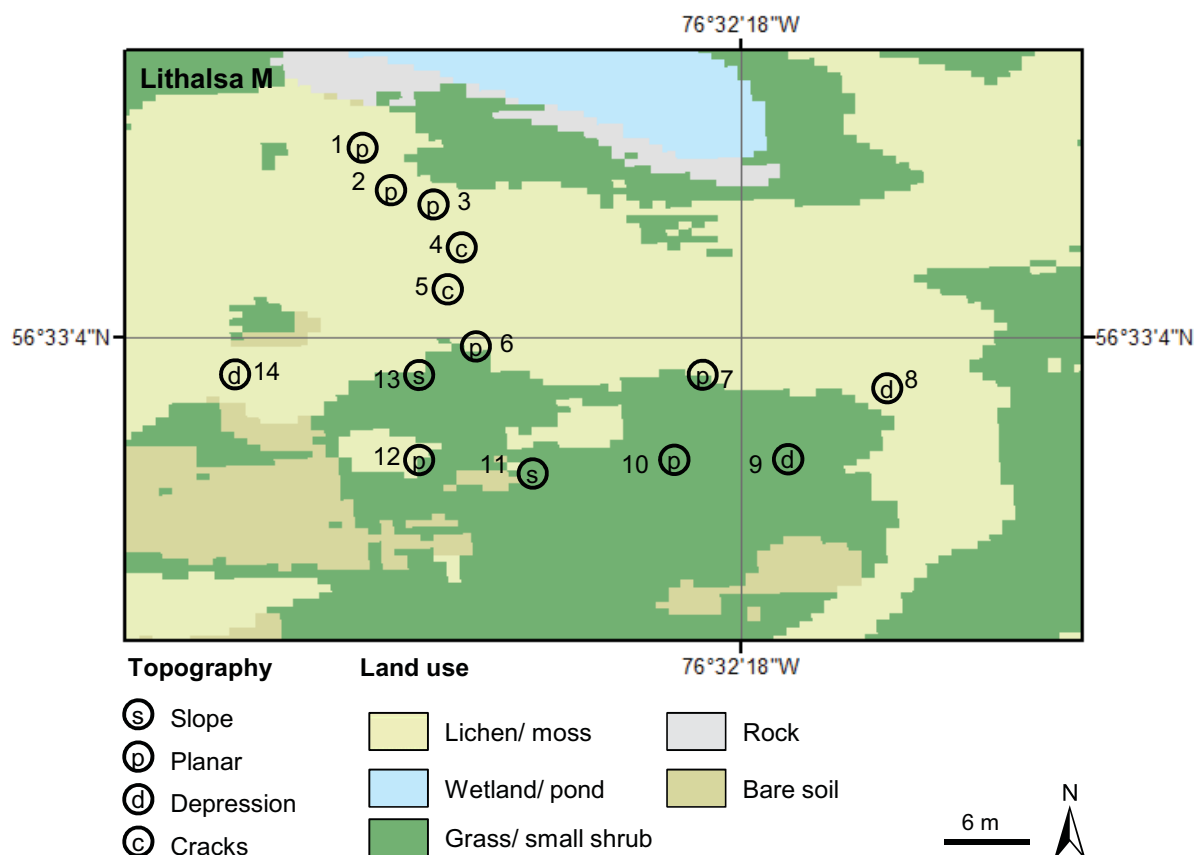


Figure 6.16: Location of the sample points of lithalsa M; in the background is the classification map is displayed. The local topography is represented by the framed letters.

Figure 6.17 charts the dzl quantities for each recording date. As with R, low values can be found during spring (March 2010, May 2010), representing a more elevated mound, whereas in the summer months (August 2009, August 2010) the dzl is higher.

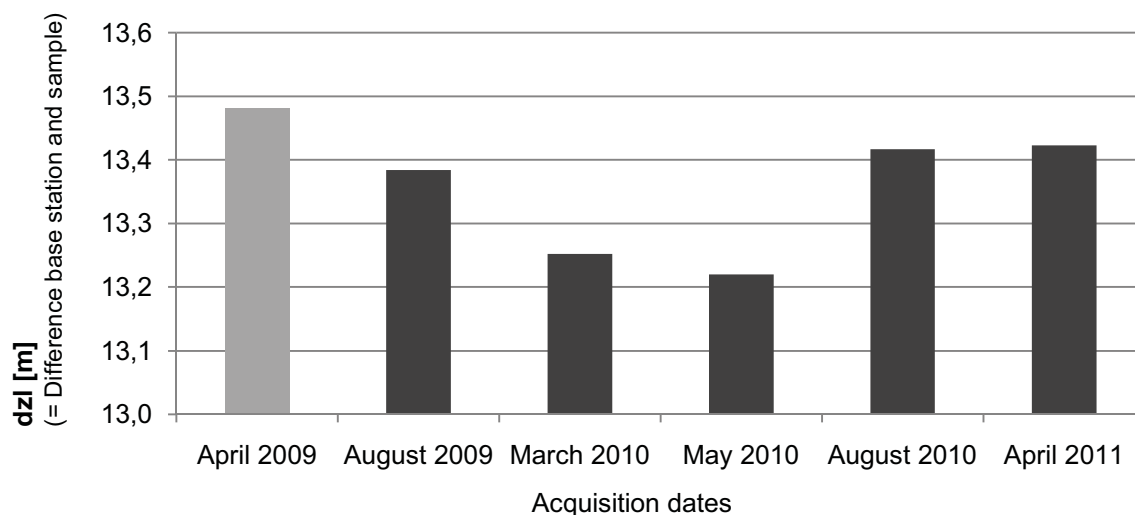


Figure 6.17: The dzl values average of all sample points of lithalsa M for each acquisition; Low values stand for higher elevations. Records for the first acquisition date are only marginally taken into account for the analysis, as the base station was placed on a different spot.

Analogous to the results from R, the number of April 2011 is slightly elevated. In contrast to R, the number decreased again during March 2010 and May 2010.

In the table (Table 6.5) below, the computed differences for each point for two following record dates are itemized.

Table 6.5: Calculated differences for all sample points on M, between the different acquisition dates. Red numbers indicate subsidence, blue numbers indicate uplift. Blue framed columns represent the dates when uplift was expected. Dashed blue framed columns could be either uplift or subsidence. Numbers of the first column are italic as the measurements of April 2009 are questionable and are only marginal considered for the analysis.

Sample Point	<i>April 09 - Aug 09</i> [m]	Aug 09 - March 10 [m]	March 10 - May 10 [m]	May 10 - Aug 10 [m]	Aug 10 - April 11 [m]
M 1	0.255	0.185	NV	NV	-0.047
M 2	0.128	0.115	0.029	-0.185	-0.069
M 3	0.194	0.053	0.349	-0.505	-0.040
M 4	0.242	0.161	0.059	-0.209	-0.295
M 5	0.182	0.103	0.035	-0.163	-0.049
M 6	0.210	0.134	-0.200	0.086	0.003
M 7	0.117	0.230	-0.399	0.257	0.054
M 8	0.161	0.241	-0.121	-0.075	0.045
M 9	0.008	0.068	0.148	-0.271	0.052
M 10	0.074	0.119	-0.001	-0.133	0.032
M 11	-0.180	0.088	0.573	-0.679	0.351
M 12	0.180	0.084	0.062	-0.198	0.025
M 13	-0.173	0.089	0.086	-0.125	-0.137
M 14	-0.025	0.177	NV	NV	0.002
Average	0.098	0.123	1.079	-0.138	-0.005
Positiv values (black) indicate uplift ; negative values (red) indicate subsidence					
Blue framed columns stand for expected uplift caused by frost heave					

Except for the subsidence measured during the last period, these outcomes reflect the expected seasonal pulsation. Between August 2009 and March 2010 all points are showing similar trends, whereas during the following time periods, there are always samples that experienced a counter trend. Therefore it is interesting to note that M 6 and M 7 highlight a downward trend during March 2010 and May 2010 but an upward trend in the consecutive time period. They are both located on a planar spot between the two land cover classes lichen/moss and grass/ small shrubs. Highest movement rates are found for M 3, M 7 and M 11, with means over +/- 0.200 m. Numbers less than 0.100 m are recorded for M 2, M 5, M 10, M 12 and M14, whereas the minimum with an average motion of +/- 0.071 m is at M 10. The comparison with the land cover or the topography does not emerge any correlation.

Concerning the comparison of the two summer acquisitions, the results graphed and listed in Figure 6.18 have been provided.

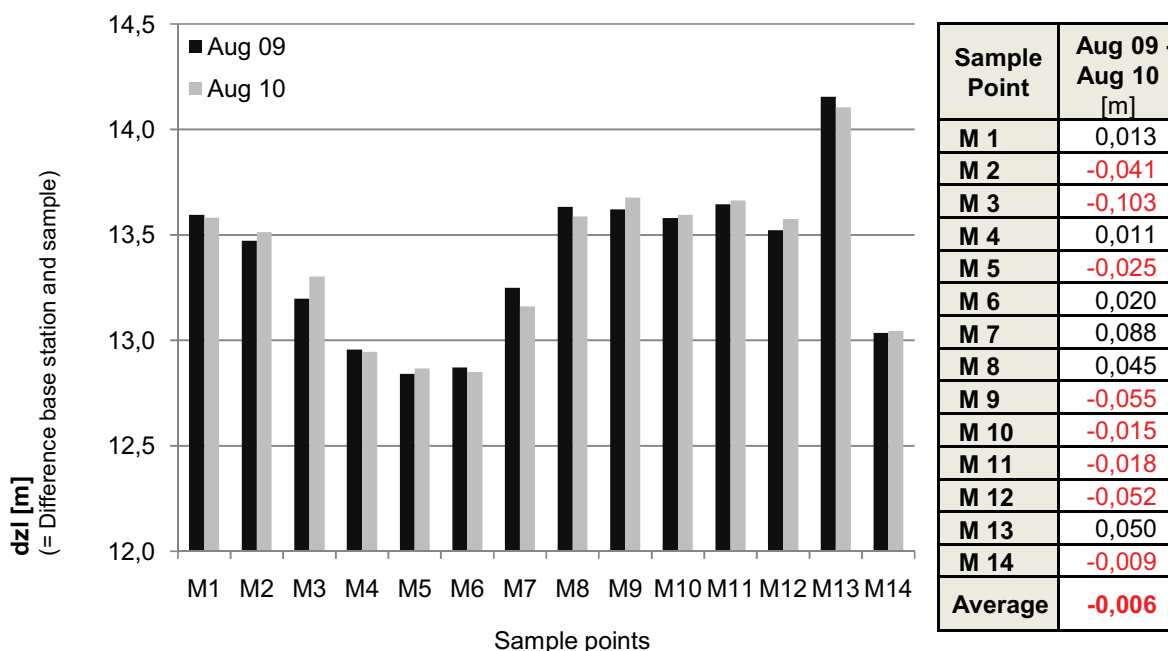


Figure 6.18: Left: Diagram showing the dzl values measured in August 2009 and 2010; Right: Table listing the differences between the dzl values of August 2009 and 2010. Red values stand for subsidence, black for uplift.

It is again obvious that the surveyed points in 2009 could be accurately relocated in 2010. Compared to R, the trend is much more heterogeneous with 8 samples revealing subsidence and 6 increasing. Nevertheless in the average, subsidence of -0.006 m was calculated. In terms of the assigned vegetation cover and topography it can be documented that all samples with an increase in elevation are located in the land cover class lichen / moss or at least at the edge. It should be mentioned at this point that the same land cover class is assigned to the two rising points on R (R 5 and R 6).

Lithalsa I

For the survey of lithalsa I 13 points were selected. In comparison to R and M an additional record from October 2010 is available. Figure 6.19 maps their location and the assigned land cover as well as the local topography.

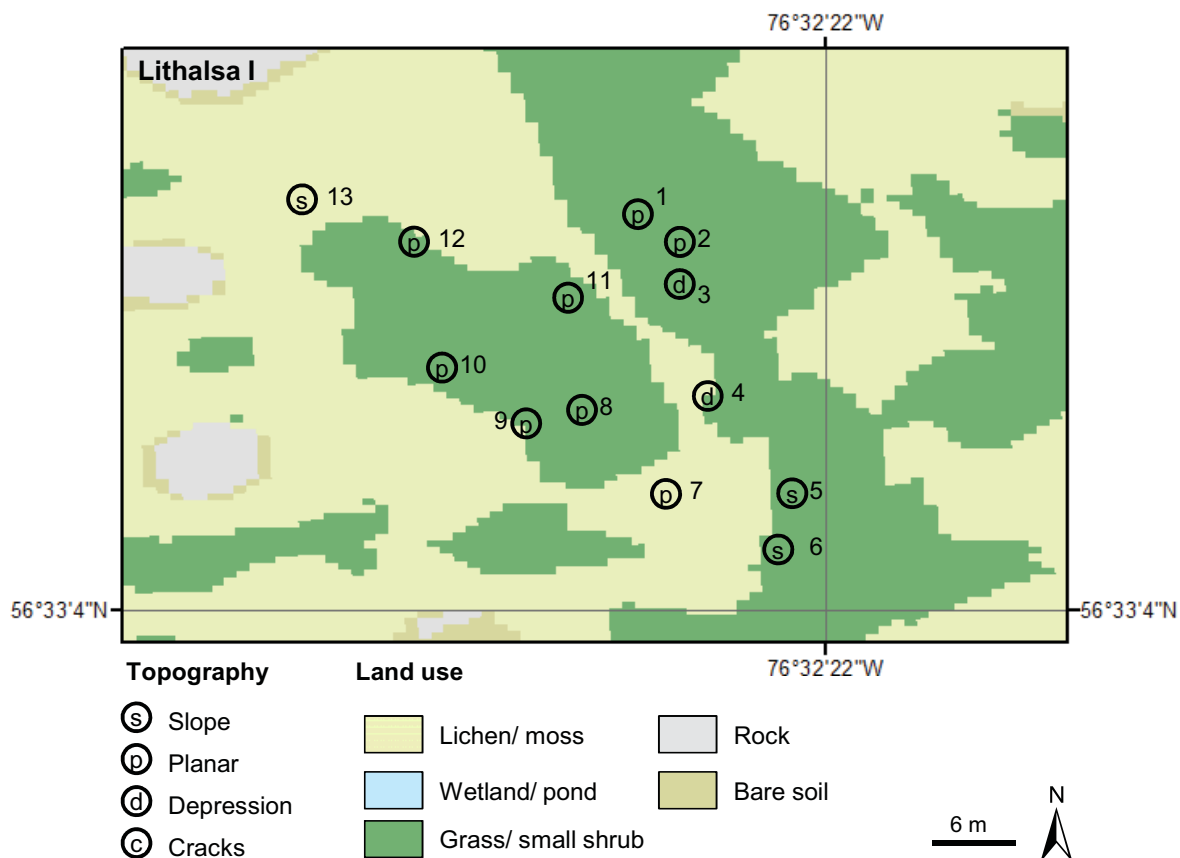


Figure 6.19: Location of the sample points of lithalsa I; in the background is the classification map is displayed. The local topography is represented by the framed letters.

In the following Figure 6.20 the dzl values recorded for I are graphed.

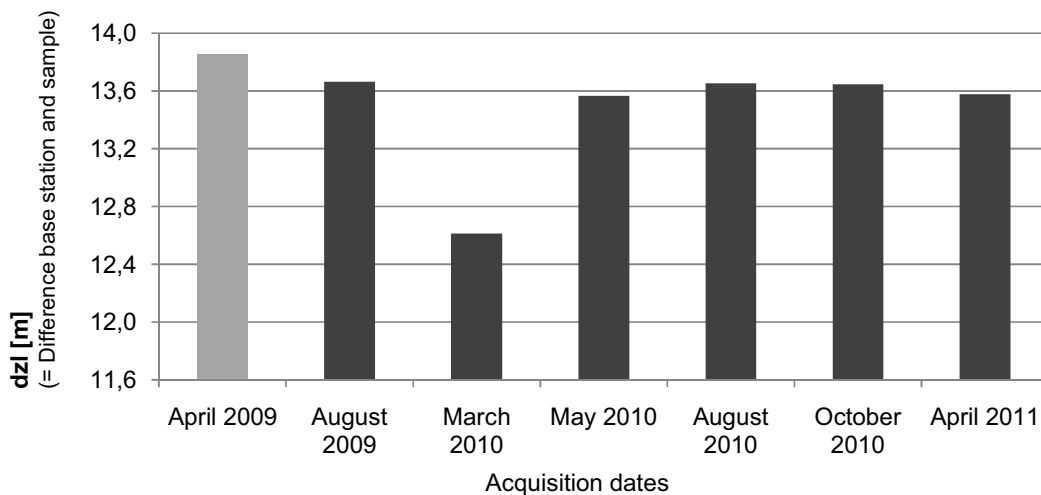


Figure 6.20: The dzl values average of all sample points of lithalsa I for each acquisition; Low values stand for higher elevations. Records for the first acquisition date are only marginally taken into account for the analysis, as the base station was placed on a different spot.

Analogous to R and M the lowest value was recorded in March 2010 and higher numbers are represented by the measurements from May 2010, August 2009 and 2010, and October 2010. In contrast to R and M, the numbers for April 2011 again show a slight decrease. The different values for each point are listed in Table 6.6.

Table 6.6: Calculated differences for all sample points on M, between the different acquisition dates. Red numbers indicate subsidence, blue numbers indicate uplift. Blue framed columns represent the dates when uplift was expected. Dashed blue framed columns could be either uplift or subsidence. Numbers of the first column are italic as the measurements of April 2009 are questionable and are only marginal considered for the analysis.

Sample Point	<i>April 09 - Aug 09</i> [m]	Aug 09 - March 10 [m]	March 10 - May 10 [m]	May 10 - Aug 10 [m]	Aug 10 - Oct 10 [m]	Oct 10 - April 11 [m]
I 1	0.196	0.817	-0.666	-0.850	-0.051	-0.439
I 2	0.217	1.220	-0.984	-1.131	0.010	0.008
I 3	-0.001	1.304	-1.520	-1.261	-0.013	0.088
I 4	-0.084	1.692	-2.126	-1.630	-0.010	0.252
I 5	0.444	1.881	-2.244	-1.879	NV	NV
I 6	0.376	1.291	-0.621	-1.371	0.005	0.149
I 7	0.229	0.629	-0.060	-0.631	-0.071	0.140
I 8	0.284	0.796	-0.747	-0.787	NV	NV
I 9	0.152	1.323	-0.959	-1.375	-0.040	0.234
I 10	0.181	1.099	-0.883	-1.081	-0.021	0.085
I 11	0.142	0.964	-0.904	-0.976	-0.048	0.122
I 12	0.225	0.133	-0.356	-0.147	-0.022	0.075
I 13	0.165	0.477	NV	-0.473	-0.051	0.588
Average	0.194	1.096	-1.006	-1.047	-0.028	0.118
Positiv values (black) indicate uplift ; negative values (red) indicate subsidence						
Blue framed columns stand for expected uplift caused by frost heave						

All means reflect the expected movement trends. Between summer and winter uplift always happened and subsidence occurred during the thawing period. Compared to the values presented for R and M, the quantities differ more between them, but disclose more homogeneity in terms of the trend: only between August 2010 and October 2010 I 2 and I 6 a different trend shows and during the last period I 1. Furthermore it is remarkable that the quantities are much higher than for R and M, often exceeding 1 m.

Concerning the activity of the single samples, I 4 and I 5 have means exceeding +/- 1.0 m, and R 7, R 12, and R 13 have quantities below +/- 0.5 m. In matters of their land cover and local relief, there is no evidence of a relation.

The differences between August 2009 and 2010 for lithalsa I were calculated and featured in Figure 6.21.

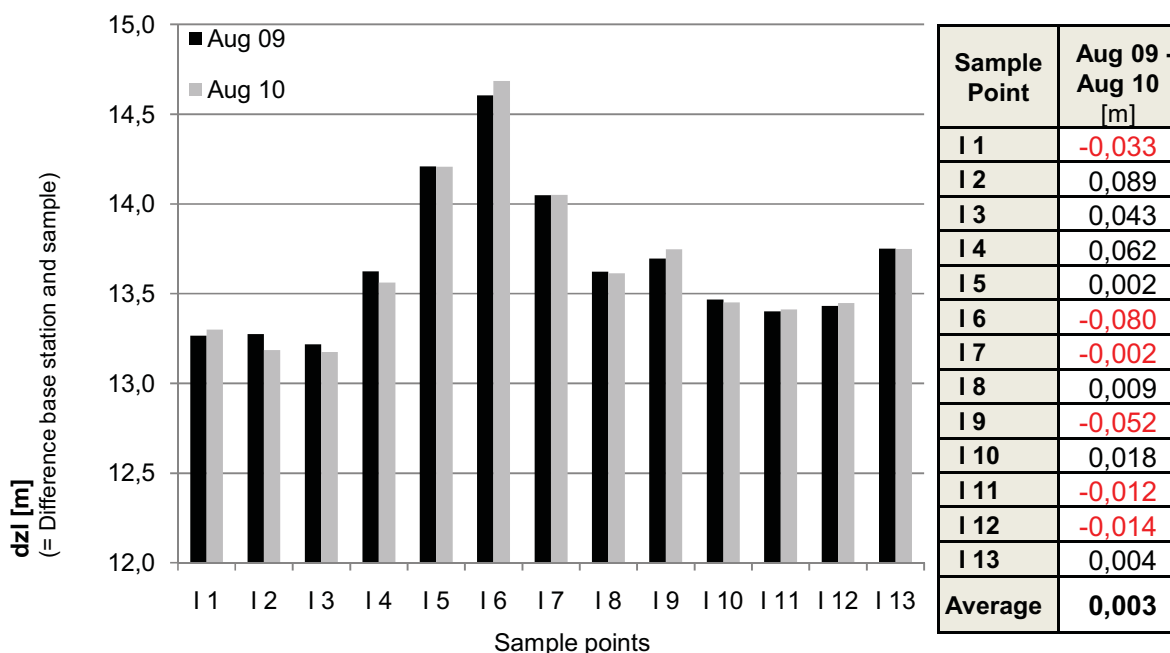


Figure 6.21: Left: Diagram showing the dzl values measured in August 2009 and 2010; Right: Table listing the differences between the dzl values of August 2009 and 2010. Red values are standing for subsidence, black for uplift

Also in the case of I, accurate relocation of the points were achieved confirmed by Figure 6.21. Movements reflect a fairly homogenous pattern with low values ranging between + 0.089 m and – 0.080 m. The mean is calculated to be + 0.003 and hence indicates slight uplift. In contrast to the correlation that could be found in uplifting samples and the land cover, in this case no relationship is obvious. However it has to be mentioned, that the numbers are very small.

6.3.1.4 Comparison and discussion

The outcomes of the field measurement feature that almost all sample points are underlying a similar movement in terms of the vertical direction. This is represented in Figure 6.22 that copies the trend of the lithalsas' elevation over 20 months in relation to the base station (multiplied by -1), averaged over all 39 sample points and interpolated for the entire period.

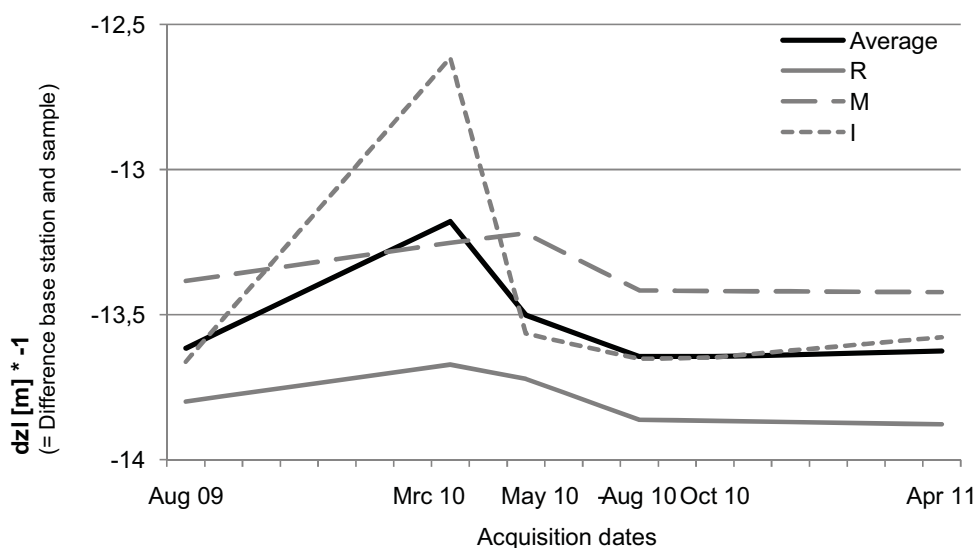


Figure 6.22: Trend of the lithalsas' elevation [m] over 20 months in relation to the base station and multiplied by -1. Averaged over 39 sample points and interpolated for the entire period. A separate curve for each lithalsa is displayed in grey.

Addressing the average curve, the first eye-catching feature is the remarkable peak in March 2010, versus minimum values measured for the dates in late summer/early autumn. The difference between the highest and lowest recorded elevations amounts to 0.47 m. Furthermore the rapid decrease between March 2010 and May 2010 is striking: during a period of only two months a subsidence of 0.35 m appears to happen, which equals 70.6 % of the entire descending rate for the year. The following negative trend between May and August is consequently much less (only 0.12 m), although the period is 2 months longer. Assuming a linear subsidence during this period, the downward rate per month would amount to 0.04 m which is only 22.9 % of the subsidence, experienced between March and May. It can hence be ascertained, that the lithalsas are underlying a season-dependent pulsation, but that this pulsation does not represent a uniform curve. Rather, parts of steep slopes are seen at the beginning of the warming period, a flattened period at the end of summer and an almost even part during autumn. This observed and described course reflects the expected effects caused by the annual freezing and thawing cycle and furthermore outlines the seasonal variations of this obviously non-linear process.

Furthermore the diagram reveals differences in the pulsating activity of the three lithalsas. In order to quantify this activity, the absolute values of all differences have been totaled and the average calculated as follows:

- R: 0.48m
- M: 0.57 m
- I: 3.22 m

Therewith lithalsa I can be clearly identified as the most active mound.

Not only the lithalsas as a whole, but also each unique point across all three was compared. The mean total movement over the entire period of 20 months of all 39 points is 1.7 m. The minimum amount is found at a point located at R (R 3), with less than 0.2 m total motion, and the most elevated numbers are measured at the previously noted points I 4, and I 5. Here the summation of all dynamics amounts to 5.7 m and even 6.0 m. These outstanding high numbers are basically caused by the rapid decline between March and May 2010 and the following atypical increase in elevation. While at most of the other points a slow decrease in height happens between spring and summer, it seems as if at these two points all subsidence already occurred during the first two warmer months in the year.

In summary the following outcomes for the seasonal behavior can be stated:

- In general all averaged movements show the expected trend, bar the measurements of R and M for the last period (August 2010 – April 2011).
- Besides the overall trend, there are always some points that reveal a counter trend. This occurs most at M and least at I.
- Most elevated changes values are recorded for I.
- The differences between the different points are highest on I.
- I is most active during the year.
- The most active points are I 4 and I 5, whereas R 3 is the point which moves least.
- Areas covered by lichen and moss demonstrate high changes, whereas points on grass and shrubs show less. This is mainly the case on R.
- R 12 is located close to a water body and always shows subsidence.

In terms of the interannual behavior it is clear that:

- In general the differences are less, compared to the seasonal changes.
- R and M depict subsiding movements.
- On I the average of all points adds up to + 0.006 m, but several points show subsidence as well.
- Points located near wetland (R 11 and R 12) experienced the greatest movement.
- On R and M, points with the assigned land cover class lichen and moss are the ones experiencing uplift.

Based on this summary, the concluding section in this chapter addresses the interpretation and possible explanations for these findings. Starting with seasonal changes, it must be mentioned first that the overall upward trend during the cold periods and in contrast the downward movement during the warmer periods confirm the assumption of the lithalsas' seasonal pulsation.

However the measurements of the last period are not quite fitting and a reasonable solution for it has to be found. Primarily it must be considered that for all three lithalsas there is almost the same amount of recorded points demonstrating subsidence as uplift, and it is only the average that computes uplift. As this average only represents a fairly small amount of the lithalsas' area, it is very questionable if the lithalsas as a whole experienced uplift. In any case, the weather conditions at this time were analyzed to see if early thawing could have already taken place and caused subsidence. As all records before the measurement show air temperatures far below zero (Environment Canada 2011), this possibility must be excluded.

A second option might be that in August 2010 the maximum state of thawing had not yet been reached. Taking into account the records of lithalsa I from October 2010, which presents ongoing decrease, this possibility can be confirmed. In such a case further shrinking would have taken place and consequently, depending on the amount of such subsidence, the difference to the April records could be positive and hence present uplift.

The second outcome concerns the counter trends of several points, mainly occurring on lithalsa R and M. This might be related to very locale conditions such as roots or other bioturbation.

Referring to the findings, it becomes obvious that most activity takes place on lithalsa I, and that it reflects the most distinct seasonal pulsations. Recalling the initial descriptions of the three mounds, lithalsa I is the one where the least degradation is visible. Hence it can be argued that its intact state is also mirrored in the typical and expected movement behavior, whereas R and M may have already partially lost this characteristic. Also, the outcomes of the interannual comparison corroborate this belief: R and M deliver with their negative values evidence for degradation, while I appears to be more or less in balance. This could also be an additional explanation of the counter move of R and M during the last recording period. The high heterogeneity occurring on I can be an indicator that degradation started here too.

Those samples on sparse vegetated areas are moving the most can probably be attributed to the more sensitive reaction to changing air temperatures. It seems very likely that the sheltering vegetation cover is buffering the in- and outgoing heat fluxes and if such buffer does not exist, the ground adapts much faster the outside temperature, and that following thawing and freezing processes this occurs more rapidly and is more pronounced.

Finally, the high subsidence values between August 2009 and 2010 of the points R 11 and R 12 are worth addressing. As they are the two only ones located close to a water body, they represent some kind of exclusion and consequently their outstanding behavior is even more interesting to note. To understand the influence of such ponds, several earlier investigation were consulted and it could be concluded that water bodies that do not freeze to the bottom in winter have a marked effect upon ground temperatures and the local configuration of permafrost (BROWN 1963). Thus it was of interest to get information about the winter situation of the water body of concern. SARRAZIN (2011) proves by his own measurements the fact that during winter there is still unfrozen water at the bottom of the pond concerned. The effect of such water body is presented in Figure 6.23.

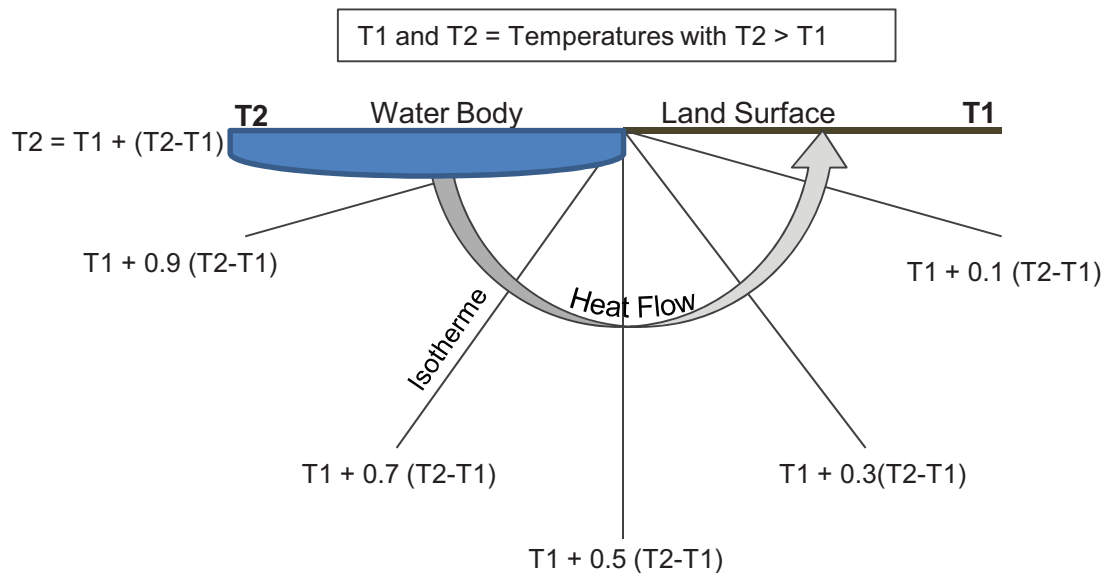


Figure 6.23: Steady- state temperature beneath the shoreline of a water body (modified after BROWN 1963)

By means of this illustration it can be seen that the warmer water body does significantly influence the thermal regime of the ground and its impact decreases with increasing distance. Translated to the case at hand, this would mean that the two points nearby the water body are impacted by the heat transfer coming from the warmer water body and consequently more thawing takes place, which in turn leads to elevated subsidence. As R 12 always shows subsidence (the only one on R for August 2009 and April 2010) and R 11 shows only little uplift during the winter period (+ 0.008 m) this possible influence is even more certain. Only the movement of R 11 during the August 2010 and April 2011 does not fit this conclusion, but may be a result to measuring inaccuracy or local bioturbation processes.

7 Remote Sensing Data

The second major component, after the practical work in the field, was the processing and analyzing of remote sensing data acquired by different sensors. Similar to the chapter dealing with the field work (Chapter 6), this part will also be divided into two subdivisions, each dealing with the same research questions as in chapter 6.2 and 6.3 respectively:

- i) Chapter 7.1 deals with the use of optical sensors to detect land cover changes. As highlighted in chapter 6.2, correlations exist between the land cover and the occurrence of permafrost and hence such changes can serve as indicators for dynamics in the permafrost.
- ii) Chapter 7.2 is related to chapter 6.3 of the field work part, and deals with the movements of the land surface caused by permafrost thawing and frost heave. For it, radar images were used to generate differential interferograms, which allow the detection of vertical displacements of the surface.

7.1 Optical Sensors

The use of remote sensing data acquired by optical sensors is a common method to observe the earth surface. The first earth observation satellite in space was the Television and Infrared Observation Satellite TIROS, launched in 1960 to monitor cloud patterns and it delivered data for the first daily weather forecast throughout the world (CAMPBELL 2009). From then on rapid technical development took place, generating much more sophisticated and multiple applicable sensors with increased spatial, temporal and spectral resolution. This process created unique challenges for scientists in the remote sensing community, but also in many related research fields, resulting in the development of numerous algorithms for exploitation and analysis of the data (PRASAD ET AL. 2011).

Optical remote sensing involves the acquisition and analysis of optical data and refers to the wavelengths ranging from the visible spectrum to the thermal infrared spectrum (0.4 – 14 μm) (PRASAD ET AL. 2010; LIANG 2004).

The basis for interpretation of remote-sensing data captured by an optical sensor is the knowledge about the interaction of the radiation with the observed target. Every single existing object features its unique physical characteristics, that determine which portion of the received electromagnetic waves is reflected, absorbed and again emitted (GIRARD & GIRARD 2003). This pattern of similar spectral response is commonly referred to as *spectral signature* and by using the graph showing the percentage of radiation of different wavelengths reflected (= *spectral response curve*) the particular material can be identified (ARONOFF 2005). Hereby, different features at the land surface can be distinguished based on their spectral behavior recorded by the sensor. Figure 7.1 charts the spectral response curve for the three main targets of interest in this study, vegetation, water and bare soil.

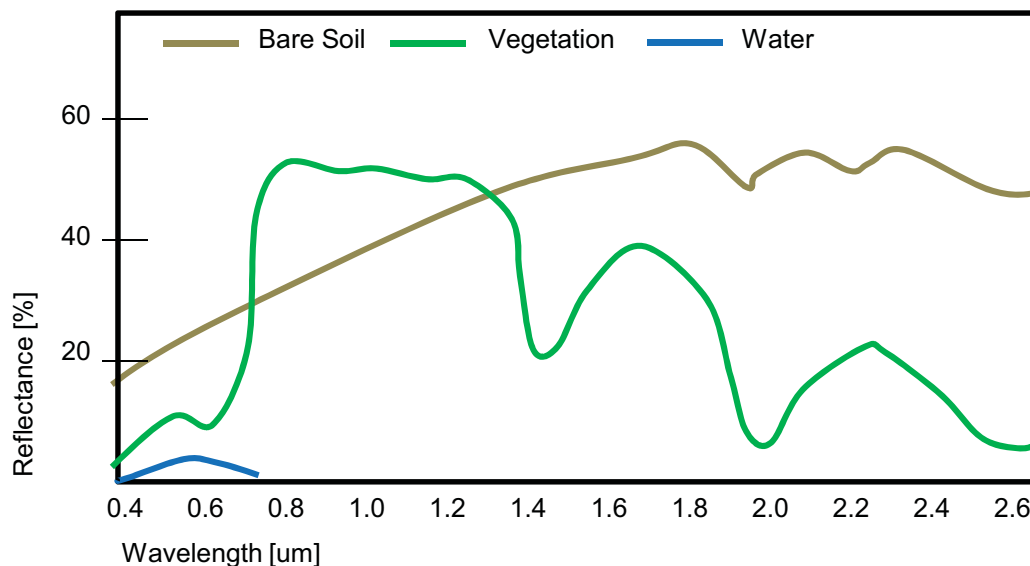


Figure 7.1: A generalized illustration of the spectral response curve for bare soil (brown), vegetation (green) and water (blue) (modified after LILLESAND ET AL. 2008)

Many elaborate books and articles are dealing with the principles of optical sensors and for further information refer to CAMPBELL (2009), LILLESAND ET AL. (2008), or PRASAD ET AL. (2011).

One major application field of remote sensing is the so-called change detection (Chapter 7.1.2). In change detection, at least two images of the same area acquired at different dates, are analyzed and compared to detect changes that happened during this period. Common fields of applications are the estimation of land use change caused by natural hazard and ecological processes, including runoff, soil erosion and sedimentation (MANONMANI & SUGANYA 2010).

As discussed in chapter 6.2 permafrost changes also evoke visible alterations at the land surface such as the vegetation pattern or the extension of wetlands. Thus change detection represents also a method to monitor permafrost dynamics and to estimate the amount of permafrost decline.

FORTIER AND AUBÉ-MAURICE (2008) published very interesting results of permafrost degradation near Umiujaq as from 1975, assessed from time-lapse aerial and satellite photographs in the proceedings of the ninth international permafrost conference (FORTIER & AUBÉ-MAURICE 2008). They made use of three series of aerial photographs from 1975, 1983 and 2003 and an additional IKONOS scene from 2005. Within this area they chose nine sectors, covering a total area of 2.25 km² in order to detect alterations in the lithalsas' extension.

Their outcomes revealed that permafrost degradation already occurred in 1957 as visible by the formation of small thermokarst ponds. Furthermore they could state a maximum of permafrost decline between 2003 and 2005, when in some of the investigated sectors almost all lithalsas were replaced by thermokarst ponds. In total they recorded an increasing rate of permafrost degradation in recent years from an annual loss rate of -380 m² or -0.8 % between 1957 and 1983, to almost twice the amount between 1983 and 2005 (-640 m² or -1.6 %). In their discussion they clearly related this decline to the warming temperatures of at least 3 °C observed as from 1992. Furthermore, they explained the degradation that happened before 1957 with the probability that the lithalsas were not yet in equilibrium with the climate that changed after the last ice age (CHOUINARD ET AL. 2007) as 'permafrost thawing is a long-term process due to the latent heat of fusion of ice delaying the impacts of climate warming on permafrost' (FORTIER & AUBÉ-MAURICE 2008).

With the investigations of this thesis, the study of FORTIER AND AUBÉ-MAURICE (2008) should be amplified by using more satellite images acquired between 1986 and 2009 (Table 7.1) with very high spatial resolution. The analysis' focus thereby was mainly on the expansion on wetlands in the study site as well as on changes in the vegetation. In contrast to the study of FORTIER AND AUBÉ-MAURICE (2008), the entire area was taken account of and not only selected parts. In the following section, the satellites delivering the utilized images are briefly presented followed by a description of the applied methods and the results.

Table 7.1: Utilized images for the detection of vegetation changes and wetland expansion.

Landsat	ASTER	QuickBird	IKONOS	GeoEye
01.07.1986				
02.08.1990				
03.07.2001	29.07.2001			
		11.07.2004		
			26.07.2005	
04.07.2008				
				24.09.2009

7.1.1 Available Data

Landsat

The Landsat program was proposed by scientists and administrators of the U.S. government in 1960 and envisioned applications of principles of remote sensing to broad-scale repetitive surveys of the Earth's land areas. The first Landsat satellite (Landsat 1) was launched in 1972 and was equipped with the MSS (Multispectral Scanner) sensor carrying four spectral channels. In a single 24-hours interval the satellite completes 14 nonsynchronous orbits (Figure 7.2) at a height of 705 km above the earth (CAMPBELL 2009).

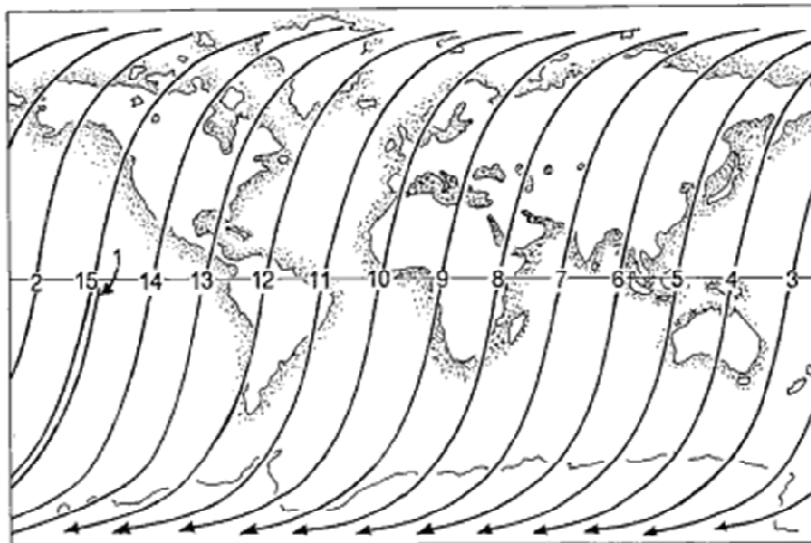


Figure 7.2: Coverage cycle, Landsat 1, 2 and 3. Each numbered line designates a northeast – to southwest pass of the satellite; the first pass on the next day (orbit 15) is immediately adjacent to pass 1 on the preceding day (CAMPBELL 2009).

Between 1972 and 1999, six further Landsat satellites were brought to space, endowed with a thematic mapper (TM) with a spatial resolution of 30 m. Currently the Landsat program offers the longest continuous global record of the earth (NASA 2011). The youngest satellite of the program (Landsat 7) operates with an Enhanced Thematic Mapper (ETM+), which even acquires images of 15 m spatial resolution in the panchromatic channel. In addition it comes with a thermal channel with a spatial resolution of 60 m (STEIN ET AL. 1999).

Although there are many images of the area existing for the time period of interest, only four scenes were considered to be useable (Table 7.1) as in all the other scenes the percentage cloud cover was too extensive. Unfortunately, of these four scenes only the scene from 2001 was recorded with the ETM+ as some problems occurred at the sensor as from the end of May 2003.

ASTER

The Advanced Spaceborne Thermal Emission and Reflection Radiometer (ASTER) is a Japanese instrument that was launched in December 1999. Its 14 bands cover a broad range of the electromagnetic spectrum starting with bands in the visible range and a spatial resolution ranging from 15 m to the thermal infrared, with a spatial resolution of 90 m (YAMAGUCHI ET AL. 1998). Similar to the Landsat satellites, it operates on a 705 km height sunsynchronous orbit with an inclination of 98.2 ° and a repetition time of 16 days (ABRAMS ET AL. 2002). ASTER is the first operational instrument that delivers high spatial resolution data of the globe, to anyone interested for reasonable prices (around 60 US \$) (ABRAMS ET AL. 2003).

Also from the ASTER images, there is unfortunately only one existing without extensive cloud cover.

QuickBird

Launched in 2001, QuickBird is a fairly new satellite mainly for commercial use with a spatial resolution of 61 cm (Digitalglobe 2010). It circles the Earth on a 482 km height sunsynchronous orbit with an inclination of 98 °. The instrument simultaneously provides high-resolution panchromatic and multispectral imagery (KRAMER 2002).

The scene used for this study was recorded in July 2004. It has to be noted that only for the western part of the test site (around 10.5 km²) the visible and near infrared bands with a spatial resolution of 2.4 m are available. For the eastern part a pan-sharpened acquisition with a spatial resolution of 0.61 m was at hand, but it only contains channels in the visible range.

IKONOS

With the launch of the IKONOS satellite, from the US-based company GeoEye, in 1999 the world of remote sensing changed dramatically, as it was the first time that images with a spatial resolution of only few meters and less (0.82 m in the panchromatic imagery and 4 m in the multispectral imagery) was widely available to the general public. With its 3-day interval, it can image any spot on the Planet within very short time and hence represents an important progress (OLSEN 2007). The instrument acquires images of the land surface in five channels (one panchromatic, three in the visible range, and one in the near infrared), whilst orbiting the Earth at a height of 681 km and an inclination of 98 ° (GeoEye 2011).

The IKONOS image for this study dates to July 2005 and comes with three, already pan-sharpened bands, in the visible range and a spatial resolution of 0.82 m.

GeoEye

The GeoEye-1 satellite, also created by GeoEye, was launched in 2008 and captures panchromatic images of 0.41 m and multispectral images of 1.65 m (RICHHARIA & WESTBROK 2010). Similar to IKONOS, it has a revisit time of three days and operates on a sunsynchronous orbit in 681 km height and 98 ° inclination (GeoEye 2011).

Due to its high spatial resolution, its swath width only amounts to 15.2 km (GeoEye 2011) and consequently four neighboring scenes were required to cover the entire test side. They were captured in September 2009 and delivered as pan-sharpened imagery.

Table 7.2: Overview of the main parameters of the satellite delivering the data for this study

	Landsat (4 -7)	ASTER	QuickBird	IKONOS	GeoEye
Start	1982 - 1999	1999	2001	1999	2008
Spatial resolution	30 – 90 m	14 – 90 m	0.65 – 2.62 m ²	0.81 – 3.2 m ²	0.41 – 1.65 m ²
Band (Spectral range)	7 (450 – 1166 nm)	14 (520 - 860 nm)	7 (430 – 918 nm)	5 (525 – 853 nm)	5 (450 – 920 nm)
Swath width	183 km	60 km	18.0 km	11.3 km	15.2 km
Orbit	705 km	705 km	482 km	681 km	681 km
Repetition time	16 days	16 days	5.6 days	3 days	< 3 days

7.1.2 Methods

For the processing and analysis of the optical remote sensing data, the image processing software ERDAS (www.erdas.com) was used and additional appraisal was done with ArcGIS version 9.1 (www.esri-germany.de).

In this chapter the implemented methods for preprocessing, classification and change detection will be briefly described, followed by the results.

7.1.2.1 Preprocessing

Geometric and radiometric correction

The geometric correction of remote sensing imagery mainly implies the conversion of data to ground coordinates by removal of distortions from the sensor geometry. In the case of Landsat, ASTER, QuickBird and GeoEye the delivered images were already corrected. They are all available in UTM coordinates, Zone 18 N in the world geodetic system WGS 84. Consequently the IKONOS image has to be transformed into the same reference system.

For it *image-to-image* registration was chosen, whereas ground control points have to be identified in the reference image as well as in the image that has to be referenced. By selecting the points it is important to guarantee a widespread distribution in the image, to avoid deformation in some parts of the scene. By means of interpolating algorithms the coordinates of the chosen points in the reference image are assigned to the corresponding pixels in the other one, whose coordinates afterwards are recalculated (JENSEN 2005). For further reading about the geometric correction refer to RICHARDS AND JIA (2006).

In contrast to the geometric correction, which does only affect size and orientation of the image, the radiometric correction of the imagery modifies the image values. It includes the removal of sensor or atmospheric noise, the correction of data loss and the removal of haze. In terms of data comparison and mosaicking this is the most important processing step in order to guarantee accurate results. Several methods exist to implement such radiometric correction, differing in their complexity and applicability. For the atmospheric correction in this study, the so-called *haze reduction* was applied for all images. This method is one of the most common methods (also named as *dark subtraction*) and is based on the hypothesis that in every image at least one pixel's reflectance equals zero. Consequently the radiance of this pixel solely results from the atmosphere and its value is hence subtracted from all other image pixels. Commonly deep and oligotrophic water bodies fulfill such conditions (GOMARASCA 2004).

In addition to the atmospheric correction, image enhancement in the form of a histogram stretch was applied to the ASTER image as well as to the four matching QuickBird scenes. The aim of a histogram stretch is to improve the image's contrast, whereas each digital number of the original image is transformed to a certain gray value in the displayed image by means of a specific mapping function (SCHOWENGERDT 1997). The way in which the histogram values are stretched (linear, nonlinear, user-defined, etc.) depends on the original image values and the desired outcomes. At the cases at hand, the aim was to contrast enhancement and this was successfully achieved by linear stretches. The final preprocessing step was the extraction of one common area for all available scenes.

7.1.2.2 Filter

Filter operations are further tools of image enhancement, especially to facilitate the analysis and interpretation. The main difference to the earlier explained enhancement methods is the switch from a one point operation to a computation that includes the values of neighboring pixels to calculate a new value for the pixel of concern. This combination of pixel values is defined by an algorithm that multiplies each pixel in the range of a certain filter mask, specified by a weighting factor and a given window size (JÄHNE 2005). Depending on the applied filter mask (=kernel) the operation can either have a sharpening (high-pass filter) or smoothing (low-pass filter) impact (Figure 7.3).

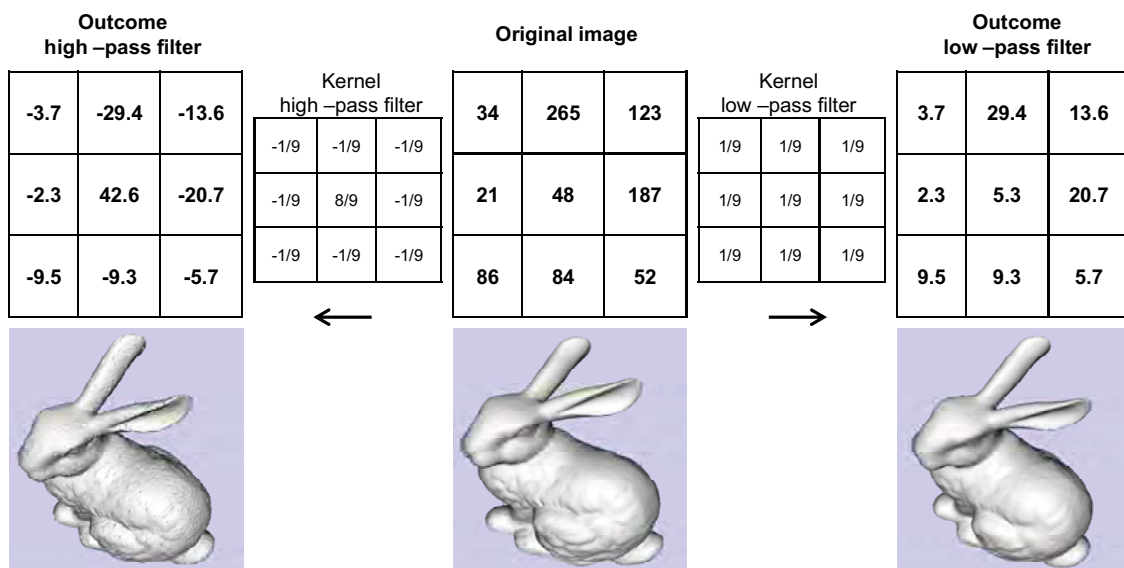


Figure 7.3: For illustrative purposes, a 3x3 kernel for high-pass filtering (left) and for low-pass filtering (right) are applied to the original image in the middle. The output values as well as the resulting image changes are displayed on both sides. It illustrates that the high-pass filter results in a contrast enhancement of the image, whereas the low-pass filter has a smoothing impact on the image.

Furthermore, the chosen window size of the filter mainly affects the outcomes of the filtering (BURGER & BURGE 2009). For this study a low-pass filter with a window size of 7 x 7 pixels was applied for the GeoEye image in order to smooth the interfaces between the four mosaic scenes. After the classification of all images, an additional filter with an 8 x 8 window was used. In this case it was the matter of a median filter, which takes the most frequent values of pixels in the window and assigns it to the central pixel (RICHARDS & JIA 2006).

7.1.2.3 Classification

Classification of satellite imagery means the division of image pixels into discrete classes (SCHOWENGERDT 1985) mainly representing land covers types, such as water, forest, buildings, etc. (Figure 7.4). The results are 'classified images' solely coping a certain amount of classes and no longer different grey values.

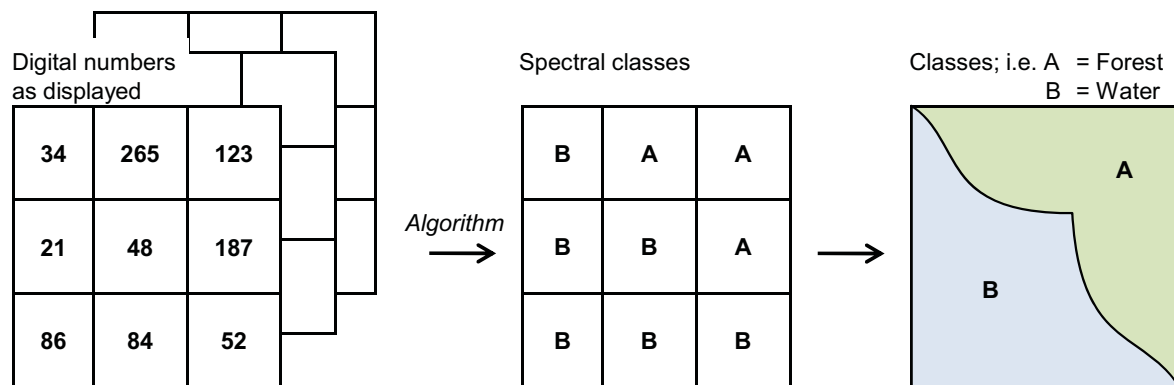


Figure 7.4: Schematic presentation of the classification process: On the left there is the original image, with different grey values in each band. The middle represent a grouping of pixels with similar values (spectral characteristics) which finally results in the image on the right, only representing the two classes A = Forest and B = Water (modified after ESPINOLA ET AL. 2008)

A large variety of different classification approaches and algorithms exists, dealing with this issue and trying to group the image pixels based on their spectral behavior, the texture or other characteristics in different categorizes. In general, two main approaches can be distinguished: the supervised and the unsupervised classification.

For a supervised classification, the analyzer has to define areas in the image – so-called training areas – of which the 'real' land cover type is known and represents the information of each desired class. In the following process the remaining pixels are assigned to these predefined classes, based on the chosen classification method (ARONOFF 2005).

When performing unsupervised classification the different classes are defined based on the clusters produced by the pixels of the occurring land covers. By means of algorithms that find statistical groupings, all image pixels are allocated to one of these clusters. Generally, the only input needed from the user is the amount of outcome classes. For good quality classification results it is often recommended to combine the two methods, by beginning with an unsupervised classification and pursuit with the supervised. An elaborate introduction and presentation of classification methods can be found in JENSEN (2005).

For the classification of the imagery used for this study, the Iterative Self-Organizing Data Analysis Algorithm ISODATA was chosen for unsupervised classification, followed by a supervised classification using the maximum-likelihood algorithm. ISODATA was developed in 1974 by TOU AND GONZALES (1974) and is based on one of the most common clustering method in remote sensing, the so-called *k-means* or *migrating means algorithm* (DUDA & HART 1973; BALL & HALL 1965; JENSEN

1996; LILLESAND ET AL. 2004; TSO & MARTHIER 2001). The only input required from the user is the amount of desired classes to be found by the algorithm. The method is an iterative process that starts by seeding randomly the defined number of classes into the multispectral space. A minimum distance algorithm then assigns each image pixel to one of the initial classes. Afterwards the classes' means gets recalculated and hence migrate. This migrated average is then used to reassign the pixels until no further adjusting is needed (ARONOFF 2005).

As amelioration to the original *k-means* algorithm, ISODATA allows changing the numbers of clusters with each iteration step. This is possible by recalculating the algorithm for each single cluster after every iteration (JENSEN 2000; MATHER 2004).

The maximum-likelihood classification belongs to the most widespread supervised classification and was initially developed by FISHER (1920) at the beginning of the last century (ALDRICH 1997). Its calculation is based on the 'comparison of each pixel's spectral values with the signature statistics from each training' area (ARONOFF 2005). In contrast to many other classification strategies it thereby not solely uses the position of pixels in the feature space, but also their distribution. Under the assumption that the values of each pixel in every dimension are normally distributed, the so-called probability density function of clusters can be computed (LILLESAND ET AL. 2004). Consequently, the pixels are assigned to the class they are most likely to belong to or with the highest probability respectively (ARONOFF 2005). In addition to the cited publication, detailed explanation of the maximum likelihood classification is provided in RICHARDS and JIA (2006).

An integral part of the classification is the accuracy assessment of the classification outcomes, driven by the need to identify the reason for errors, to optimize the results and especially to assess the outcomes reliability (GOPAL & WOODCOCK 1994).

The outcomes of the assessments are usually summarized in a *confusion matrix* that shows the correct and incorrect classified pixels for a sample of verification sites (ARONOFF 2005). This sample consists of pixels of which the land cover is known, but which were not already used in the training areas. The columns of the matrix correspond to the classes to which the pixels belong, while in the rows the classes to which the pixels are assigned are displayed (KENNETH & WU 2008). Consequently all values of the matrix's diagonal were correctly assigned, while all remaining were classified incorrect. Thereby the *error of omission* specifies the pixels incorrectly excluded from a particular call, whereas the *error of commission* stands for the pixels incorrectly assigned to a class that actually belongs in other classes (Canada Centre for Remote Sensing 2005). Figure 7.5 represents an example for such confusion matrix.

Classification	Validation Data				
		Forest	Water	Buildings	Total
	Forest	86	12	30	128
	Water	48	26	5	79
	Buildings	52	18	6	76
	Total	186	56	41	118

In bold: correct classified pixels
Overall accuracy: Relation of orrect classified pixels (118) and all pixels (283) = 89.4 %

← Total amount of correct classified pixels

Figure 7.5: Example for a confusions *matrix*. Values in bold (diagonal) are correct classified pixels. The value in the right bottom corner represents the total of correct classified pixels. The matrix shows furthermore all incorrect classified pixels, e.g. there were 48 pixels wrongly assigned to the class water, which would actually belong to the class forest (modified after MAUSER 2010)

A further value to express the classifications' quality is the *kappa coefficient* explained and validated in numerous publications of CONGALTON AND GREEN (1999), JANSSEN AND VAN DER WEL (1994) or SMITS ET AL. (1999). It is a measure of the percentage of correctly allocated pixels and generally calculated with

$$k = \frac{N \cdot \sum_{j=1}^r x_{jj} \sum_{j=1}^r (x_{j+} + x_{+j})}{N^2 - \sum_{j=1}^r (x_{j+} + x_{+j})} \quad (\text{eq. 7.1})$$

(x_{jj} = number of correct classified pixels of one class in row j and column j)

x_{j+} = sum of all classified pixels in row j

x_{+j} = sum of all classified pixels in column j

N = sum of all pixel in the matrix)

(CONGALTON & GREEN 1999).

Refer to chapter 3 'The support Machine (SVM) algorithm for supervised classification of hyperspectral remote sensing data' written by GUALTIERI (2009) in CAMPS-VALLS and BRUZZONE [Ed.] (2009) for a detailed discussion of the *kappa-coefficient*.

7.1.2.4 Change Detection

Change detection is the process of identifying and detecting differences in the state of an object or phenomenon by observing it at two or more different dates. 'Essentially, it involves the ability to quantify temporal effects using multitemporal data sets' (SINGH 1988). The increasing numbers of multisource and multitemporal satellite data in all geographic regions drove the need for the development of effective change detection techniques to exploit the available data in the context of monitoring and temporal evolution (SERPICO & BRUZZONE 1999). Consequently many different methods has been devised for this purpose and those implemented for this study, will be shortly explained in the following.

Postclassification is based on two independently produced spectral classification results from two different times, followed by a pixel-by-pixel comparison to detect changes in the land cover type. By properly coding the classification results, the outcome is a complex matrix of change (COPPIN ET AL. 2002). This method has been criticized in many ways due to its absolute dependency to the classification's accuracy. Nevertheless significant examples for satisfying results are the works of XU AND YOUNG (1990) and HALL ET AL. (1991) and hence the method was also used for this study and applied for the QuickBird image (2004) and the GeoEye (2009) due to their more or less similar spatial resolution.

Write function memory insertion

The write function memory insertion (WFMI) is a visual technique for detecting alterations in the land cover by means of two or three-date composite image data sets (GREY ET AL. 1998). For it, the first step is to define a meaningful band for the purpose of the study, available in both scenes, which then is combined to one image. When displaying the image in the RGB (red green blue) color scheme, changes, in particular their locations can be easily explored and estimated (JENSEN 2005).

The method was applied within this study for the QuickBird (2004) and the GeoEye (2009) image. One WFMI combination containing the blue spectral range and one based on the near infrared range were created. These bands were chosen to maximize the visibility of changes of water pixels.

Cross-correlation Analysis

Cross-correlation is a method developed by KOELN AND BISSONETTE (2000) and allows change detection by dint of a classified and an unclassified image acquired at a later date. It is expected that in most of the pixels no change occurs. In a first step, every pixel of the unclassified image gets a class (c) out of every class occurring at this position in the classified scene. Afterwards for every pixel of the unclassified image, now assigned to a specific land cover class, the mean and the standard deviation of every spectral band gets calculated. By dint of a comparison of the means and a division of the standard deviations every pixel value becomes z-normed. With

$$Z_{ijc} = \sum_{k=1}^n \left(\frac{r_{ijk} - \mu_{ck}}{\sigma_{ck}} \right)^2 \quad (\text{eq. 7.2})$$

a z-value for all spectral bands, for each pixel at the position i,j for a land use class c is calculated (JENSEN 2005).

(n = number of bands)

k = band number in the multispectral range

r = reflectance in band k of pixel at point i,j

μ_{ic} = mean reflectance value in band k for class c

σ_{ck} = standard deviation of the reflectance values in band k of all pixels of class c)

This process is now repeated for each land use class until every class has its specific distribution of the z-value, which represents a measure, expressing the proximity of a pixel to its expected spectral value (CIVCO ET AL. 2002). Consequently a high z-value stands for a high possibility of alterations for this pixel. Prerequisite for satisfying results of this method is a precise classification (JENSEN 2005).

Cross-correlation was only applied for the two Landsat records from 1986 and 2008.

Index differencing

The basic idea of index differencing is the combination of the radiometric pixel value and its temporal comparison. Typical combinations result in specific indices (GEIST 2006) that indicates for instance for the vegetation's activity. If computing such indices for different dates, they can be compared and changes can be depicted.

In the case of this study, the normalized differential vegetation index (NDVI) as well as the normalized differential water index (NDWI) served for this change detection analysis. The NDVI was computed for the years 2001 (ASTER), 2004 (QuickBird) and 2009 (GeoEye) while the NDWI was only applied for the Landsat images (1986, 1990, 2001, 2008).

For the calculation of the NDVI the values from the near infrared (NIR) and red spectral (Red) band are combined as follows:

$$NDVI = \frac{NIR - Red}{NIR + Red} \quad (\text{eq. 7.3})$$

thus the resulting NDVI can reach a value between -1 and 1 whereas -1 represents no vegetation and 1 a very dense and active (BELLWARD 1991).

The NDWI was introduced by McFEETERS (1996) to delineate open water objects and enhance their presence in the imagery, by taking into account the reflected near infrared and visible green radiation while eliminating soil and vegetation features. It is computed with:

$$NDWI = \frac{Green - NIR}{Green + NIR} \quad (\text{eq. 7.4})$$

Consequently water features have positive values while soil and vegetation takes zero or even negative values (McFEETERS 1996).

Tasseled-Cap-Transformation

Tasseled-Cap-Transformation (TCT) is a sensor-depending linear transformation developed by KAUTH AND THOMAS (1976) with the aim to describe vegetation development in relation to soil background by means of the three components brightness, greenness and wetness. In doing so the higher brightness values from the soil (brightness), the active vegetation (greenness) and the values from moist soil (wetness) can be considered simultaneously (LUNETTA 1999).

The method was derived from the change-vector method, based on the fact, that every pixel is located at a certain position in the feature space, defined by its spectral values, which gets modified if the values experience changes. The difference of the original and new position can be easily described by the direction and length of a vector, the so-called change vector (Figure 7.6) (JENSEN 2005).

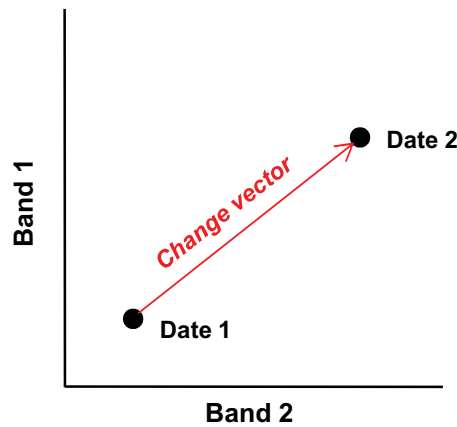


Figure 7.6: Principle of change detection analysis. The two black dots represent one pixel at different dates and their different location in the feature space. The change vector (red arrow) indicates the shift of the pixel within the feature space

As the use of all spectral bands is not necessarily convenient, a transformation of the bands can help to improve the significance. Such transformation is done for the TCT where new combinations of vectors are created by dint of coefficients of the spectral values, and which results in a new orthogonal coordinate system (ADAMS & GILLESPIE 2006). Depending on the sensor, the channel combination to express 'brightness', 'greenness' and 'wetness' varies.

In the context of this study TCT was applied for the Landsat imagery (1986, 1990, 200, 2008) as well as for QuickBird (2004) and GeoEye (2009).

7.1.3 Results

7.1.3.1 Classification

As described in the previous part of this chapter, the classification was a two-step process, starting with an unsupervised classification, using ISODATA, continued by a supervised classification by means of the maximum-likelihood algorithm. This was accomplished for all the imagery.

The main difficulties arose from areas of remaining snow patches, shallow and sedimentary lakes or pixels covered by clouds, which in most cases resulted in incorrect classification. To reduce the amount of such errors, cloud masks for the respective images were generated and areas of snow were excluded. In addition, 'water' classes were launched to account for the varying depth of the ponds and different sedimentary concentration of the water. In doing so, satisfying results could be achieved and except of case of the IKONOS image, an overall accuracy of over 90 % was attained. The lesser correctness of the IKONOS image was probably caused by the missing band in the near infrared that is of high importance to distinguish adequately between water and vegetation pixels. Classification of the Landsat data was only accomplished for the first and the last acquisition (1986 and 2008) and for images where the QuickBird image contained the required visible and near infrared channel. In table 7.3 the overall accuracy as well as the *kappa-coefficient* of the classifications is listed for each classification.

Table 7.3: Overall accuracy [%] and *kappa-coefficient* for the six acquisition dates considered in this study

Satellite	Overall accuracy [%]	kappa-coefficient
Landsat (1986)	99.9	0.997
Landsat (2008)	97.5	0.970
ASTER (2001)	95.6	0.936
QuickBird (2004)	91.3	0.900
IKONOS (2005)	86.3	0.840
GeoEye (2009)	91.7	0.900

Depending on the input data the number of output classes varies between 7 (Landsat) and 14 (IKONOS and GeoEye). To ensure none-the-less expedient data for change detection the 2001, 2004, 2005 and 2009 classifications were all normalized to one valid classification comprehending the following 8 classes:

- Lichens and Moss
- Wetland vegetation
- Grass and bushes
- Forest and dense bushes
- Water
- Barrow ground
- Rock

The classification maps for the high-resolution data are presented in Appendix 4.

A primary examination of the classified images revealed the fact of a considerable difference between the classification results of the low spatial resolution data (Landsat) and the high-resolution images. Specifically, the interesting thermokarst ponds could not be sufficiently reproduced in the low spatial resolution images. This appraisal resulted that in the subsequent change detection analysis, no comparisons were drawn between the different spatial resolution scales, but the different resolution scales were examined independently.

7.1.3.2 Change Detection

By reason of the discussed scale problems, the findings of the change detection analysis will be presented in two parts: the first part deals with the outcomes achieved using Landsat data and in the second part the results of the high-resolution images are outlined.

Landsat

For the Landsat data the following change detection methods were implemented:

- Post-classification comparison
- Cross-correlation analysis
- Index differencing (NDVI and NDWI)
- Tasseled-Cap Transformation

Before presenting and debating about the findings of the different methods, optical and statistical comparisons between the classification (post-classification comparison) of the first (1986) and last (2008) Landsat scenes were carried out and these highlighted some first changes:

It was clear that an overall increase in the vegetation happened during the time period of 22 years and that a westwards shift of the vegetation took place. In the eastern part of the scenery especially the expansion of forested areas dominated while augmented bush vegetation was found at the coastline of the Hudson Bay and protected valley habitats.

To get a quantitative estimation of the changes the percentages of each land cover was calculated for the two years and the five most frequently occurring are displayed in Figure 7.7.

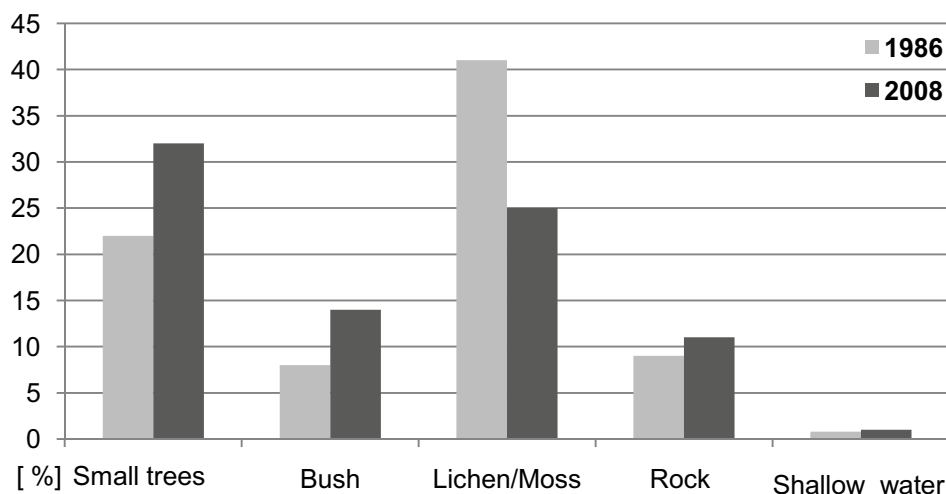


Figure 7.7: Percentages of the entire area for the five most frequently occurring land cover classes forest, bush, lichen/moss, rock and shallow water for years 1986 (blue) and 2008 (red).

This shows a remarkable rise of forest and bush vegetation as well as a distinct diminishment of lichens and mosses. The higher amount of rock pixels in 2008 is surprising and can very likely be ascribed to inaccurate classification of the rock class. To glean out which vegetation type was replaced by what kind of vegetation each single pixel was analyzed. The results are shown in Table 7.4.

Table 7.4: Percentages of of changed land cover, subdivided in the different classes, for 1986 and 2008. The percentages are related to the total amount of pixels for each class. As the class water is not represented in this table, the percentages do not sum up to 100%

2008 \ 1986	Forest	Bush	Lichen/Moss	Rock
Forest	84.7%	24.2%	20.3%	12.3%
Bush	10.0%	74.6%	12.2%	0.5%
Lichen/Moss	1.1%	0.9%	52.2%	25.5%
Rock	0.0%	0.0%	14.9%	61.1%

Table 7.4 indicates accordance of almost 85 % of forest, 75 % of bush, 52 % of low vegetation and 61 % for rock for the years 1986 and 2008. The remaining percentages are therefore covered by other vegetation at the later date, and referring to the mentioned numbers these are mainly the classes lichen and moss and rock that are suffering loss of area, followed by bushes, whereas the class 'forest' only loses 15 %. By contemplating the other numbers it also becomes clear that in the case of rock, most area was forfeited in favor of lichen and mosses (25.5 %) and that in turn lichen and mosses yield most of its area to denser vegetation such as bushes and forest (in sum 32.5 %). The class bush tends to be now overtaken by the 'higher' vegetation class 'forest'. The single shift veering toward less vegetation can be found for the lichen and moss, in 2008 also covered to 15 % by rocks. This contrary movement was already explained earlier, with improper capturing of rock pixels.

The next change detection method is the cross-correlation analysis that should mainly serve to locate areas of high changes. Thereby it could be considered that mainly rocks close to overgrown areas tend to feature variations. Similar to the observed changing of the classified images, the cross-correlation analysis highlighted protected valley habitats as locations of increased plant cover. Also analogous to the classification comparison, the eastern part is marked by active vegetation transition. For the index differencing, NDVI difference maps were created to investigate the change in the vegetation, whereas the NDWI should serve to explore the expansion of lakes and development of thermokarst ponds. Unfortunately, the results obtained by the NDWI did not allow any statement about changes as no trend could be explored. Also the attempt to improve the results by using the modified normalized differential water index (MNDWI) (XU 2006) did not show any enhancement. The reason therefore probably is the small size of such thermokarst lakes, not ascertainable with the spatial resolution.

The NDVI differences in contrast delivered reasonable and interesting results, for which four difference maps between each time step and between the first and the last acquisition (1986/1990, 1990/2001, 2001/2008, 1986/2008) served as source. By computing the mean NDVI value over all image pixels, a decrease between 1986 and 1990 (-3.2 %) was found, while in the following years the NDVI augments and during the last six year period even an increase of 7.0 % occurred. The decrease observed during the first four years was very likely attributable to the later acquisition date in the season in 1990 (2nd of August instead of early July) and hence advanced phenology with different spectral characteristics were observed.

Through a closer look at the difference map 1986/2008, to get an impression of the spatial distribution of the changes, it can be seen that most of the vegetation increase happened in the region around the Lac-Guillaume-Delisle as well as in the east part of the scene. This again confirms the findings from the classification comparison as well as those from the cross-correlation analysis.

In contrast to the earlier investigation, there are also some areas showing a decline in vegetation, visible in all difference maps. The reason therefore can be either the expansion of wetlands and hence a die-back of dense vegetation such as trees or bushes replaced by more hydrophilic species, or a timely shift of the phenological status – maybe even caused by climate change – causing derivations in the NDVI. However, as the latter reason would also bear on the rest of the image, a broadening of peats, bogs and shallow ponds is assumed. Such modification would also be evidence for permafrost thawing.

The last applied change detection method, operated for the Landsat images, is the Tasseled-Cap-Transformation. Compared to the previous methods, the results are manifesting vegetation degradation between 1986 and 2008 of almost – 33 % (-31 % for 1986/1990; -24 % for 1990/2001; -31 % for 2001/2008), whereas vegetation increase is significantly smaller in most of the time periods (+17 % for 1986/1990; +23 % for 1990/2001; +13 % for 2001/2008) and during the entire 22 years increase appeared in only 12 % of the pixels. This was also valid in terms of the changing intensity. The contrary findings can probably be explained by the fact, that initially the TCT was developed to follow the vegetation development during a season for agricultural needs. Hence the application to detect a change in a plant species might lead to misinterpretation.

Nevertheless, these findings also show highest increases in the eastern part and during 1990 and 2001 also the area around the Lac-Guillaume-Delisle and at the coastline of the Hudson Bay are most affected by increasing vegetation.

In summary it can be stated that change detection based on Landsat imagery depicted:

- vegetation increase between 1986 and 2008 with all methods, except the TCT.
- highest changes in the eastern part of the scene, around the Lac – Guillaume -Delisle and the coastline of the Hudson Bay.
- a westwards shift of the vegetation.
- an increase of trees and bushes at the expense of lichens and mosses and rocky ground.

High-Resolution imagery (ASTER, QuickBird, IKONOS, GeoEye)

Concerning the high- resolution imagery, four different change detection methods were applied for the observation of land cover changes, whereas a special focus was on the revealing of altering or expanding permafrost related features. The four executed techniques were:

- Post-classification comparison (QuickBird, IKONOS, GeoEye)
- Write Function Memory Insertion (QuickBird, GeoEye – only western part)
- Index differencing (ASTER, QuickBird, GeoEye – only western part)
- Tasseled-Cap-Transformation (QuickBird, GeoEye)

Equally to the procedure accomplished for the Landsat data, a primary look at the classification images, combined with the post-classification comparison approach, should provide a first overview of the land cover dynamics.

In doing so, it became apparent, that between 2004 (QuickBird) and 2009 (GeoEye) the overgrown areas increase, whereas the classification of 2005 IKONOS does not follow this trend. This deviation could be the result of the less accurate classification already displayed in Table 7.3.

If only taken into account the first (2004) and the last image (2009), the higher increase within the eastern part and near the Lac-Guillaume-Delisle, already stated in the Landsat classifications, could be recovered. In Figure 7.8 the percentages of the occurrence of five land cover classes are displayed for 2004 and 2009. Sandy areas as well as pixels covered by snow are not included to provide for a better comparison with Figure 7.7.

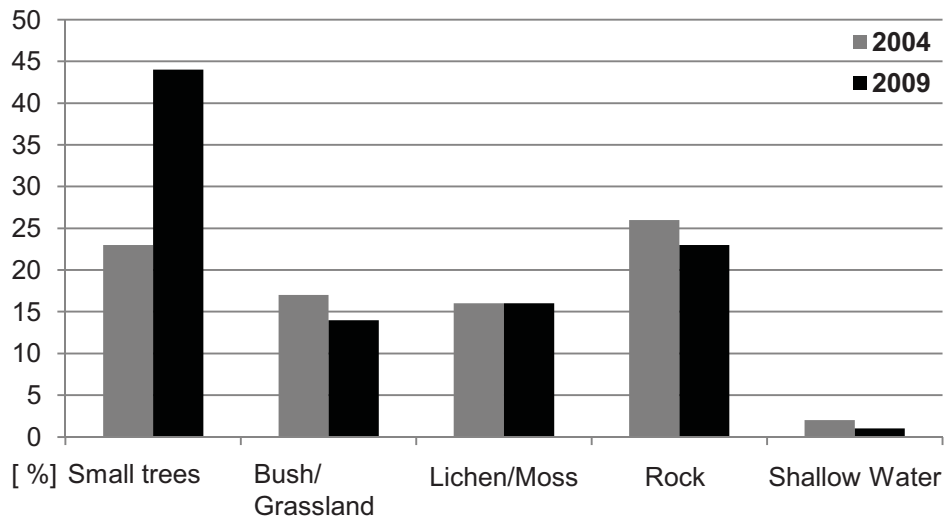


Figure 7.8: Percentages of the five land cover classes forest, bush, lichen/moss, rock and shallow water for years 2004 (grey) and 2009 (black).

A high increase of the class 'forest and other vegetation' (+21 %) as well as a decrease for the groups 'bush', 'rock' and 'water' (-7 %) were observed, whereas the amount of lichens and mosses remained the same. This is similar to the trend of the Landsat outcomes respective of the forest pixels, but different pertaining to bush and rock. Such discordance is not surprising considering the different spatial resolution but especially the different time span. Not displayed in Figure 7.8 is the class 'sand', which represents 6 % of the area in 2004 and 4 % in 2009. It is interesting to mention that the 2 % of area lost is now covered by lichens and moss. In Table 7.5 the percentages of the changed land covered based on the total area [ha] covered by the respective class is presented. It demonstrates that mainly the class bush and lichen and moss are losing area; bush primarily in favor of forest and lichen and moss to the same amount to forest in rock (2.2 %). Rock thereby remains more or less stable with 20 % of the area with only marginal change to the other three classes. Surprisingly is the gain of rock and low vegetation, derogating the class 'forest' (together 8.6 %), which presumably is an impact of constructions and dilation of infrastructure that happened during the last years around the city.

Table 7.5: Percentages of changed land cover, subdivided in the different classes, for 1986 and 2008. The percentages are related to the total area [ha] for each class. As the class water and sand is not represented in this table, the percentages do not sum up to 100%

2009 \ 2004	Forest	Bush	Lichen/Moss	Rock
Forest	20.5 %	4.3 %	2.2 %	1.1 %
Bush	8.8 %	8.0 %	0.1 %	0.1 %
Lichen/Moss	5.8 %	0.2 %	7.4 %	0.5 %
Rock	2.8 %	0.6%	2.2 %	19.9 %

A closer look at different vegetation classes and a more detailed subdivision of different vegetation types disclose an upwards trend of vegetation in dry habitats at the expense of bush land and wetlands.

As it was one of the main research aims to see the development of thermokarst ponds and lithalsas (representing indicators for the ongoing permafrost dynamics) these features were manually digitalized and counted in the image of the first (QuickBird 2004) and the latest (GeoEye 2009) acquisition.

In matters of the thermokarst lakes, the counted number added up to 531 in 2004, which equaled an area of 0.135 km². In 2009, the numbered lakes only amounted to 437 and covered an area of 0.102 km². Also the size of the ponds increased during this time interval from 254 m² to 211 m². Newly formed thermokarst ponds could only be located in the eastern part of the test site. Hence, similar to the vegetation observations, the lakes and ponds seem to experience water loss between 2004 and 2009.

The decreasing amount of humid areas is in contrast to the expected expansion of such wetlands and explanations for this reverse trend were needed. Therefore, the exact acquisition dates as well as the weather conditions of each particular year were taken into account and this delivered plausible explanations:

The QuickBird image dated back to 11 July 2004, whereas the GeoEye scene was recorded two months later in the year (24 September 2009). Although most of the precipitation falls during the summer months, the impact of melting snow and the thawing of frozen ground is much less during September than during July, and also the higher temperatures during August result in higher evaporation rates resulting in a lower availability of water in September. This can already provide a reasonable explanation for a dryer situation in 2009 and becomes even more plausible by considering the fact that in 2009 the mean temperature of July was 5 K higher than in 2004, and at many days temperatures of over 30 °C were measured.

Also the recorded precipitation sum¹ deliver some explanations: In June and July 2004 the precipitation sum amounted up to 196.4 cm, while August and September 2009 reached 158.4 cm. Such a difference of almost 40 cm definitely has an impact of the 'humidity situation'. Furthermore, it seems as if the rainfall in July 2004 was unusually high: in comparison to the mean of the years 2001 – 2010, almost twice the amount was measured (121.2 cm instead of the average of 75.4 cm), equaling to more than 160 % of the normal precipitation. This identifies July 2004 as an untypical wet month and consequently areas that normally tends to be dry, appeared humid in the 2004 image.

Concerning the lithalsas an increase of three single mounds (2004:109; 2009:112) could be spotted, whereas three new mounds were not created, but one mound was divided into three smaller mounds.

¹ Climate Station at Kuujjuarapik (ca. 150 km South of Umiujaq N55°16.587 W77°44.775), provided by D. Sarrazin (CEN)

Consequently, the total covered area decreased by approximately 6 % from 0.294 km² to only 0.276 km², whereas highest degradation rates could be found in the eastern part of the test site.

The WFMI was applied only for the western part of the 2004 (QuickBird) and 2009 (GeoEye) image. Due to the missing near infrared channel in the eastern part of the QuickBird scene as well as in the IKONOS data, they could not be considered for this analysis. WFMI difference maps were generated for the near infrared band to explore vegetation changes and for the blue channel to estimate the behavior of the water areas. The difference maps (Figure 7.9) highlighted increased overgrown areas especially along the rivers and randomly scattered around the village of Umiujaq. Concerning the difference map created with the blue band, decreasing areas dominated but were mainly located at the Cuestas or other solid or paved ground and hence have to be explained by bigger puddles remaining from the last rain.

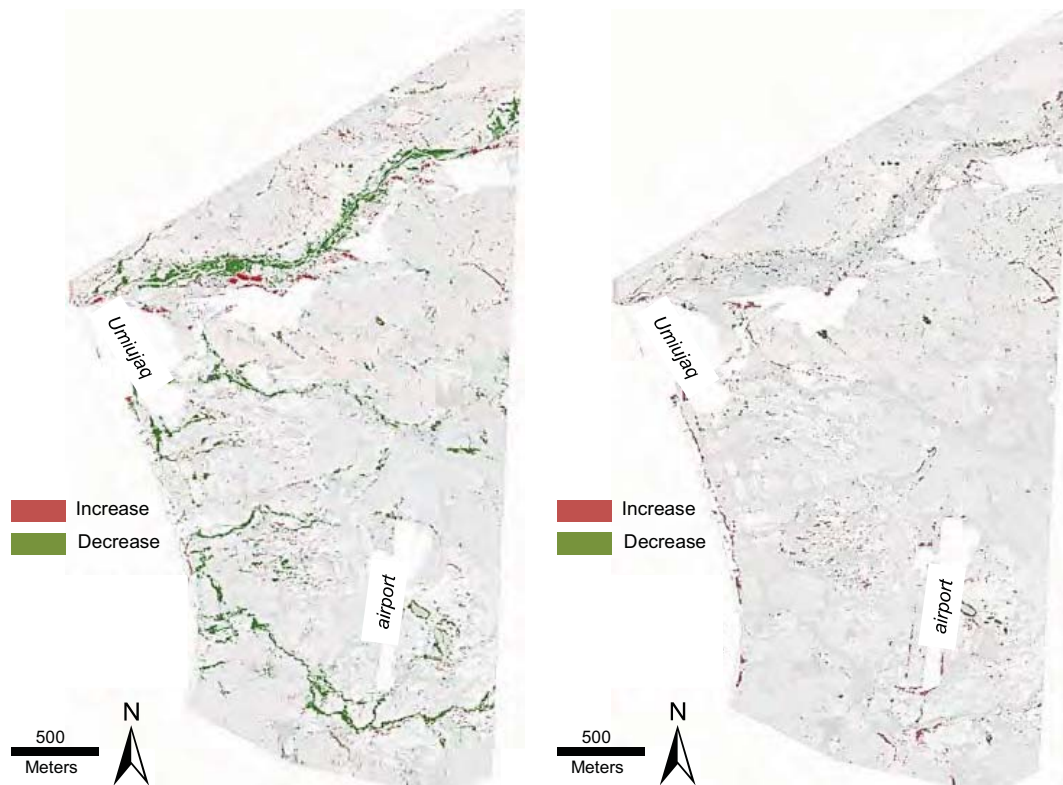


Figure 7.9: The maps show changed areas explored by the utilization of the WFMI, whereas red indicates increased vegetation and green decreased. The map on the left is generated by using the near infrared channel, the map on the right is based on the blue band.

For the index differencing the NDVI was calculated for the two images of 2004 and 2005 as well as for the ASTER scene (2001). For a facilitation of the interpretation the NDVI values were grouped into four classes, representing different vegetation activity. The outcomes can be seen in table 7.6.

Table 7.6: Occurrence of the four NDVI groups [%] in each scene

NDVI Group	ASTER (2001)	QuickBird (2004)	GeoEye (2009)
< 0.0	27 %	26 %	26 %
0.0 – 0.2	23 %	22 %	21 %
0.2 – 0.4	37 %	37 %	38 %
> 0.4	15 %	14 %	16 %

Based on the NDVI products, three difference maps were computed (2001/2004; 2004/2009; 2001/2009), whereas the difference between 2004 and 2009 showed the most increase in vegetation namely 56%. Again, concerning the spatial distribution, location with highest dynamics could be found along the stream courses, especially obvious in the northern part.

There are also waste areas that showed vegetation decline within all time steps that sometimes almost reached the same amount as the increase (2001/2004: 54 % increase; 46 % decrease). The spatial pattern of decrease is evidence of the suggestion that it is mainly caused by human activities, as major parts were located near the city or other infrastructure, such as the airport.

The TCT was again only applicable to the QuickBird and the GeoEye image, due to the missing spectral band in the near infrared of the IKONOS scene. The resulting map (Figure 7.10) confirms the coastline and the areas along the rivers as location of high vegetation increase.

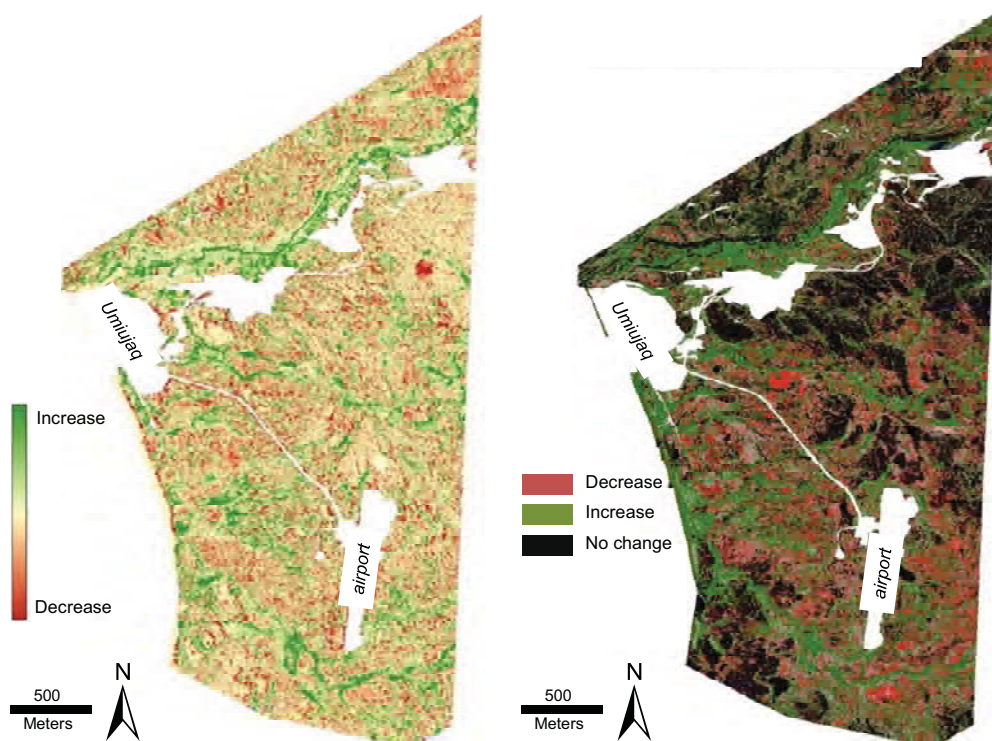


Figure 7.10: The map on the left shows the NDVI difference map of 2004 and 2005, whereas red indicates decreasing NDVI values and green increasing.

Summing up, the analysis and interpretation of the high-resolution data showed

- an augmentation of vegetation between 2001 and 2009.
- regions in the east, along the rivers, at the coastline and near the Lac-Guillaume-Delisle as areas of highest increase of vegetation.
- decreasing wetlands and ponds between 2004 and 2009, alleageable with the different acquisition date (July and September) and especially with unusual high rates of precipitation in July 2004 and very high temperatures in July 2009.
- a decline in areas covered by lithalsas, mainly in the east part.
- decreasing vegetation only near building or other infrastructure.

7.1.4 Conclusion

The findings of the change detection analysis by using optical sensors show more or less similar results irrespective of the technique that was applied. Increasing vegetation cover was discovered by all methods in the 22 years period between 1986 and 2009, whereas the eastern part of the test site was clearly highlighted as the region where most changes happened. This is not only valid for the vegetation expansion but also for the degradation of lithalsas and the generation of new thermokarst ponds. In general a westwards shift of the vegetation could be observed.

Moreover, it became evident that especially forested areas experienced an increase at the expenses on bushes, and that barrow land is more and more captured by pioneer vegetation such as lichens and mosses.

These outcomes are confirming to a great extent the expected scenic alteration, caused by climate change and permafrost degradation. They are furthermore not only confirming the already observed changes by FORTIER AND AUBÉ-MAURICE (2008) but updating their work and especially quantifying and specifying their outcomes.

Over and above, this investigation could prove and validate the application of high-resolution satellite imagery and several analysis techniques for the detection of indicators standing for permafrost changes. With this knowledge it would be possible to develop a monitoring and modeling system, fed with remote sensing data by means of data assimilation. The information content of the satellite images about landsurface conditions, combined with a database containing information about co-existence of permafrost, would serve as base for the estimation of permafrost occurrence and provide the principle for the modeling of permafrost dynamics.

7.2 Radar

Compared to the passive optical sensors discussed in the previous chapter, the function of a radar (radio detection and ranging) sensor is based on the active emission of short pulses of microwave energy.

7.2.1 Radar system theory

The acronym "radar" stands for a technique as well as for an instrument. The radar instrument emits electromagnetic waves of the radio or microwave spectrum towards a target and records the reflected signal in its line of sight.

The radar technique determines the characteristics of the reflecting object as well as its position and exposition by means of the two-way travel time of the signal and its modification caused by the specific physical behavior of the illuminated target. This is either implemented by a single antenna, referred to as monostatic radar, or by a bistatic system, using two physically separated antennas (SKOLNIK 1962). Data acquired by a radar system have a different geometry compared to optical images and the recorded signals also differ in their characteristics. This is briefly described in the following section.

7.2.1.1 Spatial resolution and geometry

The most common radar system is the side looking radar (SLAR or SLR), emitting energy sideways perpendicular to the flight direction of the sensor, resulting in a specific side-looking geometry and spatial properties. In Figure 7.11 the most important geometric features and their related scientific terminology are presented.

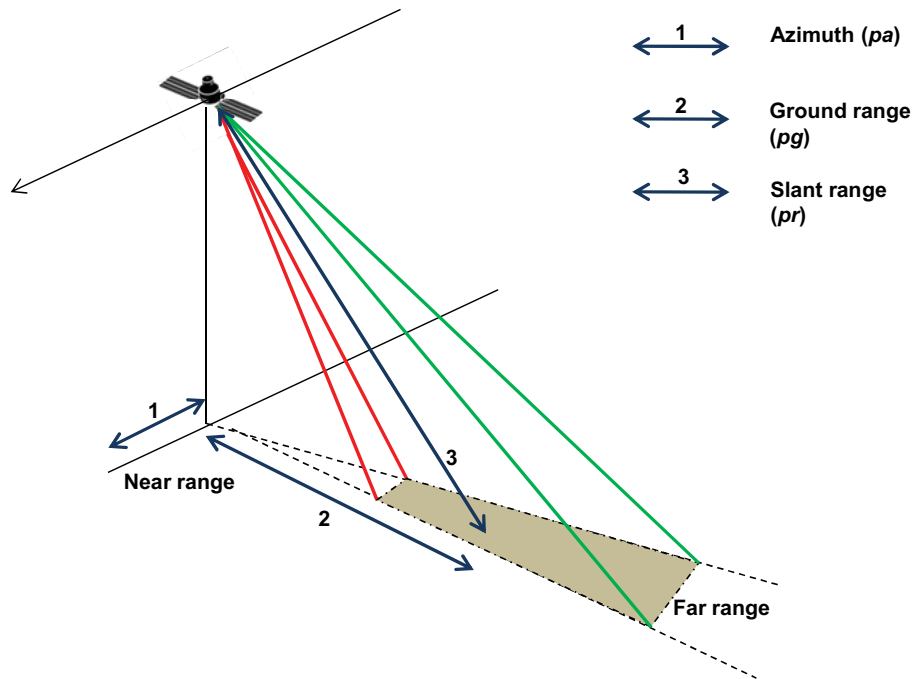


Figure 7.11: Illustration of the different spatial resolution in a radar image (modified after ARONOFF 2005)

As displayed here, the azimuth resolution (p_a [m]) can be found in flight direction, as well the resolution in the direction of the line of sight, divided in ground range (p_g [m]) and slant range resolution (p_r [m]). The azimuth resolution is determined by the beam width, controlled by the antenna length and is described by

$$p_a = (\lambda/d) * R \quad (\text{eq. 7.5})$$

whereas λ is the wavelength in m, d the antenna diameter and R the sensor – target distance [m]. The equation shows that with increasing antenna length also the azimuth resolution increases (WOODHOUSE 2006).

In contrast, ground range and slant range resolution are defining the spatial resolution in the direction of the line of sight and are mainly depending on the duration of emitted and reflected pulse (t_p) and the speed of light ($c = 3 * 10^8$ m/s).

The slant range thereby describes the actual range defined by the time delay of the radar signal and can be expressed by

$$p_r = ct_p/2, \quad (\text{eq. 7.6})$$

(WOODHOUSE 2006). Due to the fact that the slant range is only measuring the distance at an angle to the ground surface it has to be converted into the corresponding ground range, which can easily be done by simple trigonometry, and following the ground range is

$$p_g = pr/\sin \quad (\text{eq. 7.7})$$

(OLSEN 2006). While processing, it is important to be aware of the fact that the ground range resolution is not homogenous over the entire image, but changes nonlinearly across the swath (OLIVER & QUEGAN 2004).

7.2.1.2 Properties of the recorded signals

As mentioned above, the reflected signal recorded by the sensor differs from optical images. The first big difference is the much longer wavelength. Almost all radar systems operate in the microwave range of the electromagnetic spectrum; hence wavelength varies between one and several centimeters. As radar systems were initially used for military purposes, for security reasons the different bands were designated by letters listed in Table 7.7 (ARONOFF 2005).

Secondly, a radar system is able to operate in different polarizations. The polarization expresses the oscillation direction of the electromagnetic wave: the wave is horizontally polarized (H) if the electric field oscillates parallel to the Earth's surface, whereas the wave is vertically polarized (V) if the electric field arrives perpendicular to the surface. Recent radar systems can combine different transmitted and received polarizations, resulting in HH, VV, VH or VV. The signal obtained at the sensor may vary dramatically depending on the chosen polarization mode and therefore the polarization as well as its effects have to be considered in advance (LEE & POTTIER 2009).

The last very important difference between an optical and a radar sensor is the dimension of the final data: whereas an optical image contains information on the surface reflections [%] (KEREKES 2009), a radar image is comprised of complex numbers (equation 7.8) expressing the amplitude (x) of the received wavelength with the real component, and the phase (y) with the imaginary component (RICHARDS 2009).

$$z = x + i*y \quad (\text{eq. 7.8})$$

By maintaining both components, the data allows a much broader application as much more information is enclosed.

Table 7.7: Overview of the different available radar bands, the corresponding wavelength and their main applications. In bold: The band used for this study.

Band	Wavelength range [cm]	Usage and sensors
Ka	0.75 – 1.10	Weather radar systems; RAMSES
K	1.10 – 1.67	Weather radar systems
Ku	1.67 – 2.40	Weather radar systems, CryoSat, RAMSES
X	2.40 – 3.75	Military reconnaissance, terrain surveys, e.g.: TerraSAR-X, COSMO-SkyMed, GeoSAR
C	3.75 – 7.50	Many spaceborne SAR systems, Radarsat-1 & 2, SRTM, Envisat, ERS-1 & 2
S	7.50 – 15.0	Russian Almaz radar satellite (1991 – 1992)
L	15.0 – 30.0	Spaceborne: SeaSat, SIR-A, SIR-B, SIR-C, JERS-1, PALSAR
P	30.0 – 100	Airborne: NASA-JPL AIRSAR, GeoSAR, AES-3, OrbiSAR

7.2.1.3 Development of radar systems

Radar was first developed during World War II and was mainly used for military purposes (ARONOFF 2005). As an active system, radar has the advantage of providing its own source of illumination and, as it operates in larger wavelengths, it is capable of operating during night and of penetrating clouds. In the following years several sciences, especially radio astronomy, started to benefit from this technological process. Already in January 1946 the first radar echo from the Moon's surface was recorded on Earth (BUDERI 1996). In the subsequent decades the method became more and more developed and less than 30 years (1972) later, the first radar sensor was launched into space on Apollo 17 (HANSEN 2001). Since then, many new and much more sophisticated sensors have been created, and the invention of the SAR (Synthetic Aperture Radar), first launched in 1978 onboard the NASA Seasat satellite, finally brought radar technology to a new level (ELACHI ET AL. 1982).

A SAR system is a side-looking radar that synthesizes a very large effective antenna in order to increase the azimuth resolution, by using a short antenna of only 1 – 2 m length (ARONOFF 2005). The principle is based on the fact that the antenna is moving and hence a single point target gets illuminated several times by different antenna beams (Figure 7.12) (Woodhouse 2006). As a result, the synthesized antenna length becomes the distance the sensor has traveled during the time the object was in view (ARONOFF 2005). Features located farther from the sensor and illuminated by a wider beam, consequently are in the view for a longer period of time and provide more information which can then be used to enhance the spatial resolution. BROWN (1967) delivered a very detailed description about the function of a SAR sensor in his article 'Synthetic Aperture Radar', published in IEEE Transactions on Aerospace and Electronic Systems.

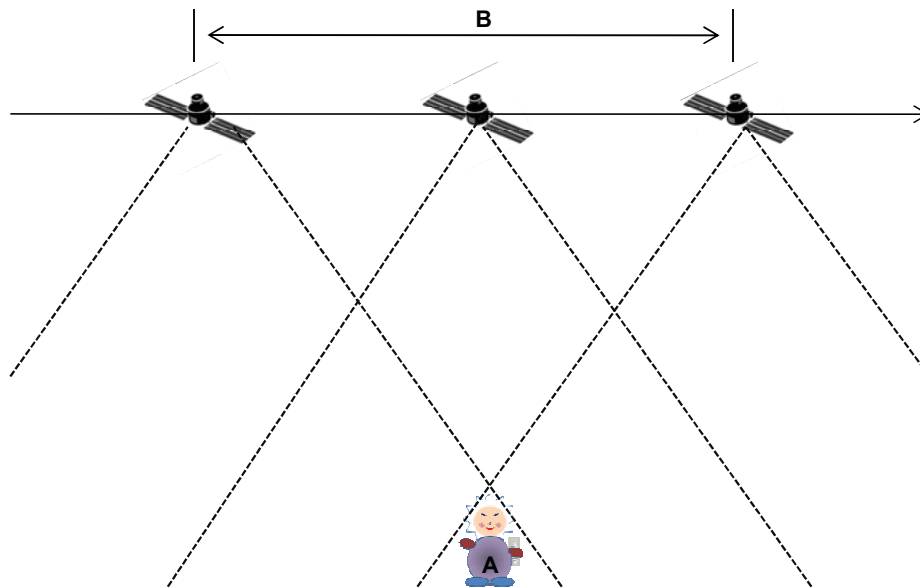


Figure 7.12: Principle of SAR operation. By processing the returns from the object (A) for the entire time it is illuminated by the radar beam, a short antenna can operate as if it was much longer (B) than its real length. This provides improved spatial resolution in the flight direction (modified after ARONOFF 2005)

Until now, over 20 SAR missions have occurred since the launch of the Seasat satellite in 1978, operating in frequencies between 1.240 GHz (SIR-C; April 1994) and 9.650 GHz (TerraSAR-X), with the most recent start in June 2010 of the TanDEM-X.

The feasibility of operating at night and of penetrating through clouds makes radar sensors highly in demand in Earth observation. Investigations addressing issues above the Arctic Circle, where no sunlight is available during several periods of the year, benefit especially from this ability. The additional possibilities to use the data for e.g. the generation of digital elevation models and deformation mapping widen the application of radar data to an even broader community.

Deformation mapping, which, in terms of radar imagery, is called differential interferometry, is also the research topic of this study.

7.2.2 Differential interferometry

Radar interferometry is a method that provides three-dimensional information about objects at the land surface by means of the phase content of the complex radar signal. Therefore a coherent SAR is required which uses the movement of the sensor to simulate a much larger antenna than its actual size.

Today, there are three main acquisition possibilities for providing this information and they differ mainly in the way the SAR antenna operates: the across-track interferometry as well as the along-track interferometry requires two antennas mounted on the same platform. Whereas across-track antennas are pointed perpendicular to the flight pass, along-track antennas are looking in flight direction. Both approaches are only applied to airborne systems, even though preliminary studies have been conducted to also implement them on satellite systems. For more information about the theoretical background of the two mentioned methods, refer to MOCCIA ET AL. (1995) and ORWIG AND HELD (1992). The third acquisition possibility is the so called repeat-pass or multi-pass interferometry. In contrast to the across- and along-track interferometry this method only requires one antenna which passes over the same area twice, with slightly different viewing angles. As for the height calculation, precise knowledge about the flight paths is essential. This information is recorded by instruments placed on spaceborne systems. The repeat-pass interferometry is also the method with which the data for this study was acquired.

Differential interferometry (D-InSAR) is a technique which allows the estimation of relative deformations of the land surface on the order of several centimeters, depending on the sensor's resolution. It is always based on at least two images provided by repeat-pass or multi-pass interferometry and requires an appropriate digital elevation model (DEM). Between the two acquisitions, there must be a time delay, the so-called *temporal baseline*, long enough to ensure alterations of the target of interest (HANSEN 2001; MASSONNET & FEIGL 1998). The time shift can also bring about numerous uncertainties for subsequent analysis, since in most cases not only the object's elevation, but also several other factors influence the radar signal. These include atmospheric conditions, changes in the vegetation cover, and the so-called *spatial baseline*. The latter is one of the most crucial factors in radar interferometry and is defined as the separation in meters 'between two antenna positions [...] realised by two ideally parallel satellite orbits' (GENS 1998). In the literature, the three representations 'horizontal', 'vertical' and 'perpendicular' baseline can be found (SMALL ET AL. 1996). These influencing factors can all have negative impacts on the coherence, which is a measure of the correlation of the phase information of two corresponding signals. To obtain adequate coherence values for D-InSAR applications (>0.3 ; optimal >0.5) a precise coregistration of the images is essential. Furthermore, the rotation of the Earth while the image is being acquired can result in incorrect reproduction of the captured scene (BOSCHI & WOODHOUSE 2006; KLAUSING & HOLPP 2000). Radar interferometry emerged after the Second World War and can be traced back to the 1960s, when the technique initially was used by the American military for mapping the Darien province in Panama. The first scientific article published in 1969 by ROGERS AND INGALLS contains the first application of the method to observe the surfaces of Venus and the Moon (GENS 1998). Since GOLDSTEIN AND ZEBKER (1988) produced the first interferogram of the Earth's surface, land surface observation by means of interferometry have become more and more developed, and in 1989 GABRIEL ET AL. (1989) used D-InSAR techniques for the first time to monitor the swelling of water absorbing clays in California. In the following decades D-InSAR was mainly applied to the detection of large-scale deformations caused by earthquakes, seismic and volcanic activity as well as to the monitoring of glacier velocity. Except for a joint U.S.-German-Italian project which implemented SIR-C/X-SAR instruments in 1994 (NASA 1994) for only two acquisitions, all approaches to use D-InSAR methods were based on data delivered by either C- or L- Band sensors.

Only since 2007 X-Band data of the system COSMO-SkyMed (an Earth observation instrument of the Italian Space Agency (ASI) operating at COSMO 1-4) as well as the radar sensor on board the German TerraSAR-X is available.

Due to its small wavelength (3 cm), the X-Band delivers the data with the best possible spatial resolution currently available. This property furthermore entails minimal penetration into the targeted medium. On the one hand this is an advantage for the purpose of this study, as it minimizes the error based on volume scattering in e.g. humid soil or snow (STEFAN ET AL. 1995). On the other hand, it also makes it more sensitive to atmospheric disruptions, a fact that needs to be borne in mind if very high air moisture is expected.

Based on this new availability of high-resolution radar data and the huge amount of unexplored possibilities for Earth observation, images of the TerraSAR-X satellite were used in this study to explore D-InSAR methods in order to monitor topographical movements related to permafrost.

For this first attempt, the seasonal dynamics between winter and summer were *in-situ* surveyed during field visits in 2009, 2010 and 2011. The TerraSAR-X imagery from the same time period with multiple acquisition parameters (ascending/ descending, polarizations (VV, HH, VH)) were also analyzed and phase-interferograms from multi-temporal image pairs were computed.

Except for the Norwegian PERMASAR project at the University Centre in Svalbard (UNIS 2010), this is the first time satellite data acquired by the X-Band is used in order to detect topographical movements of permafrost landforms.

7.2.2.1 Methods

Several methods exist for the computation of a differential interferogram and, depending on the availability and quality of data as well as the desired outcomes, one approach might be more suitable for the process than another. In general, four main techniques can be distinguished:

- 2-Pass interferometry
- 3-Pass interferometry 4-pass interferometry
- Complex combination of interferograms

The main difference between 2-Pass interferometry and the three other techniques is the requirement for an external DEM that serves to create an 'artificial' reference interferogram containing topographic information. The other methods all use an interferometric pair captured within a short time period, as a DEM reference. 3-Pass differs from 4-Pass interferometry in the numbers of images used (only 3 instead of 4). For the complex combination of interferograms, no successful phase unwrapping is even required (Table 7.8).

In the context of this study, 2-Pass, 3-Pass as well as the complex combination approach was tested. As the 3-Pass technique revealed itself to be the most appropriate method it was the approach finally applied to all images. All three methods are described below.

Table 7.8: Different approaches of differential interferometry (modified after GAMMA 2008)

Differential interferometric approach	Dataset	DEM	Unwrapping
2-Pass differential interferometry	InSAR pair and DEM	External	No
3-Pass differential interferometry	3 SAR images (= 2 InSAR pairs)	From one InSAR pair	Yes
4-Pass differential interferometry	4 SAR images (=2 InSAR pairs)	From one InSAR pair	Yes
Combination of complex interferograms	2 InSAR pairs	No	No

7.2.2.2 Processing Steps

In the following paragraphs, the processing steps to generate a differential interferogram are explained in detail, from the delivered complex SAR data in the Single-Look-Complex (SLC) format, to the fully geocoded product. A special focus is placed on the particular methods applied for this study and the possibilities offered by the GAMMA Software that was used. Used as examples are the differential interferogram formed by an acquisition in May 2009 (07.05.2009) and one in August 2009 (14.08.2009) in the case of 2-Pass differential interferometry, and an additional interferometric image pair from summer 2009 (14.08.2009 and 25.08.2009) in the case of the 3-Pass approach. As there is no difference in the processing steps between the 2-Pass and 3-Pass method until the generation of the differential interferogram, they will be only discussed for the two August scenes.

To begin with, some general statements about the designation of the different images and image pairs/products are made to make the description easier to follow:

- All images are named after their acquisition dates. E.g. the scene acquired on the 14th of August 2009 is referred to as scene 14.08.2009.
- When talking about image pairs, it is always the master scene (reference scene) that is mentioned first and the slave scene that is mentioned second.
- For all examples given in this chapter, 14.08.2009 serves as reference, hence the image pair from May and August will be titled 14.08.2009/25.08.2009.
- As soon as we cease to deal with a 'simple' interferogram and begin with differential interferograms instead, it gets named Diff2.2009, since chronologically it is the second differential interferogram in 2009 that was generated in the context of this study.
- Concerning the 3-Pass method, there is always one image pair that contains the topographic information and one that contains the displacement information. The one that includes the topography is named Int.1 and the one with the displacement is Int.2.

All the notations are valid throughout the entire thesis. Furthermore it should be mentioned at this point that all displayed images, if not already geocoded, are averaged to half size in range as well as in azimuth direction and vertically mirrored. This was done for better spatial understanding, since because of the ascending path, South is displayed at the top and North at the bottom. The scale bars in the lower left corner are only standing for an estimation of the dimension as the images are not geocoded, yet. The intensity image is always displayed in the background of the images.

Pre-processing

Depending on the available data, pre-processing is necessary, which mainly includes checking of the data for inconsistencies and calibration. In the case of the TerraSAR-X data at hand (SLC), missing lines or gaps are already filled in and a relative calibration has also already been conducted. A final absolute calibration is done automatically with the GAMMA Software by using the *.xml annotation file, delivered with the TerraSAR-X image that contains a calibration constant which is added to the data. This is done during the initial processing step: the generation of a parameter file that comprises all the acquisition information about each particular scene. An example for the parameter file for 14.08.2009 can be found in Appendix 5.

In the case of this study, it was decided to cut all images to a predefined area that only covers the test region, as there is no need to apply the processing over the entire acquired scene. In addition, zones in the western part of the image showing Hudson Bay only could be excluded and errors caused by undefined signal of the water are thereby significantly reduced.

Figure 7.13 shows 14.08.2009 before and after the cutting.

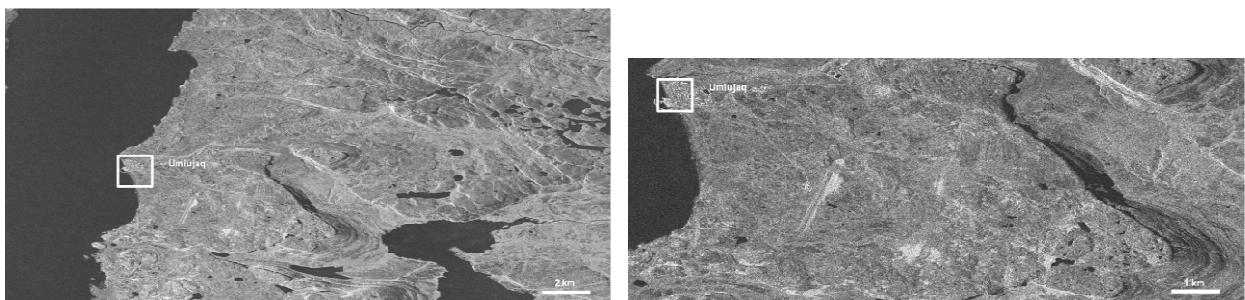


Figure 7.13: Left original SLC 140809 as delivered from the DLR; right cutted SLC 140809 as used for the processing

Coregistration, resampling and interpolation

In order to guarantee a successful interferogram generation, it is of great importance to accurately coregister the two original SLC images, which means that the offset in azimuth as well as in range direction is minimized. This shift can be up to several thousands of lines along-track and equals the parallel baseline divided by the posting in range in the across-track direction (HANSEN 2001).

For the coregistration, the cross-correlation technique was applied. It is separated into a coarse and a fine coregistration, to avoid slow computation.

Once the coregistration delivered satisfying results and the offsets are exactly known, the slave image has to be resampled to the reference geometry. This is necessary as the interferometric combination needs the accurate evaluation of the complex values in one of the two images at the pixel positions of the other. For the resampling 2D SINC interpolation is used (GAMMA 2008), a method based on the SINC (shorthand for 'sine cardinal') function which is considered as the ideal reconstruction filter for data of infinitive length (SCHÜRFER 1990) and is commonly calculated as

$$\text{sinc}(x) = \text{sine}(x) / x \quad (\text{eq. 7.9})$$

The coregistration as well as the resampling has to be repeated since accuracy of at least 1/10th of a pixel is needed. This threshold is recommended by ZHOU ET AL. (2009) and should be achieved for all image pairs. In most cases even 1/20th of a pixel should be obtained. In Table 7.13 in chapter 7.2.5 all final values for the coregistration are listed.

Baseline estimation

This processing step delivers an estimation for the parallel as well as for the perpendicular component of the spatial baseline. The knowledge about the baseline is important i) to ascertain, that it is below the critical baseline, ii) to gain useful information for the interpretation and iii) to deliver the input needed for some of the following processing steps.

The critical baseline, defined as the 'aperture separation perpendicular to the look direction at which the interferometric correlation becomes zero' (NASA no date) can be estimated by

$$B_n \leq 2R \lambda / L_c \cos \theta \quad (\text{eq. 7.10})$$

With B_n = the critical baseline, R the height of the satellite, λ = wavelength of the sensor, L_c = size of the resolution cell in slant range and θ the incidence angle (GOLDSTEIN ET AL. 1988). For the TerraSAR-X data in the utilized acquisition mode that would be

$$B_n \leq 514000 \text{ m} * 0.031 \text{ m} / 2 * 1.177 \text{ m} * \cos 40.5^\circ = 8902 \text{ m} \quad (\text{eq. 7.11})$$

The estimated baseline for the analyzed interferograms is far beyond this threshold (Table 7.13 in chapter 7.2.5).

The baseline estimation with the GAMMA Software is divided into an initial step, defining the baseline based on the orbit state vectors, the SLC registration offsets, or the interferometric fringe rate. It also is possible to use a combination of two of these methods, although it is recommended to always include the interferometric fringe rate as it usually brings best results. As the outcome of the baseline, after this first step, refers only to the centre of the image, an additional computation is necessary that takes the change of the baseline in along-track as well as across-track into account and delivers exact values for a specific position in the image.

A priori filtering and interferogram formation

At this point, noise in the range spectrum as well as in the azimuth spectrum, caused by different Doppler centroids (a frequency that expresses the phase differences between neighboring pulses (HANSEN 2001)) still remains and needs to be minimized. To do so, a *priori* filtering by dint of a determined filter function, based on the perpendicular baseline, is performed. More information about the different filtering options can be found in GATELLI ET AL. (1994) or HANSEN (2001).

For the construction of a complex interferogram, the corresponding pixels in both datasets are combined pointwise by complex multiplication. Each of the images is composed of a regular grid of phasors (y_1 and y_2), describing the amplitude and the phase component using

$$y_1 = |y_1| \exp(j\psi_1) \quad (\text{eq. 7.12})$$

$$y_2 = |y_2| \exp(j\psi_2) \quad (\text{eq. 7.13})$$

(ψ_1 and ψ_2 = phase values), and hence its complex multiplications results in

$$y_1 y_2^* = |y_1| \exp(j\psi_1) |y_2| \exp(-j\psi_2) = |y_1| |y_2| \exp(j(\psi_1 - \psi_2)) \quad (\text{eq. 7.14})$$

(HANSEN 2001).

Although it is the phase information in particular that needs to be retained for the interferogram, maintaining the complex values has the advantage that the SNR (signal to noise ratio) information is still included and that no artificial 2π phase jumps occur (HANSEN 2001). Figure 7.14 represents the initial unflattened and unwrapped interferogram 14.08.2009/25.08.2009.

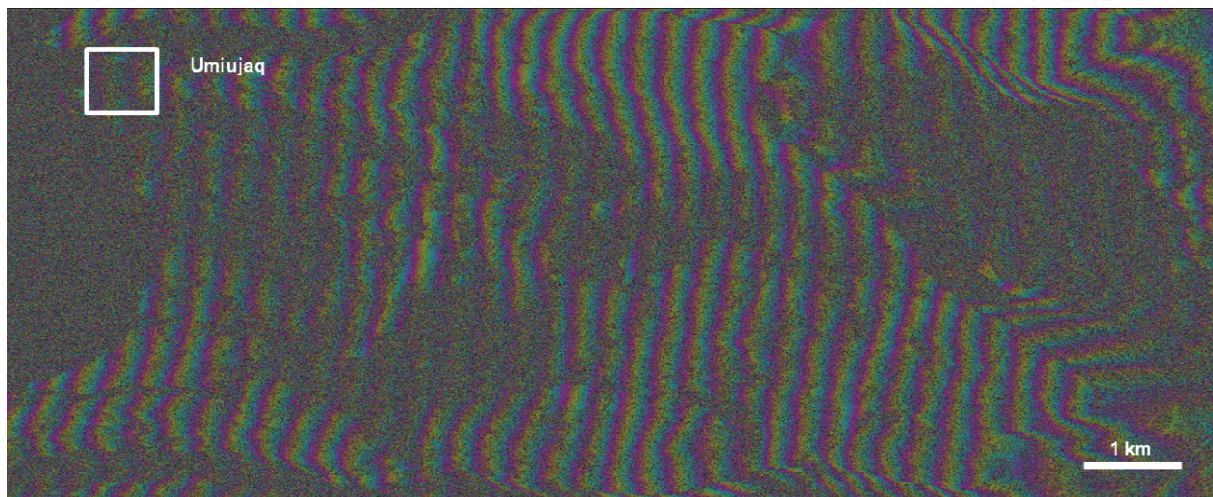


Figure 7.14: Unflattened unwrapped interferogram from 14.08.2009/ 25.08.2009

Earth flattening

At this stage the phase information of the interferogram is still composed of the six different phase components:

1. the phase difference caused by the curvature of the earth (='flat earth')
2. the topographic phase
3. the displacement phase
4. the atmospheric phase
5. the noise phase
6. phase unwrapping term

Of them, only the topographic and the displacement phase are of interest. Mathematically, the 6 factors can be combined as:

$$\phi = \left(\frac{-4\pi}{\lambda} R \right) + \left(\frac{4\pi Bn}{\lambda R \sin \phi} z \right) + \left(\frac{4\pi}{\lambda} n \right) + \left(\frac{4\pi}{\lambda} p \right) + \phi_{\text{noise}} + 2 * n\pi \quad (\text{eq. 7.15})$$

(SANTORO 2010). No method exists to get rid of the noise phase, and the atmospheric impact can only be roughly estimated at the end of the processing and only if several interferograms are available. The handling of the phase unwrapping term is discussed later in this chapter. The flat Earth component can be filtered out as follows: As it is a quasi linear trend visible in more or less parallel fringe lines (Figure 7.14) that are caused by the curvature of the Earth itself, and hence a tilt of terrain surface relative to the baseline, the effect can be removed by using a sphere with the radius of the curvature derived from the ellipsoid information.

It should be mentioned at this point that Earth flattening is only required if interferograms are the desired final outcomes. In the case of differential interferometry, the literature (GAMMA 2008) only recommends Earth flattening if larger spatial baselines have been estimated. If so, the curved Earth phase trend has to be removed before the unwrapping process and must be added back to the unwrapped image before generating the differential interferogram.

By means of the spherical Earth and a baseline model, a reference phase is generated and subtracted from the interferogram calculated earlier (BOSCHI & WOODHOUSE 2006). This procedure consists of four main steps:

1. At a few points along the orbit of the first satellite, the ranges to a few equally distributed points in the interferogram area are determined.
2. For these points, the position at the time of imaging along the orbit of the second satellite is retrieved together with the corresponding ranges.
3. The range differences are determined for every reference point and converted to phase differences.
4. And finally, the range differences are interpolated for every resolution cell of the interferogram (HANSSEN 2001).

After the removal of this phase term, a 'flattened' interferogram, including only the displacement information (as well as noise, atmosphere and displacement if existing) is generated. The flattened interferogram of 14.08.09/25.08.09 is displayed in Figure 7.15. It can be clearly seen that compared to the 'unflattened' interferogram the parallel fringes almost completely disappeared.

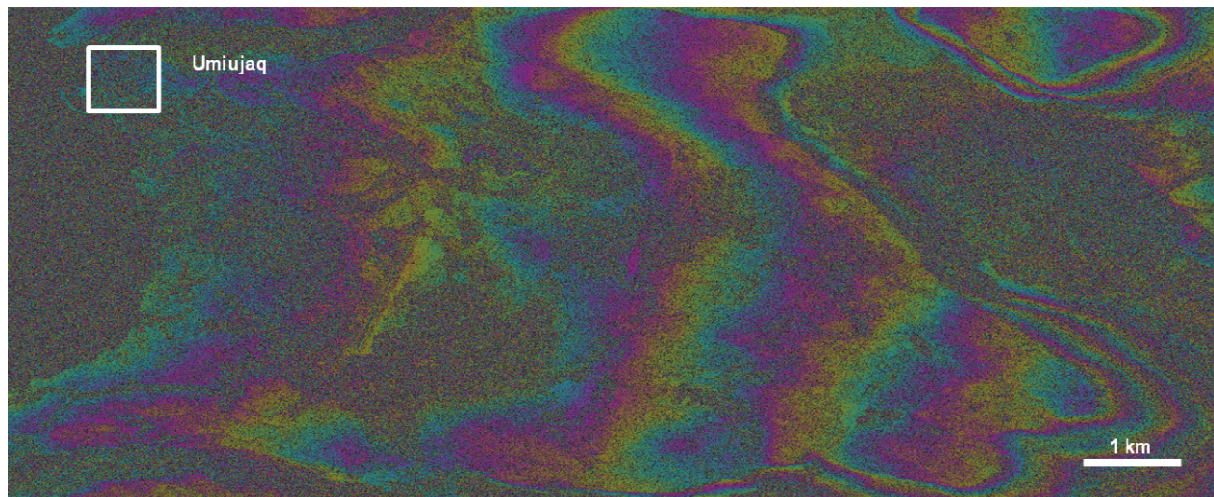


Figure 7.15: Flattened interferogram 14.08.09/ 25.08.09

A more detailed description about the mathematical operations can be found in SCHWÄBISCH (1995).

A posteriori filtering

In the previous chapter it was mentioned that no method exists to remove the phase noise component, although with filtering and multi-looking it can be distinctly reduced. With this procedure, it is proposed to enhance the interferogram, and especially to simplify the following phase unwrapping, as the number of problematic locations for phase unwrapping (= residues) are reduced.

An abundance of different filters exists, all having their advantages and disadvantages depending on the data at hand and the desired outcomes (HANSSEN 2001). In the case of this study, an adaptive filtering method was applied. The filter adapts to the local slope, i.e., the fringe rate of the interferometric phase, by computing the slope locally and averaging the interferometric phase along the local slope (GAMMA 2010). The outcome of this filtering process is shown in Figure 7.16.

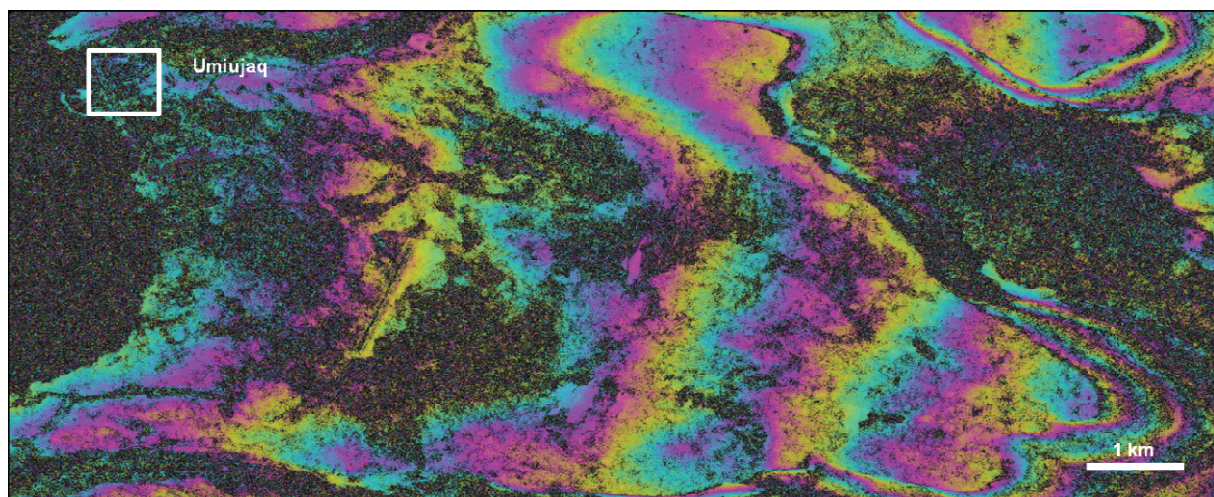


Figure 7.16: Filtered interferogram 14.08.09/ 25.08.09

Phase Unwrapping

At this stage of the processing chain, the phase information included in the interferogram contains information about topography and displacement but is only given by values between 0 and 2π . Hence, this information has to subsequently be transferred into real valued images, in order to finally retrieve linear dimensions. To do so, the phase has to be 'unwrapped' and afterwards transformed into heights by means of the precise baseline, calculated for each particular interferogram.

'Phase unwrapping' is the process of converting the 'wrapped' phases into a continuous phase response in the image, which usually gets implemented by adding integer multiples to the phase cycle. Hence phase unwrapping can be defined as the search for integer values that have to be added to values between 0 and 2π , to finally achieve a phase response which is no longer linked to modulo 2π . This task, however, is not trivial and in principle there can be no complete solution as the wrapped information is always less than the unwrapped, and additional assumptions need to be made (CHEN 2001). As a result, phase unwrapping has been the object of intensive research for many years and it is consequently not surprising that there are several approaches to generating a solution. In any case, all existing phase unwrapping algorithms are based on a 'gradient' method, which is displayed for the one-dimensional case in Figure 7.17.

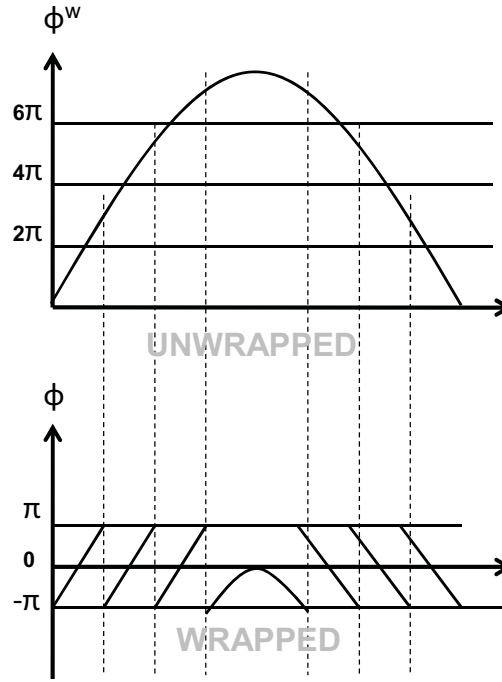


Figure 7.17: Principle of the unwrapping process, when the phase available in the sinus mode gets transformed into a continuous phase over the entire image (modified after SANTITAMNONT 1998).

In this method, the phase difference from one pixel to another has to be defined and integrated and the required integer number has to be embedded to get over this gradient. Although this can be applied relatively easily in one dimension, the two dimensional case brings the problem of how to decide the 'right' way through the pixels. Additionally this method only works correctly if the unwrapped phase difference between two pixels is less than half a cycle. Unfortunately, in almost all interferograms, values above this threshold exist, which leads to incorrect integration and so-called 'local errors'. To avoid such errors it is necessary to identify the mentioned discontinuities, referred to as residues, and to go around them during the integration process (CHEN & ZEBKER 2001). They are defined in the image with the equation

$$r = W\{(\phi_{i+1,j}^w - \phi_{i,j}^w)\} + W\{(\phi_{i+1,j+1}^w - \phi_{i+1,j}^w)\} + W\{(\phi_{i,j+1}^w - \phi_{i+1,j+1}^w)\} + W\{(\phi_{i,j}^w - \phi_{i+1,j+1}^w)\} \quad (\text{eq. 7.16})$$

and schematically explained in Figure 7.18. The value of r in this equation can be either zero, standing for 'no residue', or a +1-cycle or a -1-cycle for a positive or negative residue respectively.

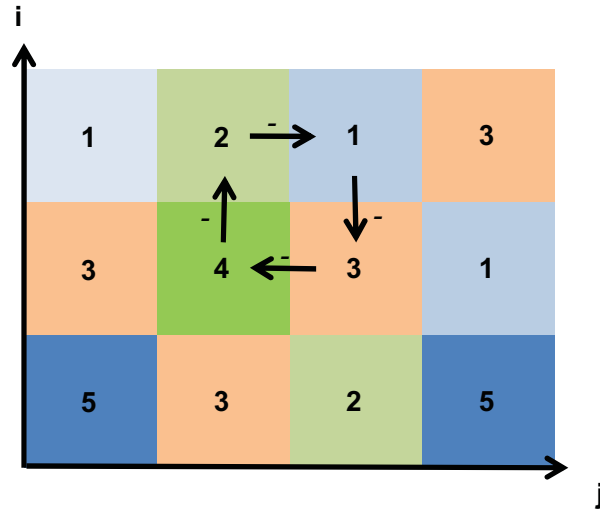


Figure 7.18: Definition of a residue: If the circle numbers reflects the values and centres of pixels, the summation of the gradients between neighbouring pixels determines whether the loop is neutral (no residue) or whether a positive or a negative residue appears. In this case according to eq. x this would be 0 = no residue.

There are many different approaches developed to deal with these residues, although the most popular one is probably the *branch-cut algorithm* (GOLDSTEIN 1988) and its derivations. It is based on a 'local' approach, the so-called '*path following*' approach that first identifies discontinuities to define barriers around which the integration gets disposed. For an elaborate description of the '*path following*' method, refer to GOLDSTEIN (1995), GOLDSTEIN ET AL. (1988) or ZEBKER AND LU (1998).

In the case of this study, different unwrap methods offered by the GAMMA Software were tried out, and the minimum cost flow (MCF) algorithm turned out to deliver the most reasonable results. For this reason it will be explained in more detail in the following section.

Minimum cost flow method (MCF)

The minimum cost flow algorithm looks for a solution for which the differences between the gradients of the wrapped phases and the gradients between the unwrapped phases is minimized, whereupon the unwrapped phase should yield $k2\pi$ differences, with $k \in \mathbb{Z}$ (HANSSEN 2001). The first process step, after the computation of the residues, is the connection of all of them with so-called *branch-cuts*, under the condition that the length of all cuts is the smallest possible. Subsequently, integer cycles are added to all cuts in order to cross them. The remaining pixels are negative, and positive residues which creates nodes. A cost function has to be identified that determines the path of integration through the residues, which will result in an equalization of the nodes.

Implementation with GAMMA

Before starting the actual unwrapping process, GAMMA offers the possibility of first generating a validity mask, highlighting pixels with low coherence values that are not valid for phase unwrapping. In doing so, sparser sampling can be implemented in areas with lower phase variation, which increases the efficiency of the phase unwrapping process (WERNER ET AL. 2002).

Once the validity mask is created, the unwrapping process starts as described. When successfully completed, remaining gaps in the unwrapped phase image are filled by interpolation (Figure 7.19). As the gaps may be of different sizes, it is useful to apply an interpolator with an adaptive window size.

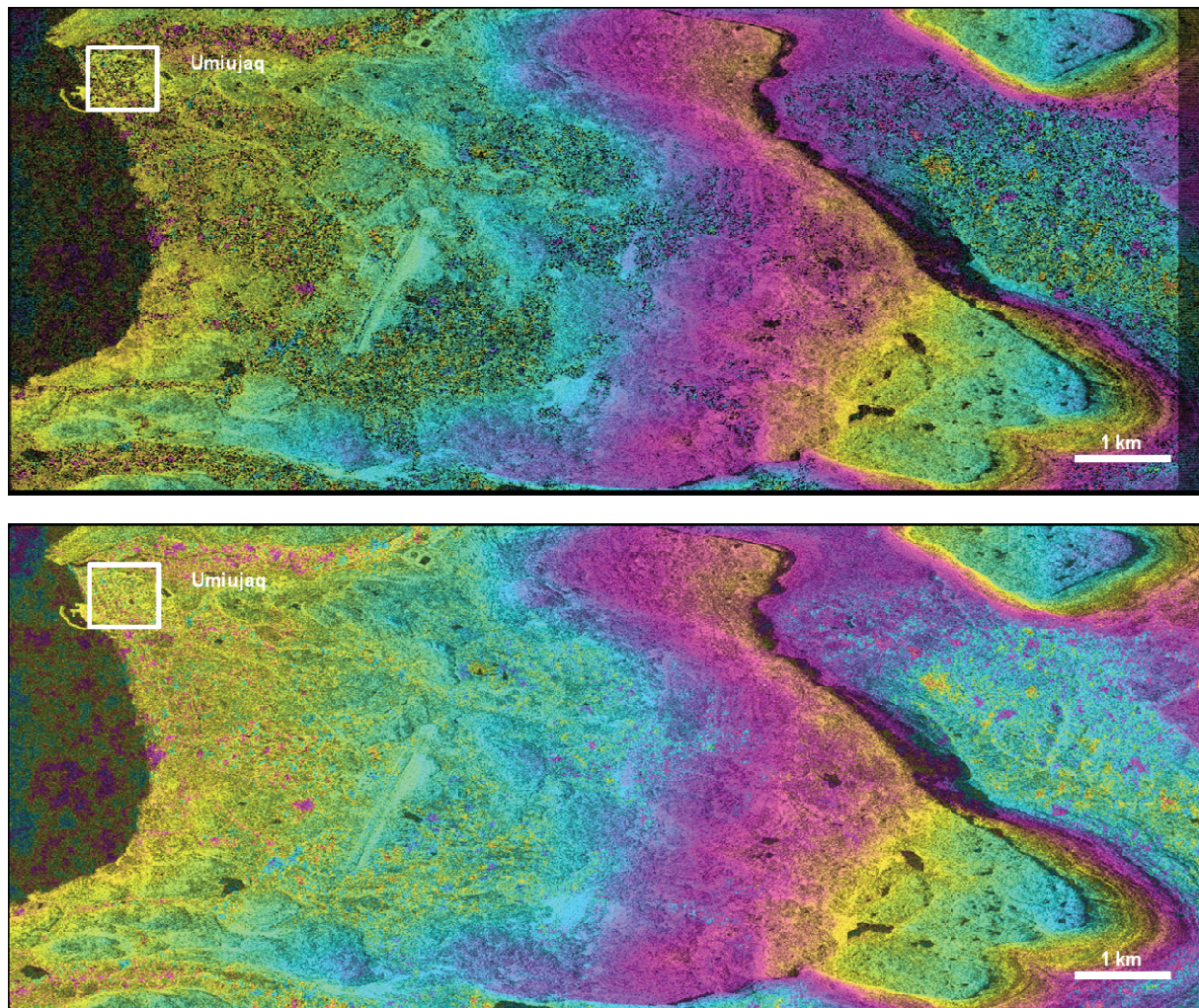


Figure 7.19: Top: unwrapped interferogram 14.08.09/ 25.08.09 which still includes excluded areas which are not unwrapped d; Bottom: unwrapped interferogram 14.08.09/ 25.08.09 with filled gaps after the interpolation process.

Differential interferogram formation

Several approaches exist for computing a differential interferogram, mainly based on the availability of different radar images, a sufficient DEM, and the number of SAR acquisitions.

For 2-Pass differential interferometry, two radar images forming the original interferogram as well as a DEM in radar coordinates are required. In this case, the interferogram contains information about the topography as well as the displacement, and for additional topographic information the DEM is consulted. By means of the DEM, the topographic component in the interferogram can be excluded and only the movement component remains. For it, a synthetic interferogram has to be generated, based on the DEM but in radar coordinates sharing the same baseline as the interferogram. For this procedure, the original interferogram needs to be unwrapped, and it is important that the flat Earth is still set out. By means of the least squares method, the fringes of the two interferograms can now be adjusted and the synthetic interferogram can afterwards be subtracted from the original. The resulting differential interferogram contains the displacement only.

A more sophisticated approach than the 2-Pass interferometry, first presented by ZEBKER ET AL. (1994), is based on interferogram stacks. He describes this method as 'i) more automatic, ii) more precise, and iii) better validated' compared to previous methods. Stacking, also referred to as multi-baseline interferometry or time-series analysis (USAI & KLEES 1999), combines more than only two SAR images in order to eliminate some parameters, e.g. topography or atmospheric influences, in

favour of others (HANSEN 2001). Referring to further studies (FERRETTI ET AL. 1997), this method seems to be preferred mainly for the detection of slow deformation processes and to minimize the atmospheric signal. Mathematically this is clearly explained by ZEBKER ET AL. (2004), who describes the phase difference (Φ) evoked by topography of one interferogram with

$$\Phi = (4\pi/\lambda) \cdot \delta p \quad (\text{eq. 7.7})$$

whereas δp equals the component of the baseline parallel to the look direction (BII). Further on, it includes the second interferogram, sharing the same orbit as the first one, having a different baseline BIII, what hence results in

$$\Phi_I = (4\pi/\lambda) \cdot B_{III} \quad (\text{eq. 7.18})$$

The ratio of the two phase differences can then be estimated by

$$\Phi / \Phi_I = B_{II} / B_{III} \quad (\text{eq. 7.19})$$

and is therefore independent of topography. In the case of movement between observations of the primed interferogram, an additional phase change has to be considered, namely the displacement Δp , and equation 7.19 has to be extended to

$$\Phi_I = (4\pi/\lambda) \cdot B_{III} + \Delta p. \quad (\text{eq. 7.20})$$

In order to receive only phase differences caused by the displacement, the data from the initial unprimed interferogram need to be scaled by the ratio B_{II} / B_{III} resulting in

$$\Phi_I = B_{II} / B_{III} \cdot \Phi = (4\pi/\lambda) \Delta p. \quad (\text{eq. 7.21})$$

The geometric relation between baseline and phase differences is also displayed in Figure 7.20.

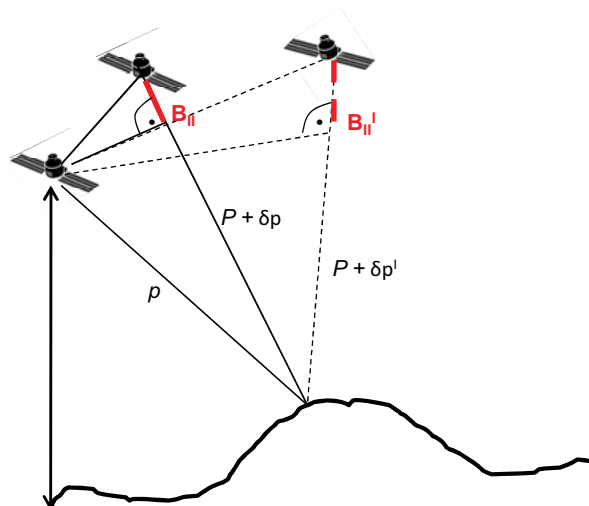


Figure 7.20: Relation between baseline and phase difference (modified after ZEBKER ET AL. 2004)

Depending on the number of SAR images, several interferograms can be stacked together. For the study at hand two interferograms, sharing one common SAR image, were used. Therefore three different radar images were required and hence this method is referred to as 3-Pass interferometry.

Similar to 2-Pass interferometry, the interferograms need to be unwrapped but retain the flat Earth component. However, for interferograms having a long baseline, it is recommended to remove the flat Earth before unwrapping and add the ellipsoidal Earth phase trend back to the unwrapped interferograms. This is what was done in this study.

3-Pass differential interferometry is based on three SAR images, or two interferometric pairs that have one image in common or the same reference geometry. The images of the first pair (= Int.1) should be acquired within a time step that is as short as possible, because this product will be used to calculate the topographic phase and therefore the maximum degree of coherence should be sought. Furthermore a large interferometric baseline is preferable to 'increase the sensitivity of the interferometric phase to topography as compared to differential effects and heterogeneity in the atmospheric path delay' (GAMMA 2008), and it should not include coherent displacement.

The second pair (= Int.2) should be generated by one image obtained before the coherent displacement and one after it. As the sensitivity to differential effects should be as high as possible, a short baseline is desired.

For the purpose of this study, 3-Pass interferometry seemed to be the most appropriate approach, which was confirmed by the outcomes of initial trials. As the images collected by the TerraSAR-X sensor have a very high resolution, the common methods for differential interferometry would have only delivered good results if a DEM with a similar resolution were available. As this was not the case for the entire study area, the 3-Pass methodology, which does not require a DEM for displacement estimation, was a very useful option. Its application was further supported by the fact that for this investigation there was no need for absolute values for the elevation changes, but only relative ones between the different dates.

Figure 7.21 displays the differential interferograms generated by means of the 3-Pass approach, based on the two interferometric pairs 14.08.09/ 25.08.09 and 14.08.09/ 07.05.09.

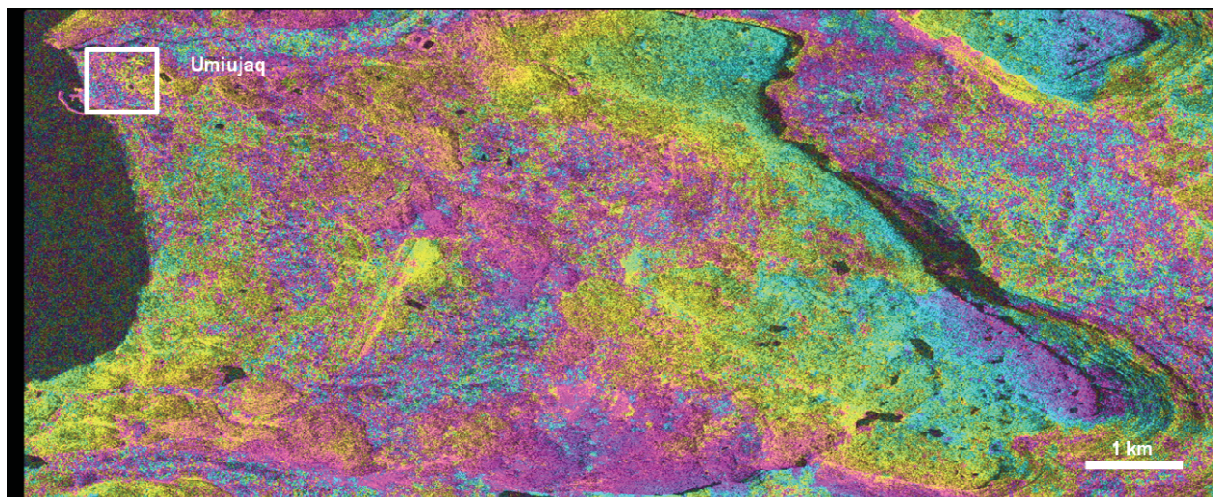


Figure 7.21: Differential interferogram based on the two interferometric pairs 14.08.09/ 25.08.09 and 14.08.09/ 07.05.09

Conversion from phase to height and geocoding

This procedure transforms the unwrapped phase to topographic height by means of the baseline geometry. In the case of differential interferometry, the outcomes of such a transformation do not represent the actual height, but the displacement in terms of horizontal or vertical deformations in relation to the interferogram containing the topography. It should be mentioned that it is only possible to observe one of the two components in an interferogram and only the additional use and combination of images acquired with e.g. inverse path can help to define the second component. Since only the vertical movement was of interest in the study and further motion could be neglected, such an approach was not necessary. An excellent mathematical description of the displacement estimation is given in HANSEN (2001). The outcome of this step is displayed in Figure 7.22.

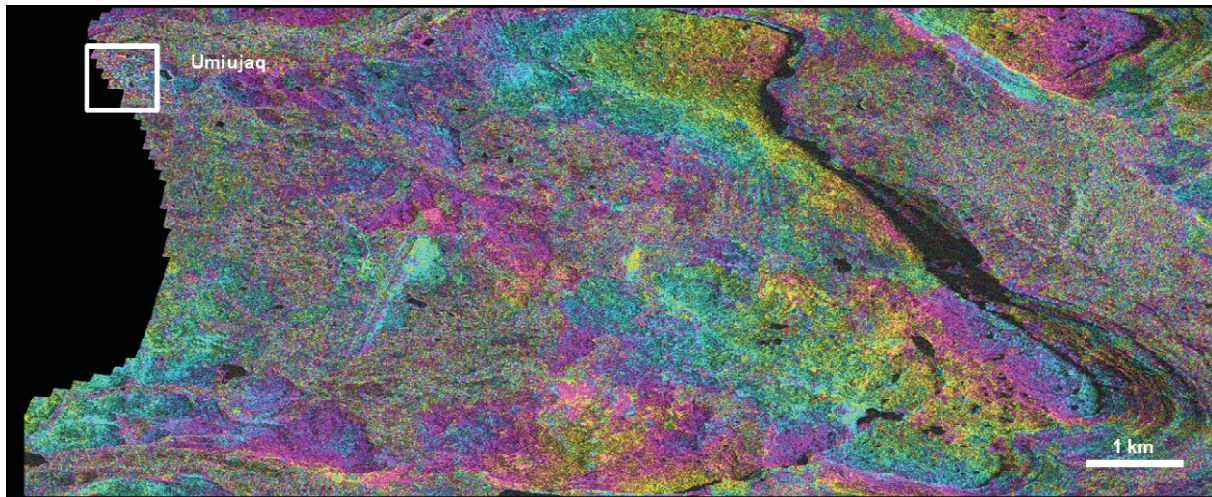


Figure 7.22: Vertical displacement map based on the differential interferogram generated by the interferometric pairs 14.08.09/ 25.08.09 and 14.08.09/ 07.05.09; one fringe represents one cm displacement

When the topographic height in SAR image geometry is known, the image can be transformed from SAR coordinates to orthonormal coordinates in a convenient geodetic reference system, which, in the case of this study, is WGS84. To do so, a procedure similar to the one already outlined is carried out to evaluate the reference phase. A DEM is not necessarily required as approaches exist that allow a conversion simply by means of the exact baseline. However, in the case of this study, the very high number of pixels representing only water caused a high error in the processing step, attributed to the fuzzy phase signal of water areas. Consequently a DEM was embedded, which made it much easier to define these pixels as zero elevation, and which helped to obtain much more reasonable results. The DEM used was the model of the Shuttle radar topography mission (SRTM). For it, tile N56W077 was downloaded and later up-scaled to a spatial resolution of 3 m to match the spatial resolution of the radar images. A copy of the final DEM used can be found in Figure 7.30 in the next chapter (Chapter 7.2.4.1).

In order to geocode the image, every pixel located on a specific circle around the velocity vector of the sensor, has to be specified in relation to the ground surface. Furthermore the look direction of the sensor (right – or left - looking) and the desired datum of the map projection need to be known and have to be integrated in the resampling of the SAR image into the map projection. Figure 7.23 represents the final geocoded displacement map for the differential interferogram generated by the interferometric pairs.

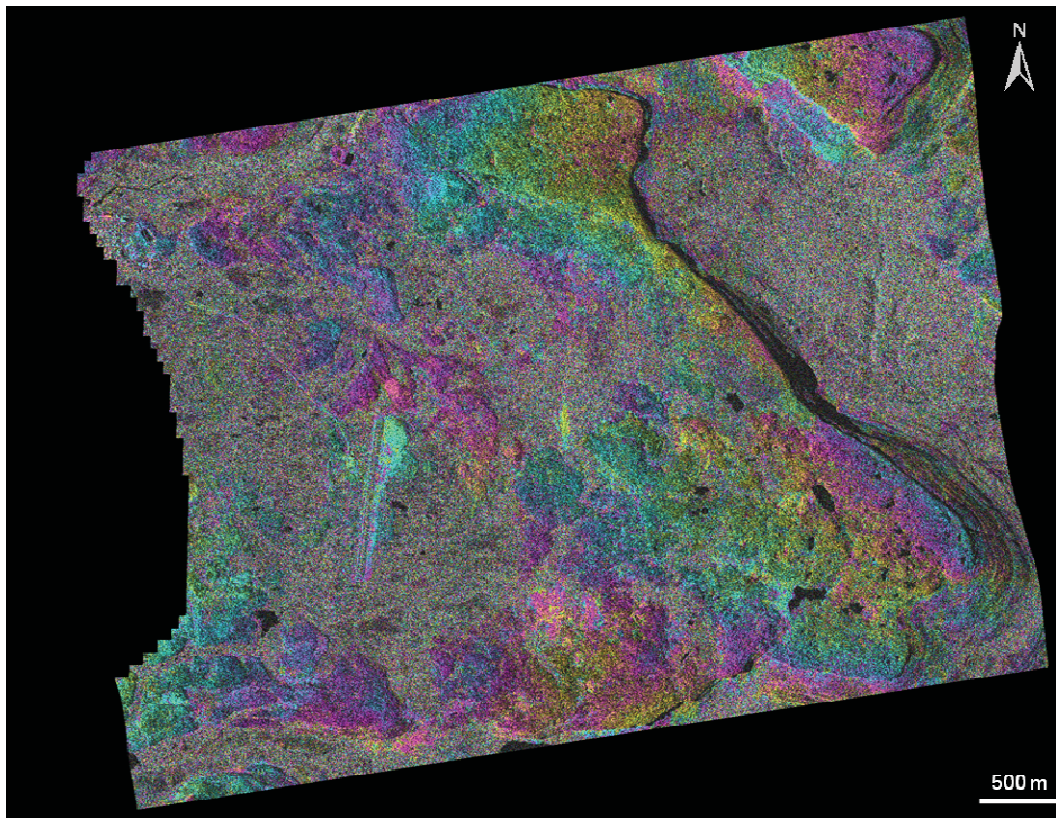


Figure 7.23: Final geocoded vertical displacement map based on the interferometric pairs 14.08.09/ 25.08.09 and 14.08.09/ 07.05.09; one fringe is equal to one 1 cm of vertical change.

Combination of complex interferograms

The combination of complex interferograms is an approach that works without a DEM and, additionally, does not require successful phase unwrapping (GAMMA 2008). It is based on the idea that the argument of the product of a complex number with the complex conjugate of a second complex number, equals the 'difference between the arguments of the two complex numbers, and the phase scaling with the integer factors results in the scaling of the wrapped phase with the same integer factor' (GAMMA 2008).

This allows for the possibility of 'artificially' modifying the spatial baseline by scaling the wrapped phase of the combined interferograms.

This approach was tried in this study for the generation of a differential interferogram based on interferogram 12.08.10/ 23.08.10 (= Int.1) and interferogram 12.08.10/ 05.05.10 (= Int.2). In this particular case the spatial baselines were estimated for - 158 m and -0.43 m respectively, therefore scaling factors of 1 and -2 result in an effective baseline of -37.29 m ($-195 - (-158\text{m}) = -511\text{ m}$). The resulting differential interferogram now contains the differential phase component of the first pair, minus two times the differential phase information of the second pair. Consequently the information about topography included in the differential interferogram is much lesser than the containing displacement information. And therefore the combined interferogram will be much better suited to detect displacements.

7.2.3 Data selection process

The first question that needs to be addressed is which satellite system should be used. In this case, the highest possible spatial resolution for radar data was desired. Additionally, the system should provide the opportunity to work with new datasets to explore their information content. The selection of

the recently launched German TerraSAR-X satellite was therefore a very quick process, since not only very good quality data could be expected from its sensor, but it also offered a lot of unexplored possibilities. Its images seemed to be perfect for this methodical research that also includes some new applications.

TerraSAR-X

Launched on June 15th 2007, the German TerraSAR-X satellite acquires new high-quality X-band radar images with a spatial resolution of up to 1 m of the entire planet, whilst circling Earth in a polar orbit at 514 km altitude. Its major purpose is the acquisition of high-accuracy global SAR data for scientific and commercial use, which is why its mission is the result of a public-private partnership between the German Federal Ministry of Education and Research, the German Aerospace Centre (DLR) and Astrium GmbH. TerraSAR-X is supposed to operate for 5.5 years. The X-band sensor operates at a frequency of 9.65 GHz which equals a wavelength of around 3 cm (DLR, 2010). The repeat period is 11 days, but due to the ascending and descending swath overlay, a 2.5 day revisit time is possible (Infoterra GmbH, 2010). Images can be acquired in either single, dual or quad polarization, and in three operational imaging modes: Spotlight (resolution 1 m; footprint 10 x 5 km), StripMap (resolution 3 m; footprint 30 x 50 km) or ScanSAR (resolution 18 m; footprint 100 x 150 km) illustrated in Figure 7.24.

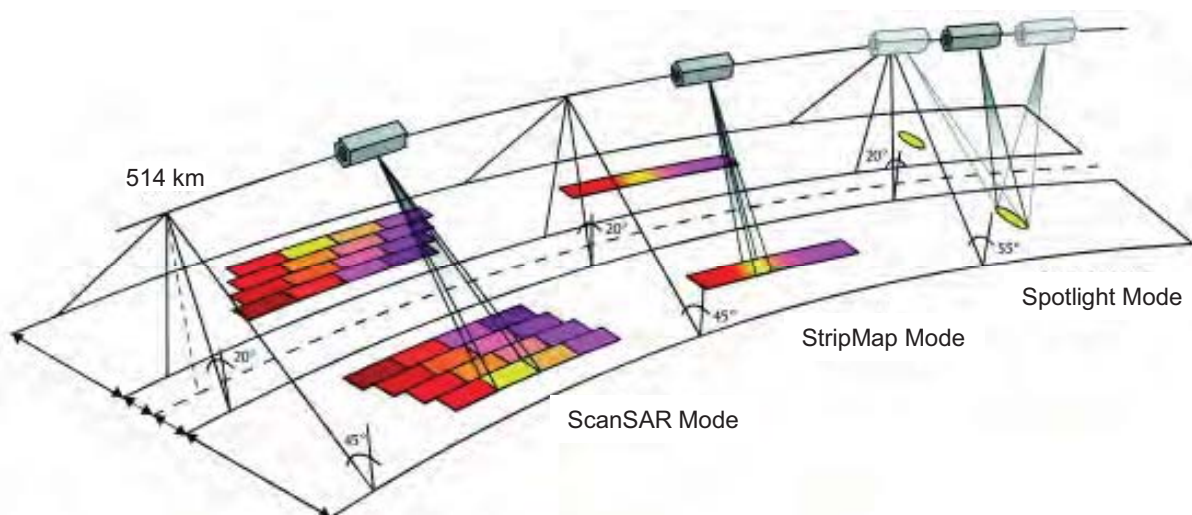


Figure 7.24: The different acquisition modes ScanSAR, StripMap and Spotlight from the TerraSAR-X satellite (modified after Infoterra GmbH 2011)

Unique features of TerraSAR-X are its high spatial resolution (up to 1 m) independent of weather conditions and illumination, and its high geometric accuracy. A further advantage of this satellite is its partner satellite TanDEM-X (TerraSAR-X add-on for Digital Elevation Measurement), in space since June 21st 2010. It is almost identical to TerraSAR-X, and together they form the first bistatic SAR mission by flying in a closely controlled formation with a distance of 250 – 500 m (DLR 2011). The cooperation of the two spacecraft will serve to generate new quality DEMs of the world, 'along-track interferometry (e.g. measurement of ocean currents) and new bi-static applications (e.g. polarimetric SAR interferometry)' (DLR 2011).

Although the launch of TanDEM-X was unfortunately too late to use its data for the purpose of this study, it might be beneficial if continuing studies in this research field and this test site are desired.

Data for this work was ordered in the StripMap mode, as these records cover the entire area and still have a very high spatial resolution. In addition to the imaging mode, decisions about the incident angle, the polarization mode, and the pass direction had to be made. The processing options for the product type, the processing level, and the orbit precision also needed to be specified. Information about the most appropriate incident angles and orbit precision were sought from the TerraSAR-X science team of DLR, who recommended angles between 30° - 45° and the orbit precision 'SCIENCE'. 'SCIENCE' represents the product useable for SAR-interferometry and has a performance of 30 cm (MONTENBRUCK 2008). This combination results in the spatial resolutions and characteristics summarized Table 7.9.

Table 7.9: Overview of the spatial resolutions resulting from the acquisition modes used for this study (modified after CAF 2009)

Spatial resolution of a TerraSAR SSC-image in dual polarization mode	
Swath width	~ 15 km
Slant range resolution	1.2 km
Ground range resolution	
- Incidence angle: 45	1.7 m
- Incidence angle: 20	3.4 m
Azimuth resolution	6.6 m
Range pixel spacing	0.9 m
Azimuth pixel spacing	2.5 m

In order to define the most advantageous acquisition modes concerning pass direction and polarization, images of the ascending (VVHV) as well as descending (VVHH) paths were ordered during the first year (2009) and analyzed to assess their suitability. Thus the main selection criterion was the coherence values of the interferometric products. This parameter was chosen due to its high impact on the quality and validity of the differential interferometric outcomes. These were calculated for each ascending and descending pair and with different polarizations over the entire image, as well as for some smaller subsets representing the main areas of interest (Ithalsas and Cuestas). This allowed the image acquisition mode combination with the highest coherence values to be identified and used for differential interferometry.

The following coherence values averaged over the different image pairs were computed:

- Ascending VV polarization: Cuesta subset 0.76; lithalsa subset 0.29; Complete image (excluding water) 0.50.
- Descending VV polarization: Cuesta subset 0.66; lithalsa subset 0.25; Complete image (excluding water) 0.49.
- Descending HH polarization: Cuesta subset 0.65; lithalsa subset 0.25; Complete image (excluding water) 0.46.
- The cross - polarization (HV) outcomes were far below these values.

The investigation therefore clearly identified the VV polarization as the polarization mode yielding the highest coherences and, consequently, the one that should be used for further processing. In terms of the pass direction, better results could be achieved by using the ascending pass. This may be related to the acquisition time and the orientation of the Cuestas. The record time of the descending path was during early morning at 7:26 am local time when the area is very often covered by dense haze, especially during the summer time, while ascending passes were in the afternoon at around 6:46 pm when the fog typically has disappeared. Although the radar signal is not strongly affected by the atmosphere, such influences on the very sensitive X-band are still possible.

The orientation of the Cuestas leads to different backscatter situations for the descending and the ascending paths (Figure 7.25). Whereas the signal of the ascending path arrives at the surface at a very small incident angle and is almost entirely reflected to the sensor, the descending situation results in a very high scatter of the signal, and consequently less information can be captured by the sensor.

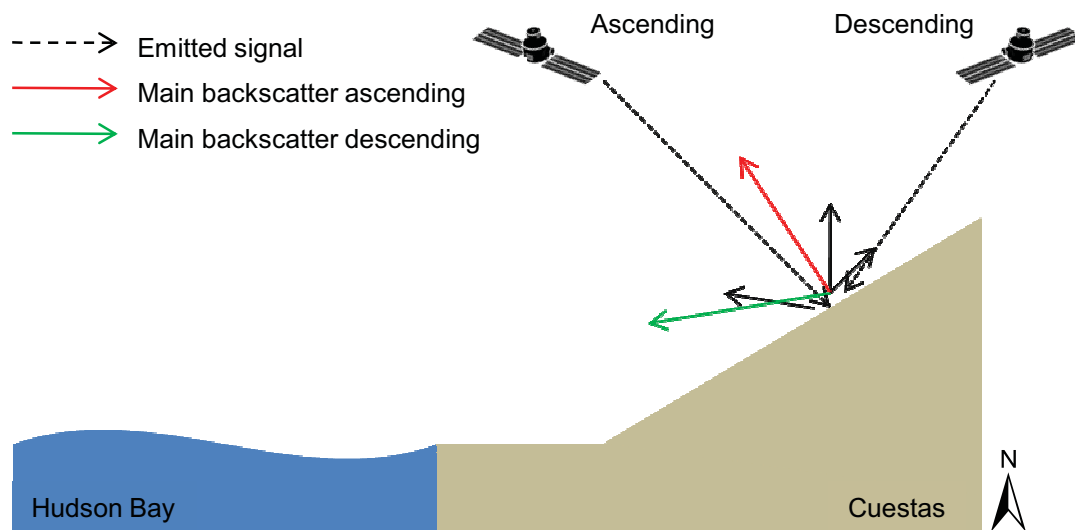


Figure 7.25: Possible impact of the Cuestas on the radar signal.

Based on the findings and recommendations discussed above, the products with the properties listed in Table 7.10 acquired at the dates shown in Table 7.11 were used for the differential interferometry. All images are level L1B products, meaning that the correction of phase pattern caused by the antenna is inherent (BREIT ET AL. 2010).

Table 7.10: Overview of the properties of the imagery used

Acquisition options	
Sensor mode	Stripmap
Polarization mode	Dual polarization
Pass direction	Ascending
Look direction	Right
Incident angle max.	40.08262561
Incident angle min	41.21486996
Phase/ Orbit	-1 /165
Polarization channels	VV HH / VV VH *
Processing options	
Product type	Single Look Slant Range Complex (SSC)
Processing level	L1B
Orbit precision	SCIENCE
Temporal selection	22:46:56 (DT Standard Time in UTC)

Table 7.11: All acquisitions used; The date for the master image is in red As the gaps may be of different sizes, it is useful to apply an interpolator with an adaptive window size

	2009	2010
Winter/ Spring	04.04	22.03
	07.05	05.05
Summer = Reference	14.08	12.08
	25.08	23.03
Fall	27.09	-
	30.10	28.10

7.2.4 Results and discussion

For the generation and interpretation of the differential interferograms, the advantages and disadvantages of the different computation approaches (2-Pass, 3-Pass interferometry, and combination of complex interferograms) were analyzed. They clearly highlighted 3-Pass interferometry as the most appropriate technique for the purpose of this study, based on the datasets at hand. Additionally, several recent studies that compared the 2-Pass and 3-Pass methods achieved better results with the 3-Pass interferometry (XU ET AL. 2010). Nevertheless an attempt using 2-Pass as well as the combination of complex interferograms was conducted, but the results showed less reasonable outcomes and therefore it was resolved to use 3-Pass interferometry

For the 3-Pass interferometry, the GAMMA Software offers an abundance of different possibilities to achieve the final product. Many different algorithms, parameters and thresholds have to be defined by the user during the processing, depending on the dataset and the desired outcome. Consequently, the first working step was dominated by an iterative process, trying all kind of combinations, to determine the best combination. During this part of the investigation, the image size and cutting was also defined. At the end of this procedure, a 'guideline' could be generated that later served for the generation of all the differential interferograms. The guideline not only accelerated the pace of work immensely, but it also ensured similar processing for all images. The guideline can be found in Appendix 6.

For both years of interest, one acquisition in the middle of the year was chosen to serve as the starting date for the differential interferograms. These are 14.08.2009 and 12.08.2010 (=master images). In order to guarantee similar geometry for all images, 12.08.2010 was first geocoded to 14.08.2009 (=master 1). Consequently, all acquisitions used are in the geometry of the scene from 4.08.2009 (Figure 7.26). The choice of this scene is based on the assumption that this is the one the most free of disruptions caused by error sources such as atmospheric water vapour and soil humidity. This assumption is made on the strength of weather observations during the field campaigns, which were confirmed by meteorological data from Environment Canada.

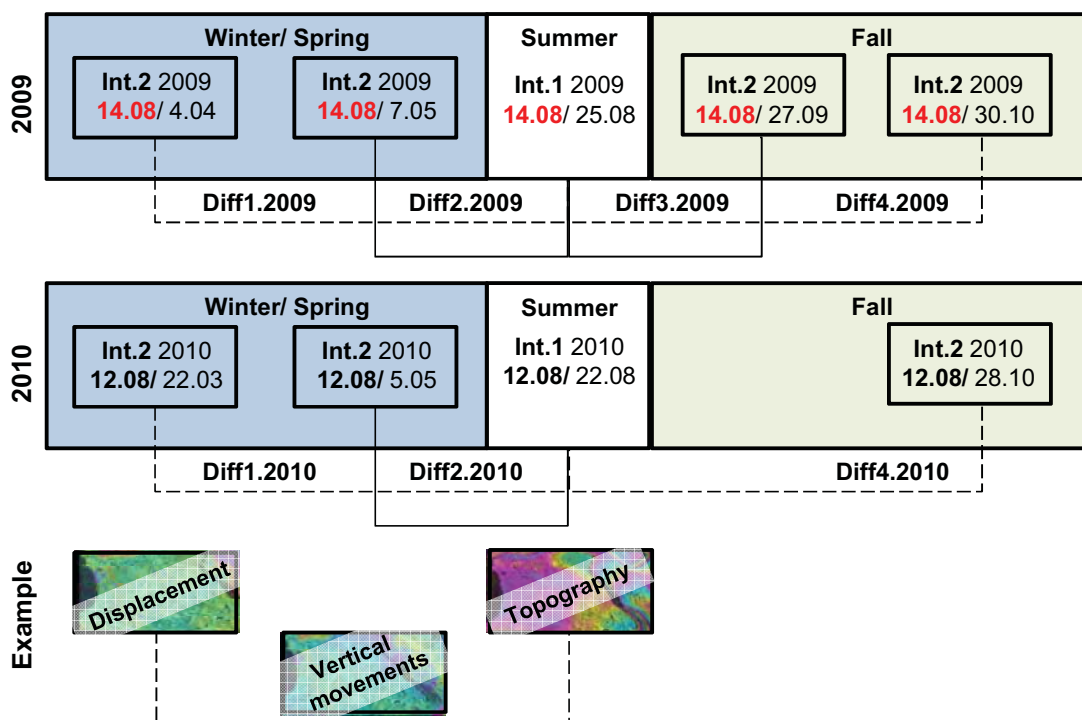


Figure 7.26: The combination of the different acquisition dates and their denotation. Top: images from 2009; middle: images from 2010; bottom: example of the combination of Int.1 and Int.2 to produce Diff.1.

In the next step, one interferogram containing the topographic information was computed for each year. It later served as reference for all the differential images created for that year (= Int.1). Int.1 for 2009 consists of the acquisitions from 14.08.2009 and the 25.08.2009, and for 2010 the records from 12.08.2010 and 23.08.2010 form the topographic image pair. In both pairs, the earlier date is used as master and therefore also represents one component of the interferogram with the displacement information (=Int.2). Int.1 and Int.2 are then used to build the differential interferogram. Figure 7.27 illustrates the combination of the different acquisitions, and describes the main processing steps to finally create the differential interferogram. In this figure, it can be seen that the outcomes present only five vertical displacement maps, although seven would have been possible (Table 7.11). This is due the fact that in the Int.2s containing the records for March and April, the coherences were much too low to guarantee adequate processing and the coregistration process failed. This can probably be attributed to the snowcover still remaining on those dates.

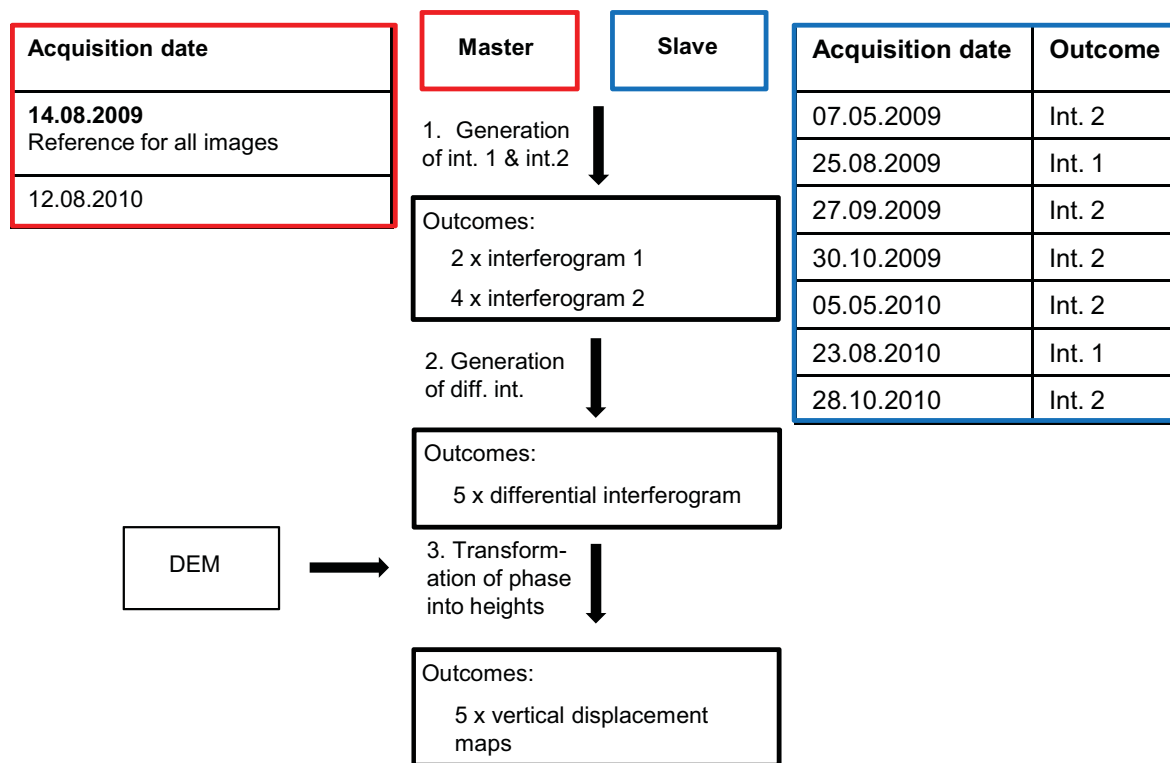


Figure 7.27: Main processing steps for the generation of a displacement map by means of the 3-Pass differential interferometry

The DEM mentioned in this illustration originates from the Shuttle radar topography mission (SRTM) and serves as reference for the calculation of the displacement map. Although it is theoretically possible to calculate the displacement simply by means of the accurate baseline and the orbit information, this did not prove satisfactory. This is very likely a result of the large number of water pixels (Hudson Bay) in the image representing arbitrary phase values in the interferogram and resulting in unrealistic elevation values. The DEM was embedded at this step of the work flow to clearly indicate the Hudson Bay as zero elevation. By doing so, the outputs were ameliorated greatly and now produce meaningful numbers, as shown in the following discussion. The DEM used is mapped in Figure 7.30 below.

7.2.4.1 Results

Before presenting and discussing the differential interferograms, the generated Int.1 for 2009 and 2010 and their characteristics are shown. After that, the two differential interferograms displaying the displacement between spring and summer (Diff1.2009 and Diff2.2010) will be interpreted. Finally, the

differential interferograms that show the motion between summer and fall (Diff2.2009 and Diff2.2010) are examined.

As mentioned, the initial step was the coregistration and resampling of 12.08.2010 to master 1. The standard deviation of the coregistration is 0.1033 for range and 0.0955 for the azimuth direction. The literature generally recommends $1/10^{\text{th}}$ of a pixel as a threshold to guarantee further accurate processing (ZHOU ET AL. 2009) and, accordingly, this was taken as the objective in this study. If the coregistration results missed this goal, the already resampled images were resampled again until they finally reached the threshold, or until no further enhancement could be achieved. Fortunately, this was very seldom the case. All outcomes are listed in Table 7.13 at the end of this chapter. The temporal baseline of the two images adds up to 363 days, the parallel component of spatial baseline amounts to 102.38 m, and the perpendicular component is 191.61 m.

The generation of the two Int.1's (14.08.09/ 25.08.09 and 12.08.10/ 23.08.10) proceeded smoothly. The standard deviation for both images, in range as well as in the azimuth direction, could be minimized to less than 0.1 (Table 7.13) and provided a perfect base for further processing. The baseline components were -66.79 m (perpendicular) and -86.98 m (parallel) for the 2009 pair, and -159.00 m (perpendicular) and -124.00 m (parallel) for the 2010 scenes. These numbers are good since rather large baselines are desirable for Int.1 in order to increase the sensitivity of topography compared to differential effects (GAMMA 2008), while short baselines are preferable for Int.2 in order to optimally consider the displacement.

Figure 7.28 provides an example of the validity mask, generated for the unwrapping and based on the coherence image. It highlights pixels that have to be excluded from the initial phase unwrapping and are only interpolated afterwards. For it, a threshold of 0.3 was defined. This mask is generally similar for all interferograms; since it has a high impact on the differential interferogram, however, this one shall now be discussed as a showcase.

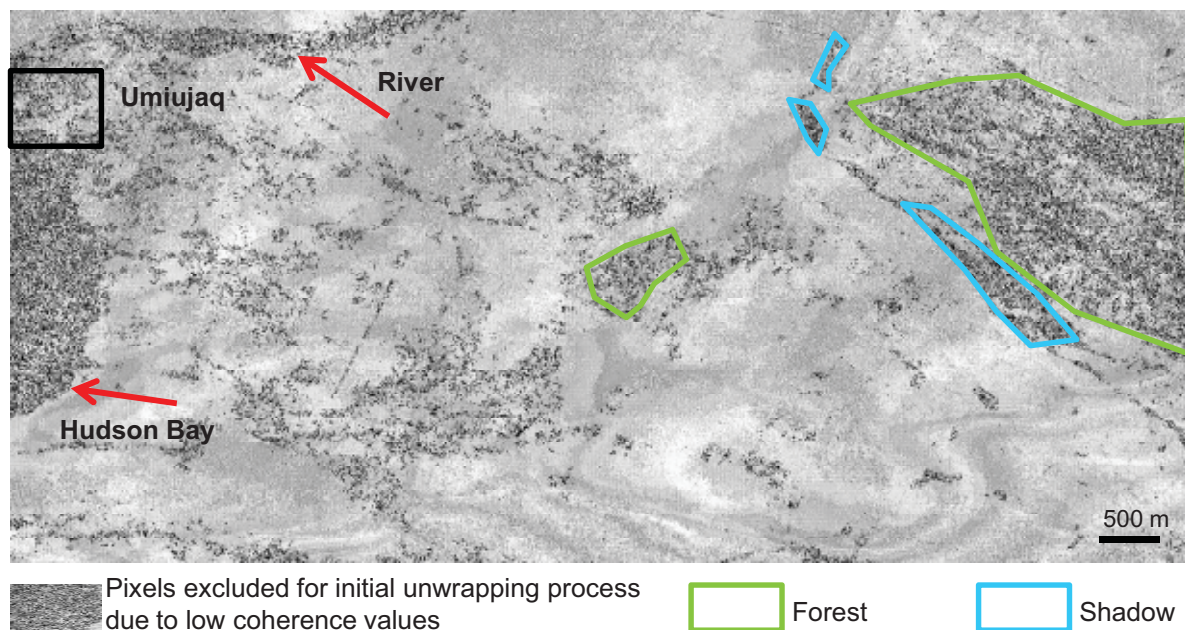


Figure 7.28: Validity mask generated for the unwrapping process of Int.1 2009. It is based on the earlier computed coherence map and highlights all areas (black) that need to be excluded from the initial phase unwrapping due to their low coherence values. The threshold used was 0.3.

The first areas to catch the eye are water, represented here primarily by Hudson Bay as well as by the river in the north (red arrows). Additionally, there is a large area in the eastern part of the image that is mainly covered by invalid pixels (green). An examination of the optical data showed that this area was covered by dense vegetation such as bushes and small trees. The same applies to some low coherence values in the west. Also remarkable are the areas to the immediate east of the Cuestas (blue). The composite image delivered with the TerraSAR-X data was consulted and clearly identifies the concerning pixels as radar shadow, which looks quite similar to water in the image (Figure 7.29).

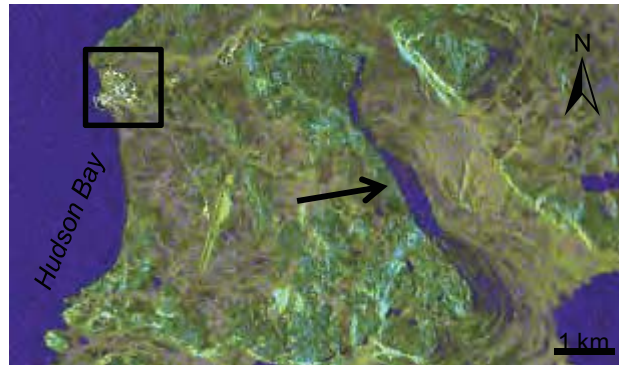


Figure 7.29: Composite image of 14.08.2009. Areas of radar shadow east of the Cuestas look very similar to water in the coherence map and appear as very low coherence pixels.

These findings are very relevant and essential for the interpretation of the differential interferograms, as they are reflected in almost all the products and necessarily have to be considered throughout the entire interpretation. This also causes that the forest area in the east will not be taken into account during the analysis. Although the interpolation algorithm finally delivers unwrapped values for the entire image, this zone seems to be too large as that the interpolation algorithm still yields to reasonable results. In contrast, for the smaller regions in the west, it is suggested that due to their little expansion, the interpolation will still result in rational values. As the area of main interest (=lithalsas) for this study is located in the west, the validity of this region was even more enhanced by seeding the starting points for the unwrapping processes closely. Due to the non-vegetated top of the lithalsas the coherences for especially the pixels covering this area, were almost in all cases not excluded by the validity mask.

Coming back to Int.1 2009 and Int.1 2010, one problem was arising while phase unwrapping of Int.1 2010. This was due to the fact, that the memory allocation required for the computation exceeded the limit of the hardware. There are two possible options existing to sort out this problem:

- i) The process is done by so-called 'patches', meaning that the images is subdivided it tiles, with some overlapping areas, in which the process operates separately.
- ii) The downscaling of the image for the phase unwrapping process to the half (third, fourth, and so on) of the size, and an afterwards up-scaling to the original size.

However the outcomes of both methods showed very poor and questionable results and hence it was decided that both approaches are not feasible to produce adequate results. Consequently, the only solution was to cut the image again in order to reduce the required memory, and the results for Int.1 2009 and Int.1 2010 are pictured in Figure 7.30, together with the up-scaled SRTM DEM which serves as a reference.

As a starting point for the unwrapping process, a pixel close to the area of the lithalsas, and which also shows high coherence, was desired. For Int.1 2009, pixel 2542/ 978 (line/range) with a coherence of 0.917 was chosen, and for Int.1 2010 the pixel 2108/1711 with a coherence of 0.978 was selected.

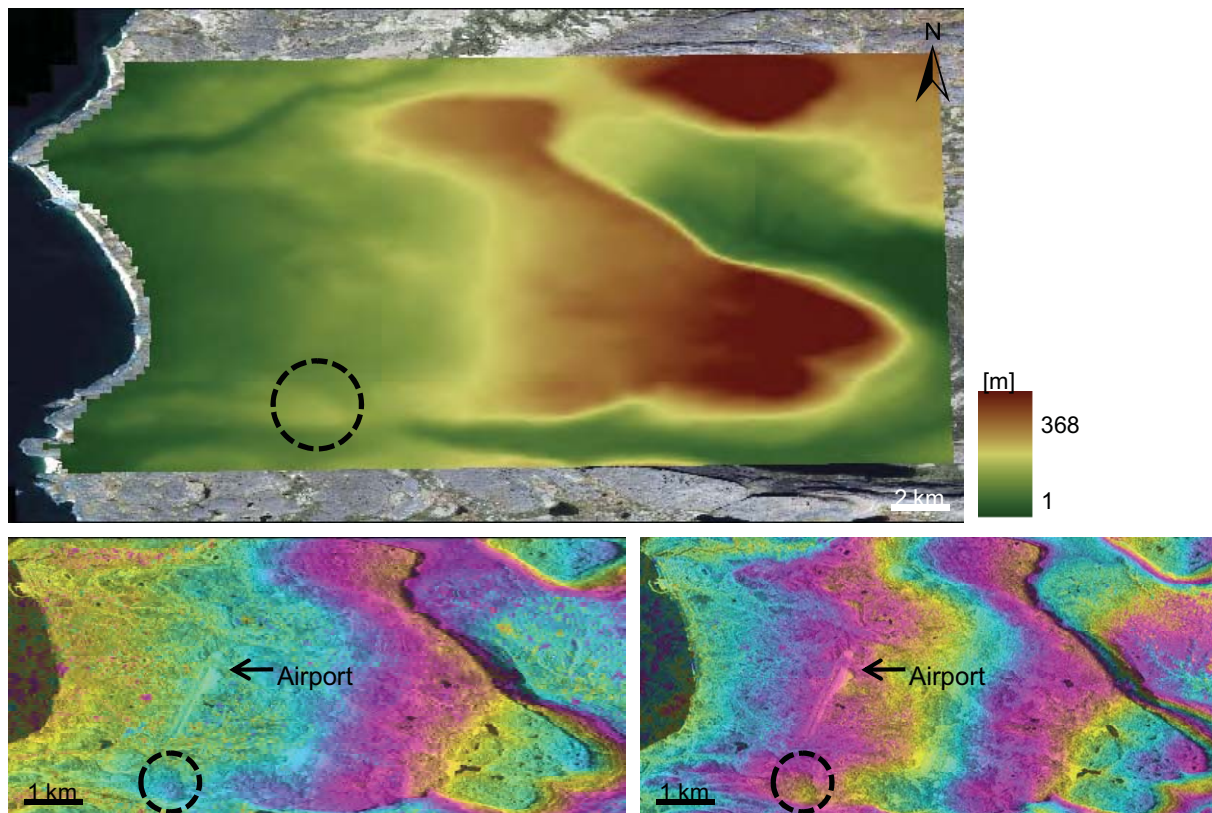


Figure 7.30: The two unwrapped interferograms Int.1 2009 (left) and Int.1 2010 (right). On top, the DEM is shown as reference. It can be clearly seen that both outcomes reproduce the topography very well. The dashed black circle depicts small hills visible in all maps. Phase display is 6π per color cycle.

They both clearly show the topography, with the slowly ascending slope on the west and the steep cliff towards the valley in the east. Besides the main relief, there are additional minor points of elevation that can be located in all three maps, with one of them shown by the black circle. It also becomes apparent that the interferograms are much better at reflecting the small-scale relief (e.g. around the airport) which becomes indistinct in the DEM. The high conformity of the two products, as well as their accordance to the DEM, is taken as evidence of successful processing.

For the next processing step, which is the generation of the differential interferograms (i.e., the combination of Int.1 and Int.2), the flat Earth has to be added back to the two interferograms.

All final differential interferograms can be found in Appendix 7.

Differential Interferograms: Spring and summer (Diff1.2009; Diff2.2009; Diff1.2010; Diff2.2010)

For the generation of the differential interferogram, it was first necessary to create the required interferograms containing the displacement (Int.2). During this procedure several problems arose: the images acquired early in the year (4.04.2009 and 22.03.2010) showed very speckled signals in some places. This is very likely due to the full snow cover still remaining on those dates; hourly climate data supplied by Environment Canada show temperatures below -5°C , often even less than -10°C , with a wind chill below -20°C (2010) for the days before the acquisition dates. In the case of the 2009 image, not even rudimentary coregistration could be carried out. With respect to the March acquisition, the accuracy did not exceed 0.823 in the range and 0.649 in the azimuth direction, even after several

iterations. As this is more than 50 % of a pixel, satisfactory processing was highly questionable and thus further processing was halted.

Much better success was obtained with the May acquisitions: with standard deviations of 0.037 and 0.141 (range/azimuth) in 2009, and of 0.071 and 0.113 (range/azimuth) in 2010, the threshold value is achieved and the base for further processing guaranteed. In Figure 7.31 shows the examples of the coregistration of the Int.2 pair from May 2009. It has to be kept in mind, however, that because of the ascending direction of the satellite, the image is upside down (top is south, bottom is north), and therefore entrance to the harbor (yellow dashed line) is downwards.

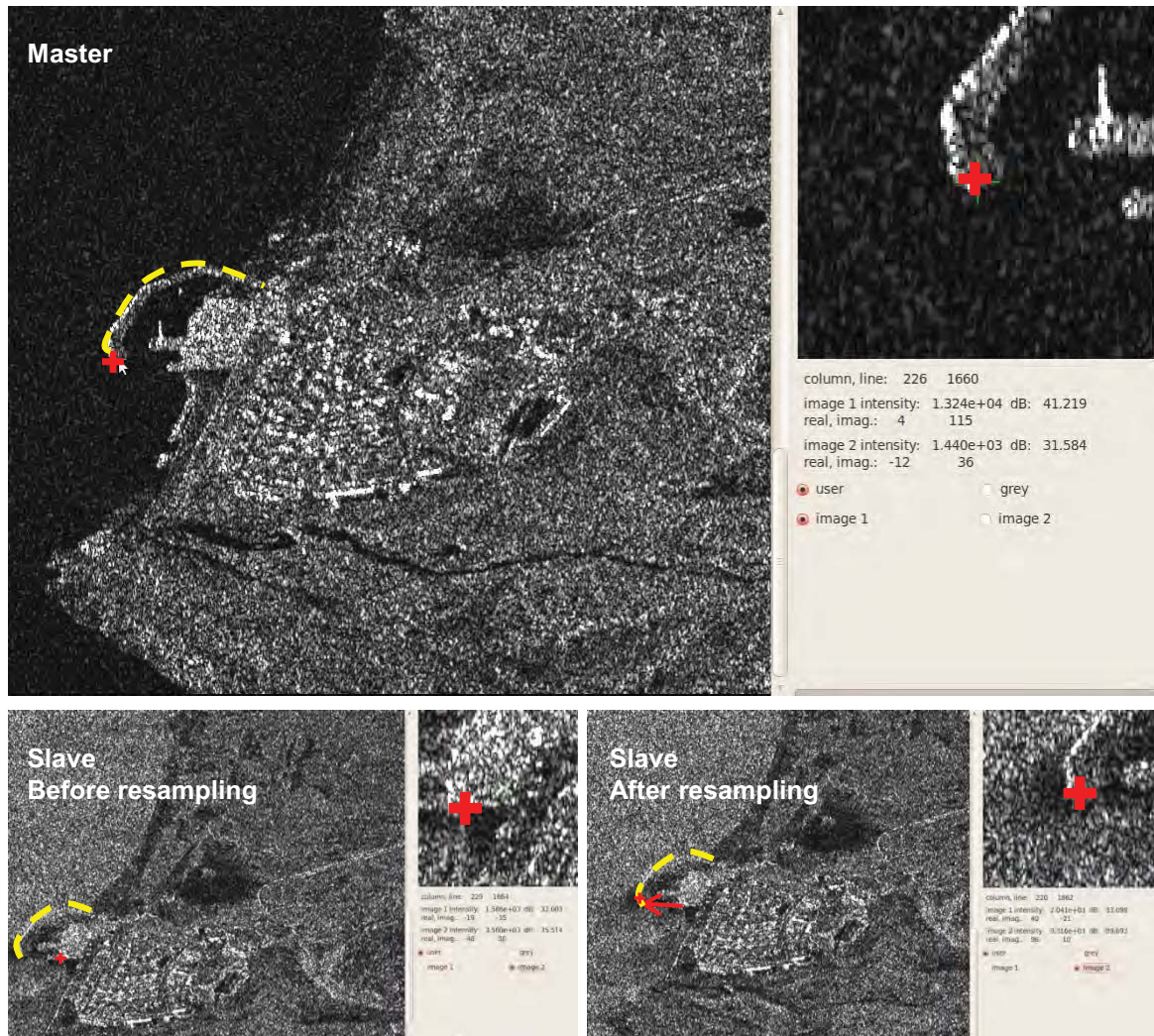


Figure 7.31: Example of the coregistration and resampling processes. The red cross indicates the pixel that corresponds to the pixel in the master image (top). The left image shows the slave image before the coregistration, with the red cross several meters east of the corresponding master pixel. In the right image, the resulting resampled image shows a much better fit of the pixels.

The estimation of the perpendicular baseline component yielded good outcomes for the image pair of 2010: As mentioned earlier, rather small spatial baselines are desired for an optimal representation of the displacement components in the interferograms, and with only 0.429 m, these conditions are definitely met. In contrast, the baseline for 2009 is unfortunately 125.361 m. This situation is a result of the orbit constellation of the satellites, so nothing can be done to change or enhance it, but it is still important to be aware of it.

Because of the complications faced during the first steps, further processing was only conducted for the May interferograms and therefore only Diff2.2009 and Diff2.2010 were generated, which are shown and interpreted below.

The processing of the differential interferogram was implemented as described earlier, starting with the unwrapping process, and using a coherence threshold of 0.3 for the validity mask. In the case of the Int.2 pairs, the coherences were in general lower than for the Int.1 pairs, which is due to the longer temporal baseline and, of course, the coherent displacement during this period. In comparison to the validity mask of Int.1 2009 discussed earlier, the areas with low values can be relocated, but additional places are affected by the low numbers. Nevertheless the unwrapping process was successfully conducted and thanks to the interpolation method, reasonable quantities for the entire image were achieved. Figure 7.32 shows the outcomes of Int.2 2009 and Int.2 2010, without the flat Earth, but which was later added for the generation of the differential interferogram.

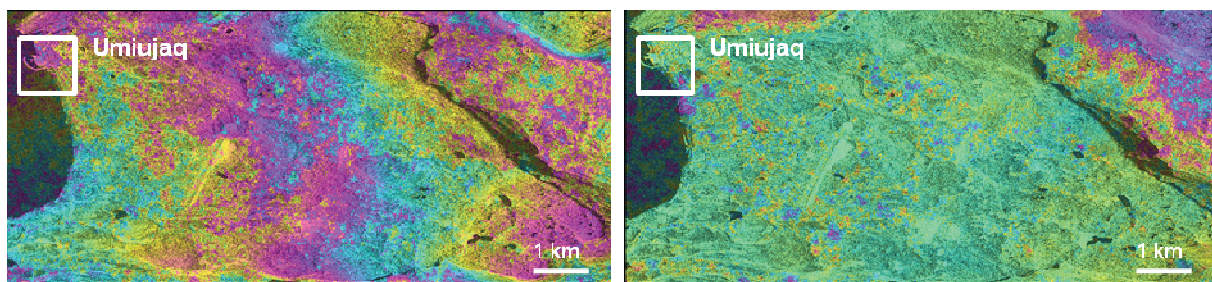


Figure 7.32: Unwrapped and unflattened Int.2 2009 (left) and Int.2 2010 (right). Int.2 2009 reflects much more of the relief than Int.2 2010, probably due to the longer spatial baseline. Phase display is 6π per color cycle.

The two images show very significant differences and, in comparison to the Int.1 pairs, the relief is much less well reproduced. This is especially the case for Int.2 2010 (right), where virtual no topography is represented by the fringes, while in Int.2 2009 (left), the relief can still be identified. Upon closer examination, it becomes clear that it is in fact the topography which is much more visible in Int.2 2009 and represented by the fringes, that creates this big difference in the appearance of the two images. Considering the spatial baselines of the two image pairs, this is a very interesting outcome: It amounts to less than a meter in the case of Int.2 2010, but to more than 100 m in Int.2 2009 - the longer the baseline, the more dominant is the topography component in the interferogram, which is impressively demonstrated by means of these interferograms. Because the final differential interferogram results from the subtraction of Int.1 from Int.2, in general less displacement and more homogeneity is expected from the outcomes of the differential interferograms calculated with Int.2, which has a longer spatial baseline. Additionally, a leveling should be visible, as the topography is more or less excluded.

A further fact that should be considered at this point, are the artifacts in the upper right corner of Int.2 2010 that can probably be attributed to atmospheric noise, and which makes this area unusable for further interpretation.

For the construction of the differential interferograms, the flat Earth, which was subtracted earlier for the unwrapping, was added back to the images.

With the four unwrapped but flattened interferograms, the differential interferograms could be computed without further problems.

In order to improve the outcomes and to get an estimate about the correctness and significance of the differential products, the movement of the Cuesta pixels was examined and compared to the expected

uplift in the region. According to the literature (LAVOIE 2008), this amounts to 1 cm/year and thus amount to 0.3 – 0.7 cm during the 4 1/2 month time period being examined (beginning of May – mid of August). It has to be clarified that these movements are non-linear processes, and fast uplift within only few months is as possible as hardly any change, but subsidence of this area is virtually impossible.

By defining a subset including only Cuesta pixels and the investigation of their movements (Figure 7.33), it should be proven if such rebound is represented. The outcomes show a vertical displacement of +4.62 cm for Diff2.2009, and delivered very persuasive results, with +0.63 cm, in the case of Diff2.2010.

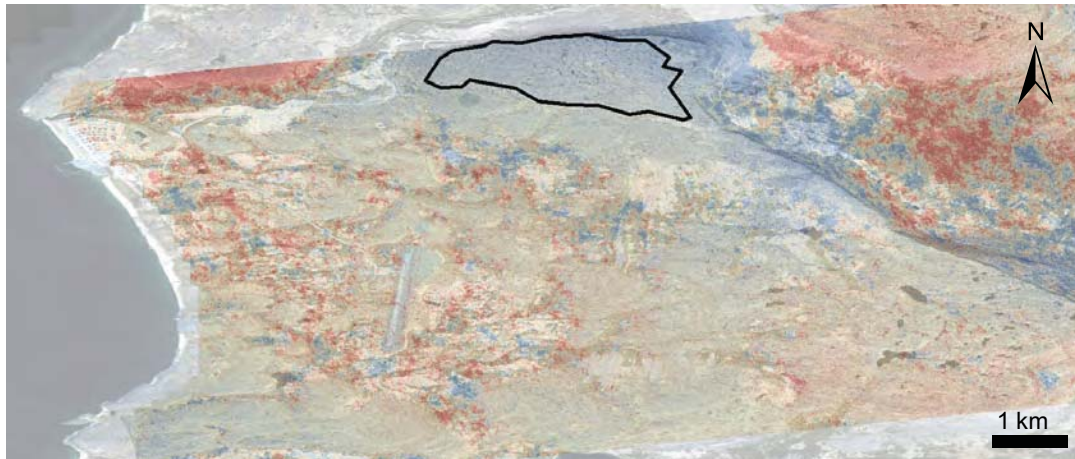


Figure 7.33: Diff.2 2009 with an IKONOS image in the background. The area outlined in black represents the Cuesta subset. The strange looking bend on the east side is a result of a small pond on the Cuestas that should not be included in the subset.

With the newly gained certainty that the general trend is correctly reproduced in the differential interferograms, deeper analysis of the movements can follow.

As the most essential research question was to explore the feasibility of detecting small-scale topographic movements, the main focus was on the three lithalsas close to Umiujaq, which were already study sites for d-GPS surveys. But before analyzing these movements, the postglacial uplift inherent in all pixels needed to be subtracted from the pixel values, in order to solely have the elevation changes caused by thawing and freezing processes. This ‘cleaning’ of the data was adopted for every differential interferogram using the value averaged over the Cuesta subset. Once this was done, and the pixel contained only the absolute values representing movements independent of the general uplift, the interpretation could be started:

First of all it should be noted that in contrast to the Cuesta area, a general downward trend is obvious and the average calculated vertical movements for every single lithalsa was – 1.16 cm (R), -2.37 cm (M) and -1.12 cm (I) in 2009, and -2.67 (R), -2.87 (M) and -2.80 (I) in 2010. See Table 7.12 at the end of this chapter). Even without further interpretation, this is a quite satisfying outcome as it indicates that the lithalsas are areas experiencing subsidence during the thaw period. This corroborates the hypothesis of the seasonal pulsating of the lithalsas – and even more importantly: these movements are detectable by means of differential interferometry.

A comparison of the results of the lithalsas depicts I as the overall most active one in both years, followed by R and M. It is remarkable that the movements between the lithalsas differ much more in

2009 (difference = 1.2 cm) than in 2010, when all the three lithalsas experience subsidence in the range of – 2.67 cm and -2.87 cm.

Figure 7.34 shows an example of the outcomes between spring 2010 and summer 2010, where lilac pixels indicate uplift and green indicates subsidence. Clearly visible is the fact that the area covered by the lithalsas shows almost only green pixels, whereas the surroundings appear in lilac.

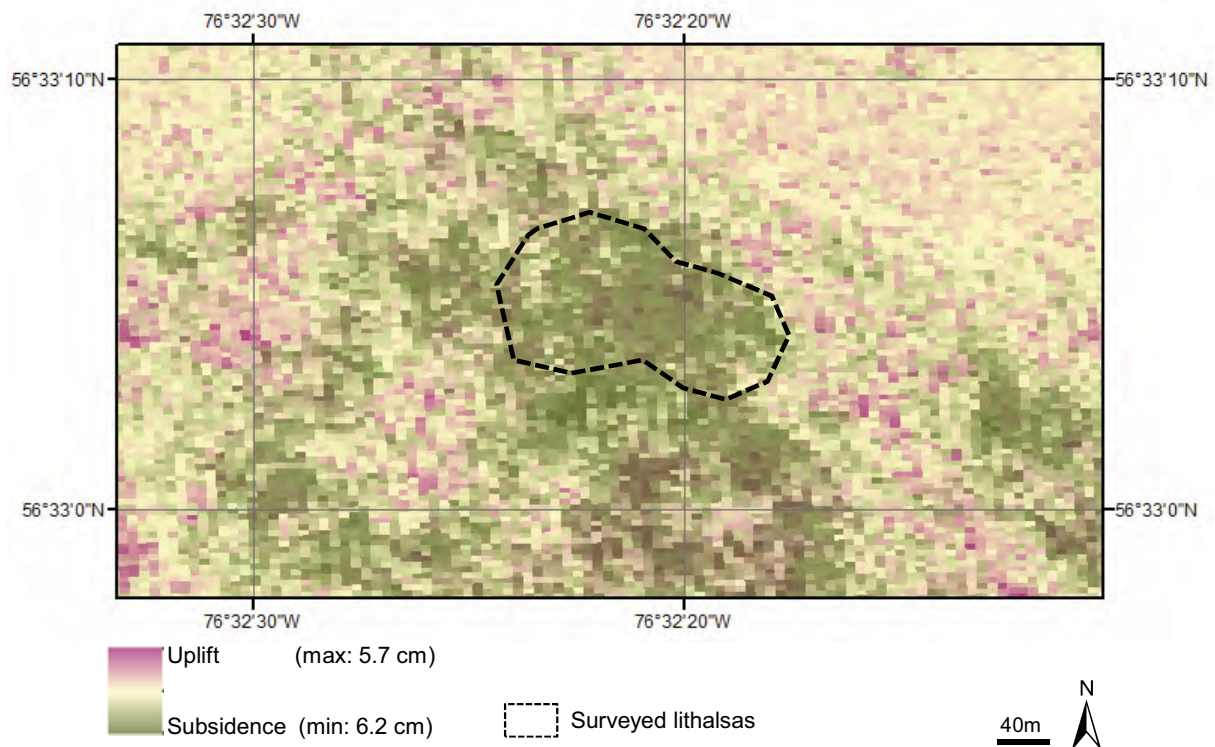


Figure 7.34: Diff2.2010 (cleaned) vertical displacement map embedded in ArcGIS. Green areas experienced subsidence, while lilac areas experienced uplift.

For 2009, similar trends are observed, although slightly less prominent and more variable. This is also already reflected in the lithalsa means, presented above. According to these findings, it appears as if the movements of the lithalsas are more pronounced in 2010 than in 2009.

The next analysis step is the comparison of single sample points distributed over the three lithalsas, using six points per lithalsa, preferably from different vegetation classes. They are called R1-6 for lithalsa R, M1-6 for lithalsa M, and I1-6 for lithalsa I; their location is mapped in Figure 7.35, and the numbers are listed in Table 7.12 together with the results of Diff.3 2009 and 2010 further below.

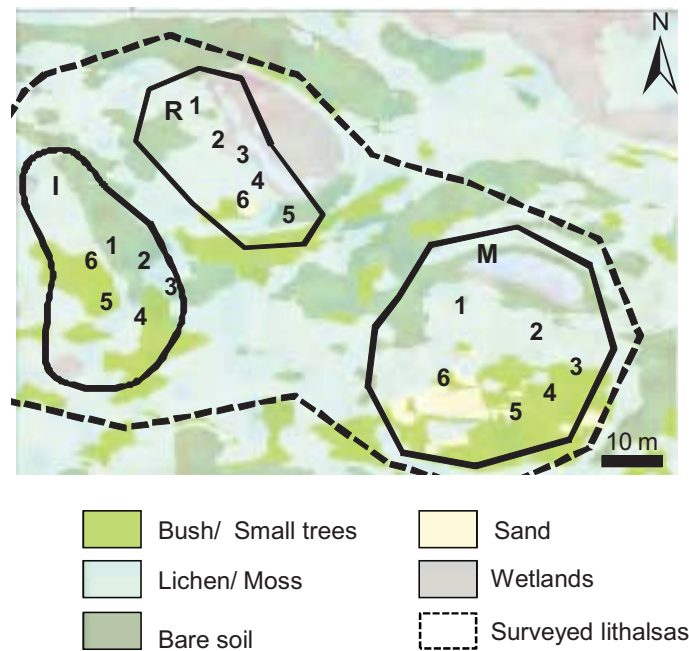


Figure 7.35: Location of the sampling points for the analysis, in the background the classification map based on the GeoEye image of 2009

The values from 2010 show a decrease for all 18 sampling points, but Diff.2 2009 reveals that although there is a general downward trend, there is one point on M and four points on I where uplift occurred. However, the amount of uplift is very low in the case of M (+0.21 cm), as well as at two points at I. In contrast, the uplift at I3 and I4 is surprisingly high, at more than +2.0 cm.

The heterogeneity in the 2009 image is again reflected in the movement of the sample points: the difference between least and highest motion for all the 18 sampled pixels in 2009 is 5.89 cm, while in 2010 it is only 2.17 cm.

Distinguished by lithalsa, the values are as follows:

- R: 2.47 cm in 2009; 1.44 cm in 2010
- M: 3.16 cm in 2009; 1.05 cm in 2010
- I: 5.03 cm in 2009; 1.52 cm in 2010

Furthermore, it should be noted that lithalsa I experiences the highest variability between points in both 2009 and 2010.

A close comparison of each point over the two years reveals no significant correlation in the magnitude of their movement. So for instance the point where the most uplift occurred in 2009 does not correspond to the one where it occurred in 2010. Still, it is remarkable that point I4, which had the greatest uplift in 2009, showed the greatest decrease of all the I points in 2010.

Besides this detailed look at the lithalsas, it should also be mentioned that areas with dense vegetation and those close to the river are marked by downwards movements. In most cases, these of course correspond to the areas excluded from the interpretation process earlier because of the low coherence values, but some aspects of them should still be considered. This phenomenon will be discussed in the conclusion and comparison part of this chapter.

If a statistical analysis of the entire scene over the two years shows that more variability exists between the most negative and positive values in Diff2.2010. This finding would confirm the initial belief that a short baseline is better for reproducing the displacement. With respect to the lithalsas, the fact that the 2009 product shows more heterogeneity, gives rise to the idea that even more movement happened in 2009 at these particular frost mounds. Presuming that no other factors influenced the outcomes, this would mean that more permafrost activity took place during May and August 2009 than in 2010. However, since the mean values show more subsidence in 2010, a reason must be found for the more unequal motion of the different points. The Environment Canada climate record shows much warmer temperatures in May and even in April 2010, which could signal an earlier thaw and therefore a more evened status in 2010. This is very likely the reason for the greater heterogeneity in 2009.

Differential Interferograms: Summer and Fall (Diff3.2009; Diff4.2009; Diff3.2010; Diff4. 2010)

The generation of Diff3 and Diff4 was a smoother process with fewer complications since it was not as influenced by a long temporal baseline. It should be remembered at this point that there is no Diff3 for 2010 because the ordered data for this date could not be delivered due to technical problems.

The coregistration was successfully applied for all Int.2 (Table 7.12) and the generation of the interferogram was also problem-free. Nevertheless, it was important to ensure that at least the area of interest (cuestas and lithalsas) showed adequate coherence values for the unwrapping process. Consultation of the coherence map did indeed show these areas to be valid.

The baseline estimate gave fairly promising perpendicular components for Int.2 October 2009 with only 12.77 m. Unfortunately, the baselines for Int.2 September 2009 and Int.2 October 2010 did not have optimal conditions, with spatial baselines measuring -96.52 m and -195.41 m, respectively. Figure 7.36 displays the three Int.2 pairs, and it is again very significant how the image pairs with the long spatial baselines reflect the topography. In Int.2 October 2009, there is also an artifact detectable in the upper right corner, as well as around the village, that needs to be interpreted further.

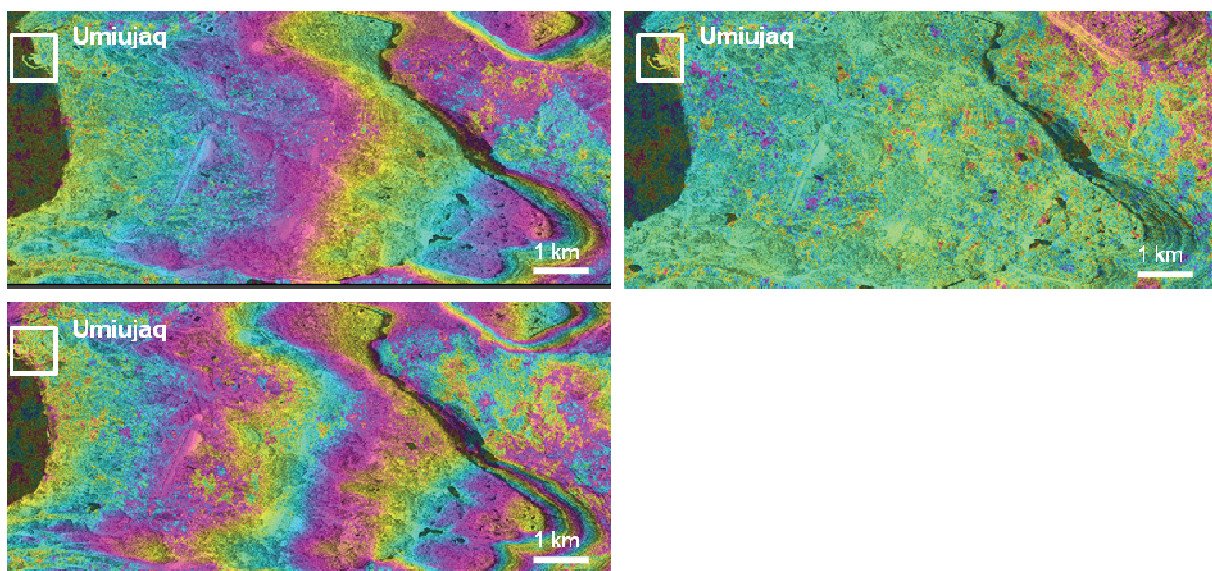


Figure 7.36: Unwrapped and flattened Int.2 September (left), Int.2 October 2009 (middle) and Int.2 October 2010 (right); Phase display is 6π per color cycle

As with the analysis of the Diff2 products, the first step was the validation of the outcomes by means of the Cuesta subset. Again, they were able to reproduce the expected uplift, with values of +0.04 cm (Diff3.2009), + 2.03 cm (Diff4.2009) and +1.20 cm (Diff4.2010). It should be noted that Diff3.2009 only represents a time period of one month.

In terms of the lithalsas, not much change is expected for this timeframe: The thaw period is more or less over in September, and the freezing has only just started in October.

And indeed, very little elevation change is observed: Diff3.2009 shows -0.07 cm for R, -0.07 for M and -0.22 cm for I. In Diff4.2009, which includes an acquisition obtained one month later, uplift is detectable for R and M (+1.06 cm and +0.14 cm) but I still shows subsidence (-1.26 cm). The same can be seen in Diff4.2010: two lithalsas (M and I) show subsidence of -0.39 cm and -0.69 cm, respectively, but R experienced little change (-0.09 cm). The positive values could be an indicator of initial frost heave and, since the Environment Canada climate station observed a longer frost period in mid-October 2009 and 2010, this is very likely. In addition, daily values just above 0 °C suggest the possibility of frost during the night. With regards to Diff3.2009, the only time there were temperatures below zero prior to the acquisition was on September 25th.

An appraisal of the single points, however, shows several points already heaving by the September date; yet, based on air temperatures, this cannot be attributed to frost heave. The climate data, however, offers another clue for this uplift: 106.3 cm of precipitation were recorded during September 2009 alone. This amount of water could definitely evoke a swelling of the soil and, consequently, appear as uplift in the images.

Inspecting Diff3.2009 further, it is significant that all the M samples show upwards trends. Except for R1, all points on R are decreasing, but the changes are minor and are all below 1 cm. With respect to the differences between samples, it is again I that shows the most variance, with 2.76 cm.

Diff4.2009, in contrast, shows very stable conditions for the six sample points. It appears that all the 18 selected points experienced uplift, and therefore serves to confirm the upward trend of the lithalsas' mean. Very low movements are seen, with all values close to, or below 1 cm. In any case, it is interesting to note that the sample experiencing the most uplift corresponds to the only point on R (R1) where an increase could be seen in the Diff3.2009 image. This may be due to its location on very sandy ground, free of lichens or moss –in contrast to all other points – and it is very likely that the thermal regime of such ground reacts much more quickly to temperature changes than it would in more vegetated areas.

For the samples of the last differential interferogram, Diff4.2010, uplift and subsidence are more or less equally distributed, but again most of the uplift occurs on R. However, the average value of heave is slightly higher than that of subsidence. Analogous to almost all the other differential products, most of the variability between the single points again occurs on I (2.86 cm difference). The only exception is Diff4.2009 where R has the highest numbers.

It is also of note that, besides the Cuestas and the lithalsas, striking areas with high subsidence crop up again as sagging spots in Diff3.2009 and Diff4.2010. This is particularly significant for the eastern zone and around the river in the north.

Although it is more difficult to compare these three images due to their different acquisition dates, it is still interesting to note that Diff4.2009, having the smallest spatial baseline, is the one with the highest standard deviation (1.4 cm, compared to 0.8 cm for Diff3.2009 and 1.1 cm Diff4.2010) and thereby again reinforces the influence of the baseline.

Table 7.12: Vertical displacement in cm in for all five of the computed differential interferograms, the cuesta subset, and the three lithalsas R, M and I (The movements of the lithalsas do not include the cuesta uplift).

	Diff2.2009	Diff2.2010	Diff3.2009	Diff4.2009	Diff4.2010
Cuesta	+ 4.62	+ 0.63	+ 0.04	+ 2.03	+ 1.12
R	- 1.12	- 2.67	+ 0.07	+ 0.09	+ 0.12
M	- 2.37	- 2.08	+ 0.07	+ 0.14	- 0.39
I	- 1.16	- 2.80	+ 0.22	- 0.07	- 1.26

Based on the observed outcomes, differential interferometry shows itself to be a possible tool for monitoring permafrost dynamics and for reproducing elevation changes caused by thawing and freezing.

Interannual differential interferogram

In addition to the inter-seasonal differential interferograms, an attempt was made to generate a differential interferogram between the two summers. Once again, 14.08.09 served as master and was combined with the later August acquisition (25.08.09) Int.1, whereas 14.08.09 and 12.08.09 were combined to Int.2. Coregistration and resampling achieved a standard deviation of 0.1033 in range and 0.0955 in the azimuth direction. Despite the long temporal baseline, the coherences were still adequate:

- Cuesta subset: 0.68
- Lithalsa R: 0.48
- Lithalsa M: 0.43
- Lithalsa I: 0.43

The computed Int.2 is mapped in Figure 7.37 and it is obvious that it reflects the relief quite well, similarly to the interferometric pairs with a long spatial baseline shown above; this is especially visible at the steep sides of the mountains. And indeed, the baseline estimate is 191.61 m.

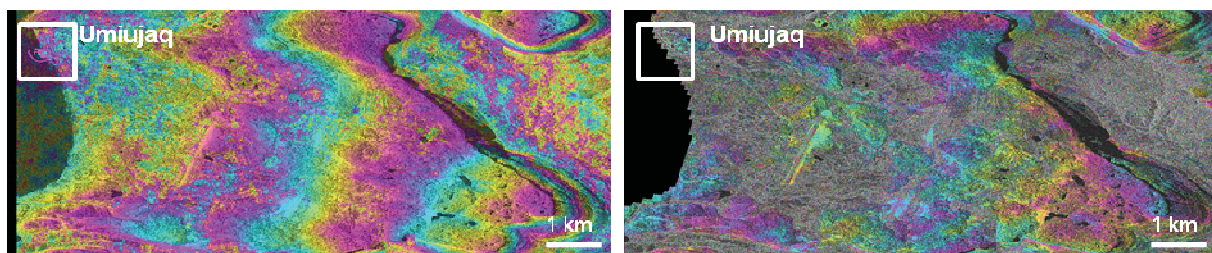


Figure 7.37: Left: Unwrapped and flattened Int.2 for the interannual differential interferogram; one fringe equals one cm; Right: The final vertical displacement map; one fringe equals one cm displacement.

The validity of the differential product was once again first proved by calculating the average uplift of the cuesta subset. The result amounts to +1.7 cm, which is a fairly good outcome for a one year time step.

The elevation difference of the lithalsas between the two years was computed to a slightly negative numbers that stands for a shrinking. This worked out to -2.0 cm for R, + 0.47 cm for R and -0.94 cm for I. This observation is important in that, if this trend were to continue in subsequent years, it would be a clear indicator of permafrost degradation.

Concerning the outcomes using the complex interferogram combination did not deliver the expected results. Nevertheless this method shall not be excluded as good alternative if no DEM exists, but would need more and detailed investigation in order to achieve satisfying results.

7.2.5 Discussion

The goal of this section is to summarize the presented findings and to offer an overview and comparison of the explanations already suggested. At the end, some ideas of potential error sources as well as their possible solutions are presented.

Beginning with the outcomes, Table 7.13 provides a summary of the different discussed parameters for all the images and Figure 7.39 illustrates the combinations of temporal and spatial baselines.

Table 7.13: Overview of the outcomes from all calculated image pairs, including coregistration accuracy, starting points and their coherences for the unwrap process, and both components of the spatial baseline.

Interferogram	Coregistration		Starting point phase unwrapping		Spatial baseline	
	Range	Azimuth	Pixel	Coherence	Perpendicular	Parallel
14.08.09/ 04.04.09	-	-	-			
14.08.09/ 07.05.09	0.0367	0.1417				
14.08.09/ 25.08.09	0.0439	0.0933	2542/ 878	0.9166	-66.7859	-86.9788
14.08.09/ 27.09.09	0.0578	0.0764	1709/ 1013	0.9599	-96.5181	-88.644
14.08.09/ 30.10.09	0.0900	0.1627	1644/ 1284	0.9593	12.7703	-5.2311
12.08.10/ 22.03.10	0.8228	0.6396	-	-	-188.2236	-113.4101
12.08.10/ 05.05.10	0.0766	0.1389	2247/ 1711	0.9218	0.4289	-1.2816
12.08.10/ 23.08.10	0.0197	0.0700	2108/ 1711	0.9780	-159.0029	-123.9595
12.08.10/ 28.10.10	0.0599	0.1285	3424/ 374	0.9309	-195.4077	-130.4253
14.08.09/ 12.08.10	0.1033	0.0955	1595/ 637	0.9590	191.61	102.38

The first essential finding of the study was the proof that an accurate reproduction of the general trend of elevation change is actually feasible by means of differential interferometry: All the images show the postglacial rebound, validated by means of the stable Cuestas.

Furthermore, in all the outcomes, the pixels representing the lithalsas experienced subsidence during the spring and summer acquisition, as hypothesized, and much less movement during the fall period, although a slight heaving trend was seen.

By comparing the various differential interferograms, it becomes clear that the length of the spatial baseline in the Int.2 pairs has an obvious impact on the values of the outcomes that should not be underestimated. This is caused by the fact that a short baseline is more sensitive to the displacement component.

With regards to the different lithalsas, it is remarkable that, according to the differential interferograms, it is lithalsa I that shows the highest variability, but that no additional trend of the individual points could be discerned.

There is still a need to discuss the zones with dense vegetation in the eastern part and near the river in the north that represent subsidence in all pictures. The movements are most pronounced in the differential interferograms of the spring period, but with the exception of Diff4.2009, they always appear. It is very likely that the reasons for these movements are not the same in the spring as they are in the fall. In spring, this might be attributed to the remaining snow cover in these regions (Figure 7.38), where the vegetation results in more accumulation and therefore a delayed melt. In addition the snow crust could influence the radar signal in particular by using the VV polarization which is the case in this study. A rough snow crust, as occurring in the test site at this date, would possibly increase the radar signal and hence even enhance the described effect (KENDRA ET AL. 1998; SHI & DOZIER 2000). In the reference image for August, the snow disappears and consequently the elevation appears to be lower. This idea can be corroborated by the fact that in small depressions (Figure 7.38), where the snow also stays longer, subsidence can be detected in the spring outcomes.



Figure 7.38: Remaining snow patches in May (07.05.2010). The snow stays until May only in depressions and where dense vegetation causes snow accumulation. (Photo I. May).

For the fall images, the explanation might be the vegetation itself: During August the trees and bushes have reached their maximum growth and, to a certain extent, hinder the radar signal from reaching the ground surface. Later in the year, in September and October, when the vegetation has lost some of its volume the signal can penetrate further and consequently indicates subsidence in the differential interferograms.

Although the general trends of all the presented outcomes are very reasonable, as are the actual values in the most cases, possible errors remaining in the images need to be considered. According to HANSEN (2001) errors are mainly caused by decorrelation attributed to different incident angles or different Doppler centroids, both of which are unlikely in this case since the exact same acquisition parameters were used. Therefore, any errors are more probably due to different volume scattering caused by penetration of the radar wave into the observed medium, or atmospheric distortion of the signal. Because of the very small wavelength, the atmospheric impact is much more probable and should be the first factor to be addressed. There are basically two different approaches for doing so. One is the so-called 'stacking' of interferograms. In this method, several interferograms are 'stacked' to estimate the linear rate of the differential phase, so as to later remove the uncorrelated atmospheric phase components (GAMMA 2008). Unfortunately, in order to apply this method, many more interferograms from one time period would have been necessary. Additionally, it is based on the assumption that atmospheric statistics are stationary from one acquisition to the next, which is very unlikely in the region.

This is why none of the atmospheric correction processes could be implemented for this study. Nevertheless, for on-going research in this field it is strongly recommended to work with more datasets in order to enable interferogram stacking, especially in view of the new possibilities offered by the TanDEM-X satellite which can provide many more records during a shorter time period.

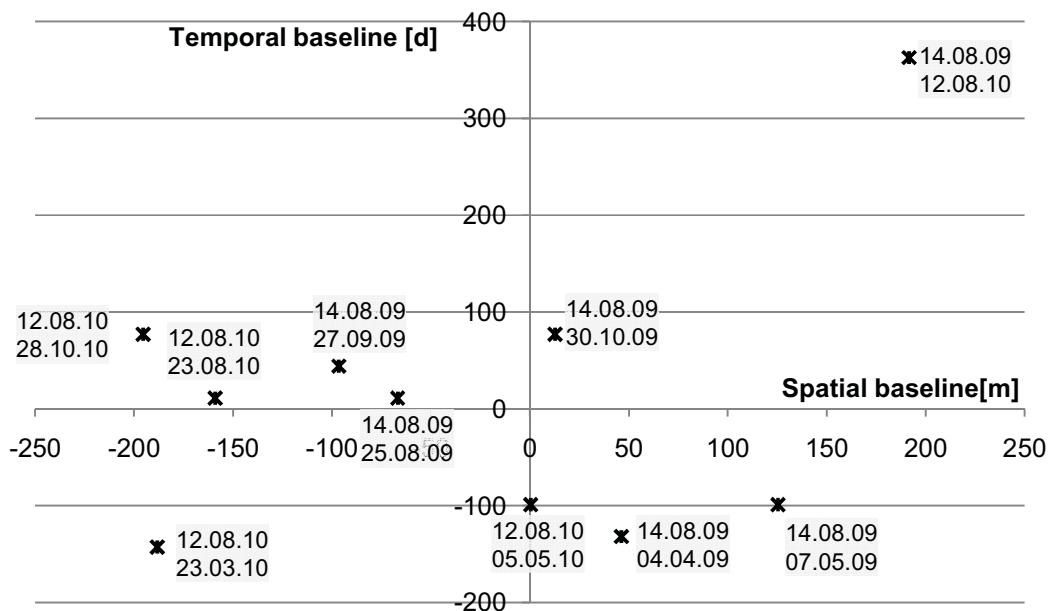


Figure 7.39: Combination of spatial and temporal baselines for the different image pairs.

7.2.6 Comparison of differential interferometry and the field data

This chapter deals with the comparison of the vertical movements, surveyed with the d-GPS, and those observed in the differential interferograms.

Table 7.14 provides an overview of the calculated differences for each lithalsa for the time period May 2010 – August 2010.

Table 7.14: Calculated differences [cm] between May 2010 and August 2010 for the three lithalsas based on the d-GPS and on the D-InSAR outcomes

	Difference [cm] May 2010 – August 2010	
Lithalsa	D-GPS	D- InSAR
R	-14.1	-2.67
M	-13.8	-2.08
I	-104.7	-2.80

Most striking are the high values recorded with the d-GPS, which are almost ten times higher than those observed in the differential interferograms. This discrepancy will be discussed later in this chapter. Besides this difference in quantity, it can be seen that the measured trends are similar for both applied methods: the d-GPS outcomes as well as those obtained by D-InSAR both reflect a downward trend during the spring, and more or less steady conditions between summer and fall.

In order to carry out assessments about the similarity of each lithalsa and single sample points, the values of the pixels that correspond to the surveyed points has been extracted from the differential products. This was done for each differential interferogram (Diff2.2009, Diff2.2010, Diff3.2009, Diff4.2009, Diff4.2010) and the outcomes are listed in Appendix 8. However a comparison with the d-GPS measurements is only possible for Diff2.2010 and Diff4.2010 (Diff4.2010 only for lithalsa I), as there are unfortunately no d-GPS measurements for the other periods. The analysis shows that with both techniques, lithalsa I is highlighted as the one that moves the most, as well as the one that shows highest variability between the points, whereas R and M are disclosing more or less similar behavior.

The lithalsas were treated separately for a more detailed investigation. Their average movements were computed using both methods. All samples showing higher/lower values than the average were then compared. In doing so, a very high concordance emerged for lithalsa R, as well as for lithalsa M. In these cases, all but one point with numbers above the d-GPS average conforms to those of the d-InSAR average and vice versa (Figure 7.40 and Figure 7.41).

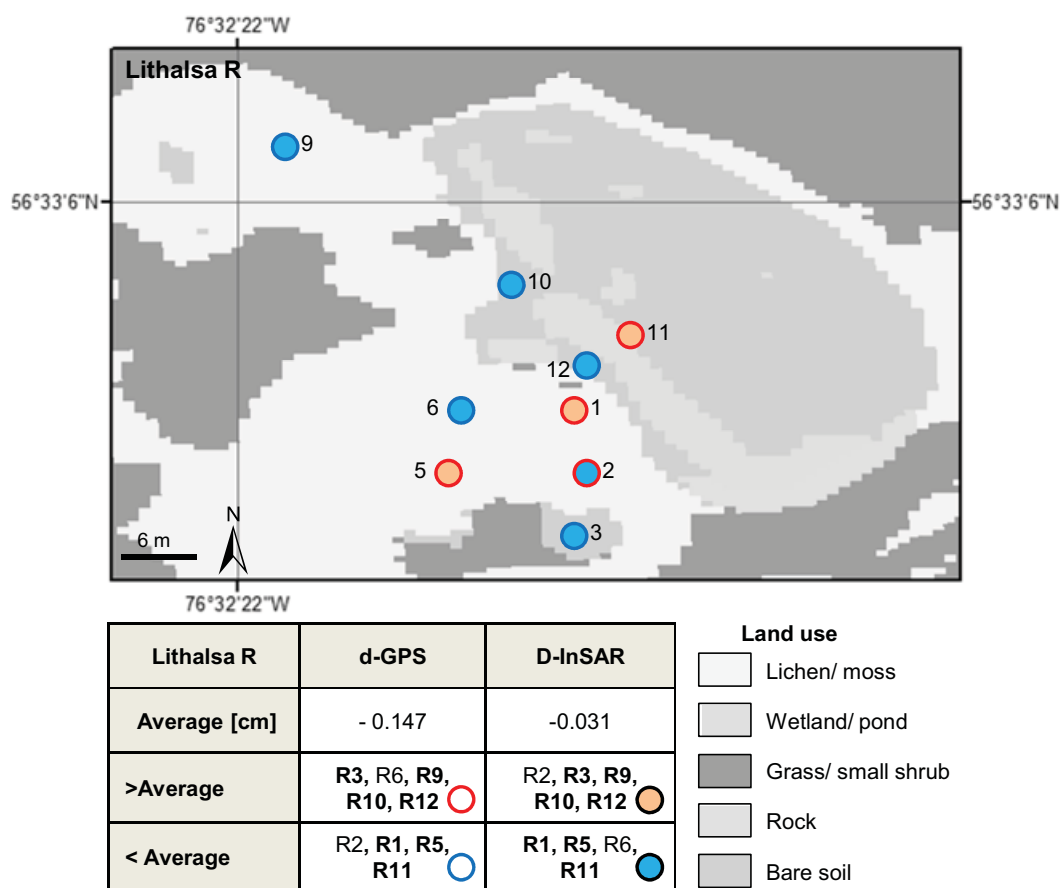


Figure 7.40: Comparison of the d-GPS measurements and the D-InSAR data for the time period May 2010 and August 2010 for the sample points on lithalsa R. All points having the same inside and outside color show similar results.

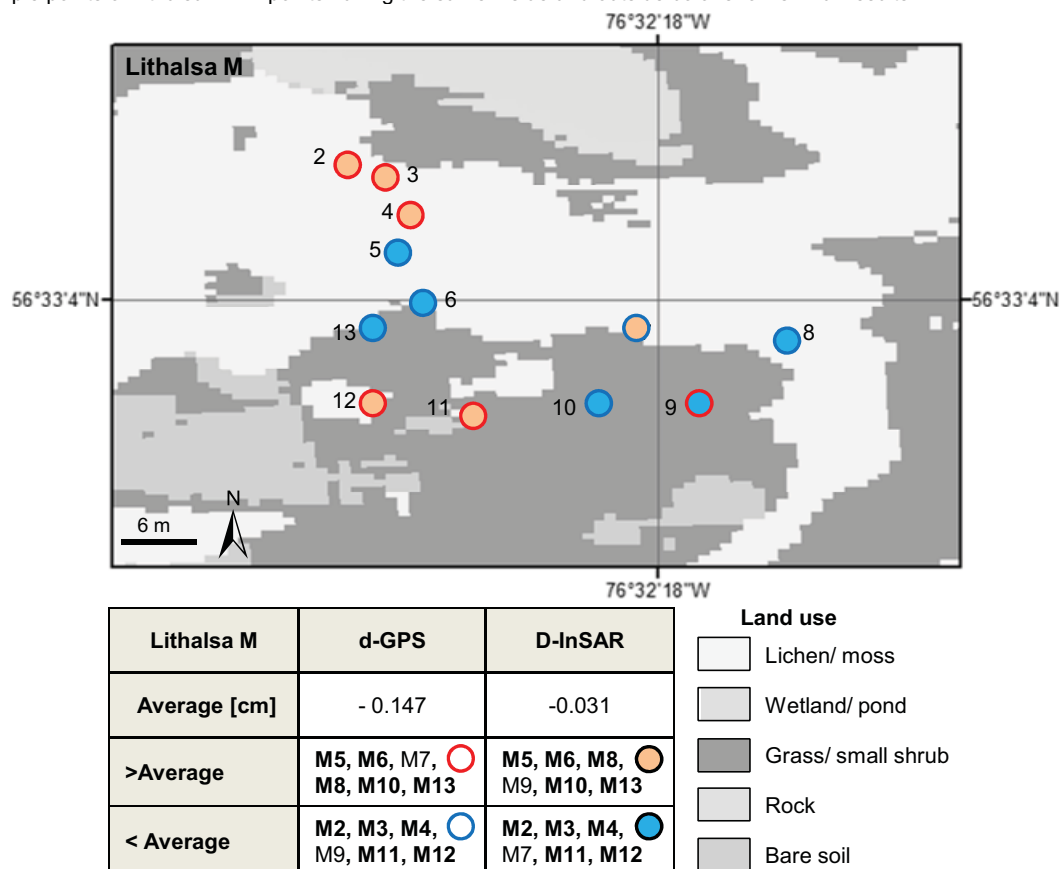


Figure 7.41: Comparison of the d-GPS measurements and the D-InSAR data for the time period May 2010 and August 2010 for the sample points on lithalsa M. All points having the same inside and outside color show similar results.

Although there is no such conformity for lithalsa I on Diff2.2010, at least 4 out of 6 points for Diff4.2010 show similar results. Regarding lithalsa I and Diff2.2010, it should be noted that there are many samples whose values are close to the average, therefore taking the mean as a threshold leads to the apparently poor correspondence. Thus, in this case, the 6 samples closest to the mean were compared, which allows for a more meaningful assessment in terms of similarity, and also depicts higher accordance (Figure 7.42).

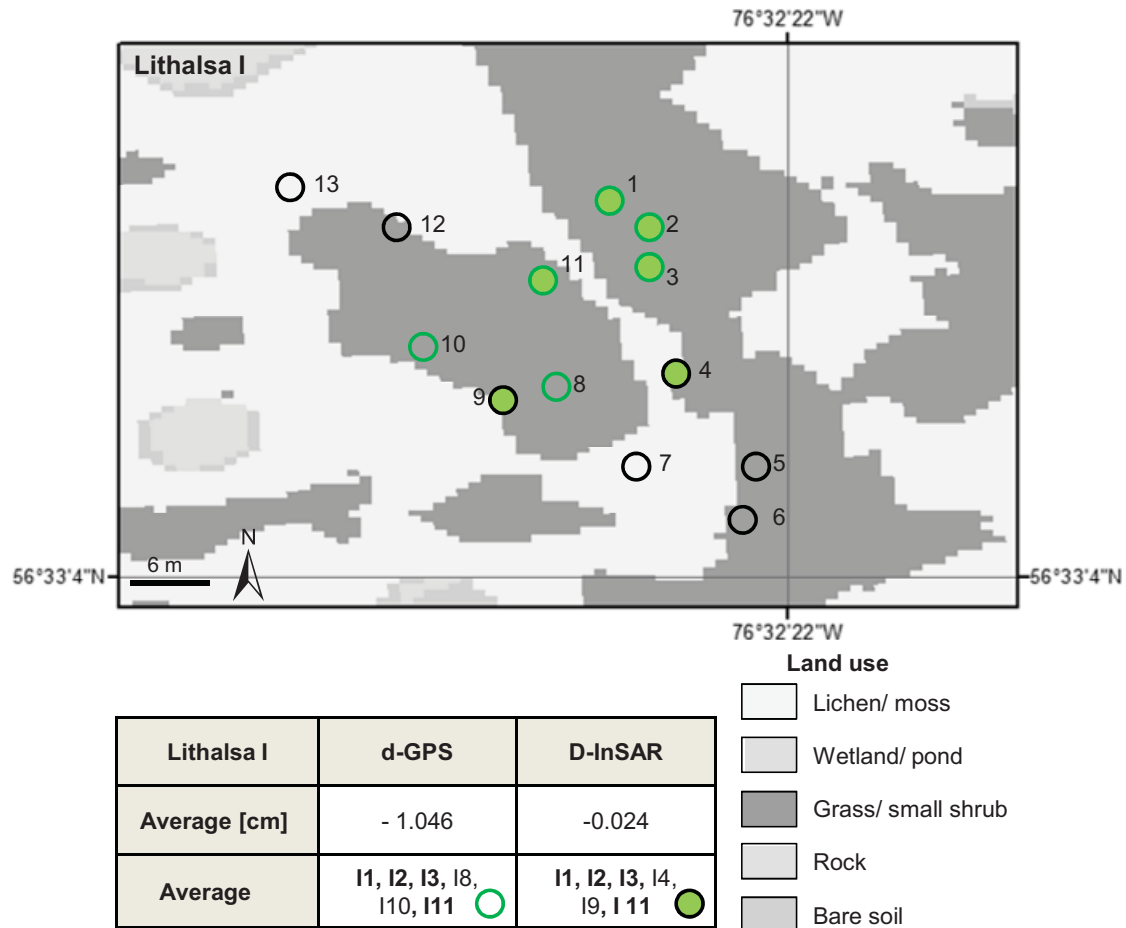


Figure 7.42: Comparison of the d-GPS measurements and the D-InSAR data for the time period May 2010 and August 2010 for the sample points on lithalsa I. All points having the same inside and outside color show similar results.

A further interesting outcome is that R 3, which shows the least movement as monitored by the d-GPS, is also the least active in the differential interferograms. This is not the case for the more active ones, which are I 4 and I 5 for the d-GPS, and I 7 and M 7 for the D-InSAR.

Although this accordance is satisfying in terms of the general trends and magnitudes, the big difference in quantity still needs to be explained. A number of well-known and widely understood errors in differential interferometry images, presented by LI AND GOLDSTEIN (1990), include errors resulting from the atmosphere or phase errors due to signal-to-noise ratios, number of looks, incorrect pixel registration, and baseline decorrelation. Furthermore, different soil moisture or changing soil cover could affect the signal and lead to misinterpretation (MIRNOVO ET AL. 2006). However in this case, the question arises as to whether or not the d-GPS may have overestimated the movement, since the outcomes in the displacement maps seem to be much more reasonable, especially as they reflect the isostatic uplift very accurately.

To answer this question, the GPS data as well as the GNSS-Solution support were consulted, yielding the following as a possible error source: The problem with the d-GPS measurements is the lack of reference stations in this remote area. This problem was thought to be solved by the use of the Canadian Spatial Reference System (CSRS) that should deliver accurate correction of the recorded coordinates. This system computes 'new' coordinates only by means of the code phase, inherent in the recorded data. This processing technique gathers data via a coarse acquisition code receiver, which uses the information contained in the satellite signals to estimate positions. Following differential correction, this method provides 1 – 5 meter accuracy (TRIMBLE 2010). For this study, this means that the coordinates used for the base station only reflect the exact position to an accuracy of several meters. Such a deviation could definitely be responsible for the questionable outcomes.

In order to improve the measurements, it would be necessary to use the carrier phase for the processing. This method collects the data via a carrier phase receiver, which uses the radio signal to calculate positions. This signal has a much higher frequency than the code phase and is more accurate than using only the code. Processing results to sub-meter accuracy can be achieved (TRIMBLE 2010). The use of this method would have required the additional record of the carrier phase, which is only possible if a real time kinematic (RTK) survey is available. To do so, the d-GPS would have need to be equipped with a RTK receiver. As such devices are very costly, it was not possible to purchase one, and thus no enhancement could be achieved.

8 Conclusion and Outlook

By means of the *in-situ* measurements in the field, indicators were identified that represent changes in the permafrost and can hence serve as proxies to estimate its behavior and dynamics. These indicators are: changes in the vegetation cover; the occurrence of snow cover; and altering topography.

These indicators all meet the essential presumption to be visible at the land surface. This allowed for observation by satellite imagery, which was investigated and proved within this study by numerous remote sensing techniques.

This investigation shows that a clear relation exists between changes in the state of the permafrost and the occurring land cover. The expansion of wetlands, the degradation of frost mounds and the spread of forest are all brought along by the decline of the frozen ground. The strong relation between the development of thermokarst ponds and the decrease and collapse of frost mounds was already studied by some other research teams, but was confirmed with this analysis.

The coexistence of changes in the vegetation cover and changes in the permafrost was stated, and although the primary driving factor could not clearly be identified, the appraisal itself is sufficient enough to deliver the required information content for the interpretation of satellite images.

The impacts of snow cover parameters on the vegetation and on the active layer deepness were also investigated. It was determined that higher snow depths usually caused warmer ground temperatures, but that this isolating effect seemed to reach its peak at a height of approximately 150 cm. A dependency of the vegetation structure and the snow depth could also be determined, indicating that it was not the tallest and most bushy plants that were accumulating most of the snow, but smaller bushes between 50 and 100 cm in height.

Furthermore, geodetical surveys of lithalsas by means of d-GPS indicated seasonal vertical movements of such frost mounds. Higher elevations were measured during the winter periods, whereas lower elevations were recorded during the summer. It appears that depending on the outside temperature, freezing or thawing processes were evoked that caused either an upward or a downward trend of the mounds' surface. Although this trend could be successfully proven with this method, the measured quantities appear to be questionably high. This can very likely be explained by the missing information of the so-called carrier phase, which would be necessary to guarantee cm elevation accuracy of the d-GPS measurements in remote areas like the test site. Due to high cost of the device required to obtain such information, an improvement of the data was unfortunately not possible.

By combining all these outcomes based on the field measurements, an elaborate knowledge system on visible features at the land surface linked to the underlying permafrost was built that can serve as interpretation basis to detect and monitor permafrost dynamics from space.

A strong focus of this thesis was the exploration of available data and tools to determine the extent to which the interpretation of satellite imagery is feasible to detect alterations in permafrost and to fathom out the most convenient combination of datasets and interpretation methods. Scenes from five optical sensors on-board of Landsat, ASTER, QuickBird, Ikonos and GeoEye were used for change detection methods. The results were subsequently interpreted, compared and validated. In addition, inter-seasonal differential interferograms based on radar imagery acquired by the TerraSAR-X sensor, were generated to discover the possibilities to observe elevation changes.

The investigation displayed the possibilities and limits of the application of satellite images and clearly highlighted the high resolution of data of QuickBird, IKONOS and GeoEye as very useful for such changing analysis, but indicated that the lower resolution of images from the Landsat satellite as well as from ASTER were less suited. These low-resolution images are particularly not useful when observing small-scale targets such as thermokarst features and lithalsas. Nevertheless, this imagery is still useful for the spatial detection of vegetation changes over a broader area and serves to give a good overview of the situation.

Considering the different applied change detection methods, no general most fitting method could be recommended, but is strongly depending on the image resolution and the desired outcomes. Nevertheless, for the five approaches investigated - postclassification, write function memory insertion, cross-correlation, index differencing, and tasseled-cap transformation - the first three delivered the most adequate results. With the index differencing method outcomes, the NDVI (normalized differential vegetation index) were useful, but the application of the NDWI failed. Also the outcomes using the tasseled-cap transformation are very poor and hence its inclusion in a monitoring system is not recommended.

The selection of the scenes from the optical sensor also presented the common problem with using optical imagery: several acquisitions that might have been useful to get a better estimate about temporal changes were covered by clouds and had to be partially or completely excluded from the interpretation process.

The generation of differential interferograms and the deduced vertical displacement maps was a new and innovative process. The application on such a small-scale (3 x 3 m) using TerraSAR-X data has never been attempted before to detect vertical elevation changes in high latitudes. Hence preliminary analysis of the data and the different process possibilities was necessary. The first important finding was the identification of the most convenient acquisition modes, which highlighted the ascending path in the VV polarization, capturing the scene with a maximum incident angle of 40.08° and a minimum incident angle of 41.21° . The selection for these characteristics was based on the analysis of coherence values in the interferograms that represent the most crucial factor for the successful creation of differential interferograms. In terms of the processing method, the 3-Pass interferometry evolved to deliver best results.

Six differential interferograms were computed in total: three for 2009, two for 2010 and one between summer 2009 and 2010. The outcomes were successfully validated by means of a stable area (the Cuestas) and are very satisfying and promising in terms of the reproduction of the land surface deformation processes. Pixels representing lithalsas displayed subsidence during the thawing period (spring/summer differential interferograms = Diff2.2009 and Diff2.2010), almost no change during a one month period in summer (Diff3.2009) and some slight heave in the summer/fall interferograms (Diff4.2009 and Diff4.2010). The outcomes also presented very reasonable values with regard to the quantities.

Another interesting finding of the analysis was an obvious impact of the spatial baselines on the interferograms. This was particularly visible in the interferogram containing the displacement of spring in 2009 (=Int2.2009), where a very long baseline (125.361 m) effect displayed the deformation in a negative way.

Apart from the consideration of the lithalsa area, this study attempted to explain the incidence in the rest of the images where denser vegetation occurred in particular zones that were displaying subsidence in all differential interferograms. The assumption was made that different explanations have to be found for the spring and fall products. In spring, the subsidence has to be attributed to the still remaining snow cover in the respective regions, where the vegetation causes more accumulation and hence a delayed melting. In fall, the explanation might be the vegetation itself, because the trees and bushes have reached their maximum in phenology in August and hinder to a certain amount the radar signal to penetrate until the ground. Later in the year, in September and October, the trees and bushes have already lost some of their volume, allowing the signal to go further, and consequently effects subsiding in the differential interferograms.

This study also depicts the limits of this approach: the images acquired early in the year (March) could not be used due to too low coherence values. As these low coherence values have to be explained by remaining snow patches and can hence not be avoided, year-round monitoring would not be possible. The same is valid for areas covered by dense vegetation. But at least for the observation of lithalsa movements overgrown areas might not be of main interest.

Although the feasibility of using differential interferometry to monitor terrain deformation caused by permafrost processes on a very small-scale could be proved, an operational application to gain exact information over broader areas would still need on-going work with the data and further exploration of available processing methods. Primarily, it is recommended that more scenes be gathered to allow for the generation of more interferograms that will allow interferogram stacking and the calculation of atmospheric influence. Provided that sufficient funding is available, the additional use of TanDEM-X data would definitely be a huge contribution, as more frequent acquisitions would be available. The combination of data from the two twin satellites would result in large advantages and open up even more possibilities to ascertain the information content of the radar images.

Considering the combination of all the newly gained information, the value and usefulness of the highly demanded spatial permafrost monitoring and modeling strategies become evident. A combination of change detection methods that use at least one high-resolution sensor could serve to feed permafrost models, by delivering the important information about changes at the surface. With the information about coexistence of surface features and permafrost embedded in the model, the permafrost distribution can be estimated. If a time-series of satellite images are available, trends and dynamics can also be simulated.

D-InSAR techniques can be employed for an estimation of small-scaled permafrost thawing, expressed by the collapse and subsidence of lithalsas. This method can also be applied to the estimation of any other permafrost features such as pingos and palsas, but also for landslides and solifluction and hence stands for a multi-applicable tool to monitor permafrost related deformation of the landsurface.

In addition to the findings concerning the use of remote sensing data, the trials and application of the different methods already revealed some interesting facts about the permafrost situation in the research area. Changes in the vegetation cover could be presented by using images over a time period of 22 years (1986 – 2008). As one of the main alterations is the increase of thermokarst ponds and the collapse of lithalsas, the observed change can be very likely be linked to permafrost degradation.

In general, a vegetation increase consisting mainly of trees and bushes at the expense of lichens and mosses was observed. Areas situated in the eastern part and along the rivers were highlighted as regions with most vegetation augmentation. It can be assumed that this is due to the sheltered location in the lee of the Cuestas, where lesser wind speeds and a smoother climate allow a faster colonization of vegetation. Also in terms of the thermokarst lakes development and the lithalsa degradation, this area was mostly affected. Consequently it can be presumed that the eastern part has recently been more impacted on by climate change than the western part. Considering the micro-climate in the two parts, this is less surprising as in the east the weather tends to be less harsh than in the west. Presuming proceeding climate warming, it is very likely that the western part will also experience more transformation.

Also the survey of the lithalsas revealed some interesting findings: With both techniques lithalsa I is highlighted as the lithalsa that reflected the seasonal pulsations the most distinctive, and showed highest variability between the points. Lithalsa R and M in contrast are disclosing more or less similar behavior. This gets even more interesting, by stating that most counter trends (against the average movements) were recorded for lithalsa M and fewest for lithalsa I. This is interesting, as lithalsa I still appeared to be in its original state, whereas lithalsa R and M already showed several features that were evidence for degradation. Hence it can be argued for the fact, that its intact state was also mirrored in the typical and expected moving behavior, whereas R and M might already have partially lost this characteristic. Also the outcomes of the interannual comparison are confirming this belief: R and M delivered with their negative values evidence for degradation, while lithalsa I appeared to be more or less in balance. This could also be an additional explanation of the counter movements of lithalsa R and M during the last recording period. Nevertheless, the high heterogeneity occurring on I could be an indicator that degradation has also begun here.

Some notable conclusions can also be made in terms of the location of the different sample points mainly based on the d-GPS measurements. Mostly areas covered by spare vegetation were disclosing many changes, whereas points on grass and shrubs were showing less. Points located close to water bodies always experienced subsidence. These facts can be explained by a more sensitive reaction to changing air temperatures of hardly vegetated areas, as well as a temperature-buffering effect of vegetation concerning in- and outgoing heat fluxes. In the matter of the sample points close to the water, the heat transfer from the unfrozen water body and consequently higher soil temperature were very likely the reason for their contrary behavior.

Furthermore, it became evident that there are more factors (e.g. bioturbation and swelling) than only thawing and freezing processes that influence the landsurface's deformation, and hence the contrary behaviors of some points have to be attributed to these factors.

In conclusion, the work and outcomes of this thesis deliver an important and interesting contribution to permafrost research and can serve to ameliorate and enhance permafrost monitoring systems for the Northern hemisphere. The successful application of remote sensing images in determining alterations in permafrost behavior and dynamics demonstrates the feasibility to use such data to substitute costly and difficult geophysical point measurements and to provide spatial knowledge about the major indicators that are used to describe permafrost dynamics and ecosystem change. These data can then be employed to feed modeling systems by ways of parameter retrieval and data assimilation.

This study confirms ongoing changes in sub-Arctic regions (here expressed by a transforming ecosystem and a modification of the recent natural scenery) highlighting the urgent need for

adaptation strategies also in the research region around Umiujaq. The intense work, collaboration and exchange with the community authorities and the indigenous inhabitants of the village fostered their interest of profiting from the scientific results, but also raised our awareness to respect and benefit from their indigenous skills. Consequently in order to establish a tool, able to monitor permafrost dynamics and related threats and risks for the communities in the North, the most important following step would be the affiliation of traditional and scientific knowledge. Only by basing adaptation strategies on a combination of these two cultures can such management be successfully implemented.

9 Summary

9.1 Summary

The work presented in this thesis contributes to permafrost research in the sub-Arctic. It represents the outcomes of a joint project between the department of Geography at the Ludwig -Maximilians University of Munich (LMU) and the Centre – Eau Terre Environment at the Institut National de la Recherche Scientifique (INRS-ETE); proposed and accomplished by Inga May under the supervision of Prof. Ralf Ludwig (LMU) and Prof. Monique Bernier (INRS-ETE). The study was mainly financed by the University of Munich, but travel costs for the field work covered by both the DFG (Deutsche Forschungsgemeinschaft) and the Canadian ArcticNet initiative, in which the project was officially embedded.

The motivation for this study was based on the need to improve permafrost monitoring in the northern hemisphere. This need arose from results of simulations of Global Circulation Models, which generally agree in predicting the highest long-term temperature rise for high latitude regions. In Northern Quebec (Nunavik), these changes will be, and indeed already are, felt in terms of a rise in summer degree days, which will eventually cause a thawing of permafrost. These impacts are manifold and include ecological, economical and social aspects. Among the most severe are the changes to northern ecosystems, including alterations of the hydrological regime, changes in vegetation cover, expanding marsh- and wetlands, and the decline of slope compaction and thus an increased risk of landslide. Damage repair and increased remedial work are expected on roads, runways, residences and community buildings in the growing villages of the North. Consequently, the native population could suffer psychosocial stresses, related to the displacement of infrastructure and hunting and fishing grounds and adverse health effects caused by modifications to nutrition.

Therefore advanced mitigation and adaptation strategies are necessary, which must be based on a sound understanding of the biogeophysical processes involved in permafrost dynamics. A problem is posed by the research subject in itself, as the acquisition of related data is difficult, due to the extreme climatic conditions for technical equipment, the size and remoteness of affected areas and the heterogeneity of permafrost in areal distribution and depth.

Consequently the basic research question was to explore the feasibility of using satellite imagery for the monitoring of permafrost dynamics, in order to provide the framework for a monitoring system strongly based on remote sensing imagery and data analysis. For the investigation a study site near the Inuit village of Umiujaq, in Northern Quebec, Canada, served as a case study (Chapter 5). The study area is located on the borderline between the sub-Arctic and Arctic regions, reflected in the presence of two important features: the northern timber line and the occurrence of discontinuous permafrost. This transitional location makes the study area an ideal site for the detection of changes in vegetation and permafrost, and associated land surface movements. Additionally, a great number of long-term climatic and environmental records are available for the area (ALLARD & SEGUIN 1985), providing the basis upon which this study is build to investigate topographical changes.

The first important findings of this study are the identification of visible features at the land surface, which represent the state of the underlying permafrost (Chapter 6), and which could be detectable in remotely sensed images. To ascertain these, several field campaigns (Chapter 6.1) during both summer and winter seasons were conducted in 2009, 2010 and 2011. The analysis of the collected

parameters and co-existence of different vegetation, snow cover and the active layer height, highlighted some interesting correlations (Chapter 6.2). The following rules were aligned:

1. An elevated area corresponds to a very thin or zero snow cover and almost no vegetation, and is related to permafrost occurrence in the upper 2 meters.
2. A wind sheltered, low area corresponds to a thick snow cover and much denser vegetation and is related to no permafrost (at least not in the upper 2 meters).

In addition, the seasonal deformation of frost mounds was surveyed (Chapter 6.3) by dint of a d-GPS, to understand their elevation changes related to the occurring air temperature. Downwards motion during the thawing season and uplift during the freezing season could be definitively stated, and hence can also serve as a proxy to describe the state of permafrost.

The second part of this thesis (Chapter 7) deals with the possibility of detecting these newly defined indicators by means of satellite images. Potential applications of remotely sensed data and the trial of different techniques to spatially detect the features are discussed and debated. Data delivered from low and high-resolution sensors (Chapter 7.1) was used for change detection methods. The results highlighted the methods postclassification, write function memory insertion, and cross-correlation as the most suitable, and disclosed the limits of low-resolution images (Landsat 30 x 30 m) for such application. The interpretation of the outcomes also confirm the impacts of climate change in this region as land vegetation changes and the expansion of wetlands could be observed over the time-series of the images.

In order to detect deformations in the relief, it was explored whether radar data, delivered by the TerraSAR-X satellite, was suitable to generate differential interferograms, presenting the seasonal displacement of the frost mounds (Chapter 7.2). The fact that the entire area is underlying an isostatic rebound of 1 cm/year was used to validate the interferometric outcomes by first analyzing areas where no other deformation processes takes place (stable Cuesta area). After this was successfully ascertained, the pixels representing three lithalsas near the community were scrutinized: uplift movements during the freezing period and downwards movements during the thawing periods could be clearly identified for these areas. These outcomes strongly confirm the expected motions, and the results show good accordance to the geodetical surveys in the field. Deviations were stated quantitatively.

This study has shown that it is possible to detect permafrost dynamics from space by interpreting visible targets at the surface that are indicative of the condition of the underlying ground. For adequate and correct estimation, a multi-sensoral approach is definitely required to guarantee the involvement of all influencing factors. This is also necessary to overcome any shortcomings in data availability. In order to maximize the transformation of knowledge gathered by the satellite into action, a strong and active collaboration with the local communities is needed, in order to develop adaptation strategies that can effectively be implemented in these northern villages.

9.2 Zusammenfassung

Die vorliegende Arbeit stellt einen Beitrag zur Permafrost-Forschung in der Sub-Arktis dar. Sie präsentiert die Resultate eines Gemeinschaftsprojektes zwischen dem Department für Geographie der Ludwig-Maximilians Universität in München (LMU), (Deutschland) und dem Centre-Eau Terre Environment des Institut national de la recherche scientifique (INRS), Quebec (Kanada) das unter der

der Aufsicht von Prof. Dr. Ralf Ludwig (LMU) und Prof. Dr. Monique Bernier (INRS) von Inga May durchgeführt wurde.

Die Studie wurde hauptsächlich durch Mittel der Universität München finanziert, zusätzliche Kosten für Forschungsreisen und Feldarbeit wurden teilweise von der Deutschen Forschungsgemeinschaft (DFG) und teilweise von der kanadischen ArcticNet Initiative, in die das Projekt offiziell eingebunden ist, gedeckt.

Die Motivation dieser Arbeit gründet auf der dringenden Notwendigkeit ein flächenhaftes und präzises Monitoringsystems zu entwickeln, welches es ermöglicht die Entwicklung und Dynamiken der Permafrostböden auf der nördlichen Hemisphäre genau zu beobachten. Diese Notwendigkeit basiert auf den Simulationsergebnissen globaler Zirkulationsmodelle, die einheitlich stärkste Temperaturanstiege für die höheren Breiten prognostizieren. Im Norden Quebecs (Nunavik), wird eine solche Erwärmung eine Bandbreite an Folgen mit sich bringen und unter anderem früher oder später zu einem Auftauen des momentan vorherrschenden Permafrostbodens führen. Die dadurch zu befürchtenden Folgen sind beträchtlich und werden sowohl ökologische, ökonomische sowie soziale Aspekte betreffen. Primär wird sich dies durch eine Veränderung des sub-arktischen Ökosystems bemerkbar machen. Ein veränderter Wasserkreislauf und ein Wandel der Landbedenkung, wie zum Beispiel die Ausbreitung von Feuchtgebieten und Mooren und eine zunehmende Abnahme der Hangstabilität, einhergehend mit einem steigendem Risiko für Hangrutsche, stellen eine große Bedrohung dar. Schäden an Häusern und Straßen, sowie steigender Aufwand und Kosten um die Infrastruktur zu erhalten und wiederaufzubauen, werden in den ständig wachsenden Gemeinden im Norden erwartet. Als Folge dessen sind psychosoziale Probleme in der ansässigen Bevölkerung zu befürchten, ausgelöst durch den Umbruch ihres ursprünglichen Lebens, durch das Verlegen von infrastrukturellen Einrichtungen, dem Verlust ihrer traditionellen Fisch- und Jagdgründen und eine sich daraus ergebende Änderung ihrer Nahrung.

Solche Veränderungen erfordern ein gut durchdachtes Handeln und Anpassungsstrategien, welche auf einem fundierten Wissen der biogeophysikalischen Prozesse der Permafrostböden basiert sein muss. Das größte Problem ist dabei das Untersuchungsobjekt an sich, da durch die äußeren vorherrschenden Bedingungen, die Abgeschiedenheit sowie die Heterogenität in Auftreten und Form des Permafrostbodens, dessen genaue Erfassung extrem schwierig ist.

Die Hauptforschungsaufgabe dieser Arbeit war daher zu ergründen, inwieweit es möglich ist, Satellitenbilder für das Beobachten der Permafrost-Dynamiken einzusetzen, um damit die Basis für ein räumlich verteiltes Monitoringsystem zu liefern. Für diese Untersuchung wurde ein Testgebiet in der Nähe Umiujaqs, in Nord Quebec, Kanada als Fallstudie ausgewählt (Kapitel 5). Das Gebiet befindet sich an der Grenze zwischen der Sub-Arktis und der Arktis, was sich insbesondere durch die zwei folgenden Eigenschaften widerspiegelt: Der Verlauf der nördlichen Baumgrenze befindet sich in dem Untersuchungsgebiet und es befindet sich in der diskontinuierlichen Permafrostzone. Die Lage in dieser Übergangszone stellt ideale Bedingungen für eine Klimawandelfolge-Studie die sich mit Veränderungen in der Vegetation, dem Permafrost und damit verbundenen Oberflächendeformationen beschäftigt. Hinzu kommt eine bereits gute Datenlage für diese Gebiet, welche die Grundlagen für diese Studie stellt.

Die erste wichtige Aufgabenstellung der Arbeit war demnach die Identifikation von Oberflächenmerkmalen, die die Situation des Permafrostbodens widerspiegeln (Kapitel 6) und welche in Satellitenbildern auffindbar sind. Dafür wurden mehrere Feldkampagnen im Sommer und Winter 2009, 2010 und 2011 durchgeführt. Die Analyse der dabei aufgenommenen Parameter verschiedener Vegetationsformen, der Schneedecke und der Auftautiefe des ‚Active Layers‘, konnte dabei einige

interessante Zusammenhänge feststellen und folgende Regeln konnten abgeleitet werden (Kapitel 6.2).

1. Auf einer exponierten Fläche befindet sich im Winter kaum bis gar kein Schnee, die Vegetation ist sehr spärlich. Die Auftauschicht in diesen Bereichen beträgt oft nur wenige Zentimeter und immer unter 2 m.
2. In windgeschützten Bereichen und Synklinalen hingegen akkumuliert sich eine mächtige Schneedecke und auch die Vegetation ist hier sehr viel dichter. In solchen Bereichen taut der Boden über 2 m tief auf.

Zusätzlich wurden mithilfe eines differentiellen GPS saisonale Schwankungen in der Höhe dreier Frosthügel vermessen, um diese Änderungen in Abhängigkeit von der Temperatur zu analysieren. Hierbei konnte eine Abwärtsbewegung während der Tauperiode (Frühjahr) und eine Aufwärtsbewegung während des Gefrierprozesses (Winter) ausgemacht werden. Anhand dieser Feststellung kann demnach auch eine sich ändernde Topographie als Indikator für Permafrost - Dynamiken, bedingt durch sich ändernde Temperaturen, dienen.

Der zweite große Aufgabenbereich dieser Arbeit (Kapitel 7) beschäftigt sich nun mit der Möglichkeit, diese im Feld identifizierten Indikatoren in Satellitenbildern wiederzuerkennen. Dafür wurden verschiedene Fernerkundungsdaten verwendet und Techniken zur Detektion räumlicher Veränderungen ausprobiert, analysiert und diskutiert.

Aufnahmen von gering- und hochauflösenden Sensoren wurden verwendet um verschiedene *Change Detection* Methoden anzuwenden und zu vergleichen. Die Ergebnisse zeigten, dass mit den Methoden ‚Postclassification‘, ‚Write Memory Insertion‘ und ‚Cross-Correlation‘ die besten Resultate erzielt werden konnten. Gleichzeitig wurden damit auch die Grenzen der Verwendung von geringauflösenden Bildern (Landsat 30 x 30 m) deutlich.

Die Interpretation der Ergebnisse machte außerdem bereits stattfindende Folgen des Klimawandels sichtbar, da eine klare Veränderung der Vegetation sowie eine Ausweitung der Feuchtgebiete in den Zeitreihen erkennbar sind.

Um die Änderungen im Relief zu beobachten, wurde untersucht, ob Radar Daten des TerraSAR-X Satelliten geeignet sind differentielle Interferogramme zu generieren, welche diese jährlichen Höhenschwankungen wiedergeben können (Kapitel 7.2). Die Tatsache, dass die gesamte Region einer postglazialen Hebung von 1 cm / Jahr unterliegt, wurde hierbei genutzt um die Resultate der differentiellen Interferogramme zu validieren, indem zunächst Gebiete in denen keine weitere Bewegung stattfindet, analysiert wurden. Nachdem diese Validierung erfolgreich durchgeführt werden konnte, wurden die Pixel von drei Lithalsen in der Nähe der Gemeinde genauer untersucht: Aufwärtsbewegungen während des Gefrierens und Abwärtsbewegungen während des Tauens konnten klar für diese Regionen festgestellt werden. Diese Ergebnisse bestätigen die erwarteten Bewegungen und zeigen zudem eine gute Übereinstimmung mit den Resultaten der Feldmessungen. Nur bezüglich der Quantitäten der Veränderungen weisen diese zwei Messmethoden einige Abweichungen auf.

Die Studie zeigt die Möglichkeit, Veränderungen in Böden mit Permafrost anhand von sichtbaren Merkmalen an der Landoberfläche aus dem All zu beobachten. Für eine detaillierte und fehlerfreie Analyse ist dafür allerdings in jedem Fall ein multi-sensoraler Ansatz nötig, damit eine Berücksichtigung aller beteiligten Faktoren garantiert ist. Zudem kann somit einem Ausfall von Daten, zum Beispiel hervorgerufen von Wolken, vorgebeugt werden und eine Lücke in Zeitreihen vermieden werden.

Um weiterführend die durch die Interpretation der Satellitendaten gewonnene Information sinnvoll einzusetzen zu können und Anpassungsstrategien zu entwickeln, die in den Gemeinden effektiv umgesetzt werden, ist zusätzlich eine starke und aktive Zusammenarbeit mit den lokalen Behörden von absoluter Bedeutung.

9.3 Résumé

Cette thèse est une contribution à la recherche sur le pergélisol dans les zones sub-arctiques. Elle présente les résultats d'un projet conjoint entre le département de Géographie de l'Université Ludwig-Maximilians de Munich (LMU) et du Centre Eau-Terre-Environnement de l'Institut national de la recherche scientifique (INRS-ÉTÉ), qui a été proposé et réalisé par Inga May sous la supervision du professeur Ralf Ludwig (LMU) et du professeur Monique Bernier (INRS-ÉTÉ). L'étude a été financée en majeure partie par l'Université de Munich mais les frais de déplacements pour le travail de terrain ont été partiellement couverts par la DFG (Deutsche Forschungsgemeinschaft) et par l'initiative canadienne d'ArcticNet dans lequel ce projet s'inscrit formellement.

La motivation derrière ce projet est liée au besoin d'améliorer les activités de suivi du pergélisol dans l'hémisphère nord. Ce besoin découle des résultats des simulations des modèles de circulation générale, qui concordent généralement pour projeter les augmentations de températures les plus grandes pour les latitudes élevées. Dans le nord du Québec (région du Nunavik), ces changements sont et se feront sentir au travers l'augmentation des degrés-jours d'été, qui est un des facteurs qui contribue à la dégradation du pergélisol. Les impacts attendus sont multiples et couvrent des aspects écologiques, économiques et sociaux. Les impacts les plus sévères incluent des changements pour les écosystèmes nordiques provoqués par des modifications du régime hydrologique et du couvert végétal, l'expansion des milieux humides et des tourbières, ou la diminution du compactage des pentes et le risque de glissement de terrain qui en résulte. Des dommages de même que l'augmentation du besoin des travaux de réfection et d'entretien sont attendus en ce qui concerne les infrastructures routières, les pistes d'atterrissage, les résidences et bâtiments communautaires dans les villages nordiques en pleine expansion. La population résidente pourrait subir plusieurs conséquences dont des stress psychologiques associés à la relocalisation des infrastructures, l'accès plus difficile aux territoires de chasse et de pêche ou une modification du régime alimentaire.

Ainsi, les conséquences attendues pour la région exigent des stratégies d'adaptation et de mitigation basées sur une connaissance approfondie des processus biogéophysiques associés aux dynamiques du pergélisol. Toutefois, l'enjeu majeur réside en le sujet de recherche lui-même car l'acquisition et la collecte de données sur ce sujet demeurent difficile en raison des conditions climatiques extrêmes pour l'équipement technique (froid, vents forts, ...), l'étendu et le caractère isolé de la région et des endroits affectés de même que l'hétérogénéité du pergélisol dans sa distribution et sa profondeur sur le territoire.

Par conséquent, le principal objectif de recherche visait à explorer la faisabilité d'utiliser des images satellites pour faire le suivi des dynamiques de pergélisol, et d'établir les bases pour un système de suivi utilisant essentiellement la télédétection et l'analyse des données d'images. Un secteur situé à proximité du Village Nordique d'Umiujaq, dans le nord du Québec au Canada a servi de zone d'étude pour l'analyse (chapitre 5). Le territoire d'étude, situé au zone sub-arctique, est caractérisé par deux éléments importants: la limite nordique des arbres et l'occurrence de zones de pergélisol discontinu. Cette zone de transition constitue un site idéal pour détecter des changements au niveau de la végétation et du pergélisol ainsi que les mouvements de surfaces terrestres. De plus, une quantité

à cette fin. L'analyse des paramètres colligés et la présence de différents végétaux, du couvert de neige ainsi que l'épaisseur de la couche active pourraient mettre en évidence des corrélations intéressantes (chapitre 6.2). Les règles suivantes pourraient être appliquées :

1. Un secteur élevé s'accompagne d'un faible couvert de neige (ou absence d'un couvert de neige) et quasiment aucune végétation et est lié à la présence de pergélisol dans les deux premiers mètres du sol.
2. Un secteur bas à l'abri du vent s'accompagne d'un couvert de neige épais et d'une végétation plus dense, et est lié à l'absence de pergélisol (dans les deux premiers mètres).

De plus, la déformation saisonnière des buttes cryogènes a été jaugé (chapitre 6.3) à l'aide d'un GPS afin de mieux comprendre les changements d'élévation en lien avec la température de l'air. Le mouvement vers le bas au cours de la saison de dégel et la surrection au cours de la saison de gel a été observé et peuvent ainsi servir d'indicateurs pour décrire l'état du pergélisol.

La deuxième partie de la thèse (chapitre 7) traite de la possibilité de repérer ces nouveaux indicateurs à l'aide d'images satellite. L'application potentielle de la télédétection et l'essai de différentes techniques visant à relever des caractéristiques ont été expérimentés et discutés. Les données provenant de capteurs à haute et basse résolution (chapitre 7.1) ont été utilisés afin de modifier les méthodes de détection. Les résultats suggèrent que les méthodes de postclassification, *write function* *memory insertion* et de corrélations croisées sont les plus appropriées, et montrent les limites de l'utilisation d'images à faible résolution (Landsat 30 x 30 m) pour de telles applications. L'interprétation des résultats confirme également que les impacts des changements climatiques pour cette région, comme la transformation de la végétation et l'extension des milieux humides, pourraient être identifiés au travers de séries temporelles de ces images.

Pour déceler des déformations dans le relief, le projet a aussi examiné l'utilisation des données radar du satellite TerraSAR-X pour générer des interférograms différentiels qui présenteraient le déplacement saisonnier des buttes cryogènes (chapitre 7.2). Étant donné que la zone complète est soumise à un relèvement isostatique d'un centimètre par année, la validation des résultats d'interférograms s'est d'abord faite en analysant des zones où aucun processus de déformation n'est observé (endroits stables de Cuesta). Une fois ceci démontré, les pixels représentant trois lithales proches de la communauté ont fait l'objet d'analyse. Des mouvements de surrection au cours de la période de gel et des mouvements vers le bas au cours de la période de dégel ont clairement été identifiés pour ces sites. Ces résultats confirment les mouvements attendus et montrent une bonne concordance avec les relevés géodétiques sur le terrain.

L'étude montre qu'il est possible de détecter les dynamiques de pergélisol en se basant sur l'interprétation de cibles visibles à la surface qui sont des indicateurs des conditions de sol. Une approche multi-sensorielle serait requise pour une estimation adéquate qui tienne compte de tous les facteurs qui influencent ces dynamiques. Cette approche permettrait également de compenser le manque de données disponibles.

Une forte collaboration active avec les communautés locales permettrait de mieux passer de la collecte et l'analyse des données à l'action concrète pour développer des stratégies d'adaptation qui sont effectivement mis en œuvre dans les villages nordiques.

Une forte collaboration active avec les communautés locales permettrait de mieux passer de la collecte et l'analyse des données à l'action concrète pour développer des stratégies d'adaptation qui sont effectivement mis en œuvre dans les villages nordiques.

10 References

- ABRAMS, M. J., HOOK, S., ABRAMS, M. C. (2003): Thermal Infrared Remote Sensing. In: VAN DER MEER, F., DE JONG, S. M. [Ed.] (2003): *Imaging Spectrometry. Basic Principles and Prospective Applications*. Kluwer Academic Publishers, Dordrecht
- ABRAMS, M. J., HOOK, S., RAMACHANDRAN, B. (2002): *ASTER UserHandbook. Version 2*. Jet Propulsion Laboratory, California Institute of Technology.
- ADAMS, J.B. & GILLEPSIE, A. R. (2006): *Remote Sensing of Landscape with Spectral Images – A physical modelling approach*. Cambridge University Press, New York.
- ALDRICH, J. (1997): R. A. Fisher and the Making of Maximum Likelihood 1912-1922. In: *Statistical Sciences*, 12 (8), pp. 162 – 176.
- ALLARD, M., CARON, S., BEGIN, Y. (1996): Climatic and ecological controls on ice segregation and thermokarst: the case history of a permafrost plateau in Northern Quebec. In: *Permafrost and Periglacial Processes*, 7, pp. 207-227.
- ALLARD, M., FORTIER, R., SARRAZIN, D., CALMELS, F., FORTIER, D., CHAUMONT, D., SAVARD, J.P., TARUSOV, A. (2007) : L'impact du réchauffement climatique sur les aéroports du Nunavik : caractéristiques du pergélisol et caractérisation des processus de dégradation des pistes
- ALLARD, M. & ROUSSEAU, L. (1999): The internal structure of a palsa and a peat plateau in the riviere Boniface region, Quebec: inferences on the formation of ice segregation mounds. In: *Geographie physique et Quaternaire*, 53, pp. 373-387.
- ALLARD, M., & SEGUIN, M. K. (1985) : La déglaciation d'une partie du versant hudsonien Québécois: Bassin des rivières Nastapoca, Sheldrake et à l'Eau Claire. In : *Géographie physique et Quaternaire*, 39 (1), pp. 13-24
- ALLARD, M., & SEGUIN, M.K. (1986): The Holocene evolution of permafrost near the tree line, on the eastern coast of Hudson Bay (northern Quebec). In: *Canadian Journal of Earth Sciences*, 24, pp. 2206-2222.
- ALLARD, M. & SEGUIN, M. K. (1987): Le pergélisol au Québec Nordique: bilan et perspectives. In : *Géographie Physique et Quaternaire*, 41 (1), pp. 141-152.
- ALLARD, M., SEGUIN, M.K., LEVESQUE, R. (1986): Palsas and mineral permafrost mounds in Northern Quebec. In: GARDINER, V.[Ed.] (1986): *International Geomorphology, Part II..* In *Proceedings of the 1st International Conference on Geomorphology*, John Wiley & Sons Ltd., London, pp. 285-309.
- ALLARD, M., SEGUIN, M. K. LÉVESQUE, R. (1987): The Holocene evolution of permafrost near the tree line, on the eastern coast of Hudson Bay (Northern Quebec). In: *Canadian Journal of Earth Sciences*, 24, pp. 2206-2222.
- ALLARD, M., TREMBLAY, C., PILON, J.A., FRYDERICKI, J. (1993): Quaternary geology and geocryology in Nunavik, Canada. In: *Proceedings 6th International Conference on Permafrost*, Beijing, China. South China University of Technology Press, pp. 5-10.
- ALLARD, M., WANG, B, PILON, J.A. (1995): Recent cooling along the southern shore of Hudson Strait Quebec, Canada, documented from permafrost temperature measurements. In: *Arctic and Alpine Research*, 27, 157–166.

- AN, W. (1997): Palsa formation: mathematical modeling and field information. Thèse de doctorat. Faculté des études Supérieures, Université Laval, Québec, 202 pp.
- AN, W., & ALLARD, M. (1995): A mathematical approach to modeling palsa formation: insights on processes and growth conditions. In: *Cold Regions Science and Technology*, 23, pp. 231-244.
- ANISIMOV, O. & FITZHARRIS, B. (2001): Polar Regions (Arctic and Antarctica). In: *Climate Change 2001. Impacts, Adaptation, and Vulnerability. Contribution of Working Group II to the Third Assessment Report of the Intergovernmental Panel on Climate Change*, Cambridge University Press, pp. 801 – 841.
- ANNERSTEN, L.J. (1964): Investigations of permafrost in the vicinity of Knob Lake, 1961-1962. In: *McGill Sub-Arctic Research papers*, 161, pp. 51 -137.
- ANTPAS (no date): ANTPAS – Antarctic Permafrost and Soils. Available at: <http://erth.waikato.ac.nz/antpas/index.shtml>. Accessed on 02.03.2011.
- ArcticNet (2004): ArcticNet. Available at <http://www.arcticnet.ulaval.ca/>. Accessed on 28.08.2009.
- ARMSTRONG, R.L. & BRODZIK, M.J. (2001): Recent northern hemisphere snow extent: A comparison of data derived from visible and microwave satellite sensors. In: *Geophysical Research Letters*, 28, pp 3673 -3676.
- ARMSOTRONG, R.L. & BRUN, E. [Eds.] (2008): Snow and Climate. Physical Processes, Surface Energy Exchange and Modeling. Cambridge University Press. Cambridge.
- ARONOFF, S. (2005): Remote Sensing for GIS Managers. ESRI Press. Redland, California.
- BALL, G.H, & HALL, D. J. (1967): A clustering technique for summarizing multivariate data. In: *Behavioral Science*, 12, pp. 153 – 155.
- BELWARD, A. S. (1991): *Remote Sensing and geographical information systems for resource management in developing countries*, 1, pp. 31 – 53.
- BOSCHI, L., WOODHOUSE, J. H. (2006): Surface wave ray-tracing and azimuthal anisotropy: a generalized spherical harmonic approach. In: *Geophysical Journal International*, 164, pp. 569-578.
- BOVIELL, B.A., KIEHL, J.T., RASCH, P.J., BRYAN, F.O. (2001): Improvements to the NCAR CSM-1 for transient climate simulations. In: *Journal of Climate*, 14, pp. 164-179.
- BRADLEY, R.S. (1999): Paleoclimatology: Reconstructing Climates of the Quarternary. Academic Press.
- BREIT, H., FRITZ, T., BALLS, U., ACHAISE, M., NIEDERMAIER, A., VONAVKA, M. (2010): TerrSAR-X SAR Processing and Products. In: *Geoscience and Remote Sensing, IEEE Transactions on*, 48, 2, pp. 747 – 740.
- BRETON, J., VALLIÈRES, C., LAURION, I. (2009) : Limnological properties of permafrost thermokarst ponds in northern Canada: carbon cycling and greenhouse gas production. In: *Canadian Journal of Fisheries and Aquatic Sciences*, 66, pp. 1635 – 1648.
- BROWN, R.J.E. (1963): Influence of vegetation on permafrost. In: *Proceedings, Permafrost International Conference*, Washington D. C.: NAS/NRC Publications 1287, pp. 20-25.

- BROWN, R.J.E. (1965): Some observations of the influence of climate and terrain features on permafrost at Norman Wells, N.W.T..In: *Canadian Journal of Earth Sciences*, 2, pp. 15-31.
- BROWN, R.J.E. (1970) : Permafrost in Canada – its influence on northern development. Canadian Building Series No.4, University of Toronto Press, Toronto.
- BROWN, R.J.E. (1974): Permafrost terminology (Technical memorandum – Associate Committee on Geotechnical Research, National Research Council of Canada). National Research Council of Canada, Canada.
- BROWN, R.J.E. (1979) : Permafrost distribution in the Southern part of discontinuous zone in Québec and Labrador. In: *Géographie Physique et Quartenaire*, 33, pp. 279-289.
- BROWN, R. J. E., FERRIANS, J. R., HEGINBOTTOM, J. A., MELNIKOV, E. S. (1997): Circum-Arctic Map of Permafrost and Ground-Ice Conditions. In: *U.S. Geological Survey Washington, D.C. Circum-Pacific Map Series CP-45*.
- BROWN, W. M. (1967): Synthetic Aperture Radar. In: *IEEE Transactions on Aerospace and Electronic Systems*, 2, pp 217-229.
- BURGER, W. & BURGE M. J. (2009): Principles of Digital Image Processing. Fundamental Techniques. Springer Verlag, London.
- BURGESS, M. M., SMITH, S. L. (2000): Shallow ground temperatures. In: *The physical environment of the Mackenzie Valley, Northwest Territories: a base line for the assessment of environmental change*; Dyke, L D; Brooks, G R. Geological Survey of Canada, Bulletin 547, pp. 89-103.
- BUTEAU, S., FORTIER, R., DELISLE, G., ALLARD, M. (2004): Numerical simulation of the impacts of climate warming on a permafrost mound. In: *Permafrost and Periglacial Processes*, 15, pp. 41-57.
- CAF-CLUSTER APPLIED REMOTE SENSING (2009): TerraSAR-X. Ground Segment. Basic Product Specification Document. Oberpfaffenhofen.
- CAFF (Conservation of Arctic Flora and Fauna) (2010): Arctic Biodiversity Trends 2010. Available at <http://www.arcticbiodiversity.is>. Accessed on 23.11.2010.
- CALMELS, F. (2008) : Genèse et structure du Pergélisol. Etude de forms péeriglaciaires de soulèvement au gel au Nunavik (Québec nordique), Doctoral thesis, Dep. of Geography, Université Laval, Quebec, Canada.
- CAMPBELL, J. B. (2009): Introduction to Remote Sensing. Guilford Press, New York.
- Canada Centre for Remote Sensing (2005): Glossary of remote sensing terms. Available at http://www.ccrs.nrcan.gc.ca/glossary/index_e.php?id=2963. Accessed on 09.05.2011.
- CHARBONNEAU. M., LORD, G., BERNIER, L. (2005): Road safety report of the MTQ road in Nord-du-Québec. Technical Study, Transportation Plan of Nord-du-Quebec. Transport Quebec.
- CHEN, C.W. (2001): Statistical-cost network-flow approaches to two-dimensional phase unwrapping for radar interferometry, Dissertation, Stanford University, USA.

- CHEN, C.W., ZEBKER, H.A. (2001): Network approaches to two-dimensional phase unwrapping: intractability and two new algorithms. In: *Journal of the Optical Society of America*, 17, pp. 401-414.
- CHOUINARD, C., FORTIER, R., MARESCHAL, J.- C. (2007): Recent climate variations in the sub-Arctic inferred from three borehole temperature profiles in Northern Quebec, Canada. In: *Earth and Planetary Science Letters*, 263(3-4), pp. 355-369.
- CIVCO, D. L., HURD, J. D., WILSON, E. H., SONG, M., ZHANG, Z. (2002): A comparison of Land Use and Land Cover Change Detection Methods. In: *Proceedings, ASPRS-ACSM Annual Conference and FIG XXII Congress*, Bethesda, pp. 10.
- COMISMO, J. C. (2002): Warming Trends in the Arctic from Clear Sky Satellite Observations. In: *Journal of Climate*, 16, pp. 3498 – 3510.
- COMISMO, J.C. & PARKINSON C.L. (2004): Satellite-observed changes in the Arctic. In: *Physics Today*, 57, pp- 38-44.
- CONGALTON, R. G. & GREEN, K. (1999): *Assessing the Accuracy of Remotely Sensed Data*. CRC Press, Boca Raton.
- CONGALTON, R. G. & MEAD, R. A. (1983): A quantitative method to test for consistency and correctness in photointerpretation. In: *Photogrammetric Engineering & Remote Sensing*, 49, pp. 69-74.
- COPPIN, P., JONCHEERE, I., MUYS, B., LAMBIN, E. (2002): Digital change detection methods in natural ecosystem monitoring: A review. In: BRUZZONE, L. & SMITS, P. [Eds.] (2002): *Analysis of Multi-Temporal Remote Sensing Images*. World Scientific Publishing Co. Pte. Ltd, Singapor.
- COULTISH, S.I. & LEWKOWICZ A.G. (2003): Palsa dynamics in a sub-Arctic mountainous environment, Wolf Creek, Yukon Territory, Canada. In: PHILLIPS, M. SPRINGMAN, S.H., ARENSON, L.U [Eds.]: *Permafrost, Proceedings of the Eighth International Conference on Permafrost*, Zürich, Lisse, Swets and Zeitlinger, pp. 163-168.
- DANG, H., GENTHON, C., MARTIN, E. (1997): Air-Snow interactions and atmospheric chemistry. In: *Science*, 297, pp. 170-176.
- DELWORTH, T.L. & KNUTSON, T.R. (2000): Simulation of the early 20th century global warming. In: *Science*, 287, pp. 2256 – 2250.
- DIGITALGLOBE (2011): Quickbird. Available at www.digitalglobe.com/index.php/85/QuickBird. Accessed on 5.05.2011.
- DINGS, Y., GRIGGS, D. J., NOGUER, M., VAN DER LINDEN, P. J., DAI, X., MASKELL, K., JOHNSON, C.A. [Eds.] (2001): *Intergovernmental Panel on Climate Change*. Cambridge University Press.
- DIONNE, J.-C. (1984) : Paleses et limite meridionale du pergélisol dans l'hémisphère nord: le cas de Blanc-Sablon, Québec. In : *Géographie physique et Quaternaire*, 38, pp. 165-184.
- DLR, (2010). TerraSAR-X- Deutschlands Radar-Auge im All. Available at: http://www.dlr.de/eo/desktopdefault.aspx/tabid-5725/9296_read-15979/. Accessed 20.01.2010.

- DLR (2011): TanDEM-X – A New High Resolution Interferometric SAR Mission. Available at http://www.dlr.de/hr/desktopdefault.aspx/tabid-2317/3669_read-5488/. Accessed on the 23.05.2011.
- DUDA, R. O., HART, E. H., STORK, D. G. (2000): Pattern Classification. 2nd Edition. Wiley-Interscience, England.
- EFRON, B. (1982): Maximum likelihood and decision theory. In: *Annual Statistics*, 10, pp. 340-356.
- ELACHI, C., BICKNELL, T., JORDAN, R. L., WU, C. (1982): Spaceborne Synthetic-Aperature Imaging Radar: Applications, Techniques and Technology. In: *Proceedings of IEEE*, 70 (10), pp. 1174-1209.
- ENVIRONMENT CANADA (2004). Canadian Climate Normals, 1971-2000. Environment Canada, Atmospheric Environment Service, Ottawa. In: *The open knowledge Society, a computer science and information systems manifesto*, 19, pp. 521- 526.
- ESPÍNOLA, M., AYALA, R., LEGUIZAMÓN, S., MENETI, M. (2008): Classification of Satellite Images Using the Cellular Automata Approach.
- ESRI (2011): Understanding our world. Available at www.esri.com/news/arcuser/0103/differential1of2. Accessed on the 07.08.2010.
- FERRETTI, A., PRATI, C., ROCCA, F., MONTI GUARNIERI, A. (1997): Multibaseline SAR interferometry for Automatic DEM Reconstruction. In: *Third ERS Symposium – Space at the Service of our Environment*, Florence, Italy, 17-21 March, 1997. ESA SP-414, 1809 -1820.
- FISHER, R. A. (1920): A mathematical examination of the methods of determining the accuracy of an observation by the mean error, and by the mean square error. In: *Monthly Notices of the Royal Astronomical Society*, 80, pp. 758-770.
- FLATO, G.M. & BOER, G.J. (2001): Warming asymmetry in climate change experiments. In: *Geophysical Research Letters*, 28, pp. 195 – 198.
- FORBES, D.L., KREMER, H., RACHOLD, V., LANTUIT, H. [Eds.] (2011) : The State of the Arctic Coast 2010. Helmholtz-Zentrum, Geesthacht.
- FORTIER, R. & AUBÉ-MAURICE, B. (2008): Fast Permafrost Degradation Near Umiujaq in Nunavik (Canada) Since 1957 - Assessed from Time-Lapse Aerial and Satellite Photographs. In: *NICOP proceedings University of Alaska*, Fairbanks.
- GAGNON, R.M., & FERLAND, M. (1967) : Climat du Québec septentrional. Québec, Service de la météorologie Ministère des richesses naturelles, 107 p.
- GAMMA REMOTE SENSING AG (2006): Gamma Software Introduction. Documentation – User's Guide. Gümligen, Swiss.
- GAMMA Remote Sensing AG (2008): Differential Interferometry and Geocoding Software – DIFF&GEO. Vers.1.2.
- GAMMA Remote Sensing AG (2010): Interferometric SAR Processor – ISP. Documentation – User's Guide. Vers. 1.5. Gümligen, Swiss.

- GATELLI, F., MONTI GUARNIERI, A., PARIZZI, F., PASQUALI, P., PRATI, C., ROCCA, F. (1994): The wavenumber shift in SAR Interferometry. In: *IEEE Transactions on Geoscience and Remote Sensing*, 32 (4), pp. 855 – 865.
- GEIST, H. (2006): *Our Earth Changing Land*. Greenwood Press, Westport.
- GeoEye Elevating Insight (2011): Imagery Sources. Available at <http://www.geoeye.com/CorpSite/products-and-services/imagery-sources/>. Accessed on the 05.05.2011.
- GHIHLIA, D.C. & PRITT, M.D. (1998): *Two-dimensional Phase Unwrapping: Theory, Algorithms, and Software*, Wiley, New York, USA.
- GILPIN, R.R. (1980): A model for the prediction of ice lensing and frost heave in soils. In: *Journal of Water Resources Research*, 16 (5), pp. 918 – 930.
- GIRARD, M.-C. & GIRARD, C.M. (2003): *Processing of Remote Sensing Data*. Dunod, Paris.
- GOLDSTEIN, R. M. (1995): Atmospheric limitations to repeat-track radar interferometry. In: *Geophysical Research Letters*, 22(18), 2517-2520.
- GOLDSTEIN, R. M., ZEBKER, H. A., WERNER, C. L. (1988): Satellite radar interferometry: Two dimensional phase unwrapping. In: *Radio Science*, 23(4), pp. 713-720.
- GOLUBEV, V.N., FROLOV, A.D. (1998) : Modelling the change in structure and mechanical propoertire in dry-snow densification to ice. In: *Annals of Glaciology*, 26, pp. 45-50.
- GOMARSCA, M. A. (2004): *Basics of Geomatics*. Springer Verlag, Dordrecht, Heidelberg, London, New York.
- GODDSSION, B.E., LOUIE, P.Y.T., YANG, D. (1998): WMO Solid Precipitation Intercomparison, Final Report. In: *Instruments and Observing Methods Report 67, WMO/TD 872*, World Meteorological Organization, Geneva., pp. 87.
- GOODRICH, L.E. (1982): An introductory review if numerical methods for ground thermal calculations. National Research Council of Canda, Division of Buidling Research, Paper 1061, pp. 32.
- GOPAL, S. & WOODCOCK, C. (1994): Theory and methods for accuracy assessment of thematic maps using fuzzy sets. In: *Photogrammetric Engineering and Remote Sensing*, 60, pp181-188.
- GORDON, C., COOPER, C., SENIOR, C. A., BANKS, H., GREGORY, J. M., JOHNS, T. C., MITCHELL, J. F. B., WOOD, R. A. (2000): The simulation of SST sea cie extents and ocean heat transports in a version of the Hadley Centre coupled model without flux adjustments. In: *Climate Dynamics*, 16, pp. 147-168.
- GORHAM, E. (1991): Northern Peatlands: Role in the Cabon Cycle and Probable Response to Climate Warming. In: *Ecological Applications*, 1, pp. 182-195
- GREY, D. R., GESSLER, P. E., HOPPUS, M., BOUDREAU, S. L. (1998): Change Detection using NALC MSS Triplicates to Set Forest Planning Context. In: *Proceedings of the International conference on integrated tools for natural resources inventories in the 21th century*. Boise, Idaho. pp. 623 – 653.

- GUALTIERI, J. A. (2009): The support Machine (SVM) algorithm for supervised classification of hyperspectral remote sensing data. In: CAMPS- VALLS, G. & BRUZZONE, L. [Eds.] (2009): *Kernel Methods for Remote Sensing Data Analysis*. John Wiley & Sons, West Sussex.
- HACHEM, S. (2008): Cartographie des températures de surface, des indices de gel et de dégel de la répartition spatiale du pergélisol, à l'aide du Moderate Resolution Imaging Spectrometer (MODIS). Thèse de Doctorat, Département de Géographie, Université Laval, 144.p
- HACHEM, S., ALLARD, M., DUGUAY, C. (2008): A new permafrost map of Québec-Labrador derived from near-surface temperature data of the Moderate Resolution Imaging Spectroradiometer (MODIS). In: *Proceedings of the Ninth International Conference on Permafrost*, University of Fairbanks: Fairbanks, Alaska 1, pp. 591–596.
- HALL, F. G., BOTKIN, D. B., STREBEL, D. E., WOODS, K. D., GOETZ, S. J. (1991): Large-scale patterns of forest succession as determined by remote sensing. In: *Ecology*, 72, pp. 628 – 640.
- HAMILTON, L.C. & MITIGUY, A.M. (2009): Visualizing population dynamics of Alaska's Arctic communities. In: *Arctic*, 62, pp. 393 – 398.
- HAN, K.-S., VIAU, A. A., ANCTIL, F. (2004): An analysis of GOES and NOAA derived land surface temperature estimated over a boreal forest. In: *International Journal of Remote Sensing*, 25 (21), pp. 4761 -4780.
- HANSEN, R. F. (2001): *Radar Interferometry. Data Interpolation and Error Analysis*. Kluwer Academic Pub. Stadt
- HARRIS, C., MÜHLL, D.V., ISAKSEN, K., HAEBERLI, W., SOLLID, J.L., HOLMUND, P., DRAMIS, F., GGUGLIELMIN, M., PALACIOS, D. (2003): Warming permafrost in European mountains. In: *Global Planet Change*, 39, pp. 215–225.
- HARRIS, S. A. (1993): Palsa-like mounds developed in a mineral substrate, Fox Lake. In: *Proceedings of the Sixth International Conference on Permafrost*, Beijing July 5-9, 1993, South China University of Technology Press, 1, pp. 238-243.
- HEBEL, H.-P. (2011). Monitoring of mining induced land subsidence - Differential SAR Interferometry (DInSAR) and Persistence Scatter Interferometry (PSI) using TerraSAR-X data in comparison with ENVISAT data. 4. TerraSAR- X Science Team Meeting, 2011, Oberpfaffenhofen, Deutschland.
- HEGINBOTTOM, J. A. & DUBREUIL, M. A. (1993): A new permafrost and ground ice map for the National Atlas of Canada. In: *proceedings of the Sixth International Conference on Permafrost*, Beijing, pp. 225-260.
- HOUGHTON, J. T., DING, Y., GRIGGS, D. J., NOGUER, M., VAN DER LINDEN, P. J., DAI, X., MASKELL, K., JOHNSON, C. A. (2001): *Climate Change 2001: The Scientific Basis*. Contribution of Working Group I to the Third Assessment Report of the Intergovernmental Panel on Climate Change.
- HUBBERTEN, H-W. (2010): oral information
- HUBBERTEN, H-W. (2011): oral information
- HUGGETT, R. J. (2003): *Fundamentals of Geomorphology*. Routledge.

- HUNTINGTON, H. & WELLER, G. (2005): An Introduction to the Arctic Climate Impact Assessment. In: SYMON, C., ARRIS, L., HEAL, B. [Eds.] (2005): Arctic Climate impact Assessment. Cambridge University Press, New York.
- ICSU (2006): The World Data Centre. Available at www.ngdc.noaa.gov/wdc/. Accessed on the 13.05.2011.
- Infoterra GmbH (2010): TerraSAR-X: Satellite & Mission. Available at <http://terrasar.de/terrasar-x/terrasar-x-satellite-mission.html>. Accessed on 09.04.2010.
- Infoterra GmbH (2011): TerraSAR-X Satellite and Mission. Available at <http://www.infoterra.de/terrasar-x-satellite>. Accessed on the 23.05.2011.
- IPA (2010): What is permafrost? Available at <http://ipa.arcticportal.org/resources/what-is-permafrost.html>. Accessed on 2.02.2011.
- IPCC (2000): Resource Availability. An Overview of Scenarios. In: NAKICENOVIC, N. & SWART, R. [Eds.] (2000): IPCC Special Report on Emissions Scenarios. Cambridge University Press, UK.
- ISAKSEN, K., HOLMLUND, P., SOLLID, J.L., HARRIS, C. (2001): Three deep alpine-permafrost boreholes in Svalbard and Scandinavia. In: *Permafrost and Periglacial Processes*, 12, pp. 13-25.
- JÄHNE, B. (2005): Digital Image Processing. Springer Verlag, Heidelberg.
- JANSSEN, S. C. & VAN DER WEL, F. J. M. (1994): Accuracy assessment of satellite derived land-cover data: a review. In: *Photogrammetric Engineering & Remote Sensing*, 60, pp. 419-426.
- JENSEN, J. R. (1996): Introductory digital image processing: A remote sensing perspective. 2nd Edition, N.J.: Prentice Hall, Upper Saddle River.
- JENSEN, J. R. (2000): Remote Sensing of the Environment. N.J.: Prentice Hall, Upper Saddle River.
- JENSEN, J. R. (2005): Introductory Digital Image Processing – A remote sensing perspective. 3rd Edition. N.J.: Prentice Hall, Upper Saddle River.
- JOHANNESSEN, O.M., BENGTSSON, L., MILES, M.W., KUZMINA, S.I., SEMENOV, V.A., ALEKSEEV, G.V., NAGUMYI, V.F., ZAKHAROV, V.F., BOBYLEV, L.P., PETTERSON, L.H., HASSELMANN, K., CATTLE, H.P. (2004): Arctic climate change: observed and modeled temperatures and sea-ice variability. In: *Tellus A*, 56, pp 328 – 341.
- JOHANSON, M. & AKERMAN, H.J. (2008): Thawing permafrost and thicker active layer in Sub-Arctic Sweden. In: *Permafrost and Periglacial Processes*, 19, pp. 279 – 292, DOI: 10.1002.
- JOHNSTON, G. H. (1981): Permafrost: Engineering Design and Construction, John Wiley and Sons, Toronto.
- JORGENSEN, M.T., RACINE, C.H., WALTER, J.C., OSTERKAMP, T.E. (2001): Permafrost Degradation and Ecological Changes Associated with a Warming Climate in Central Alaska. In: *Climate Change*, 48, pp. 551 -579.
- KASPER, J.N. & ALLARD, M. (2001): Late-Holocene climate changes as detected by the growth and decay of ice wedges on the southern shore of Hudson Strait, Northern Quebec, Canada. In: *The Holocene*, 11, pp. 563-577.

- KATTSOV, V.M. & KÄLLEN, E. (2005): Future Climate Change: Modeling and Scenarios for the Arctic. In: SYMON, C., ARRIS, L., HEAL, B. [Eds.] (2005): Arctic Climate Impact Assessment. Cambridge University Press, New York.
- KAUTH, R. J. & THOMAS, G. S. (1976): The Tasseled Cap-A graphic Description of the Spectral Development of Agriculture Crops as seen by Landsat. In: *Proceedings of LARS 1976 Symposium on Machine Processing of Remotely Sensed Data*, Purdue.
- KENDRA, J.R., SARABANDI, K., ULABY, F.T. (1998): Radar measurements of snow: Experiment and analysis. In: *IEEE Transactions on Geoscience and Remote Sensing*, 36, pp. 864 -879.
- KENNETH, R. C. & WU, Q. (2008): Object classification. In: WU, Q., MERCHANT, F., A., KENNETH, R. C. [Eds.] (2008): *Microscope Image Processing*. Elsevier Inc., London.
- KEREKES, J. P. (2009): Optical Sensor Technology. In: WARNER, T. A., NELLIS, M. D., FOODY, G. M. (2009) [Eds]: *The SAGE Handbook of Remote Sensing*. Sage Publications Ltd, London.
- KERSHAW, G.P. & GILL, D. (1979): Growth and decay of palsas and peat plateaus in the Macmillan Pass--Tsichu River area, North-west Territories, Canada. In: *Canadian Journal of Earth Sciences*, 16, pp. 1362-1374.
- KLAUSING, H., & HOLPP, W. (2000): *Radar mit realer und synthetischer Apertur*. R. Oldenbourg Verlag München, Wien.
- KOELN, G. & BISSONETE, J. (2000): Cross-correlation analysis: mapping landcover change with a historic landcover database and a recent, single-date multispectral image. In: *Proceedings 2000 ASPRS Annual Convention*, Washington, D.C.
- KONRAD, J.-M. & MORGENSTERN, N.R. (1980): A mechanistic theory of ice lens formation in fine-grained soils. In: *Canadian Geotechnical Journal*, 17, pp. 473 – 486.
- KONRAD, J.-M. & MORGENSTERN, N.R. (1981): The segregation potential of a freezing soil. In: *Canadian Geotechnical Journal*, 19, pp. 482- 491.
- KONRAD, J.-M. & MORGENSTERN, N.R. (1982): Frost susceptibility of soils in terms of their segregation potential. In: *Proceedings of the 4th International Conference on Permafrost*, Fairbanks, Alaska. National Academy Press, Washington D.C., pp. 660 - 665.
- KONRAD, J.-M. & SETO, J. T. C. (1994): Frost heave characteristics of undisturbed sensitive Cañmplain Sea clay. In: *Canadian Geotechnical Journal*, 31, pp. 285 – 298.
- KONRAD, J.-M. (1990): Theoretical modeling of massive icy beds. In: *Proceeding, 5th Canadian Permafrost Conference*, Nordicana, 54, pp. 31 – 36.
- KOUSHIK, D., SCHUUR, J., NEFF, C., ZIMOV, S. A. (2006): Potential carbon release from permafrost soils in Northeastern Siberia. In: *Global Change Biology*, 12, pp. 2336 – 2351.
- KOVACS, A. (1992): *Glaciers, River and Sea Ice Blister Observations*. Special report. U.S. Army Corps of Engineers.
- KRAMER, H. J. (2002): *Observation of the Earth and Its Environment. Survey of Missions and Sensors*. 4th Edition. Springer Verlag, Heidelberg, New York.

- KRANCK, E. H. (1951): On the geology of the east coast of Hudson Bay and James Bay, observations during a research journey in summer 1947. In: *Acta Geografica*, 11, pp. 1-71.
- LABERGE, M.-J. & PAYETTE, S. (1995): Long-Term Monitoring of Permafrost Change in a Palsa Peatland in Northern Quebec, Canada: 1983-1993. In: *Arctic and Alpine Research*, 27, pp 167-171.
- LACHENBRUCH, A.H. & MARSHAL, B.V. (1986): Changing climate: geothermal evidence from permafrost in the Alaskan Arctic. In: *Science*, 234, pp. 689–696.
- LAGAREC, D. (1980): Étude géomorphologique de paises et autres buttes cryogènes en Hudsonie, Nouveau-Québec. Thèse de doctorat, Université Laval, Québec, 290 pp.
- LAGAREC, D. (1982): Cryogenic mounds as indicators of permafrost conditions, northern Quebec. In: *Proceedings of the Fourth Canadian Permafrost Conference*, pp. 43-48.
- LAJEUNESSE, P. (2000): Géologie et géomorphologie du Quaternaire de la région de la rivière Nastapoka, côte est de la Baie d'Hudson, Québec. Thèse de doctorat, Faculté des études supérieures, Université Laval, 246 pp.
- LANTUIT, H. & POLLARD, W.H. (2005): Temporal stereophotogrammetric analysis of retrogressive thaw slumps on Herschel Island, Yukon Territory. In: *Natural Hazards and Earth System Science*, 5, pp. 413 – 423.
- LARSEN, Y. (2011): Seasonal Periglacial Activity in Permafrost Landscapes Measured with High-Resolution InSAR Time Series. 4. TerraSAR- X Science Team Meeting, 2011, Oberpfaffenhofen, Deutschland.
- LAURION, I., VINCENT, W.F., MACINTYRE, S., RETAMAL, L., DUPONT, C., FRANCUS, P., PIENITZ, R. (2010) : Variability in greenhouse gas emissions from permafrost thaw ponds. In: *Limnology and Oceanography*, 55, pp- 115-133.
- LEE, J. – S., POTTIER, E. (2009): Polarimetric Radar Imaging: From basics to applications. CRC Press.
- LEMPKE, P., REN, J., ALLEY, R.B., ALLISON, I., CARRASACO, J., FLATO, G., THOMAS, Y., ZHANG, T.. (2007): Observations: Changes in Snow, Ice and Frozen Ground. In: SOLOMON, S.D., QIN, D., MANNING, CHEN, Z., MARQUIS, M., AVERYT, K.B., TIGNOR, M., MILLER, H. L. [Eds.] (2007): *Climate Change 2007: The Physical Science Basis. Contribution of Working Group I to the Fourth Assessment Report of the Intergovernmental Panel on Climate Change*. Cambridge University Press, Cambridge, pp. 337-383.
- LEVESQUE, E. & TREMBLAY, B. (2010): oral information about their vegetation observation methods
- LÉVESQUE, R., ALLARD, M., SEGUIN, M. K. (1988): Distribution et épaisseur du pergélisol aux rivières Nastapoka et Sheldrake, Hudsonie, en relation avec les dépôts quaternaires, Université Laval, Québec, Centre d'études nordiques, Collection Nordicana, No 51, 23 pp., 18 cartes.
- LÉVESQUE, R., ALLARD, M., SEGUIN, M. K. (1989): Regional factor of permafrost distribution and thickness, Hudson Bay coast Québec, Canada, paper presented at 5th International Permafrost Conference, Trondheim, Norway.
- LIANG, S. (2004): Quantitative Remote Sensing of Land Surface. John Wiley & Sons, New Jersey.
- LILLESAND, T. M., KIEFER, R., W., CHIPMAN, J. W. (2008): Remote sensing and image interpretation. John Wiley & Sons.

- LOEW, A. (2004): Coupled modelling of land surface microwave interactions using ENVISAT ASAR data. Dissertation at the Faculty of Geosciences, LMU Munich.
- LUNETTA, R. S. (1999): Application, Project, and Analytical Approach. In: ROSS, S. L. & ELVIDGE C. D. [Eds] (1999): Remote Sensing change Detection Environmental Monitoring Methods and Applications. Taylor and Francis Ltd., London.
- MACKAY, J. R. (1970): Disturbances to the tundra and forest tundra environment of the Western Arctic. In: *Canadian Geotechnical Journal*, 7, pp. 420-32.
- MACKAY, J. R. (1972): The world underground ice. In: *Annals of the Association of American Geographers*, 62, pp. 1-22.
- MACKAY, J. R. (1984): Downward water movement into frozen ground, western arctic coast, Canada. In: *Canadian Journal of Earth Sciences*, 17, pp. 996-1006.
- MANONMANI, R., SUGANYA, G. M. D. (2010): Remote Sensing and GIS Application In Change Detection Study In Urban Zone Using Multi Temporal Satellite. In: *International Journal of Geomatics and Geosciences*, 1 (1), pp. 60 – 65.
- MATHER, P. M. (2004): Computer Processing of Remotely-Sensed Images. 3rd Edition. John Wiley & Sons, West Sussex.
- MAUSER, W. (2010): Fernerkundung. Available at <http://www.geographie.uni-muenchen.de/internetvorlesung/index.php>. Accessed on the 12.05.2011.
- MAY, I., LUDWIG, R., BERNIER, M. (2011): Using TerraSAR-X imagery for the monitoring of permafrost dynamics in Northern Quebec. In: *Proceedings of the 4th TerraSAR-X science Team meeting*, Oberpfaffenhofen.
- MCBEAN, G. (2005): Arctic Climate: Past and Present. In: SYMON, C., ARRIS, L., HEAL, B. [Eds.] (2005): Arctic Climate impact Assessment. Cambridge University Press, New York.
- MCFEETERS, S. K. (1996): The use of the Normalized Difference Water Index (NDWI) in the delineation of open water features. In: *International Journal of Remote Sensing*, 17 (7), pp. 1425 – 1432.
- MEKIS, E & HOGG, W.D. (1999): Rehabilitation and analysis of Canadian daily precipitation time series. In: *Atmosphere – Ocean*, 37, pp. 53 -85.
- MÉNARD, É., ALLARD, M., MICHAUD, Y. (1998): Monitoring of ground surface temperatures in various biophysical micro-environments near Umiujaq, Eastern Hudson Bay, Canada. In: *Proceedings Permafrost – Seventh International Conference*, Yellowknife (Canada), Collection Nodircana, no. 55, 1998, pp. 723- 729.
- MIALON, A., ROYER, A. B., FILY M., PICARD, G. (2007): Daily microwave-derived surface temperature over Canada/ Alaska. In: *Journal of Applied Meteorology*, 46, pp. 591 – 604.
- MILLER, P.C. (Ed.) (1983): Carbon Balance in Northern Ecosystems and the Potential Effect of Carbon Dioxide Induced Climate Change, Springfield, Virginia.
- MONTEIRA, L., S., MOORE, T., HILL, C. (2005): What is the accuracy of DGPS. In: *Journal of Navigation*, (58), pp. 207 – 225.

- MONTENBRUCK, O. (2008): TerraSAR-X Precise Orbit Determination. Available at: <http://www.weblab.dlr.de/rbrt/GpsNav/TSX/TSX.html>. Accessed on the 23.05.2011.
- NAGLER, T. (2011). Ice flow dynamics and mass balance of Vatnajökull outlet glaciers observed by TerraSAR-X. 4. TerraSAR- X Science Team Meeting, 2011, Oberpfaffenhofen, Deutschland.
- NAHO (2011): Drug Abuse Major Concern Among First Nations and Inuit. Available at: <http://www.naho.ca/blog/2011/06/27/>. Accessed on 10.08.2011.
- NASA (1994): SIR-C/X-SAR Space Radar Images of Earth. Available at: <http://www.jpl.nasa.gov/radar/sircxsar/>. Accessed on: 20.08.2010.
- NASA (2011): Landsat then and now. Available at: <http://landsat.gsfc.nasa.gov/about/>. Accessed on 04.05.2011.
- NCDC (2011): Online Climate Data Directory. Available at: www.ncdc.noaa.gov/oa/climate/climatedata.html. Accessed on the 13.05.2011.
- NCDC, NESDIS, NOAA, U.S. Department of Commerce (2000): Comprehensive Aerological Reference Data Set (CARDS) (DSI-6305). Available at: gcmd.nasa.gov/records/GCMD_gov.noaa.ncdc.C00503.html. Accessed on the 13.05.2011.
- NICHOLSON, F.H. (1978): Permafrost modification by changing the natural energy budget. In: *Proceedings of the Third International Conference on Permafrost*, Edmonton, Canada, vol. 1, pp. 61-67.
- NICHOLSON, F.H., GRANBERG, H.B. (1973): Permafrost and snow cover relationships near Schefferville. In *Proceedings to the 2nd International Conference on Permafrost*, Yakutsk, USSR; North American Contribution, pp. 151-8. Washington, D.C.: Nat.Acad.Sci.
- NOAA (2011): Global Historical Climatology Network –Daily. Available at: www.ncdc.noaa.gov/oa/climate/ghcn-daily/. Accessed on the 13.05.2011.
- NSIDC (2008-a): All about Frozen Ground. Available at: http://nsidc.org/frozenground/whereis_fg.html. Accessed on 2.03.2011.
- NSIDC (2008-b): State of the Cyosphere. Available at: <http://nsidc.org/sotc/permafrost.html>. Accessed on 2.03.2011.
- OBERMAN, N.G. & MAZHITOVA, G.G. (2001): Permafrost dynamics in the north-east of European Russia at the end of the 20th century. In: *Norwegian Journal of Geography*. 55, pp. 241-244.
- OECHEL, W.C., HASTINGS, S.J., VOURLITIS, G., JENKINS, M., RIECHERS, G., GRULKE, N. (1993): Recent change of Arctic tundra ecosystems from a net carbon dioxide sink to a source. In: *Letters to Nature*. 361, pp. 520-523.
- OLIVER, C. & QUEGAN, S. (2004): Understanding Synthetic Aperture Radar Images, SciTech Publishing, Boston.
- OLSEN, R. C. (2007): Remote Sensing from Air and Space. SPIE – The International Society for Optical Engineering, Bellingham, Washington.

- OSTERKAMP, T. (2005): The recent warming of permafrost in Alaska. In: *Global and Planetary Change*(2005). 49, pp. 187-202.
- ÖSTREM, G. (1963): Ice-cored moraines in Scandinavia. In: *Geografiske Annaler.*, 46, pp. 282-337.
- PAVLOV, A.V. (1996): Permafrost-climate monitoring of Russia: analysis of field data and forecast. In: *Polar Geography.* 20, pp. 44-64.
- PAYETTE, S. (1983): The forest tundra and present tree-lines of the northern Quebec-Labrador peninsula. In: *Proceedings of the northern Quebec tree-line conference, Québec.* Collection Nordicana, 47, pp. 3-24.
- PETERSON, T. C., GALLO, K. P., LIVEMORE, J., OWEN, T.W., HUANG, A., MCKITTRICK, D.A. (1999): Global rural temperature trend. In: *Geophysical Research Letters*, 26, pp. 329 – 332.
- PETERSON, T. C. & VOSE, R. S. (1997): An overview of the Global Historical Climatology Network temperature database. In: *Bulletin of the American Meteorological Society*, 78, pp. 2837 – 2849.
- PHILIPPS, D.W. (1984): Climatic atlas Canada: a series of maps portraying Canada's climate, Ottawa, Canada. In: Gouvernement du Canada [Ed.] (1984): Climatic atlas Canada: a series of maps portraying Canada's climate, Ottawa, Canada.
- PISSART, A. (1974): Determination experimentale des processus responsables des petits sols polygonaux triés de haut montagne. In : *Abh. Akad. Wiss Gottingen*, 3, pp. 86-101.
- PISSART, A. (2002): Palsas, lithalsas and remnants of these periglacial mounds. A progress report. In: *Progress in Physical Geography*, 26, pp. 605-621.
- PLANK, S. (2011): Suitability evaluation of the differential radar interferometry method for the detection and deformation monitoring of mass movements. 4. TerraSAR- X Science Team Meeting, 2011, Oberpfaffenhofen, Deutschland.
- POLLARD, W. H., & FRENCH, H.M. (1985): The internal structure and ice crystallography of seasonal frost mounds. In: *Journal of Glaciology*, 31, pp. 157-162.
- POLYAKOV, I. V., BEKRYAEV, R. V., ALEKSEEV, G. V., RHATT, U. S., COLONY, R. L., JOHNSON, M.A., MAKSHITAS, A. P., WALSH, D. (2003): Variability and trend of air temperature and pressure in the maritime Arctic 1875 -2000. In: *Journal of Climate*, 16, pp. 2067 – 2077.
- PRASAD, S., BRUCE, L. M., CHANUSSOT, J. (2011): Optical Remote Sensing, Advances in Signal Processing and Exploitation Techniques. Springer Verlag, Heidelberg, Dordrecht, London, New York.
- QIU, G., ZHOU, Y., GUO, D., WANG, Y. (2000): The map of geocryological regionalization and classification in China. In: ZHOU, Y., GUO, D., QIU, G., CHENG, G., LI, S. [Eds.] (2000): Geocryology in China, Science Press, Beijing.
- QU, N.-N., GUANG, Z., ZHAO, X., JING, C.-F., LV, J. (2010): The analysis of surface deformation base on two-pass and three-pass D-InSAR. In: *Geoscience and Remote Sensing Symposium (IGARSS), 2010 IEEE International*, pp. 4561-4563.
- RACHOLD, V., EICKEN, H., GORDEEV, V. V., GRIGORIEV, M.N., HUBBERTEN, H.-W., LISITZIN, A.P., SHEVCHENKO, V. P., SCHIRRMERISTER, L. (2003): Modern terrigenous organic carbon input to the

- Arctic Ocean. In: STEIN, R. & MACDONALD, R. W. [Eds.] (2003): Organic Carbon Cycle in the Arctic Ocean: Present and Past, Springer Verlag, Berlin, pp. 33–55.
- RAGHUNATH, H. M. (2006): Hydrology. Principles, Analysis, Design. New Age international, Delhi.
- RICHARDS, J. A. (2009): Remote Sensing with Imaging Radar. Springer Verlag, Heidelberg, Berlin.
- RICHARDS, J. A. & JIA, X. (2006): Remote Sensing Digital Image Analysis. 4th Edition. Springer Verlag, Berlin, Heidelberg.
- RICHHARIA, M. & WESTBROOK, L. D. (2010): Satellite Systems for Personal Applications. Concepts and Technology. John Wiley and Sons, Singapore.
- RICHTER-MENGE, J. & OVERLAND, J.E. (2010): 2010 Arctic Report Card. Available at www.arctic.noaa.gov/reportcard. Accessed on the 4.05.2011.
- RISEBOROUGH, D.W. (1985): Modelling climatic influences on permafrost at a boreal forest site. Unpublished M.A.thesis, Carleton University, Ottawa, 172 pp.
- ROECKNER, E., OBERHUBER, J.M., BACHER, A., CHRISITOPH, M., KIRCHNER, I. (1996): ENSO variability and atmospheric responses in a global coupled atmosphere-ocean GCM. In: *Climate Dynamics*, 12, pp. 737-754.
- ROOTS, E.F. (1989): Climate Change: High-latitudes regions. In: *Climatic Change*, 15, pp. 223-253.
- ROSOW, W. B. & SCHIFFER, R. A. (1999): Advances in understanding clouds from ISCCP. In: *Bulletin of the American Meteorological Society*, 80, pp. 2261 – 2287.
- ROUSE, W.R (1982): Microclimate of low Arctic tundra and forest at Curchill, Manitoba. In: *Proceedings of the Fourth Canadian Permafrost Conference*, Calgary, Alberta. Pp. 68-80. Ottawa: N.R.C.C.
- ROUSE, W.R (1984): Microclimate of Arctic tree line. 2: Soil microclimate of tundra and forest. In. *Water Resources Research*, 20, pp. 67-73.
- ROUSE, W.R. (1991): Impacts of Hudson Bay on the terrestrial climate of the Hudson Bay Lowlands. In: *Arctic and Alpine Research*, 23, pp. 24-30.
- ROUSSEAU, J. (1968): The vegetation of Québec-Labrador peninsula between 55° and 60°N. In: *Natur Canada*, 95, pp. 469-563.
- SANTITAMNONT, P. (1998): Interferometric SAR Processing for Topographic Mapping, Dissertation, Fachbereich Bauingenieur- und Vermessungswesen, Universität Hannover, Deutschland.
- Satellite Image Corporation (2010): About ASTER. Available at <http://www.satimagingcorp.com/satellite-sensors/aster.html>. Accessed on the 5.05.2011.
- SCHOWENGERDT, R. A. (1985): Techniques for Image Processing and Classification in Remote Sensing. Academic Press, London.
- SCHOWENGERDT, R. A. (1997): Remote Sensing. Models and Methods for Image Processing. Elsevier Academic Press, San Diego.
- SCHRÜFER, E. (1990): Signalverarbeitung, Carl Hanser Verlag, München.

- SCHWÄBISCH, M. (1995): Die SAR-Interferometrie zur Erzeugung digitaler Geländemodelle, Forschungsbericht 95-25, Deutsche Forschungsanstalt für Luft- und Raumfahrt, Oberpfaffenhofen.
- SEGUIN, M. K. & ALLARD, M. (1984): Le pergélisol et les processus thermokarstiques de la région de la rivière Nastapoca, Nouveau-Québec. In : *Géographie physique et Quaternaire*, 38, pp. 11-25.
- SEPPÄLLÄ, M. (1979): Recent palsa studies in Finland. In: *Palaeohydrology of the temperate zone*. Geologica, 3, pp. 81-7.
- SERPICO, S. B. & BRUZZONE, L. (1999): Change Detection. In: CHEN, C. H. [Ed.] (1999): *Information Processing for Remote Sensing*. World Scientific Publishing Co. Pte. Ltd., London.
- SERREZE, M. C. & BARRY, R.G. (2005): *The Arctic Climate System*. Cambridge University Press, New York.
- SHI, C. AND DOZIER J. (2000): Estimation of snow water equivalence using SIR-C/X-SAR, part II: Inferring snow depth and particle size. In: *IEEE Transactions on Geoscience and Remote Sensing*, 38, pp. 2475 – 2488.
- SHORT, N.M. (no date): Glacial landforms. Available at: http://rst.gsfc.nasa.gov/Sect17/Sect17_5a.html. Accessed on the 12.03.2011)
- SINGH, A. (1988): Digital change detection techniques using remotely-sensed data. In: *International Journal of Remote Sensing*, 10 (6), pp. 989 -1003.
- SKAVEN HAUG, S. (1959): Protection against frost heaving on Norwegian railways. In: *Geotechnique*, 9, pp. 87-106.
- SKOLNIK, M. I. (1962): *Introduction to Radar Systems*, McGraw-Hill Kogakusha, Ltd., Tokyo.
- SMITH, J.B., HULME, M., JAAGUS, J., KEEVALLIK, S., MEKONNEN, A., HAILEMARIAN, K. (1998): *Climate Change Impact Assessment and Adaptation Strategies*. Version 2.0. United Nations Environment Programme and Institute for Environmental Studies, Vrije Universiteit, Amsterdam. Pp. 31 -40.
- SMITH, M.W. (1975): Microclimate influences on ground temperatures and permafrost distribution, Mackenzie Delta . Northwest Territories. *Canadian Journal of Earth Sciences*, 12, 1421-38.
- SMITH, S. L., BURGESS, M. M., RISEBOROUGH, D., NIXON, F. M. (2005): Recent trends from Canadian permafrost thermal monitoring network sites. In: *Permafrost and Periglacial Processes*, 16, pp. 19–30.
- SMITH, S.L., ROMANOSKI, V.E., LEWKOWICZ, A.G., BUM, C.R., ALLARD, M., CLOW, G.D., YOSHIKAWA, K., THROOP, J. (2010): Thermal State of Permafrost in North America: A Contribution to the International Polar Year. In: *Permafrost and Periglacial Processes*, 21, pp. 117-135
- SMITS, C., USTIN, S. L., ADAMS J. B., GILLEPSIE, A. R. (1999): Quality assessment of image classification algorithms for land-cover mapping: a review and a proposal for a cost-based approach. In: *International Journal of Remote Sensing*, 14, pp. 1461 – 1486.
- SNOWBALL, M. (2010): oral information
- SOLOMON, S., QIN, D., MANNING, M., CHEN, Z., MARQUIS, M., AVERYT, K.B., TIGNOR, M., MILLER, H.L. [Eds.] (2007): *Contribution of Working Group I to the Fourth Assessment Report of the*

- Intergovernmental Panel on Climate Change, 2007. In: *IPCC Fourth Assessment Report, 2007*, Cambridge University Press, Cambridge, New York.
- STAMMLER, F. (2009): Mobile phone revolution in the tundra? Technological change among the Russian reindeer nomads. In: *Folklore*, 14, pp. 47 -78.
- Statistics Canada (2004): Community Profile. Available online <http://www.nunivaat.org/TableViewer.aspx?S=1&ID=1381>. Accessed on 10.04.2011.
- Statistics Canada (2010): 2006 Aboriginal Population Profile. Available at: <http://www.nunivaat.org/TableViewer.aspx?S=1&ID=9527>. Accessed on 10.04.2011.
- Statistics Canada (2011): Age (123) And Sex (3) For The Population Of Canada, Provinces, Territories, Census Divisions And Census Subdivisions, 2006 Census - 100% Data. Available online <http://www.nunivaat.org/TableViewer.aspx?S=1&ID=8433>. Accessed on 10.04.2011.
- STEFAN, E.R., EVAND, D.L., SCHMULLIUS C., HOLT, B., PLAUT, J.J., VAN ZYL, J., WALL, S.D., WAY, J. (1995): Overview of results of Spaceborn Imaging Radar-C, X-Band Synthetic Aperature Radar (SIR-C/ X-SAR). In: *IEEE Transactions on Geoscience and Remote Sensing*. 33, pp. 817 -828.
- STEIN, A., VAN DER MEER, F., GORTE, B. (1999): *Spatial Statistics for Remote Sensing*. Kluwer Academic Publishers, Dordrecht.
- STEVENSON, I. M. (1968): A geological reconnaissance of Leaf River Map-Area, New-Québec and Northwest Territories. Geological Survey of Canada, memoir no. 356.
- STIEGLITZ, M., DÉRY, S. J., ROMANOVSKY, V. E., OSTERKAMP, T.E. (2003): The role of snow cover in the warming of arctic permafrost. In: *Geophysical Research Letters*, 30, pp. 1721- 1725.
- STONE, D. A., WEAVER, A. J., ZWIERS, F. W. (2000): Trend in Canadian precipitation intensity. In: *Atmosphere –Ocean*, 33, pp. 321 -347.
- STOW, D. A., HOPE, A., MCGUIRE, D., VERBYLA, D., GAMONA, J., HUEMMERICH, F., HOUSTON, S., RACINE, C., STURM, M., TAPE, K., HINZMAN, L., YOSHIKAWA, K., TWEEDIE, C., NOYLE, B., SILAPASWAN, C., DOUGLAS, D., GRIFFITH, B, JIA, G., EPSTEIN H., WALKER, D., DEASCHNER, S., PETERSON, A., ZHOU, L., MYNENI, R. (2004): Remote sensing of vegetation and land-cover change in Arctic Tundra Ecosystems. In: *Remote Sensing of Environment*, 89, pp. 281 – 308.
- SUSHAMA, L., R. LAPRISE, M. ALLARD (2006), Modeled current and future soil thermal regime for northeast Canada, In: *J. Geophys. Res.*, 111,
- TABONY, R.C (1981): A principal component and spectral analysis of European rainfall. In: *Journal of Climatology*, 1, pp. 283- 294.
- TARNOCAIL, C. (2006): The effect of climate change on carbon in Canadian peatlands. In: *Global and Planetary Change*, 53: 222-232
- THOMPSON, D. W. J. & WALLACE, J. M. (1998): The Arctic Oscillation signature in the wintertime geopotential height and temperature fields. In: *Geophysical Research Letters*, 25, pp: 1297 – 1300.
- TOU, J. T. & GONZALEZ, R.C. (1974): *Pattern Recognition Principles*. London.

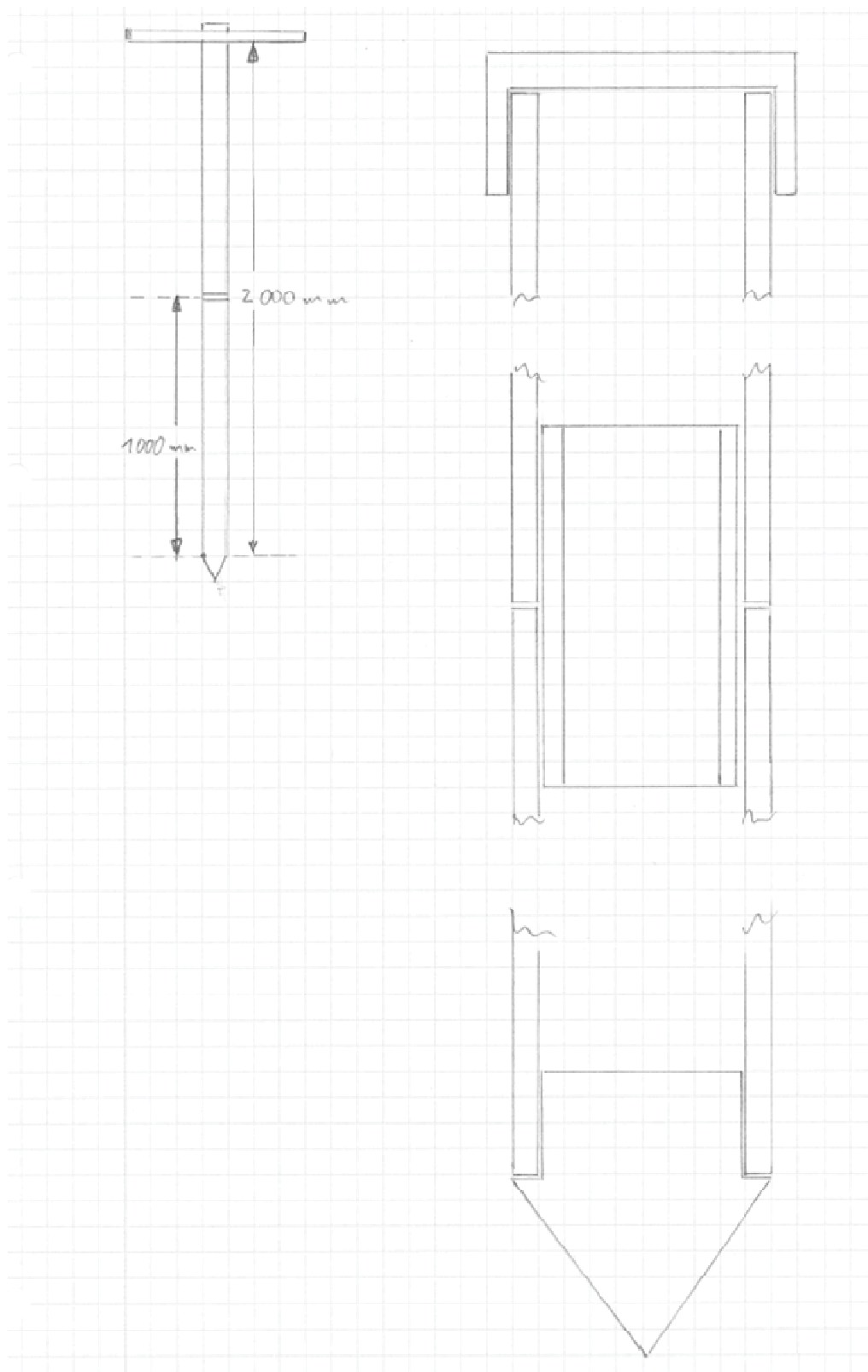
- TRAORÉ, P. C. S, ROYER, A. B., GOITA, K. (1997) : Land surface temperature time series dervied from weekly AVHRR GVI composite datasets : Potential and constraints for northern latitudes. In: *Canadian Journal of Remote Sensing*, 4, pp. 390 – 400.
- TRESHNIKOV, A. F. (1985) Atlas Arktiki, Central Administrative Board of Geodesy and Cartography of Ministeral Council of the USSR, Moscow.
- TRIMBLE (2010): Differential correction. Code phase vs. carrier phase. Available at <http://www.trimble.com/gps/dgps-advanced2.shtml>. Accessed on 15.06.2011.
- TRIMBLE (2011): GPS Tutorial. Available at www.trimble.com/gps/dgps-how.shtml. Accessed on 16.05.2011.
- TSO, B. & MATHER, P. M. (2001): Classification methods for remotely sensed data. Taylor and Francis, London.
- TSYTOVICH, N. A. ET AL. (1959): Principles of Geocryology. Part I, General Geocryology. In: *Acad.Sci. USSR*, 459 pp.
- United States Central Intelligence Agency (1978): Polar Regions Atlas.
- USAI, S. & KLEES, R. (1999): SAR Interferometry on very long time scale: A Study of the interferometric characteristics of man-made features. In: *IEEE transactions on Geoscience and Remote Sensing*, 37 (4), pp. 2118-2123.
- VENKATARAMAN, G. (2011). Glacier Surface motion estimation in the Himalays using TerraSAR-X spotlight repeat pass data. 4. TerraSAR- X Science Team Meeting, 2011, Oberpfaffenhofen, Deutschland.
- WALTER, K. M., EDWARDS, M., GROSSE, G., ZIMOV, S. A., STUART CHAPIN III, F. (2007): Thermokarst lakes as a source of atmospheric CH₄ during the last deglaciation. In: *Science*, 318, pp. 633-636.
- WALTER, K. M., ZIMOV, S. A., CHANTON, J. P., VERBYLA, D., STUART CHAPIN III, F. (2006): Methan bubbling from Siberian thaw lakes as a positive feedback to climate warming. In: *Nature*, 443, pp. 71-75.
- WERNER, C., WEGMÜLLER, U., STROZZI, T., WIESMANN, A. (2002): Processing strategies for phase unwrapping for INSAR applications. In: *Proceedings EUSAR 2002*, Cologne, 4-6 June, 2002.
- WIELICKI, B. A., CESS, R.D, KING, M.D., RANDALL, D.A., HARRISON, E.F. (1995): Mission to planet Earth: role of clouds and radiation in climate. In: *Bulletin of the American Meteorological Society*, 76, pp. 2125 – 2153.
- WILLIAMS, P. J. & SMITH, M. W. (1989): The Frozen Earth. Fundamentals of Geocryology. Cambridge University Press, New York.
- WILSON, C. (1971) : Le climat du Québec. Première partie: atlas climatique, Ottawa, Canada. Service météorologique du Canada (Ed.) (1971), Information Canada, Études climatologiques 11.
- WOODHOUSE, I. H. (2006): Introduction to microwave remote sensing. Taylor and Francis Group.
- XU, H. (2006): Modification of moramlised difference water index (NDWI) to enhance open water features in remotely sensed imagery. In: *International Journal of Remote Sensing*, 27 (14), pp 3025 -3033.

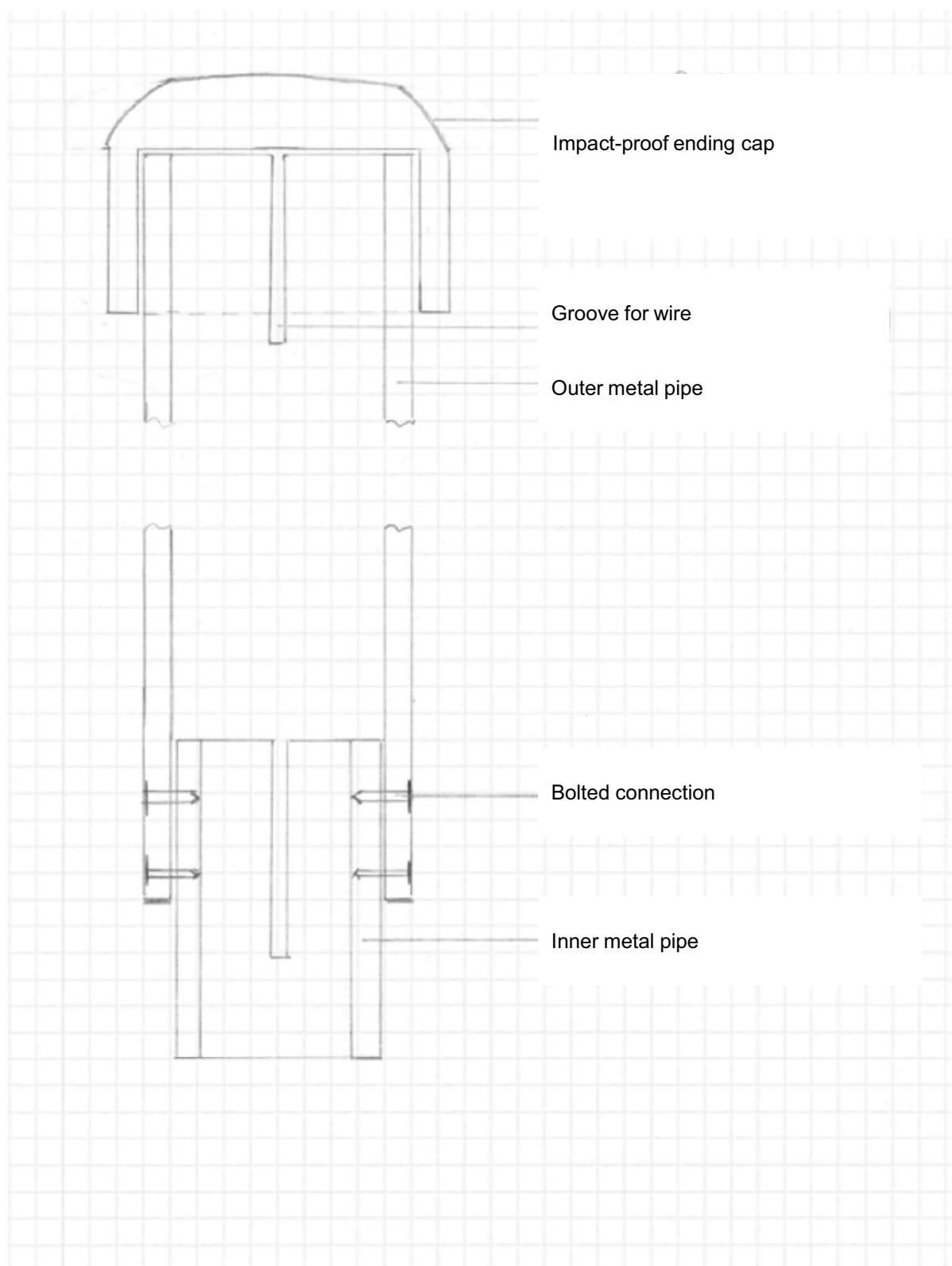
- XU, H. & YOUNG, J. A. (1990): Monitoring changes in land use through integration of remote sensing and GIS. In: *Proceedings of IGARSS '90 Symposium*, Maryland, pp. 957 – 960.
- YAMAGUCHI, Y., KAHLE, A. B., TSU, H., KAWAKAMI, T., PNIEL, M. (1998): Overview of Advanced Spaceborne Thermal Emission and Reflection Radiometer (ASTER). In: *IEEE Transactions on Geoscience and Remote Sensing*, 36 (4), pp. 1062 – 1071.
- YERSHOV, E.D. (1990): Obshchaya Geokriologiya.
- YOUNG, T. K & BJERREGAARD, T. M. [Eds.] (2008): Health Transition in Arctic Populations. University Toronto Press, Toronto.
- YOUNG, T. K. & MÄKINEN, T. M. (2009): The health if Arctic populations: Does cold matter? In: *American Journal of Human Biology*, 22, pp. 129 – 133.
- ZEBKER, H. A. & LU, Y. (1998): Phase unwrapping algorithms for radar interferometry: residue-cut, leastsquares, and synthesis algorithms. In: *Journal of the Optical Society of America A*, 15(3), pp. 586-598.
- ZEBKER, H. A., ROSEN, P. A., GOLDSTEIN, R. M., GABRIEL, A., WERNER, C. L. (1994): On the derivation of coseismic displacement fields using differential radar interferometry: The Landers earthquake. In: *Journal of Geophysical Research*, 99, pp.19617-19634.
- ZHANG, P., ANDERSON, B., BARLOW, M., TAN, B., MYNENI, R.B. (2004): Climate related vegetation characteristics derived from Moderate Resolution Imaging Spectroradiometer (MODIS) leaf area index and normalized difference vegetation index. In: *Journal of Geophysical Research*, 109, pp. 1–13.
- ZHANG, T. (2005): Influence of the seasonal snow cover on the ground thermal regime: an overview. *Reviews of Geophysics* 43, pp. 421 – 432.
- ZHANG, T., BARRY, R. G., KNOWELS, K., LING, F., ARMSTRONG, R. L. (2003): Distribution of seasonally and perennially frozen ground in the Northern Hemisphere. In: PHILLIPS, M., SPRINGMAN, S., ARENSON, L [Eds.] (2003): *Permafrost*. Swets and Zeitlinger.
- ZHANG, T., BARRY, R. G., KNOWELS, K., HEGINBOTTOM, J. A., BROWN, J. (1999): Statistics and characteristics of permafrost and ground-ice distribution in the Northern Hemisphere. In: *Polar Geography*, 32 (2), pp.132-154.
- ZHAO, L., PING, C.-L., YANG, D., CHENG, G., DING, Y., LIU, S. (2004): Changes of climate and seasonally frozen ground over the past 30 years in Qinghai-Xizang (Tibetan) Plateau, China. In: *Global and Planetary Change*, 43, pp. 19–31.
- ZHOU, X., CHANG, N. B., LI, S. (2009): Applications of SAR Interferometry in Earth and Environmental. In: *Science Research Sensors*, 9, pp. 1876-1912.
- ZHOU, Y., GAO, X., WANG, Y. (1996): The ground temperature changes of seasonally freeze-thaw layers and slimate warming in Northeast China in the past 40 years. In: *Proceedings of the 5th Chinese Conference on Glaciologie and Geocryology*, 1. Gansu Culture Press, Lanzhou, 3-9.
- ZIMOV, S. A., SCHUUR, E. A. G., STUART CHAPIN III, F. (2006): Permafrost and the global carbon budget. In: *Science*. 312, pp. 1612-1613.

11 Appendix

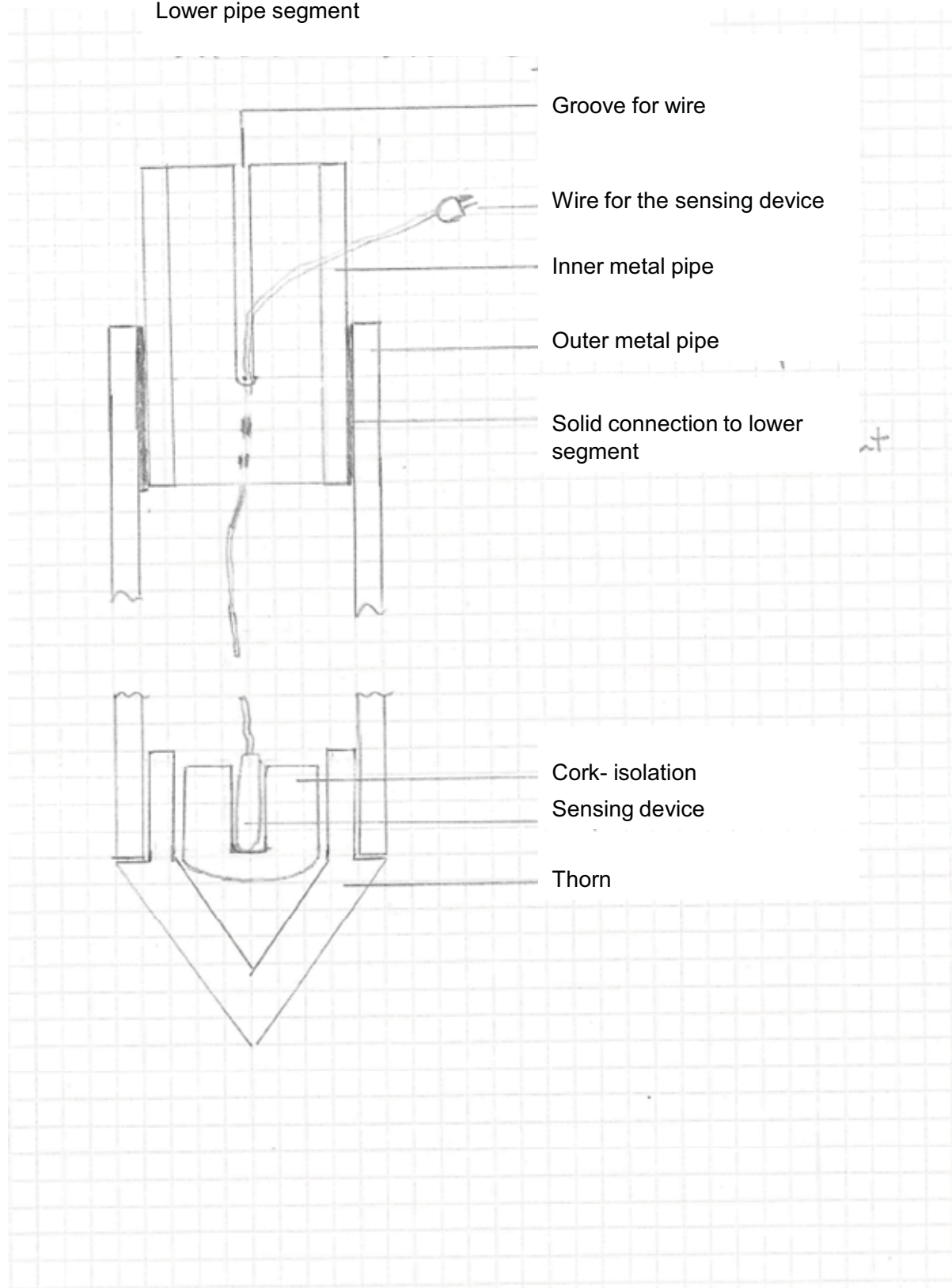
APPENDIX 1

Sketch of the self-made instrument to measure snow depth, snow temperature and active layer depth



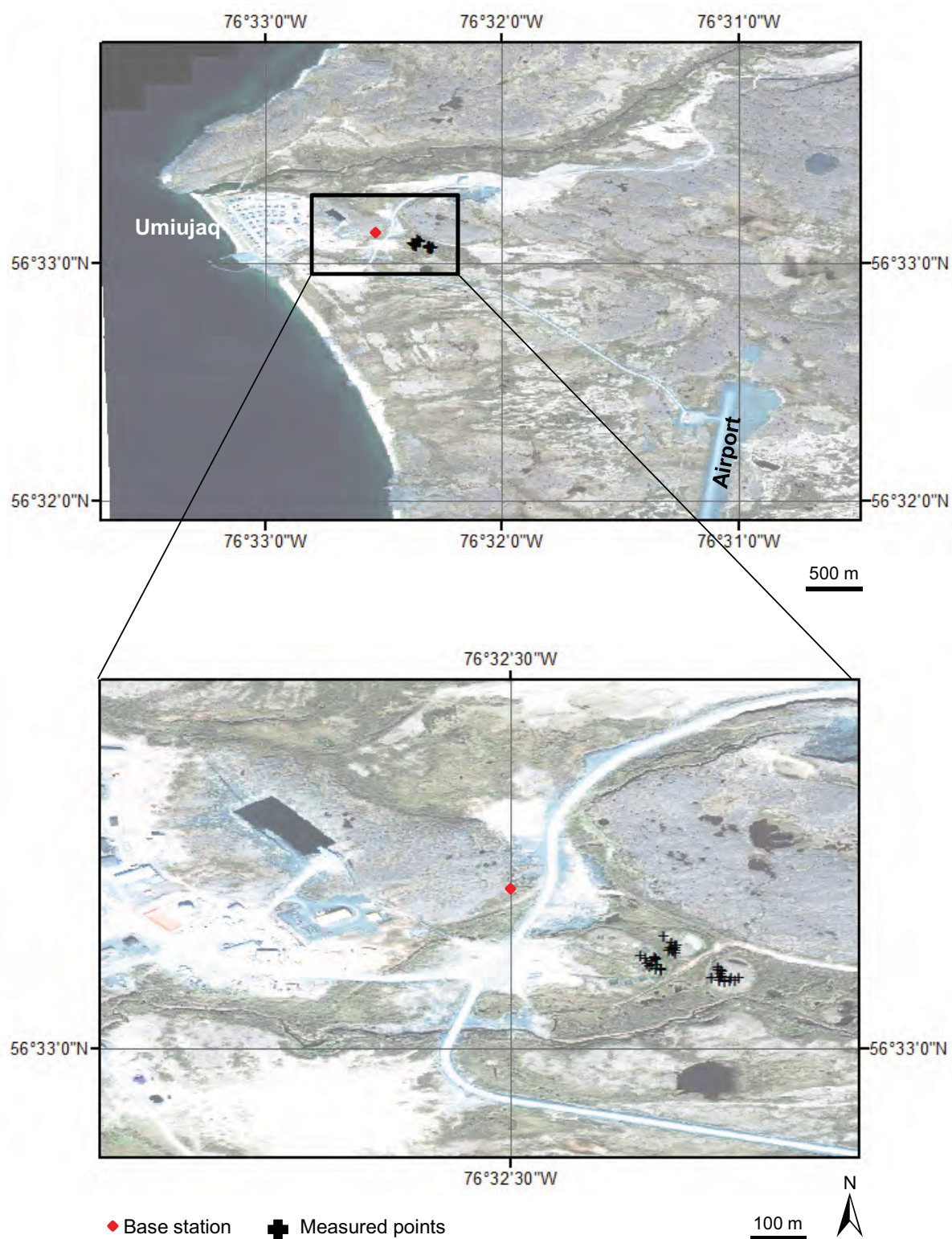


Lower pipe segment



APPENDIX 2

Location of the base station and the measured points for the geodetical survey by means of a d-GPS



APPENDIX 3

Description of the recorded points on the three lithalsas R, M, and I

Lithalsa R

	Coordinates		Vegetation	Notes
Basis	56°33'07,07424"	76°32'19,35866"	- no vegetation -	
P 1	56°33'05,50024"	76°32'21,02497"	<i>Sphagnum</i>	planar
P 2	56°33'05,34408"	76°32'21,00985"	- no vegetation -	Planar, westwards small depression
P 3	56°33'05,20574"	76°32'21,02176"	<i>Sphagnum</i>	Steep slope
P 4	56°33'05,33299"	76°32'21,13118"	<i>Sphagnum</i> , <i>Betula nana</i>	planar
P 5	56°33'05,38129	76°32'21,34052"	<i>Betula nana</i> (- 50cm)	Konkave / parallel slope
P 6	56°33'05,50267	76°32'21,32257"	<i>Betula nana</i>	Konkave/ parallel slope
P 7	56°33'05,44929"	76°32'21,17383"	<i>Sphagnum</i> Lichen	planar
P 8	56°33'05,39987"	76°32'21,13327"	<i>sphagnum</i> , Grass	planar
P 9	56°33'06,13215"	76°32'21,68630"	<i>Betula nana</i> (- 20 cm)	planar
P 10	56°33'05,80443"	76°32'21,20164"	<i>Betula nana</i> (- 20 cm)	Planar, slope / pond
P 11	56°33'05,68144"	76°32'20,96052"	shrub	Slope / pond
P 12	56°33'05,61717"	76°32'21,07062"	<i>Sphagnum</i> , sand	Slope / pond
P 13	56°33'07,07424"	76°32'19,35866"	- no vegetation -	

Lithalsa M

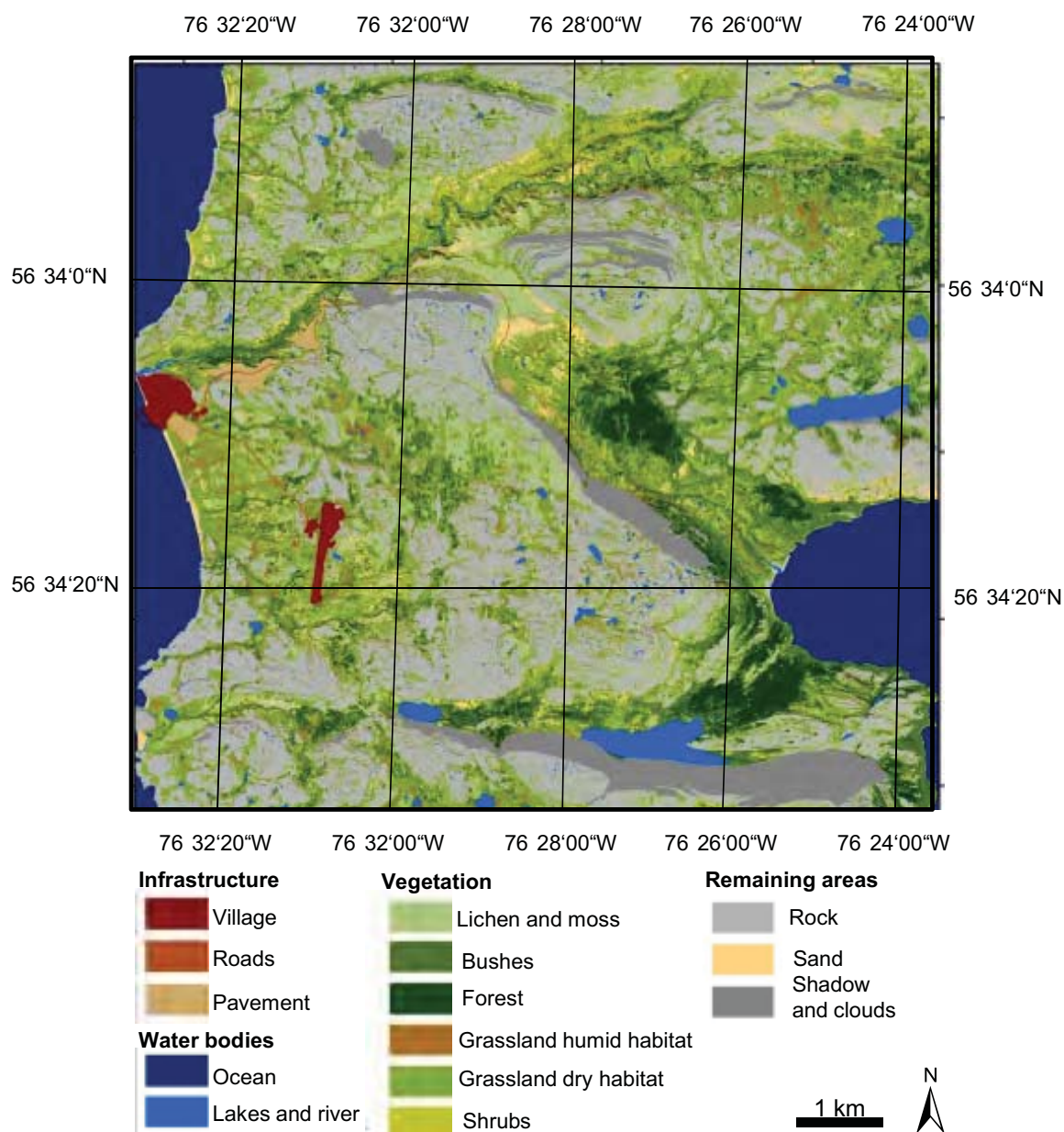
	Coordinates		Vegetation	Notes
Basis	56° 33' 07.06590"	76° 32' 19.35897"	- no vegetation -	
P 1	56° 33' 04.45054"	76° 32' 18.72315"	<i>Sphagnum</i>	planar
P 2	56° 33' 04.35706"	76° 32' 18.66631"	<i>Sphagnum</i> , <i>betula nana</i>	planar
P 3	56° 33' 04.29214"	76° 32' 18.57078"	<i>Sphagnum</i> , <i>betula nana</i>	planar
P 4	56° 33' 04.22342"	76° 32' 18.50268"	<i>Sphagnum</i>	Cracked soil
P 5	56° 33' 04.12166"	76° 32' 18.53885"	<i>Sphagnum</i>	Cracked soil
P 6	56° 33' 03.98515"	76° 32' 18.46049"	<i>Sphagnum</i>	
P 7	56° 33' 03.91417"	76° 32' 17.97208"	<i>Sphagnum</i>	planar
P 8	56° 33' 03.90102"	76° 32' 17.55430"	Lichen	Small (50 cm) depression
P 9	56° 33' 03.72433"	76° 32' 17.77892"	Lichen	Small (50 cm) depression, very dry
P 10	56° 33' 03.72056"	76° 32' 18.02819"	Lichen	
P 11	56° 33' 03.71629"	76° 32' 18.35757"	<i>Betula nana</i>	Konkave slope, dry
P 12	56° 33' 03.72095"	76° 32' 18.61074"	<i>Betula nana</i>	
P 13	56° 33' 03.92972"	76° 32' 19.01229"	<i>Betula nana</i>	Parallel slope
P 14	56° 33' 03.90731"	76° 32' 18.59369"	<i>Betula nana</i>	Small depression

Lithalsa I

	Coordinates		Vegetation	Notes
Basis	56°33'07,07600"	76°32'19,35822"		
P 1	56°33'05,04869"	76°32'22,15950"	shrub	planar
P 2	56°33'04,96755"	76°32'22,07800"	<i>sphagnum</i>	planar Small depression
P 3	56°33'04,86276"	76°32'22,07141"	<i>Sphagnum</i> , shrub	Small depression
P 4	56°33'04,62111"	76°32'21,98475"	Bodendecker	Small depression
P 5	56°33'04,39629"	76°32'21,81790"	<i>Sphagnum</i> , Grass	Steep slope
P 6	56°33'04,27307"	76°32'21,83989"	<i>sphagnum</i>	Parallel slope
P 7	56°33'04,40337"	76°32'22,08492"	Grass	planar
P 8	56°33'04,54682"	76°32'22,43079"	Grass	planar
P 9	56°33'04,61103"	76°32'22,28135"	Grass	planar
P 10	56°33'04,70985"	76°32'22,61359"	Grass	planar
P 11	56°33'04,84560"	76°32'22,32717"	<i>sphagnum</i>	planar
P 12	56°33'04,97802"	76°32'22,65357"	shrub	planar
P 13	56°33'05,06039"	76°32'22,92485"	frostblister	Parallel slope

APPENDIX 4

Classification map based on the GeoEye image from 2009



APPENDIX 5**Parameter file for TerraSAR-X acquisition of the 14.08.2009**

Gamma Interferometric SAR Processor (ISP) - Image Parameter File

```

title:      SSC____SM_D
sensor:     TSX-1
date:       2009 8 14 22 47 8.6100
start_time:      82028.957123    s
center_time:     82029.304072    s
end_time:        82029.651022    s
azimuth_line_time: 3.4712298e-04 s
line_header_size:      0
range_samples:        5000
azimuth_lines:        2000
range_looks:          1
azimuth_looks:        1
image_format:         SCOMPLEX
image_geometry:       SLANT_RANGE
range_scale_factor:   1.0000000e+00
azimuth_scale_factor: 1.0000000e+00
center_latitude:      56.5419907 degrees
center_longitude:     -76.4980481 degrees
heading:              -10.2336095 degrees
range_pixel_spacing:  0.909403    m
azimuth_pixel_spacing: 2.444816    m
near_range_slc:        659870.7079 m
center_range_slc:      662143.7607 m
far_range_slc:         664416.8135 m
first_slant_range_polynomial: 0.00000    0.00000    0.00000e+00
0.00000e+00 0.00000e+00 0.00000e+00 s m 1 m^-1 m^-2 m^-3
center_slant_range_polynomial: 0.00000    0.00000    0.00000e+00
0.00000e+00 0.00000e+00 0.00000e+00 s m 1 m^-1 m^-2 m^-3
last_slant_range_polynomial: 0.00000    0.00000    0.00000e+00
0.00000e+00 0.00000e+00 0.00000e+00 s m 1 m^-1 m^-2 m^-3
incidence_angle:      40.6956    degrees
azimuth_deskew:       ON
azimuth_angle:        90.0000    degrees
radar_frequency:      9.6500000e+09 Hz
adc_sampling_rate:    1.6482919e+08 Hz
chirp_bandwidth:      1.5000000e+08 Hz
prf:                  2880.823406 Hz
azimuth_proc_bandwidth: 1380.00000 Hz
doppler_polynomial:   21.88717    -3.27381e-05    0.00000e+00
0.00000e+00 Hz      Hz/m      Hz/m^2      Hz/m^3
doppler_poly_dot:     -7.08745e+00    0.00000e+00    0.00000e+00
0.00000e+00 Hz/s    Hz/s/m    Hz/s/m^2    Hz/s/m^3
doppler_poly_ddot:    0.00000e+00    0.00000e+00    0.00000e+00
0.00000e+00 Hz/s^2 Hz/s^2/m    Hz/s^2/m^2    Hz/s^2/m^3
receiver_gain:        5.8940    dB
calibration_gain:     49.9420    dB
sar_to_earth_center:  6880293.9926    m
earth_radius_below_sensor: 6363482.7267    m
earth_semi_major_axis: 6378137.0000    m
earth_semi_minor_axis: 6356752.3141    m
number_of_state_vectors: 12
time_of_first_state_vector: 81985.000000    s
state_vector_interval: 10.000000    s

```

state_vector_position_1:	614554.8482	-4110392.9144	5483696.0573
m m m			
state_vector_velocity_1:	-2792.07500	5578.54500	4482.87100
m/s m/s m/s			
state_vector_position_2:	586638.1621	-4054338.6320	5528188.4569
m m m			
state_vector_velocity_2:	-2791.19300	5632.19800	4415.52000
m/s m/s m/s			
state_vector_position_3:	558732.3752	-3997751.2468	5572004.6426
m m m			
state_vector_velocity_3:	-2789.89500	5685.16500	4347.63000
m/s m/s m/s			
state_vector_position_4:	530841.6512	-3940637.6656	5615139.2753
m m m			
state_vector_velocity_4:	-2788.18100	5737.43600	4279.21100
m/s m/s m/s			
state_vector_position_5:	502970.1402	-3883004.8655	5657587.1031
m m m			
state_vector_velocity_5:	-2786.05300	5789.00700	4210.27000
m/s m/s m/s			
state_vector_position_6:	475121.9833	-3824859.8905	5699342.9579
m m m			
state_vector_velocity_6:	-2783.51100	5839.87000	4140.81700
m/s m/s m/s			
state_vector_position_7:	447301.3041	-3766209.8534	5740401.7538
m m m			
state_vector_velocity_7:	-2780.55700	5890.01800	4070.86000
m/s m/s m/s			
state_vector_position_8:	419512.2164	-3707061.9357	5780758.4927
m m m			
state_vector_velocity_8:	-2777.19300	5939.44500	4000.40700
m/s m/s m/s			
state_vector_position_9:	391758.8165	-3647423.3809	5820408.2618
m m m			
state_vector_velocity_9:	-2773.42000	5988.14500	3929.46700
m/s m/s m/s			
state_vector_position_10:	364045.1845		-3587301.4981
5859346.2349 m m m			
state_vector_velocity_10:	-2769.23900		6036.11000
3858.04900 m/s m/s m/s			
state_vector_position_11:	336375.3887		-3526703.6645
5897567.6740 m m m			
state_vector_velocity_11:	-2764.65300		6083.33400
3786.16200 m/s m/s m/s			
state_vector_position_12:	308753.4761		-3465637.3121
5935067.9291 m m m			
state_vector_velocity_12:	-2759.66300		6129.81200
3713.81400 m/s m/s m/s			

APPENDIX 6

Guideline for differential interferogram processing

The output of every processing step is marked in yellow.

1. Preprocessing

1. par_TX_SLC 301009.xml VV301009.cos 301009.slc.par 301009.slc VV
 2. SLC_copy 250809.slc 250809.slc.par 250809.kslc 250809.kslc.par - - 1800 6000 2500 2000
- Bzw: 2000 5000 1000 2000
- disSLC 250809.aslc 6000

Output at this stage:

Scene1.aslc (+ par)
Scene2.aslc (+par)
Scene3.aslc (+par)

2. Int 1 (topographie) and Int 2 (displacement)

COREGISTRIERUNG

1. create_offset 120810.rslc.par 230810.rslc.par 120810_230810.off.par 1 1 1
2. init_offset 120810.rslc 230810.kslc 120810.rslc.par 230810.kslc.par 120810_230810.off.par
3. init_offset_orbit 120810.rslc.par 230810.kslc.par 120810_230810.off.par
4. offset_pwr 120810.rslc 230810.kslc 120810.rslc.par 230810.kslc.par 120810_230810.off.par
offs snr 128 128 offsets 1 8 8 7.0
5. offset_fit offs snr 120810_230810.off.par coeffs coeffs - 4 0

COREGISTRIERUNG

RESAMPLING

6. SLC_interp 230810.kslc 120810.rslc.par 230810.kslc.par 120810_230810.off.par 230810.rslc
230810.rslc.par

RESAMPLING

Optional: Refinement

1. create_offset 120810.rslc.par 220310.rslc.par 120810_220310.ref.off.par 1 1 1
2. offset_pwr 120810.rslc 220310.rslc 120810.rslc.par 220310.rslc.par
120810_220310.ref.off.par offs2 snr2 128 128 offsets2 1 8 8 7
3. offset_fit offs2 snr2 120810_220310.ref.off.par coeffs2 coeffs2 - 4 0

4. *Erstes .off.par unbenannt in .off1.par*
5. *offset_add 120810_220310.off1.par 120810_220310.ref.off.par 120810_220310.off.par*
6. *SLC_interp 220310.kslc 120810.rslc.par 220310.kslc.par 120810_220310.off.par 220310.fslc 220310.fslc.par*

Output at this stage

Unflattened unwrapped interferogram including topography
Unflattened unwrapped interferogram including displacement

3.Unwrapping with scaled interferograms – int 1

BASELINE ESTIMATION

1. base_init 120810.rslc.par 230810.rslc.par 120810_230810.off.par 120810_230810.int
120810_230810.base 2 - -
2. base_perp 120810_230810.base 120810.rslc.par 120810_230810.off.par
120810_230810.base.perp

BASELINE ESTIMATION

INTERFEROGRAM

3. SLC_intf 120810.rslc 230810.rslc 120810.rslc.par 230810.rslc.par 120810_230810.off.par
120810_230810.int 1 1 - - 1 1

INTERFEROGRAM

FLATTENING

4. ph_slope_base 120810_230810.int 120810.rslc.par 120810_230810.off.par
120810_230810.base 120810_230810.flr 1

FLATTENING

ADAPTIVE FILTERING

5. adf 120810_230810.flr 120810_230810.sm 120810_230810.smcc 5000 .5 32 7 4
dismph 120810_230810.sm 5000

ADAPTIVE FILTERING

SCALING

6. multi_cpx 120810_230810.sm 120810_230810.off.par 120810_230810.cpx
120810_230810.cpx.par 2 2
7. multi_look 120810.rslc 120810.rslc.par 120810.k2mli 120810.k2mli.par 2 2
multi_look 230810.rslc 230810.rslc.par 230810.k2mli 120810.k2mli.par 2 2

SCALING**COHERENCE ESTIMATION**

8. cc_wave 120810_230810.cpx 120810.cml 230810.k2mli 120810_230810.cc 2500 5. 5. 1

discc 120810_230810.cc – 3000 -> **Initialisierungspunkt!**

COHERENCE ESTIMATION**ADAPTIVE FILTERING**

9. adf 120810_230810.cpx 120810_230810.sm2 120810_230810.smcc2 2500 .5 32 7

ADAPTIVE FILTERING**VALIDITY MASK**

10. rascc_mask 120810_230810.smcc2 120810_230810.sm2 2500 1 1 0 1 1 0.3 .1 .9 1.
.35 – 120810_230810.mask.ras

VALIDITY MASK**UNWRAPPING**

11. mcf 120810_230810.sm2 120810_230810.smcc2 120810_230810.mask.ras
120810_230810.unw0 3000 1 - - - - 1 1 - **1549 270** (this point has to be chosen)

disrmg 120810_230810.unw0 120810.cml 2500

rasrmg 120810_230810.unw0 120810.cml 2500 1 1 0 1 1 - 1. .35 - -
120810_230810.cpx.unw0.bmp

UNWRAPPING**BACK SCALING**

12. multi_real 120810_230810.unw0 120810_230810.cpx.par 120810_230810.b.unw0
120810_230810.off.par -2 -2
disrmg 120810_230810.b.unw0 120810.mli 5000

BACK SCALING

INTERPOLATION

13. interp_ad 120810_230810.b.unw0 120810_230810.unw_interp 5000 16 16 16 2
14. unw_model 120810_230810.sm 120810_230810.unw_interp 120810_230810.unw 5000 **2180 540** - (this point has to be chosen)
 rasrmg 120810_230810.unw 120810.mli 5000 1 1 0 2 2 - 1. .35 - 1
 120810_230810.unw.bmp

INTERPOLATION**FLATTENING - back**

15. ph_slope_base 120810_230810.unw 120810.aslc.par 120810_230810.off.par
 120810_230810.base 120810_230810.f.unw 0

FLATTENING - backOutput at this stage

Interferogram including topography; unwrapped; unflattened; original size

Unwrapping with scaled interferograms – int 2 (the same)Output at this stage

Interferogram including displacement; unwrapped; unflattened; original size

4. Differential interferogram**DIFFERENTIAL INTERFEROGRAM**

1. create_diff_par 120810_050510.off.par 120810_230810.off.par diff2.2010.diff.par
2. diff_ls_fit 120810_050510.f.unw 120810_230810.f.unw diff22010.diff.par 32 32 –
3. diff_ls_unw 120810_050510.f.unw 120810_230810.f.unw diff22010.diff.par diff2.2010.diff 0
4. rasrmg diff2.2010.5diff 120810.kmli 5000 1 1 0 2 2 - 1. .35 0.0 1 diff2.2010.5diff.bmp

DIFFERENTIAL INTERFEROGRAM**DISPLACEMENT**

5. dispmap diff2.2010.5diff **140809.4.dem** 120810.aslc.par 120810_050510.off.par
 diff2.2010.displ 1
6. dishgt diffx.2010.displ 120810.kmli 5000 1 1 0 0.04 1. .35
7. rashgt diffx.2010.displ 120810.kmli 5000 1 1 0 2 2 0.04 1. .35 diffx.2010.displ.bmp

DISPLACEMENT

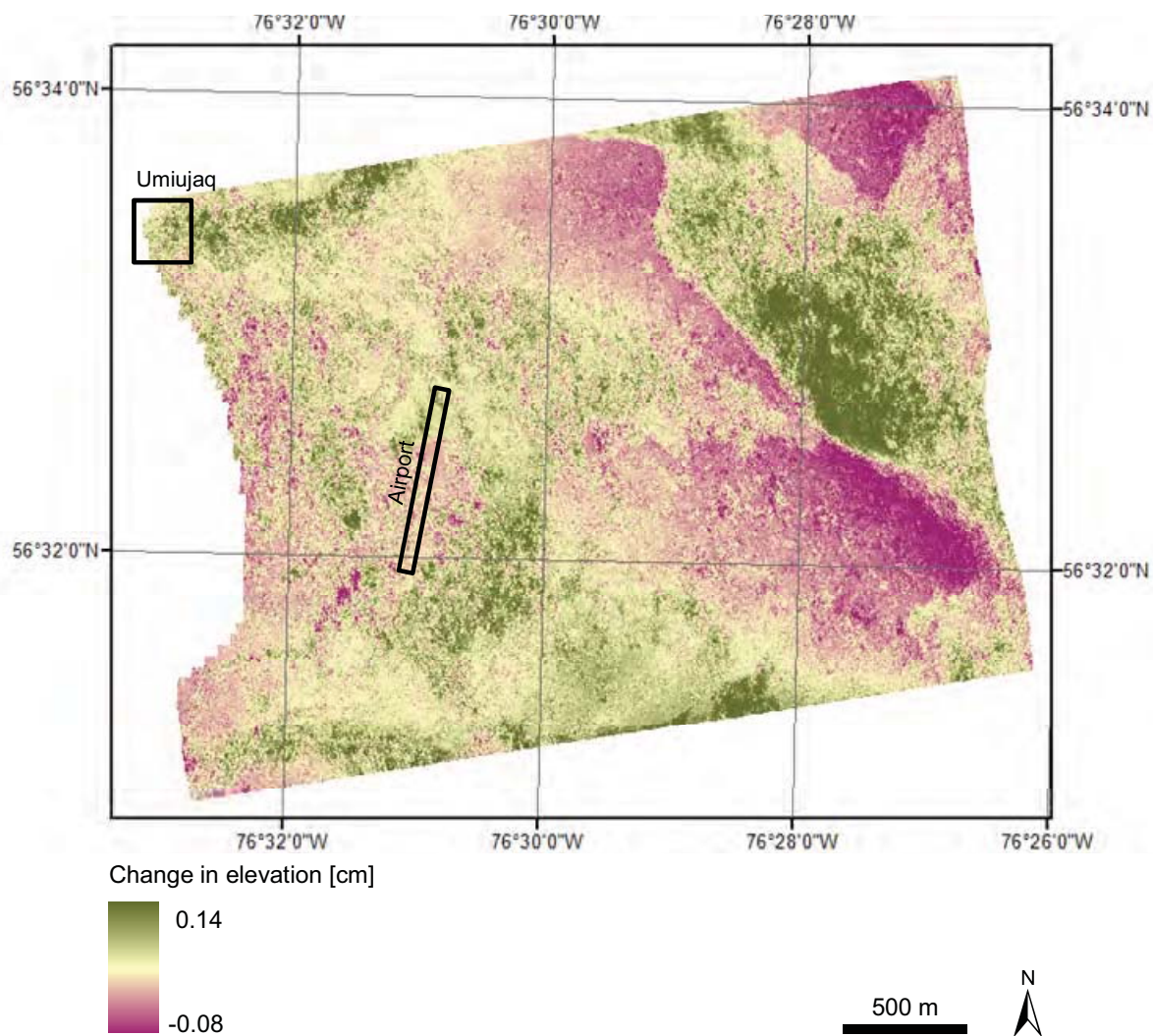
GEOCODING

8. geocode_back diffx.20xx.displ 5000 kumi4.utm2rdc diffx.20xx.displ.utm 1950 1502 0 0
9. data2geotiff kumi4.dem.par diffx.20xx.displ.utm 2 diffx.20xx.displ.tif

GEOCODING

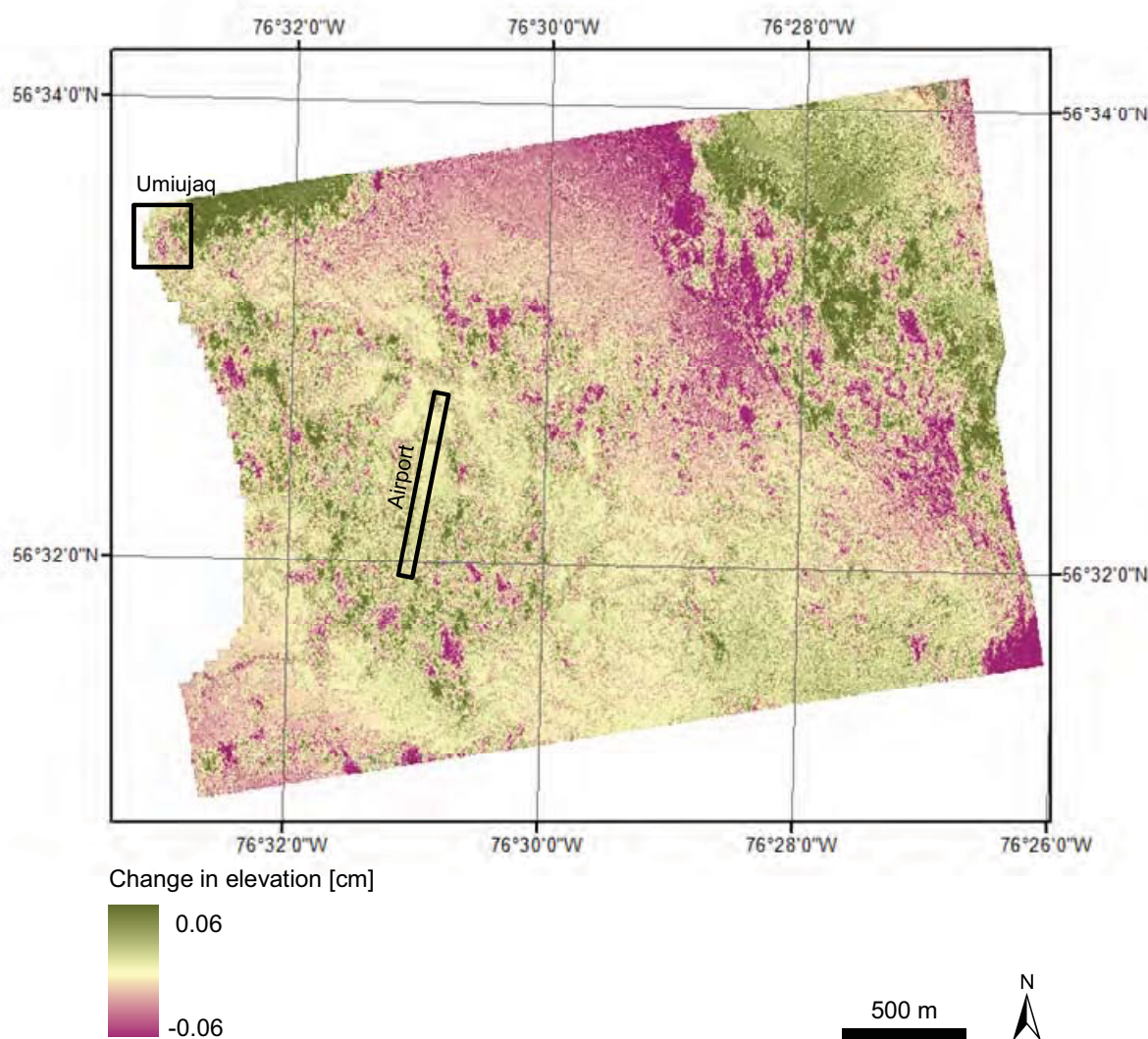
APPENDIX 7**Differential interferograms****Vertical displacement map Diff.2.2009 (Difference May 09 and August 09)**

The displayed values are representing the movements without the postglacial rebound



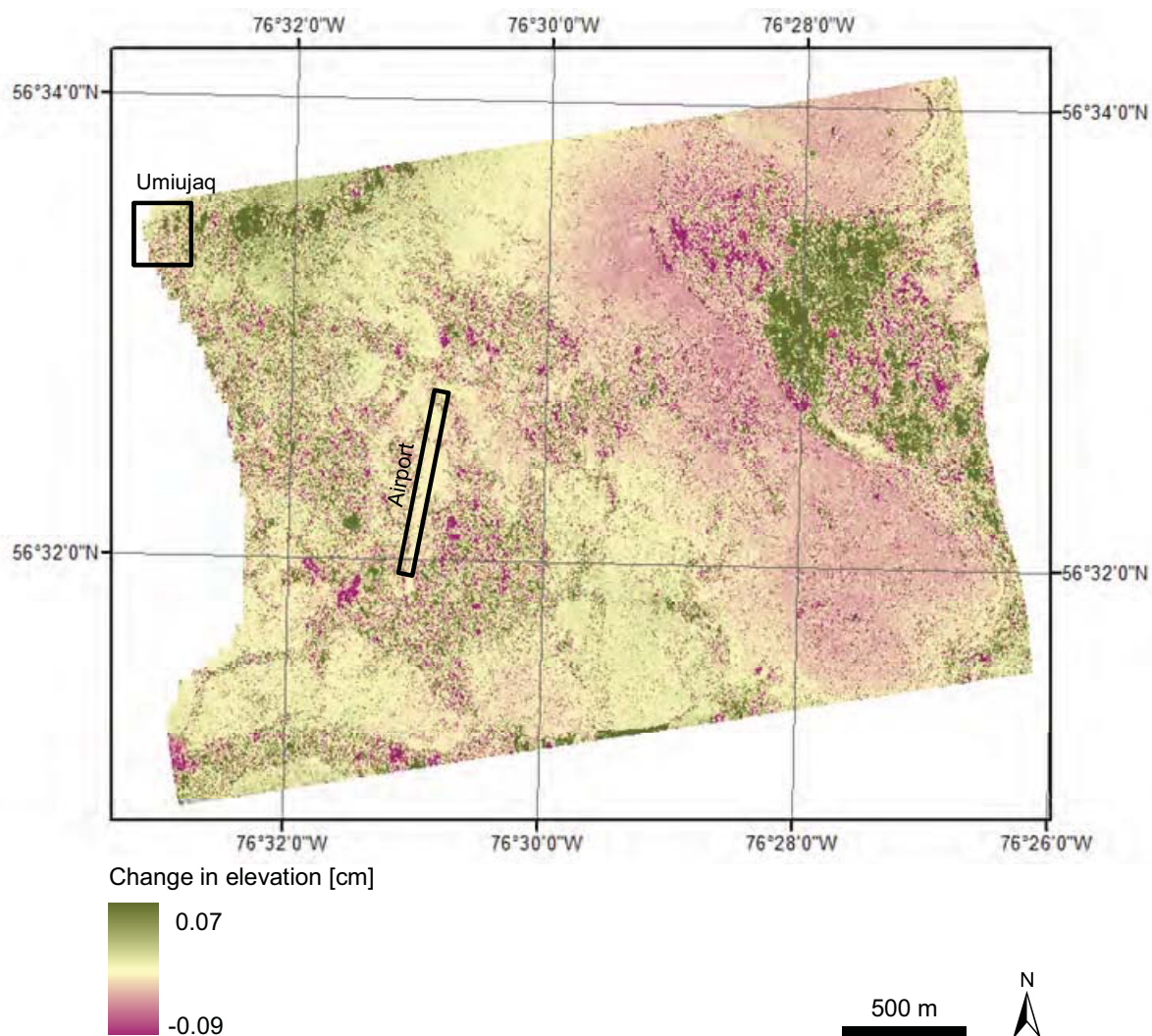
Vertical displacement map Diff2.2010 (Difference May 10 and August 10)

The displayed values are representing the movements without the postglacial rebound



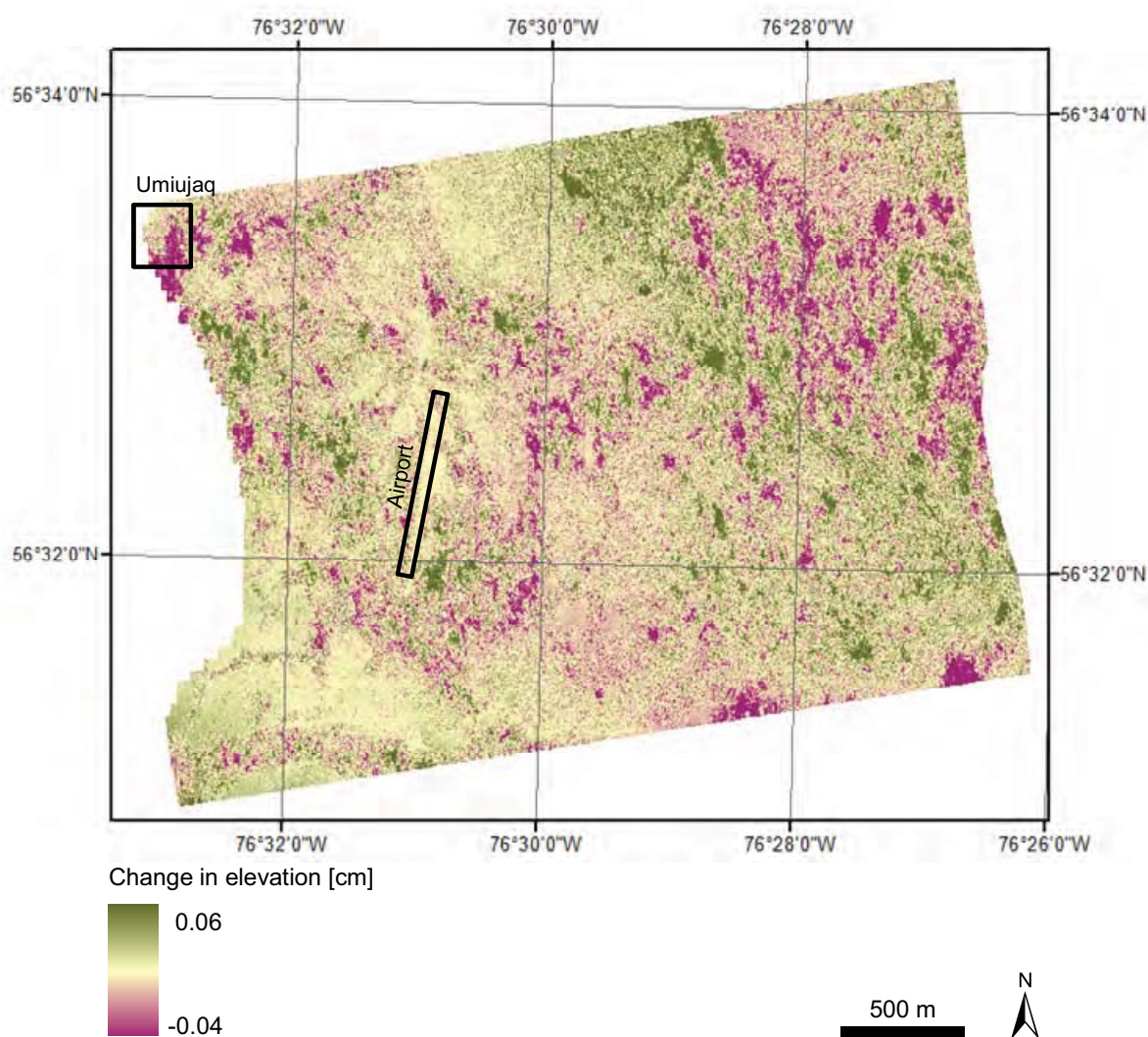
Vertical displacement map Diff3.2009 (Difference August 09 and September 09)

The displayed values are representing the movements without the postglacial rebound



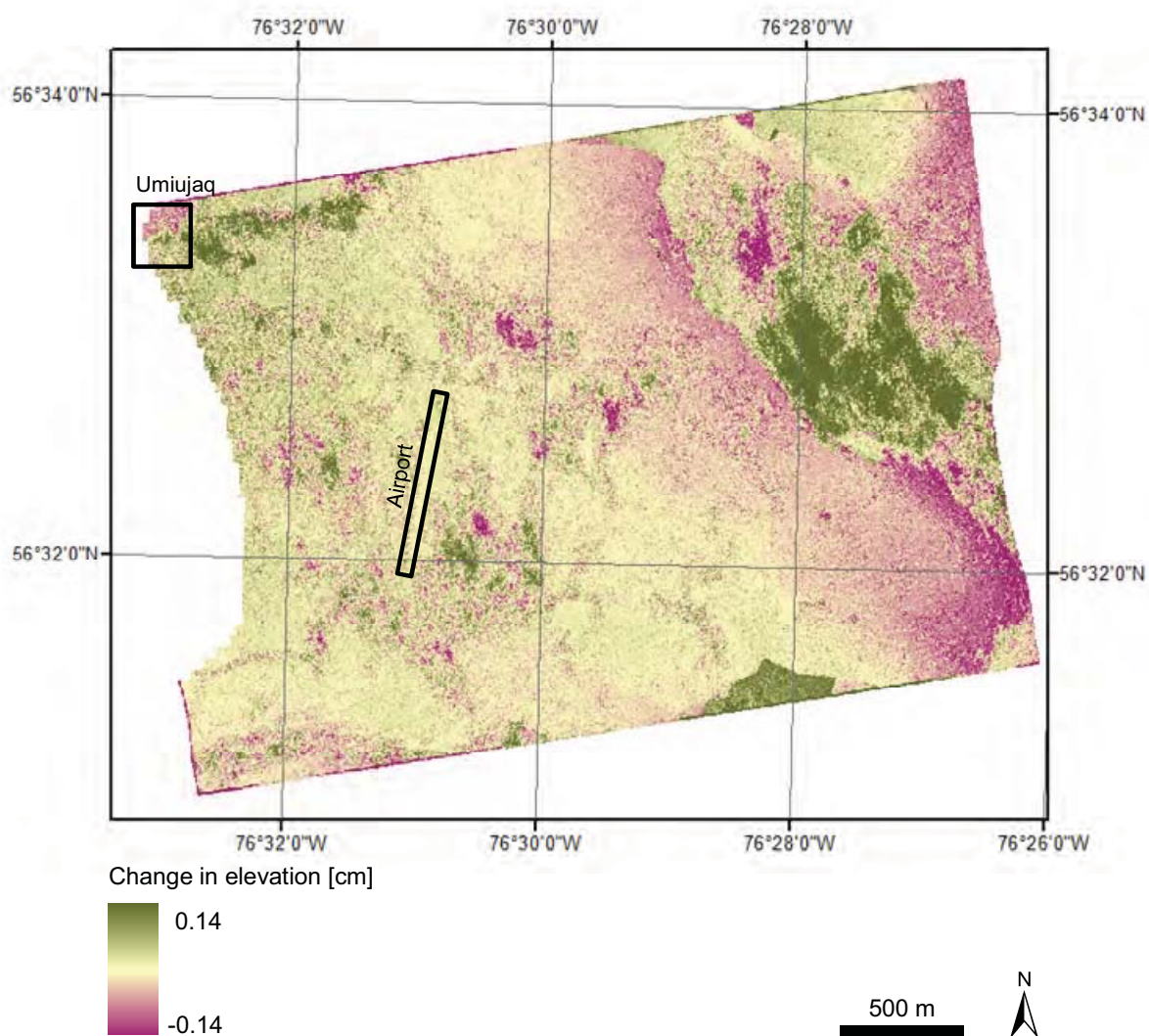
Vertical displacement map Diff4.2009 (Difference August 09 and October 09)

The displayed values are representing the movements without the postglacial rebound



Vertical displacement map Diff4.2010 (Difference August 10 and October 10)

The displayed values are representing the movements without the postglacial rebound



APPENDIX 8

Displacement values for measured points and the related pixels in Diff2.2010

ID	D-InSAR (=- uplift)	D-GPS (- = Uplift)
R1	-0,036	-0,168
R2	-0,030	-0,169
R3	-0,028	-0,134
R5	-0,032	-0,745
R6	-0,037	0,418
R9	-0,022	-0,093
R10	-0,030	-0,141
R11	-0,032	-0,167
R12	-0,029	-0,122
M1	-0,031	NV
M2	-0,033	-0,185
M3	-0,030	-0,505
M4	-0,029	-0,209
M5	-0,017	-0,163
M6	-0,014	0,086
M7	-0,027	0,257
M8	-0,023	-0,075
M9	-0,014	-0,271
M10	-0,019	-0,133
M11	-0,027	-0,679
M12	-0,026	-0,198
M13	-0,021	-0,125
M14	-0,032	NV
I1	-0,025	-0,85
I2	-0,023	-1,131
I3	-0,024	-1,261
I4	-0,024	-1,63
I5	-0,022	-1,879
I6	-0,022	-1,371
I7	-0,030	-0,631
I8	-0,028	-0,787
I9	-0,027	-1,375
I10	-0,015	-1,081
I11	-0,027	-0,976
I12	-0,017	-0,147
I13	-0,035	-0,473

APPENDIX 9

Pictures of field work

Spring 2009



ie from the airport to ards the illage



Ta ing sno samplings
(in this photo: . ay)



asuring the sno temperature
(in this photo: . ay)



Getting ready for the day



gloo for the lunch brea



d-GPS measurements

Summer 2009



Digging for the top of the permafrost 1
(in this photo: I. May)



Digging for the top of the permafrost 2
(in this photo: R. Ludwig)



View at the Richmond Golf



2 meters deep: Finally frozen ground



Cracking soil due to frost heave



Measuring of the soil temperature

Winter/ Spring 2010



Measuring snow in the Lac-Guillaume Delisle graben



Measuring the snow temperature
(in this photo: P. Novalinga)



Installing the base station of the d-GPS
(in this photo: I. May)



Installing a corner reflector
(in this photo: Y. Duguay)



Lac- Guillaume Delisle graben 1
(in this photo: Y. Duguay)



Lac- Guillaume Delisle graben 2

II 20 0



ie to ards the village and theudson ay



Lac-Guillaume Delisle graben



Retracting the corner reflector
(in this photo: D. Sarrazin)



Thermo arst la es south-east of Umiujaq (1)



easuring of lithalsa



Thermo arst la es south-east of Umiujaq (2)

12 Curriculum Vitae

Personal Information

Name: Inga Beate May
 Office address: Department of Geography
 Physical Geography and Environmental Modeling
 Luisenstraße 37
 80333 Munich
 Germany
 Phone: 089 2180-6698
 Email: inga.may@lmu.de

Education

2008 – 2012 PhD studies at the Ludwig-Maximilians-University of Munich, Germany and the Insitute national de la recherché scientifique in Quebec City, Canada
 2003 – 2008 Studies of physical geography at the Ludwig-Maximilians-University of Munich, Germany, with the degree: Diplom-Geographin (Univ.), naturwissenschaftliche Richtung
 Minor subjects: meteorology, remote sensing
 Diploma thesis: „Comparison of two hydrological models for climate change impact assessment“.
 2000 – 2003 Secondary School at the Chrisoph-Probst Gymnasium, Gilching, Germany, with the Abitur (university-entrance diploma)
 1994 – 2000 Secondary School at the Geschwister-Scholl Gymnasium, Sillenbuch, Germany
 1991 – 1994 Elementary School in Heumaden, Germany
 1990 – 1991 Elementary School in Tübingen, Germany

Scientific Career

Since 2008 Lecturer at the Chair of Geography and Geographical Remote Sensing, Department of Geography, Ludwig-Maximilians-University of Munich, Germany
 Since 2008 Scientific assistant at the university of Munich; Working group ‘Physical Geography and Environmental Modeling’ (Prof. Dr. Ludwig)
 03 – 07/ 2007 Student researcher at the chair for Geography and Geographical Remote Sensing at the university of Munich: International project about Integrative watershed modelling in the context of Climate Change
 2005 – 2007 Student researcher at the chair for Geography and Geographical Remote Sensing at the university of Munich. Project GLOWA (Global Changes in the Hydrological Cycle)

Internships

- | | |
|--------------|---|
| 09 – 11/2006 | Internship at Ouranos (Montréal, Canada). Consortium on regional climatology and Adaptation to Climate Change |
| 06 -07/2006 | Internship at GAF AG (Munich, Germany). Application Field: Remote Sensing; Agriculture |
| 04 – 05/2006 | Internship at DLR (German Aerospace Center, Oberpfaffenhofen, Germany). Remote Sensing Technology Institute, Image Science Department |
| 03 2004 | Internship at a reforestation Sation in Jatun Sacha, Ecuador |